The Dissertation Committee for Ming Gu Certifies that this is the approved version of the following dissertation:

Shale Fracturing Enhancement by Using Polymer-Free Foams and Ultra-Light Weight Proppants

Committee:

Kishore K. Mohanty, Supervisor

Julia F. W. Gale

David A. DiCarlo

Jon E. Olson

Mukul M. Sharma

Shale Fracturing Enhancement by Using Polymer-Free Foams and Ultra-Light Weight Proppants

by

Ming Gu, B.E.; M.E.

Dissertation

Presented to the Faculty of the Graduate School of
The University of Texas at Austin
in Partial Fulfillment
of the Requirements
for the Degree of

Doctor of Philosophy

The University of Texas at Austin
December 2013

Dedication

This dissertation is dedicated to my dear wife, Dana Zhang, and my beloved parents, Zhiwei Gu and Bin Liu for their endless love and constant support.

Acknowledgements

I would like to express my sincere gratitude to my supervisor, Dr. Kishore K. Mohanty for his guidance and support throughout my Ph.D. study. The work presented in this dissertation would not have been possible without his continuous encouragement and unreserved knowledge sharing. It has been a really enjoyable and memorable experience to work under his supervision.

I would like to extend my thanks to the members of my dissertation committee, Dr. Julia F.W. Gale, Dr. David A. DiCarlo, Dr. Jon E. Olson and Dr. Mukul M. Sharma for their valuable advice and comments in the course of my dissertation.

My special gratitude goes to Dr. Eric Dao for his constant help and support to my experiments. Glen Baum, Gary Miscoe, Mark Smith and Daryl Nygaard also gave me a lot of help in setting up and conducting my experiments.

I would like to thank my lab mates, Abhishek Gaurav, Arman Shantayev, Eric Schulz, Peila Chen, Rahul Kumar, Shashvat Doorwar, Leizheng Wang, Krishna Panthi, and all other colleagues for extending their help and cooperation to me.

I would like to acknowledge Barbara Messmore for her remarkable work, helpfulness and heart-warming smile during my Ph.D. study.

My appreciation also goes to the Department of Energy, RPSEA (Research Partnership to Secure Energy for America), Schlumberger and Statoil for their financial support, and BJ Services for their supply of experimental samples.

Finally, I would like to thank my family, Zhiwei Gu, Bin Liu and Dana Zhang, for all the love, support and encouragement they gave to me all the way through.

Shale Fracturing Enhancement by Using Polymer-Free Foams and Ultra-Light Weight Proppants

Ming Gu, Ph.D.
The University of Texas at Austin, 2013

Supervisor: Kishore K. Mohanty

Slickwater with sand is the most commonly used hydraulic fracturing treatment for shale reservoirs. The slickwater treatment produces long skinny fractures, but only the near wellbore region is propped due to fast settling of sand. Adding gel into water can prevent the fast settling of sand, but gel may damage the fracture surface and proppant pack. Moreover, current water-based fracturing consumes a large amount of water, has high water leakage, and imposes high water disposal costs. The goal of this project is to develop non-damaging, less water-intensive fracturing treatments for shale gas reservoirs with improved proppant placement efficiency. Earlier studies have proposed to replace sand with ultra-light weight proppants (ULWP) to enhance proppant transport, but it is not used commonly in field. This study evaluates the performance of three kinds of ULWPs covering a wide range of specific gravity and representing the three typical manufacturing methods. In addition to replacing sand with ULWPs, replacing water with foams can be an alternative treatment that reduces water usage and decreases proppant settling. Polymer-added foams have been used in conventional reservoirs to improve proppant placement efficiency. However, polymers can damage shale permeability in unconventional reservoirs. This dissertation studies polymer-free foams (PFF) and evaluates their performance.

This study uses both experiments and simulations to assess the productivity and profitability of the ULWP treatment and PFF treatment. First, a reservoir simulation model is built in CMG to study the impact of fracture conductivity and propped length on fracture productivity. This model assumes a single fracture intersecting a few reactivated natural fractures. Second, a 2D fracturing model is used to simulate the fracture propagation and proppant transport. Third, strength, API conductivity and gravity settling rates are measured for three ULWPs. Fourth, foam stability tests are conducted to screen the best PFF agents and the selected foams are put into a circulating loop to study their rheology. Finally, empirical correlations from the experiments are applied in the fracturing model and reservoir model to predict productivity by using the ULWPs with slickwater or using the PFFs with sand.

Experimental results suggest that, at 4000 psi with concentrations varying from partial monolayer (0.05 lb/ft^2) to multilayer (1 lb/ft^2), ULW-1 (polymeric) is the most deformable with conductivity of 1-10 md-ft. ULW-2 (resin coated and impregnated ground walnut hull) is the second most deformable with similar conductivity. ULW-3 (resin coated porous ceramic) is the least deformable with conductivity of 20-1000 md-ft, which is comparable to sand. Three foam formulations (A, B: regular surfactant foam, C: viscoelastic surfactant foam) are selected based on the stability results of fourteen surfactants. All PFFs exhibit power-law rheological behavior in a laminar flow regime. The power law parameters of the regular surfactant PFF depend on both quality and pressure when quality is higher than 60% but depend on quality only when quality is lower than 60%.

Simulation results suggest that under the optimal concentration of 0.04-0.06 v/v (0.37-0.55 lb/gal) for both ULW-1 and ULW-2, and 0.1 v/v (1.46 lb/gal) for ULW-3, 1-year cumulative production for 0.1 µD shale reservoir is higher than sand by 127% for ULW-1, 28% for ULW-2, and 38% for ULW-3. The productivity benefits decrease as shale permeability increases for all three ULWPs. ULW-1 and ULW-2 have higher productivity benefits for longer production time, while ULW-3 has relatively constant productivity benefits over time. The economic profit of ULW-1 when priced at $5/lb is 2.2 times larger than that of sand for 1-year production in 0.1 µD shale reservoirs; the acceptable maximum price is $10/lb for ULW-1, $6/lb for ULW-2, and $2.5/lb for ULW-

3. The maximum price increases as production time increases. The PFFs with a quality of 60% carrying mesh 40 sand at a partial monolayer concentration of 0.04 v/v (0.88 lb/gal) can generate 50% higher productivity, 74% higher economic profit, and over 300% higher water efficiency than the best slickwater-sand case (mesh 40 sand at 0.1 v/v) for 1-year production in 0.1μD shale reservoirs. The benefits of using the PFFs decrease with increasing shale permeability, increasing production time, or decreasing pumping time. This dissertation gives a range of field conditions where the ULWP and PFF may be more effective than slickwater-sand fracturing.

Table of Contents

List of Tables xiv

List of Figures xvi

Chapter 1 Introduction 1

1.1 Background and Motivation 1

1.2 Objective and Methodology..4

1.3 Outline of the Dissertation 6

References...9

Chapter 2 Impact of Hydraulic Fracture Conductivity and Propped Length on Well Productivity 12

2.1 Literature Review...12

2.2 Reservoir Simulaton Model Built for Parametric Study........................17

2.2.1 Description of Reservoir Simulation Model 17

2.2.2 Gas Desorption...19

2.2.3 Non-Darcy Flow 20

2.2.4 Natural Fracture Modeling..21

2.2.5 Water Recovery 22

2.2.6 Reservoir Fluid Type (Oil vs. Gas)..22

2.2.7 Parameters for Parametric Study 23

2.3 Results and Discussions..25

2.3.1 Dependence of Cummulative Production on Conductivity 25

2.3.2 Critical Conductivity Chart...26

2.3.3 Effects of Nautral Fracture Properties on Critical Conductivitiy.... 27

2.3.3.1 Critical Conductivity vs. NFC 29

2.3.3.2 Normalized Critical Conductivity vs. NFC 31

2.3.3.3 Critical Conductivity vs. NFSPC 32

2.3.3.4 Normalized Critical Conductivity vs. NFSPC 33

2.3.4 Effects of Other Parameters on Critical Conductivity 34

2.3.4.1 Effect of HFSPC 34

2.3.4.2 Effect of Gas Desorption 35

2.3.4.3 Effect of Water Recovery 35

2.3.4.4 Effect of Reservoir Fluid Type 36

2.3.4.5 Effect of BHP...37

2.4 Conclusions..37

Nomenclature..40

References..41

Chapter 3 Modeling of Fracture Propagation, Proppant Transport and Fracture Productivity 64

3.1 Review of Existing Fracture Models 64

3.2 Formulation Applied In Current Fracture Modeling 66

3.2.1 Fracture Propagation Equations for Incompressible Fluids........66

3.2.2 Fracture Propagation Equations for Compressible Fluids 70

3.2.3 Leak-off Modeling...72

3.2.4 Proppant Transport Equations...74

3.2.5 The Solution Algorithm of Current Simulator............................77

3.3 Model Validation 78

3.3.1 Model Verification with Analytical Solutions for Incompressible Fluids..79

3.3.2 Validation of Foam Fracturing Modeling 80

3.3.2.1 The Pressure Impact on Foam Fracturing 81

3.3.2.2 The Leak-off Impact on Foam Fracturing 82

3.3.3 Proppant Settling Predicted by Stokes Law vs. Modified Stokes Law 83

3.4 Coupling Fracture Modeling with Reservoir Simulator 85

3.5 Conclusions..85

Nomenclature..87

References..88

Chapter 4 Experiment and Simulation Study of Ultra-Light Weight Proppants and Their Application in Shale Gas Fracturing......................................99

4.1 Background and Motivation 99

4.2 Review of Existing Light Proppant Study 101

4.3 Experimental Study of ULWPs 105

4.3.1 Approach and Methodology 105

4.3.1.1 Equipment and Process for Testing Mechanical Properties 105

4.3.1.2 Equipment and Process for Testing Proppant Conductivity 106

4.3.2 Experimental Results 107

4.3.2.1 Physical Properties 107

4.3.2.2 Mechanical Properties 108

4.3.2.3 Conductivity 109

4.3.3 Empirical Equations Development 111

4.3.3.1 Empirical Equations for ULWPs Deformability 111

4.3.3.2 Empirical Equations for ULWPs Conductivity 112

4.4 Fracture Modeling & Simulation Study of ULWPs 116

4.4.1 Effects of ULWPs on Propped Area and Conductivity 117

4.4.2 Effects of ULWPs on Fracture Productivity............................118

4.4.3 Effects of ULWPs on Return-On-Fracturing-Investment, "ROFI" 122

4.4.4 Effects of Mixing ULWPs with Sand on Net Present Value (NPV) 125

4.5 Conclusions..127

Nomenclature 132

References...133

Chapter 5 Stability and Rheology Study of Polymer-Free Foam Fracturing Fluids 158

5.1 Introduction..158

5.1.1 Background and Motivation 158

5.1.2 Review of Foam Stability Study..159

5.1.3 Review of Foam Rheology Study 160
5.1.4 Review of Theoretical Foam Rheological Models 162
5.1.5 Objective and Outline 164
5.2 Methodology 165
5.2.1 Static Foam Stability Test...165
5.2.2 Foam Rheology Test (Foam Loop)..166
5.2.3 Rheology Determination...168
5.3 Results and Discussions for Foam Stability Test.................................170
5.3.1 Results for the Qualitative Test (*Step 1*) 170
5.3.2 Results for the Quantitative Test (*Step 2*) 171
5.4 Results and Discussion for Foam Rheology Test 174
5.4.1 Foam Base Fluids...174
5.4.2 Preliminary Results of Shear Stress vs. Shear Rate.................174
5.4.3 Effect of Shear Rate 176
5.4.4 Effect of Foam Quality 177
5.4.5 Effect of Temperature 177
5.4.6 Effect of Pressure 178
5.4.7 Effect of Liquid Composition 178
5.4.8 Comparison with Theoretical Models.....................................179
5.4.9 Empirical Rheological Correlation Development....................180
5.5 Conclusions 182
Nomenclature 184
References 185

Chapter 6 Fracture Modeling and Simulation Study of Polymer-free Foam in Shale Fracturing...205

6.1 Objective 205
6.2 Methodology 206
6.2.1 Foam Rheological Model...206
6.2.2 Propped Fracture Conductivity Model....................................207
6.2.3 Gas Production Simulation 209

6.2.4 Parametric Study Strategy 209

6.3 Results and Discussions 211

6.3.1 Fracture Geometry Created by Water Pad vs. Foam Pad 211

6.3.2 Conductivity and Propped Area Created by Slickwater vs. Foams 212

6.3.3 Fracture Productivity Generated by Slickwater vs. Foams 215

6.3.3.1 Water vs. Foams for Different Permeability Shales 215

6.3.3.2 Water vs. Foams for Different Sand Sizes 218

6.3.3.3 Water vs. Foams for Different Sand Concentrations 220

6.3.4 ROFI Generated by Slickwater vs. Foams 221

6.3.5 ROWI Generated by Slickwater vs. Foams 224

6.3.6 Slickwater vs. Foams at Different Pumping Schedules 225

6.4 Conclusions 228

Nomenclature 231

References 232

Chapter 7 Summary, Conclusions, and Recommendations 252

7.1 Summary 252

7.2 Conclusions 253

7.3 Recommendations for Future Work 258

References 261

Bibliography 263

Vita 273

List of Tables

Table 2.1: Simulation input values for parametric study (Marcellus Dry Gas). 44

Table 2.2: Parametric (hydraulic fracture conductivity & propped length) study matrix. 44

Table 2.3: Natural fracture properties for parametric study. 44

Table 3.1: Reservoir property input for incompressible fluid fracturing verification. 90

Table 3.2: Selected input parameters for foam fracturing modeling. 90

Table 4.1: Comparison of some typical light weight proppants. 136

Table 4.2: Input of reservoir properties and completion parameters for parametric study of ULWP treatment. 136

Table 4.3: Cases for parametric study of ULWP treatment. 137

Table 4.4: Treatment volumes and costs for a single wing of a planar fracture. 138

Table 5.1: Foam base fluids and test matrix. 187

Table 5.2: Power law parameters for foam A at 95 ^{o}F. 188

Table 5.3: Power law parameters for foams A, B and C at 1000 psi. 189

Table 6.1: Input of reservoir properties and completion parameters for parametric study of polymer-free foam fracturing. 233

Table 6.2: Cases of parametric study for polymer-free foam fracturing. 234

Table 6.3: Treatment volumes and costs for single wing of a planar fracture. 235

Table 6.4: Cases for parametric study of impact of pumping time on foam fracturing. 236

List of Figures

Figure 2.1: McGuire and Sikiora's producing-rate folds-of-increase curves (McGuire and Sikiora, 1960). 45

Figure 2.2: Tinsley's producing-rate folds-of-increase curves (Tinsley et al., 1969). 45

Figure 2.3: Agarwal's type curves with propped vertical fractures at transient flow (Agarwal et al., 1979). 46

Figure 2.4: Cinco's type curves with propped vertical fractures at transient flow (Cinco et al., 1978)...46

Figure 2.5: Tannich and Nierode's type curves for gas wells (base case) (Tannich and Nierode, 1985)...47

Figure 2.6: The reservoir simulation model of the one fourth of the fracture and the corresponding drainage area. 47

Figure 2.7: The validation of grid refinement strategy.......................................48

Figure 2.8: Gas Desorption vs. Non Gas Desorption (Lf: 400ft, HFC: 1000 md-ft, NFSPC: 50ft, NFC: 0.1md-ft). 48

Figure 2.9: Darcy Flow vs. Non-Darcy Flow (Rubin,2010). 49

Figure 2.10: Single Porosity Effective Perm. Model vs. Discrete Natural Fracture Model (Lf: 400ft, HFC: 1000 md-ft, NFSPC: 50ft, NFC: 0.1md-ft).49

Figure 2.11: Water Flowing-back vs. Dry Gas (Lf: 400ft, HFC: 1000 md-ft, NFSPC: 50ft, NFC: 0.1md-ft)..50

Figure 2.12: Black Oil vs. Dry Gas (Lf: 400ft, HFC: 1000 md-ft, NFSPC: 50ft, NFC: 0.1md-ft). 50

Figure 2.13: Cumulative Productions vs. HF Conductivity at different production time (200 nD, no NF). 51
Figure 2.14: Title of Relative Cum. Prod. vs. HF Conductivity at different production time (200 nD, no NF). 51
Figure 2.15: Critical Conductivity vs. Propped Length for different production time (200 nD, no NF). 52
Figure 2.16: Critical Conductivity vs. Propped Length for different production time (20 nD, no NF). 52
Figure 2.17: Pressure fields after different production time for non-naturally fractured and naturally fractured shale reservoirs (k_m=200 nD). 53
Figure 2.18: Critical Conductivity vs. Production Time for 200 nD matrix with and without natural fractures. 53
Figure 2.19: Pressure fields after different production time for non-naturally fractured and naturally fractured shale reservoirs (k_m=20 nD). 54
Figure 2.20: Critical Conductivity vs. Production Time for 20 nD matrix with and without natural fractures. 54
Figure 2.21: Critical Conductivity vs. NFC at different propped lengths and production time (k_m=200 nD). 55
Figure 2.22: Critical Conductivity vs. NFC at different propped lengths and production time (k_m=20 nD). 55
Figure 2.23: Normalized Critical Conductivity vs. NFC at different propped lengths and production time (k_m=200 nD). 56
Figure 2.24: Normalized Critical conductivity vs. NFC at different propped lengths and production time (k_m=20 nD). 56

Figure 2.25: Critical Conductivity vs. NFSPC at different propped lengths and production time (k_m=200 nD). 57
Figure 2.26: Critical Conductivity vs. NFSPC at different propped lengths and production time (k_m=20 nD). 57
Figure 2.27: Normalized Critical Conductivity vs. NFSPC at different propped lengths and production time (k_m=200 nD). 58
Figure 2.28: Normalized Critical Conductivity vs. NFSPC at different propped lengths and production time (k_m=20 nD). 58
Figure 2.29: Comparison of critical conductivity at different hydraulic fracture spacing. 59
Figure 2.30: Relative error of critical conductivity caused by hydraulic fracture spacing. 59
Figure 2.31: Comparison of critical conductivity with and without considering gas desorption. 60
Figure 2.32: Relative error of critical conductivity caused by gas desorption. ...60
Figure 2.33: Comparison of critical conductivity with and without considering water recovery. 61
Figure 2.34: Relative error of critical conductivity caused by water recovery. ..61
Figure 2.35: Comparison of critical conductivity of different reservoir fluid types.62
Figure 2.36: Relative error of critical conductivity caused by the change of the reservoir fluid type. 62
Figure 2.37: Comparison of critical conductivity at different flowing BHPs. 63
Figure 2.38: Relative error of critical conductivity caused by the increase of the BHP. 63
Figure 3.1: Schematic of the fracture model (PKN). 91

Figure 3.2: Different leak-off periods and the corresponding governing parameters. 91
Figure 3.3: Flowchart for fracture modeling. 92
Figure 3.4: Comparison of predicted fracture dimensions from analytical and numerical models (no leak-off). 93
Figure 3.5: Comparison of predicted fracture dimensions from analytical and numerical models (high leak-off). 93
Figure 3.6: Pressure distribution along the propagation direction for different foam qualities at 10 μD. 94
Figure 3.7: Foam quality distribution along the propagation direction for different foam qualities at 10 μD. 94
Figure 3.8: Maximum fracture width distribution for different foam qualities (solid line: modeling with pressure impact, dashed line: no pressure impact). 95
Figure 3.9: Relative permeability curve for water-gas two-phase flow. 95
Figure 3.10: Foam quality distribution along the propagation direction for different foam qualities with different leak-off assumptions at 1 μD. 96
Figure 3.11: Maximum fracture width distribution along the propagation direction for different foam qualities with different leak-off assumptions at 1 μD.96
Figure 3.12: Proppant distribution in water frac predicted by Stokes Law vs. Modified Stokes law. 97
Figure 3.13: Proppant distribution in foam (75%) frac predicted by Stokes Law vs. Modified Stokes law. 97
Figure 3.14: The schematic figure of the optimization loop. 98

Figure 4.1: A comparison of static proppant settling rates in water (Rickards et al., 2003). 139

Figure 4.2: Mfrac graphs of the propped width profiles for Ottawa sand and ULW1.25 in a slickwater treatment at 80BPM (Rickards et al., 2003). 139

Figure 4.3: Permeability & Conductivity vs. Closure Stress @ 150 °F & 1 lb/ft^2 for different resin coated and non-coated proppants (Wood et al., 2003). 140

Figure 4.4: Fracture conductivity vs. 20/40 sand concentration at low temperature and closure stress (Darin and Huitt, 1960). 140

Figure 4.5: Conductivity of partial monolayer to multi-layers of 12/20 ULW-1.25 at various closure stresses and 100 °F (Brannon et al., 2004). 141

Figure 4.6: Conductivity vs. Proppant concentration for 14/40 ULW-1.05 at 150 °F, 1000-5000 psi closure stress (Brannon and Starks II, 2008). 141

Figure 4.7: Comparison of different treatments of using sand and ULW-1.05 through fracture modeling (Brannon and Starks II, 2008). 142

Figure 4.8: Light microscope images of 40/70 SSP grain at low and high brightness (Mahoney et al., 2013). 142

Figure 4.9: Equipment for proppant strength test. 143

Figure 4.10: System for proppant API conductivity test. 143

Figure 4.11: Dimensions of three ULWPs and their close-up images. 144

Figure 4.12: Sieve size distributions of the three ULWPs. 144

Figure 4.13: Stress vs. Strain for proppant packs of three ULWPs at 203 °F. ..145

Figure 4.14: Strength test for single particle of three ULWPs at 203 °F. 145

Figure 4.15: Conductivity vs. Areal Concentration for ULW-1 at 203 ^{o}F, 1000-6000 psi. 146

Figure 4.16: Conductivity vs. Areal Concentration for ULW-2 at 203 ^{o}F, 1000-6000 psi. 146

Figure 4.17: Conductivity vs. Areal Concentration for ULW-3 at 203 ^{o}F, 1000-6000 psi. 147

Figure 4.18: The schematic figure of the proppant deformation at increasing load for three ULWPs. 147

Figure 4.19: Fracture Flow Capacity vs. Areal Concentration for ULW-1 at partial monolayer concentration. 148

Figure 4.20: Fracture Flow Capacity vs. Areal Concentration for ULW-2 at partial monolayer concentration. 148

Figure 4.21: Fracture Flow Capacity vs. Areal concentration for ULW-3 at partial monolayer concentration. 149

Figure 4.22: Conductivity predicted by empirical correlations and experimental results for ULW-1 at 203^{o}F and 4000 psi. 149

Figure 4.23: Conductivity predicted by empirical correlations and experimental results for ULW-2 at 203^{o}F and 4000 psi. 150

Figure 4.24: Conductivity predicted by empirical correlations and experimental results for ULW-3 at 203^{o}F and 4000 psi. 150

Figure 4.25: Conductivity distributions for different proppants in a long-time treatment and 0.1 μD shale. 151

Figure 4.26: Conductivity distributions for different proppants in a long-time treatment and 10 μD shale. 151

Figure 4.27: Conductivity distributions for different proppants in a short-time treatment and 0.1 μD shale. 152
Figure 4.28: Conductivity distributions for different proppants in a short-time treatment and 10 μD shale. 152
Figure 4.29: Normalized Productivity vs. Production Time for different proppants, long time treatment and 0.1 μD shale. 153
Figure 4.30: Normalized Productivity vs. Production Time for different proppants, long time treatment and 1 μD shale. 153
Figure 4.31: Normalized Productivity vs. Production Time for different proppants, long time treatment and 10 μD shale. 154
Figure 4.32: Normalized Productivity vs. Production Time for different proppants, short time treatment and 0.1 μD shale. 154
Figure 4.33: Normalized Productivity vs. Production Time for different proppants, short time treatment and 1 μD shale. 155
Figure 4.34: Normalized Productivity vs. Production Time for different proppants, short time treatment and 10 μD shale. 155
Figure 4.35: Normalized ROFI versus Proppant Injection Volume Concentration for ULW-1. 156
Figure 4.36: Normalized ROFI versus Proppant Injection Volume Concentration for ULW-2. 156
Figure 4.37: Normalized ROFI versus Proppant Injection Volume Concentration for ULW-3. 156
Figure 4.38: Normalized NPV (NPV/ROFI of Base Sand Case) generated from adding ULW1 at different volume ratios in a sand treatment. 157

Figure 5.1: Testing example results from qualitative foam static stability test - *step 1*. 190

Figure 5.2: Setup for quantitative foam static stability test - *step 2* (a: schematic figure; b: photograph of real system). 190

Figure 5.3: Schematic figure of the foam loop for foam rheology test. 191

Figure 5.4: Photograph of the foam loop system. 191

Figure 5.5: Foam stability for different liquid compositions (surfactant types and the addition of stabilizer: *Glycero*). 192

Figure 5.6: Foam stability for different NP numbers. 192

Figure 5.7: Foam stability for different surfactant concentrations. 193

Figure 5.8: Foam stability for different temperatures. 193

Figure 5.9: Foam stability for different bubble sizes. 194

Figure 5.10: Wall Shear Stress vs. Apparent Shear Rate for foam A at 95 °F. .194

Figure 5.11: Wall Shear Stress vs. Apparent Shear Rate for foam B at 95 °F. .195

Figure 5.12: Wall Shear Stress vs. Apparent Shear Rate for foam C at 95 °F. .195

Figure 5.13: Apparent viscosity as a function of intrinsic shear rate for foam A at 95 °F. 196

Figure 5.14: Apparent viscosity as a function of intrinsic shear rate for foam B at 95°F. 196

Figure 5.15: Apparent viscosity as a function of intrinsic shear rate for foam C at 95 °F. 197

Figure 5.16: Effect of temperature on apparent viscosity for foam A at 500 s^{-1}. 197

Figure 5.17: Effect of temperature on apparent viscosity for foam B at 500 s^{-1}. 198

Figure 5.18: Effect of temperature on apparent viscosity for foam C at 500 s^{-1}. 198

Figure 5.19: Apparent Viscosity vs. Shear Rate for foam base fluids B and C. 199

Figure 5.20: Pressure dependence of the apparent viscosity for foam A at 500 s^{-1}.199

Figure 5.21: Pressure effect on the power law index n (solid dots: experimental results, lines: regression results, blank dots: predictions from Eqs. 5.22 &33). 200

Figure 5.22: Pressure effect on the consistency index K (solid dots: experimental results, lines: regression results, blank dots: predictions from Eqs. 5.22 &33). 200

Figure 5.23: Effect of foaming agents on apparent foam viscosity at 95 °F, 1000 psi and 200^{-1}. 201

Figure 5.24: Foam bubble texture images for foam A, 95 °F and 1000 psi. 201

Figure 5.25: Bubble size distribution for foam A, 95 °F and 1000 psi. 202

Figure 5.26: Viscosity ratio, H as a function of foam quality Q as predicted by different theoretical models and as measured (Foam A, 95 °F and 1000 psi). 202

Figure 5.27: Comparison of the experimental results and predictions by Princen and Kiss model (Foam A, 95 °F and 1000 psi). 203

Figure 5.28: Power law index n for foam A at 1000 psi (n_0). 203

Figure 5.29: Consistency index K for foam A at 1000 psi (K_0). 204

Figure 6.1: Conductivity of 20 and 40 mesh sands at 4000 psi confining pressure. 237

Figure 6.2: Schematic of the reservoir simulation model. 237

Figure 6.3: Schematic of the parametric study loop. 238

Figure 6.4: Average fracture widths along fracture length created by different pads for a 0.1 μD shale. 238

Figure 6.5: Average fracture widths along fracture length created by different pads for a 1 μD shale. 239
Figure 6.6: Average fracture widths along fracture length created by different pads for a 10 μD shale. 239
Figure 6.7: Leak-off volume percentages as a function of foam quality for different permeability shales. 240
Figure 6.8: Conductivity distributions created by slickwater with mesh 20 and 40 sand in a 1 μD shale. 240
Figure 6.9: Conductivity distributions created by 60% foam with mesh 20 and 40 sand in a 1 μD shale. 241
Figure 6.10: Conductivity distributions created by 70% foam with mesh 20 and 40 sand in a 1 μD shale. 241
Figure 6.11: Conductivity distributions created by 80% foam with mesh 20 and 40 sand in a 1 μD shale. 242
Figure 6.12: 1 Year Cumulative Productivity vs. Sand Injection Amount for slickwater and different quality foams in 0.1 μD. 242
Figure 6.13: 1 Year Cumulative Productivity vs. Sand Injection Amount for slickwater and different quality foams in 1 μD. 243
Figure 6.14: 1 Year Cumulative Productivity vs. Sand Injection Amount for slickwater and different quality foams in 10 μD. 243
Figure 6.15: 5 Year Cumulative Productivity vs. Sand Injection Amount for slickwater and different quality foams in 0.1 μD. 244
Figure 6.16: 5 Year Cumulative Productivity vs. Sand Injection Amount for slickwater and different quality foams in 1 μD. 244

Figure 6.17: 5 Year Cumulative Productivity vs. Sand Injection Amount for slickwater and different quality foams in 10 μD. 245
Figure 6.18: 10 Year Cumulative Productivity vs. Sand Injection Amount for slickwater and different quality foams in 0.1 μD. 245
Figure 6.19: 10 Year Cumulative Productivity vs. Sand Injection Amount for slickwater and different quality foams in 1 μD. 246
Figure 6.20: 10 Year Cumulative Productivity vs. Sand Injection Amount for slickwater and different quality foams in 10 μD. 246
Figure 6.21: Normalized ROFI vs. Sand Injection Amount for slickwater and different quality foams in 0.1 μD. 247
Figure 6.22: Normalized ROFI vs. Sand Injection Amount for slickwater and different quality foams in 1 μD. 247
Figure 6.23: Normalized ROFI vs. Sand Injection Amount for slickwater and different quality foams in 10 μD. 248
Figure 6.24: Normalized ROWI vs. Sand Injection Amount for slickwater and different quality foams in 0.1 μD. 248
Figure 6.25: Normalized ROWI vs. Sand Injection Amount for slickwater and different quality foams in 1 μD. 249
Figure 6.26: Normalized ROWI vs. Sand Injection Amount for slickwater and different quality foams in 10 μD. 249
Figure 6.27: Conductivity distributions created by slickwater and 60% foam at different pumping time and different permeability shales. 250
Figure 6.28: Normalized ROFI and Normalized ROWI vs. Total Pumping Time for slickwater and 60% foam in a 0.1 μD shale. 250

Figure 6.29: Normalized ROFI and Normalized ROWI vs. Total Pumping Time for Slickwater and 60% foam in a 1 μD shale. 251
Figure 6.30: Normalized ROFI and Normalized ROWI vs. Total Pumping Time for Slickwater and 60% foam in a 10 μD shale. 251

Chapter 1: Introduction

1.1 BACKGROUND AND MOTIVATION

Production of oil and gas from shale reservoirs has revitalized the domestic energy production in US in the last 5 years (King, 2010). It is reported in 2011 that more than 40% of total natural gas produced in US came from tight and shale gas resources (Newell, 2011). The success of gas production from ultra-low permeability reservoirs like shale, which has matrix permeability commonly less than 1 μd, can be mainly attributed to horizontal drilling and multiple hydraulic fracturing stimulations (McDaniel, 2010). Hydraulic fracturing is a stimulation technique to create high conductivity conduits and large contact areas between wellbores and ultra-low permeability reservoirs by injecting a pressurized fluid mixed with proppants into the subsurface. Proppants are solid particles preventing the created fractures from closure after the hydraulic pressure is relieved (Economides and Martin, 2007). The proppant laden fluids most often used are either gelled fluids, which favor enhanced fracture width, or slickwater fluids, which favor enhanced fracture length (Biot and Medlin, 1985). The commonly used proppants are sand, ceramics and bauxite.

For reservoirs with permeability of greater than 1 mD, gelled fluids (linear or cross-linked) are usually used to place sands or ceramics in a thick pack across the fracture face. Although gelled fluid can efficiently carry and place the sand proppants due to its high viscosity, polymer residues lead to permeability damage to formation and proppant pack. Furthermore, due to the high water leakage, a gel filter cake may be built upon fracture face, which has a large yield stress and is hard to remove without adding breakers (Xu et al., 2011, Ouyang et al., 2012). Another issue is that high viscosity fluids can break out of the pay zone in later treatment stages due to the fast building-up of the net pressure in the upstream of the fracture. These characteristics from gel fluid fracturing treatment can result in negative impacts on well production (Fredd et al., 2000).

For ultra-low permeability shale reservoirs, the most desirable hydraulic fracture system is long and skinny fractures. Thus, the lower viscosity slickwater could be a better fracturing fluid than gelled fluids for shale reservoirs. Typical slickwater is composed of over 99% water and less than 1% other additives including acid, anti-bacterial agent, breaker, clay stabilizer, corrosion inhibitor, friction reducer, surfactant etc. (Palisch et al., 2010). Early days of trial and error experiences in the Barnett play show that pumping large volumes of slickwater with high mesh sand at a high flow rate can create economically successful wells (Baihly et al., 2010, Coulter et al., 2004).

The success of the slickwater treatment is mainly attributed to its cheap price and capability of creating large stimulated reservoir volumes (Warpinski et al., 2005). Other advantages of using slickwater are less complicated facilities, lower gel residues and better fracture containment. However, because of its lower viscosity, conventional proppants, such as sand, ceramic, and sintered bauxite, will settle down fast to the bottom of the propagating fracture, which highly increases the screening out risks and decreases the propped lengths and areas (Mahoney et al., 2013, Gadde and Sharma, 2005). It is known that hydraulic fracture deliverability is largely defined by the propped area exhibiting sufficient conductivity contrast to the reservoir (Brannon and Starks II, 2008). So the low proppant transport efficiency may reduce the benefits of using slickwater, leading to sub-optimal production rates (Bulova et al., 2006). Another big issue of slickwater fracturing is large water consumption and disposal. The large water consumption not only brings great competition with other activities for fresh water demands, but also becomes a big economic problem for some fields without enough water sources. The inappropriate water disposal after fracturing can also bring environmental problems and largely increase post-treatment cost (Nakhwa et al., 2013).

To make the proppants travel further into the fractures before settling, one can use lighter proppants, more viscous fracturing fluids, or a combination of the two.

For ultra-light weight proppants (ULWPs), they are lighter than conventional proppants (specific gravity or SG: 1-2), but strong enough to withstand reservoir stresses (Mahoney et al., 2013, Brannon and Starks II, 2009, Gaurav et al., 2010, 2012). Some of them are made of light materials like polymer (Brannon and Starks II, 2009, Gaurav et al., 2010, 2012). Some of them are made of heavy, hard materials coated by light materials, such as resin (Brannon and Starks II, 2009, Gaurav et al., 2010, 2012) or hydrogels (Mahoney et al., 2013), to decrease the nominal specific gravity. Others may be made by creating a large amount of dead pores inside the strong materials such as porous ceramic (Gaurav et al., 2010, 2012). However, most ULWPs cannot provide as much conductivity as conventional proppants due to their weaker strengths. Furthermore, if the same volume of ULWPs and sand are pumped, ULWPs would form a thinner pack than sand because they cover more area. These two factors lead to much lower fracture conductivity for the ULWP treatment compared with sand. Another big issue of ULWP is the more complex manufacturing process and hence higher proppant cost.

For high viscosity fluids, there are usually two ways to increase the fracturing fluid viscosity. One way is to add polymers, such as guar and guar derivatives. Common linear gel fluids have Fann viscosities from 10 to 200 cp depending on the polymer concentrations ranging from 20 to 80 lbm/Mgal (Sudhakar and Shah, 2004). Cross-linking these polymers can further increase their viscosities to an order of 1000 cp. However, the polymer molecules can plug the small pores of the fracture surface and decrease the gas flow (Gidley et al. 1989). The second way is to use foam-based fracturing fluids or energized fracturing fluids. Typical foams applied in the field have a quality (gas percentage) of 70 to 80%. At this quality range, foam bubbles are pushed against each other to form a cellular structure, which promise an effective viscosity much higher than water. The commonly used foams in fracturing treatment are composed of water, a foaming agent (surfactant), a stabilizer/viscosifier (polymer additives such as guar gum, HPG, or Xanthan gum) and gas (Reidenbach et al., 1986, Bonilla and Shah, 2000, Sani et al., 2001, Khade and Shah, 2002). In addition to the advantage of better proppant transport capacity, compared with slickwater fracturing, foam fracturing has other advantages including minimization of water use and disposal, reduced water damage, better leak-off control, and higher water recovery efficiency. The disadvantages include higher costs, higher surface pumping pressure, more complex facilities, and lower proppant carrying concentration (Gidley et al. 1989).

1.2 OBJECTIVE AND METHODOLOGY

The major goal of this dissertation is to evaluate ultra-light weight proppants (ULWPs) and polymer-free foams to improve the efficiency of current slickwater fracturing treatment in shale reservoirs. The efficiency includes proppant placement efficiency (uniform and deep proppant distribution) and water usage efficiency (using less water to generate comparable or better economic profits). Through the study, treatments with ULWPs and polymer-free foams will be developed to place proppant more efficiently and minimize polymer damage, water damage, water usage and post-treatment cost for fluid disposal.

For the proppant study, the work focuses on three ultra-light weight proppants, ULW-1 (polymeric), ULW-2 (resin coated and impregnated ground walnut hull) and ULW-3 (resin coated ceramic), supplied by BJ services. The physical properties of these three proppants have been evaluated along with their mechanical properties. These tests are followed by API conductivity measurements of various concentrations of proppants at different stresses levels. Based on the experimental results, long-term conductivity is developed as a function of proppant concentration and closure stress for the ULWPs.

For the polymer-free foam study, the work focuses on developing aqueous foams without polymer additives, which are stable enough to withstand high temperature and pressure. Surfactant and temperature are varied for the foam stability experiment to find the best formulations for polymer-free foams. The selected foaming agents, gas and brine are put in a recirculating foam loop to create homogeneous foams and study foam rheology under the typical shear conditions of fracturing, various pressures and temperatures. Based on the test, rheological models for polymer-free foams are developed as a function of foam quality, temperature and pressure.

The experimental results of the ULWPs and polymer-free foams are incorporated in fracture modeling and reservoir simulation to evaluate their performances in shale fracturing. For fracture modeling, a simulator is developed to model the bi-wing planar fracture propagation coupled with proppant transport. The simulator can either deal with incompressible fracturing fluid (e.g. slickwater) or compressible fracturing fluid (e.g. foam). The simulation results of fracture geometries (width and length) and proppant distributions are imported into the reservoir simulator CMG to predict the fracture productivity. For different permeability shale reservoirs, the performance of stimulated wells completed by injecting different fracturing fluids (water and different quality polymer-free foams) with different kinds of proppants (sand, ULW-1, 2, 3, mixture) at different proppant concentrations are compared. Based on the simulation results, the impact of the polymer-free foams and ULW proppants on shale fracturing are evaluated.

1. 3 OUTLINE OF THE DISSERTATION

Chapter 1 introduces the background and motivation, the objective and methodology, and the structure of the dissertation.

Chapter 2 focuses on the study of the impact of hydraulic fracture conductivity and propped length on well productivity in naturally fractured shale reservoirs. It first reviews the various graphical and computerized methods developed in the past for estimating the effects of fracture length and fracture conductivity on well productivity in conventional, non-naturally fractured reservoirs. Then, it introduces a comprehensive reservoir model built for the parametric study. Through the study, the effect of hydraulic fracture conductivity and propped length on fractured well productivity in a naturally fractured reservoir is examined. The critical conductivity, beyond which the production is insensitive to the conductivity, is found as a function of propped length, production time, and other parameters, such as reactivated natural fracture properties, cluster spacing, gas desorption, water recovery, reservoir fluid type and flowing BHP. This study helps understand the minimum conductivity required to fully stimulate different propped lengths within different production time frames for different treatment designs and shale reservoirs with or without natural fractures.

Chapter 3 focuses on the development of a fracture modeling simulator. It first reviews past fracturing models, then introduces the formulations and algorithm implemented in our fracture modeling simulator, and finally illustrates the important features of the simulator through discussion of some preliminary results. This chapter and Chapter 2 are methodology sections, where we have built some tools to evaluate ULWP and PFF in the next chapters.

Chapter 4 focuses on the experiment and simulation study of three ultra-light weight proppants (ULWPs). It first reviews the existing study on light proppants.

Following that, the physical properties, mechanical properties and conductivity of the three ULWPs are tested. Based on the experimental results, empirical conductivity correlations for the three light proppants are developed as a function of proppant concentration for different confining stresses. The physical properties and conductivity correlations are combined with fracture modeling developed in Chapter 3 and reservoir simulation model developed in Chapter 2 to evaluate the impact of the ULWPs on fracture deliverability and stimulation value for typical shale reservoirs.

Chapter 5 focuses on the development of polymer-free foams (PFFs) through stability test and foam rheology test. It first reviews the past experimental work on foam fracturing fluids. Then it introduces the experimental setups and procedures for foam stability test and rheology test in this study. Following that, important experimental results are exhibited and discussed. Based on the stability test, the best liquid formulations are developed to generate foams sufficiently stable to withstand harsh reservoir conditions during typical treatment time. Based on the rheology test, empirical rheological models are developed as a function of the foam quality for wet foams ($Q<60\%$) and as a function of the foam quality and pressure for dry foams ($Q\geq60\%$).

Chapter 6 utilizes the rheological models developed in Chapter 5 in the fracture modeling developed in Chapter 3 to predict the fracture geometry and proppant distribution created by the PFFs. The predictions are then incorporated into the reservoir simulation model developed in Chapter 2 to evaluate the resulting fracture productivity, Return-On-Fracture-Investment (ROFI), and Return-On-Water-Investment (ROWI). By comparing the results, the fracturing performance of the polymer-free foams versus slickwater is investigated for different permeability shales and varied treatment design parameters including foam quality, sand size, sand injection concentration, and pumping schedule.

Chapter 7 summarizes major conclusions and contributions from this dissertation and provides recommendations for future work.

References

Baihly, J., Altman, R., Malpani, R., and Luo, F. 2010. Shale Gas Production Decline Trend Comparison Over Time and Basins. Paper SPE 135555, presented at the SPE Annual Technical Conference and Exhibition, Florence, Italy, Sep. 19-22.

Biot, M.A. and Medlin, W.L. 1985. Theory of Sand Transport in Thin Fluids. Paper SPE 14468, presented at the SPE Annual Technical Conference and Exhibition, Las Vegas, Nevada, Sep. 22-25.

Bonilla, L.F. and Shah, S.N. 2000. Experimental Investigation on the Rheology of Foams. Paper SPE 59752. Presented at the SPE/CERI Gas Technology Symposium, Alberta, Canada, Apr. 3-5.

Brannon, H.D. and Starks II, T.R. 2008. The Impact of Effective Fracture Area and Conductivity on Fracture Deliverability and Stimulation Value. Paper SPE 116057, presented at the 2008 SPE Annual Technical Conference and Exhibition, Denver, Colorado, Sep. 21-24.

Brannon, H.D. and Starks II, T.R. 2009. Maximizing Return-On-Fracturing-Investment by Using Ultral-lightweight Proppants to Optimize Effective Fracture Area: Can Less Be More? Paper SPE 119385, presented at the SPE hydraulic fracturing technology conference, Woodlands, Texas, Jan. 19-21.

Bulova, M., Nosoca, K., Willberg, D., and Lassek, J. 2006. Benefits of the Novel Fiber-laden Low-viscosity Fluid Systems in Fracturing Low-permeability Tight Gas Formations. Paper SPE 102956, presented at the SPE Annual Technical Conference and Exhibition, San Antonio, Texas, Sep. 24-27.

Coulter, G.R., Benton, E.G. and Thomson, C.L. 2004. Water Fracs and Sand Quantity: A Barnett Shale Example. Paper SPE 90891, presented at the SPE Annual Technical Conference and Exhibition, Houston, Texas, Sep. 26-29.

Economides, M.J. and Martin, T. 2007. Modern Fracturing, 1st Edition.

Fredd, C.N., McConnell, S.B., Boney, C.L. and England, K.W. 2000. Experimental Study of Hydraulic Fracture Conductivity Demonstrates the Benefits of Using Proppants. Paper SPE 60326, presented at the SPE Rocky Mountain Regional/Low-Permeability Reservoirs Symposium and Exhibition, Denver, Colorado, March 12-15.

Gadde, P.B. and Sharma, M.M. 2005. The Impact of Proppant Retardation on Propped Fracture Lengths. Paper SPE 97106, presented at the SPE Annual Technical Conference and Exhibition, Dallas, Texas, Otc. 9-12.

Gaurav, A. 2010. Ultra-Light Weight Proppants in Shale Gas Fracturing. Thesis of Master of Science in Engineering. University of Texas at Austin.

Gaurav, A., Dao, E.K. and Mohanty, K.K. 2010. Ultra-lightweight Proppants for Shale Gas Fracturing. Paper SPE 138319, tight gas completions conference, San Antonio, Texas, Nov. 2-3.

Gaurav, A., Gu, M. and Mohanty, K.K. 2012. Improvement of Fracturing for Gas Shales. RPSEA Final Report 07122-38, August.

Gidley, J.L., Holditch, S.A., Nierode, D.E., and Veatch Jr., R.W. 1989. Recent Advances in Hydraulic Fracturing. SPE Monograph 12, Society of Petroleum Engineers, Richardson, TX.

Khade, S.D. and Shah, S.N. 2002. New Empirical Friction Loss Correlation For Foam Fluids in Coiled Tubing. Paper SPE 74810. In: Proceedings of the 2002 SPE/ICoTA Coiled Tubing Conference and Exhibition, Houston, April 9-10.

King, G.E. 2010. Thirty Years of Gas Shale Fracturing: What Have We Learned?, Paper SPE 133456, SPE Annual Technical Conference and Exhibition, Florence, Italy, Sept. 19-22.

Mahoney, R.P., Soane, D., Kincaid, K.P., Herring, M., and Snider, P.M. 2013. Self-suspending Proppant. Paper SPE 163818, presented at the SPE hydraulic fracturing technology conference, Woodlands, Texas, Feb. 4-6.

McDaniel, B.W. 2010. Horizontal Wells with Multi-Stage Fracs Provide Better Economics for Many Lower Permeability Reservoirs. Paper SPE 133427. SPE Asia Pacific Oil and Gas Conference and Exhibition, Brisbane, Queensland, Australia, Oct. 18-20.

Nakhwa A.D., Huggins K. and Sweatman R. 2013. New Technologies in Fracturing for Shale Gas Wells Are Addressing Environmental Issues. Paper SPE 164270. In: Proceedings of the 2013 SPE Middle East Oil and Gas Show and Conference, Manama, Bahrain, March 10-13.

Newell, R. 2011. Shale Gas and the Outlook for U.S. Natural Gas Markets and Global Gas Resources. Presented to the Organization for Economic Cooperation and Development (OECD), Paris, France.

Ouyang, L., Yango, T., Zhu, D., and Hill, A.D. 2012. Theoretical and Experimental Modeling of Residual Gel Filter-Cake Displacement in Propped Fractures. SPE Production & Operations. 27(4): 363-70.

Palisch, T.T., Vincent, M.C., and Handren, P.J. 2010. Slickwater Fracturing: Food for Thought. SPE Production & Operations. 25(3): 327-44.

Reidenbach, V.G. Harris, P.C., Lee, Y.N., and Lord, D.L. 1986. Rheological Study of Foam Fracturing Fluids Using Nitrogen and Carbon Dioxide. SPE Production Engineering. 1 (1): 31-41.

Sani, A.M., Shah, S.N., and Baldwin, L. 2001. Experimental Investigation of Xanthan Foam Rheology. Paper SPE 67263. Presented at the SPE Production and Operations Symposium, Oklahoma City, Oklahoma, March 24-27.

Sudhakar, D.K. and Shah, S.N. 2003. New Rheological Correlations for Guar Foam Fluids. Paper SPE 88032. Presented at the SPE Production and Operations Symposium, Oklahoma City, Oklahoma, March 22-25.

Warpinski, N.R., Kramm, R.C. Heinze, J.R., and Waltman, C.K. 2005. Comparison of Single- and Dual- array Microseismic Mapping Techniques in the Barnett Shale. Paper SPE 95568, presented at the 2005 SPE Annual Technical Conference and Exhibition, Dallas, Texas, Oct. 9-12.

Xu, B., Hill, A.D. and Zhu, D. 2011. Experimental Evaluation of Guar-Fracture-Fluid Filter-Cake Behavior. SPE Production & Operations. 26(4): 381-7.

Chapter 2: Impact of Hydraulic Fracture Conductivity and Propped Length on Well Productivity

In this chapter, a comprehensive parametric study is conducted by using reservoir simulations (CMG-IMEX). Through the study, the impact of hydraulic fracture conductivity and propped length on fractured well productivity in a naturally fractured reservoir is examined. The threshold conductivity, beyond which the production is insensitive to the conductivity, is found as a function of propped length and production time. The effects of other parameters, such as reactivated natural fracture conductivity (NFC), natural fracture spacing (NFSPC), cluster spacing, gas desorption, water recovery, reservoir fluid type and flowing BHP are also investigated.

2.1 LITERATURE REVIEW

Various graphical/computerized methods have been developed to estimate the effects of fracture length and fracture conductivity on fractured well productivity. For reservoirs under the (pseudo) steady-state flow, Type Curves 2.1 (McGuire and Sikora, 1960) and 2.2 (Tinsley et al., 1969) can be used to estimate the productivity increase resulting from the increase of length and conductivity. These curves were developed from electrical and mathematical models. The assumptions behind the two charts restrict their use to

- Steady state or pseudo steady state flow
- Homogeneous, isotropic reservoir
- Constant rate production
- Square drainage area (Fig.2.1) or circular drainage area (Fig. 2.2)
- Single phase, incompressible or slightly compressible fluid
- Entire interval is propped (Fig.2.1) or partially propped (Fig. 2.2)

- The fracture has uniform length, height and conductivity
- The fracture has two equal length wings

In both Figures 2.1 and 2.2, the relative fracture productivity index increases with the relative conductivity, but at a decreasing rate. Beyond a certain value of the relative conductivity, the productivity does not increase further. This cutoff point is larger for longer propped length. Within the high relative conductivity regime, the growth of the productivity is only induced by the increase of the propped length. These two charts are mainly applied to conventional, high permeability reservoirs, where flow remains in steady state or pseudo steady state throughout the major portion of the life of a well.

For transient flow regime, which is commonly observed in ultra-low permeability reservoirs, such as shale, Figures 2.3 (Agarwal et al., 1979) and 2.4 (Cinco et al., 1978) are developed to evaluate the fracture production performances at different fracture conductivities and propped lengths. Figure 2.3 is developed under the constant wellbore pressure assumption, while Figure 2.4 is developed under the constant producing rate assumption. Similar to the curves for steady state flow, the curves 2.3 and 2.4 have the following assumptions:

- Transient flow
- Homogeneous, isotropic reservoir
- Single phase flow
- The fracture has uniform length, height and conductivity
- Bi-wing planar fracture with equal length wings
- Infinite acting reservoir

In both charts, there is a relative fracture conductivity index (dimensionless conductivity) F_{CD} defined as the ratio of the fracture conductivity to the product of the reservoir permeability and fracture half length. The dimensionless producing rate increases with

F_{CD}. Given a production time, there exists an optimal F_{CD}, beyond which the production becomes insensitive to further increases in F_{CD}. Taking Figure 2.3 as an example, the optimal F_{CD} is >500 at $t_{DXf} < 10\text{E-}4$, 100 at $10\text{E-}4 < t_{DXf} < 10\text{E-}3$, 50 at $10\text{E-}3 < t_{DXf} < 10\text{E-}1$, and 5-10 at $t_{DXf} > 10\text{E-}1$.

For gas wells, where the high Reynolds number, non-Darcy flow has a major effect on stimulation productivity because of the low viscosity and high compressibility of gases, Tannich and Nierode (1985) generated pseudo steady state type curves (Figure 2.5) from many computer calculations for a fractured gas well in a finite-difference reservoir-flow model. The curve shapes are similar to the shapes of the McGuire-Sikora curves, but the correlating parameters are different. The y-axis is the PI ratio J/J_0 modified by the spacing term. The x-axis is the relative non-Darcy conductivity, C_{rB},

$$C_{rB} = \frac{w_{hf}\mu}{k}\sqrt{\frac{z(T+460)}{\beta_f \gamma_g (P_e^2 - P_{well}^2)}}\sqrt{\frac{2640}{r_e}} \tag{2.1}$$

where k is the effective reservoir permeability in md, w_{hf} is the producing fracture width in inch, μ is the gas viscosity in cp, z is the gas compressibility factor, T is the static reservoir temperature in ^{o}F, β_f is the fracture turbulence coefficient in ft^{-1}, γ_g is the gas specific gravity, P_e is the reservoir pressure in psi, P_{well} is the flowing BHP in psi, and r_e is the drainage radius in ft.

All the type curve charts introduced above are developed based on the single porosity, single permeability model assuming a uniform effective permeability throughout the whole drainage area, which is no longer valid for naturally fractured shale reservoirs. As computers become faster and cheaper, direct simulation by using a finite-difference reservoir flow model to assess the response of a fractured well to fracture stimulation, such as the way of generating Tannich and Nierode type curves, is becoming increasingly popular, since it can model more complicated depletion processes for heterogeneous reservoirs and different flow regimes. Many experimental (Fisher et al. 2005, Olson et al. 2012, Wang et al. 2013) and modeling (Meyer and Lucas 2011, Weng et al. 2011, Olson and Wu 2012) research work has been conducted to evaluate the complex fracture network growth in naturally-fractured shale reservoirs. For reservoir simulation study, Mayerhofer et al. (2006) and Warpinski et al. (2008) have presented the results of integrating microseismic fracture mapping with numerical production modeling of fracture networks in the Barnett shale. A parametric study was conducted to show how fracture network size and density, fracture conductivity, matrix permeability and gas in the network affect a horizontal well productivity. In their reservoir model, an orthogonal fracture network with uniform conductivity was assumed. The results suggested that, for 0.1 μD shales, the gas recovery factor or cumulative gas production increases with decreasing network spacing or increasing fracture conductivity at a decreasing rate. Cipolla et al. (2008) focused on fracture-conductivity requirements for complex fracture networks. Two reservoir models were built for parametric study. One model assumes uniform fracture conductivity throughout fracture networks based on the assumption of even proppant distribution in the network. The other model assumes that proppants would be concentrated in the primary fracture, leading to infinite conductivity for the primary fracture. Parametric study was conducted to obtain the optimal network conductivity as a function of reservoir permeability, the degree of fracture complexity, fracture spacing, and network width. One conclusion is that increasing fracture complexity reduces network conductivity requirements. Cipolla et al. (2009b) also studied how well performance is affected by proppant transport distance in network, proppant bank height in the primary fracture, and the high conductivity arch at the top of the bank. Cohen et al. (2013) conducted numerous parametric and case studies to investigate the impact of fracturing treatment design and reservoir properties on production from shale gas reservoirs by using the Unconventional Fracture Model (Weng et al., 2011) integrated with the Unconventional Production Model (Cohen et al., 2012). The relation between production and treatment design parameters such as fracturing fluid viscosity, proppant size, proppant concentration, proppant injection order, treatment volume, pumping rate, pad size and hybrid treatment were investigated. Yu and Sepehrnoori (2013) employed Response Surface Methodology (RSM) to optimize six uncertain parameters, such as permeability, porosity, fracture spacing, fracture half-length, fracture conductivity, and well distance for the Barnett Shale development. Khan (2013) integrated the fracture networks from miscroseismic mapping with a commercial numerical production simulator to optimize treatment parameters (e.g. fracture spacing) for improving well performance. In reservoir simulation, porosity instead of permeability was used as a scaling parameter for the fracture width. Two different fracture geometries have been proposed for a multi-stage horizontal well, orthogonal and transverse.

In this chapter, a similar parametric study for fracture productivity response to the hydraulic fracture properties (conductivity & length) in naturally fractured reservoirs is conducted by using a state-of-art finite difference reservoir simulator (CMG-IMEX). A bi-wing planar primary fracture intersected perpendicularly with uniformly distributed reactivated natural fractures is simulated explicitly. Unlike the model used in Mayerhofer et al. (2006) and Warpinski et al. (2008), and the first model in Cipolla et al. (2008) which assume uniform fracture conductivity throughout fracture networks, our model is more similar to the second model in Cipolla et al. (2008) as different conductivities for the primary fracture and natural fractures are assumed. However, in contrast to the model in Cipolla et al. (2008), our model does not assume infinite conductivity for the primary fracture. Instead, hydraulic fracturing conductivity for the primary fractures is varied to obtain the optimal conductivity that achieves near-Maximum production for different propped lengths and production times. Then, natural fracture properties such as conductivity and spacing are varied to examine how they affect the optimal hydraulic fracturing conductivity for the primary fracture. In addition, the impacts of other factors such as reservoir permeability, hydraulic fracture spacing, gas desorption, water recovery, reservoir fluid type, and flowing BHP, on optimal primary fracture conductivity are investigated. The reservoir model built in this chapter is further combined with a fracturing model to evaluate the shale fracturing performance of the ultra-light weight proppants and polymer free foams in Chapter 4 and 6.

2.2 RESERVOIR SIMULATION MODEL BUILT FOR PARAMETRIC STUDY

2.2.1 Description of Reservoir Simulation Model

Figure 2.6 shows the reservoir-fracture domain simulated for gas production. Only half of a bi-wing fracture and half of the matrix between two adjacent fractures are included in the simulated domain. Assuming that all fractures are symmetric bi-wing planar fractures with equal length wings, the total well production can be calculated by multiplying the simulated fracture productivity with four and the number of the fractures along the horizontal well.

According to Figure 2.6, the hydraulic fracture and natural fractures are modeled explicitly as discrete grid blocks. The logarithmic-local-grid-refinement (LLGR) strategy (Cipolla et al. 2009a) is applied to fracture blocks to accurately simulate the transient flow behavior from low permeability matrix zone to high permeability fracture conduits. The natural fractures are perpendicular to the hydraulic fracture at a constant NFSPC and penetrate to the whole drainage area. The permeability of both the hydraulic fracture and natural fractures are uniform across the whole interval and fracture length. The well bore is connected to the system at the first fracture grid block (1, 1, 1) and set at a constant flowing BHP throughout the whole production life. The matrix as well as the fracture is assumed to be 100% filled with the natural gas (SG=0.55) at the initial reservoir pressure. For a gas-water two-phase system, the gas-water module in the IMEX simulator is adopted to simulate the subsequent pressure field, flow-rate field and gas cumulative production.

For the current study, there are over one thousand cases to be simulated. So the model needs to be accurate and, most importantly fast. Various validation and verification works have been done for developing the reservoir model. Besides, the total grid number is chosen to be as small as possible subject to the condition that the simulation results being insensitive to the number of grids.

Figure 2.7 compares different LLGR strategies. Strategy 1 refines the fracture grid, the well grid, and the grids along the fracture direction. It generates the most grids, but has the best accuracy. Strategy 2 only has the fracture grid refined, generating the least number of grids, while strategy 3 has both the fracture and well grids refined, generating the medium number of grids. The relative differences among their thirty-year cumulative productions are less than 3%. To save the computation time, strategy 2 & 3 could be better than strategy 1. Besides, the refining number also affects the simulations. More refined the grid is, higher the simulation accuracy can be. The chart at the right bottom corner of Figure 2.7 compares the results simulated from strategy 2 at different refining numbers. It is found that the cumulative results increase with the refining number at a decreasing rate. Once the refining number is above seven, the simulation error resulting from the grid number is within 1% and could be neglected.

The current reservoir simulation model includes:

- Gas desorption

- Non-Darcy flow inside fractures
- Local grid refinement with logarithmic grid spacing
- Single porosity model with discrete fractures
- Dual porosity/permeability model

2.2.2 Gas Desorption

Shale gas is organic-rich formation. The gas storage is mainly from three sources: free gas stored in natural fractures, free gas in matrix pores, and absorbed gas in organic materials. The first source is small and only contributes to the initial production, while the other two sources are large and contribute to short/medium-term production and medium/long-term production, respectively. The gas from the third source is described by Langmuir equation:

$$G_s = V_L P / (P + P_L) \tag{2.2}$$

where G_s is the gas absorbed by the unit matrix in scf/ton, V_L is the Langmuir volume in scf/ton, P_L is the Langmuir pressure in psi, and P is the reservoir pressure in psi. Langmuir volume is the maximum adsorption gas volume at the infinite pressure, while Langmuir pressure is the pressure corresponding to half Langmuir volume. In the current study, the value of V_L is 85 scf/ton, and the value of P_L is 468 psi (Thompson et al., 2011). From the equation, it is noted that, at the early stage, with small decreases in the reservoir pressure, the contribution of the gas desorption is small. As the reservoir pressure further decreases, more gas is desorbed from the surface of the matrix, and the gas desorption becomes more and more significant. The newest version (after 2012) of both CMG IMEX (black oil simulator) and GEM (compositional simulator) are capable of taking the gas desorption effect into account. Figure 2.8 compares the production predictions with and without considering gas desorption for a sample case (Lf: 400ft, HFC: 1000 md-ft, NFSPC: 50ft, NFC: 0.1md-ft). It shows that the productions considering gas desorption (blue line) are higher than the ones without considering gas desorption (red line). The difference increases sharply within the first 2000 days and becomes stable at 13% since then, as shown by the relative error curve (black dashed line).

2.2.3 Non-Darcy Flow

In CMG, the non-Darcy flow effect due to high gas flow rate and low gas viscosity in fracture channels is modeled with the Forchheimer equation,

$$-\nabla\Phi_g = \frac{\mu_g}{k_g} u_g + \beta\rho_g \left|u_g\right| u_g \tag{2.3}$$

where Φ_g is the potential of the gas phase, and β is the non-Darcy flow coefficient. If β is zero, the equation above turns into Darcy's Law. The β factor is given by

$$\beta = \frac{\alpha_g}{\left(kk_{rg}\right)^{N1_g}\left(\phi S_g\right)^{N2_g}} \tag{2.4}$$

The factors α_g and $N1_g$ are set as 1.485E9 and 1.021, which are proposed by Evans and Civan (1994) by correlating over 180 data points. $N2_g$ is usually assigned a value of zero to eliminate the dependence of β on porosity and saturation when modeling non-Darcy flow in fractures.

If the fracture width adopted in CMG is x times larger than the true fracture width, the fracture permeability should be reduced by $1/x$ to produce the same conductivity. Similarly, the Forchheimer number should be also corrected to account for the reduced fracture permeability. The correction factor is $x^{(2-N1g)}$.

Figure 2.9 (Rubin, 2010) compares the gas rates predicted by Darcy flow and non-Darcy flow in 0.0001 md and 0.01 mD shales. It shows that the gas flow rate is lower for the non-Darcy flow. The non-Darcy effect decreases with increasing time and decreasing matrix permeability.

2.2.4 Natural Fracture Modeling

Figure 2.10 compares the simulation results of two different natural fracture models. Both models have the same natural fracture properties and assume that natural fractures are perpendicular to the hydraulic fracture with a constant NFSPC. The first model is the discrete natural fracture model. The second model is the single porosity model with an effective permeability (SPEP) applied to all cells. The effective permeability is calculated by

$$k_{eff} = k_m + \left(k_{nf} w_{nf}\right) / NFSPC \tag{2.5}$$

For this example case, the matrix permeability is 200 nD. There are only natural fractures along the *i* direction with a conductivity of 0.1 md-ft and spacing of 50 ft. So the effective permeability of *i* direction is 2200 nD. The permeability of *j* direction is still 200 nD, and the permeability of k direction is one tenth of that of *i* direction, which is 220 nD. It shows the SPEP (red line) model overestimates the flow capacity of natural fractures, leading to a higher gas productions especially in the short term (<1000 days in this case). One possible reason is that the SPEP model ignores the non-Darcy effect of the gas flow in natural fractures. Another important reason is that the effective permeability is calculated by assuming parallel connection of matrix and its neighboring natural fractures. However, this assumption deviates from the real flowing condition that is closer to a series connection: natural fractures accept the fluids from the neighboring matrix and fractures, and then deliver them to the adjacent downstream fractures.

2.2.5 Water Recovery

In the above parametric study, a dry gas model is adopted by assuming no mobile water in matrix and fractures. However, in the water fracturing treatment, a large amount of water could leak into the formation and get trapped in the small pores and fissures of shales due to the high capillary pressure. The trapped water flows back with natural gas during production. To investigate the water recovery impact on the gas production, the water saturation of the matrix is set to be 10% higher than the residual water saturation and the water saturations of the natural and hydraulic fractures are 90%. The gas-water capillary curve and relative permeability curve are generated by the default values from in the CMG. Figure 2.11 compares the production results with and without considering the water recovery. It shows that the gas production without water flowing back (blue line) is higher than the gas production under water recovery (red line). The reason is that the gas permeability is highly reduced under the two-phase flow condition. The relative curve (black dashed line) shows that the impact of water on producing rate sharply decreases with time within the first year and gradually becomes negligible after three years.

2.2.6 Reservoir Fluid Type (Oil vs. Gas)

Figure 2.12 compares the production trends of gas and oil at the same reservoir and fracture properties. It shows that the gas production rate (time derivative along the blue line) decreases much faster than the oil production rate (time derivative along the red line). The reason is that the gas viscosity (0.02 cp) is much lower than the oil viscosity (1 cp). Thus, the gas reservoir is depleted much faster than the oil reservoir.

2.2.7 Parameters for Parametric Study

Table 2.1 lists the reservoir properties (left two columns) and the completion parameters (right column) used in reservoir simulations for this parametric study. The values of the reservoir properties are the average property values of Marcellus Shale concluded from several papers (Jacot et al., 2010; Thompson et al., 2011; Cohen et al., 2013). Reservoir is 6000 ft deep. The initial pore pressure is 3300 psi with a pressure gradient of 0.55 psi/ft. The minimum horizontal stress is 4500 psi with a gradient of 0.74 psi/ft. Temperature is 130 ^oF. Payzone thickness is 150 ft. The matrix permeability is either 200 nD (base case) or 20 nD horizontally. The vertical permeability is one tenth of the horizontal ones. Pore compressibility is 6E-6 psi^{-1}. The values of the Langmuir volume and the Langmuir pressure are from the paper of Thompson et al. (2011). To simplify the model, a dry gas model is assumed with residual water saturation of 20%. The gas consists of 100% of methane. In the column of the completion parameters, the horizontal well is 5000 ft long with 2000 ft well spacing. The cluster spacing (fracture spacing) is 100 ft (50 fractures) for the base case. The fracture is assumed to be fully covered by the proppants with a propped height equal to the payzone thickness. The flowing BHP is constant at 500 psi. The following study focuses on the impacts of the hydraulic fracture conductivity and propped length on the fracture productivity. So the conductivity and length are varied for the sensitivity study. The variations of the two parameters are shown in Table 2.2. The conductivity has ten values ranging from 1 to 1000 md-ft. The propped length has 6 values ranging from 200 to 700 ft. The total number of cases to run for each group of sensitivity study is 60. By running the 60 cases, the minimum conductivity (defined as the critical conductivity) required to fully stimulate the hydraulic fracture is obtained for different propped lengths and production time. Another focus of the study in this chapter is the impact of the natural fracture properties (NFC and NFSPC) on the critical conductivity. Table 2.3 lists the possible natural fracture conductivity values and natural fracture spacing values. The red colored ones (0.1 md-ft & 50 ft) are the values used in the base case for natural fracture study. In this parametric study, the natural fracture conductivity is assumed to vary from 0.001 md-ft to 10 md-ft. The corresponding aperture, according to the cubic law of fractures, varies from 1.5 µm to 33 µm. The natural fractures assumed in the current model are the reactivated natural fractures after treatments which are not sufficiently propped. The values chosen for parametric study is based on Cohen et al. (2013). In reality, this unpropped conductivity can vary by several orders of magnitude, depending on parameters such as formation properties, the size and distribution of asperities, the degree of fracture displacement, rock mechanical properties and cement fill (Fredd et al. 2001, Laubach et al. 2004). Fredd et al. (2001) tested the unpropped conductivity of aligned fracture faces, which was < 1 md-ft at 2000 psi and <0.1 md-ft at 3000 psi. The value increases by 100 times if the fracture is displaced. Gale et al. (2007) studied four core samples and observed that natural fractures in the Barnett Shale are mostly sealed and follow a power-law aperture size distribution ranging from 0.05 mm to 1mm. They act as planes of weakness that can reactivate. The mean value of their measured aperture sizes is larger than the aperture size range we assumed. The reason is that the fractures they tested from the core samples cannot be simply assumed as parallel plates due to their rough, tortuous surface and cement fills inside fractures. Zhang et al. (2013) measured the conductivity of cemented natural fractures with in-situ infill in a modified API conductivity cell. The unpropped conductivity is 4 md-ft at 500 psi and 0.4 md-ft at 3000 psi, which is covered by the conductivity range we assumed.

2.3 RESULTS AND DISCUSSIONS

In this section, over 1000 sensitivity study cases are run in the reservoir model to fully study the stimulation impact on the production in naturally fractured shale reservoirs. First, the minimum conductivity (critical conductivity) required to fully stimulate the fracture is obtained as a function of propped length and production time for two base cases of non-naturally-fractured reservoirs. Then, the natural fracture properties are varied according to Table 2.3, and the impact of the natural fracture properties on the critical conductivity is investigated. Finally, the impacts of other parameters, such as fracture spacing, gas desorption, non-Darcy flow, water recovery, and reservoir fluid type on the prediction of the critical conductivity are investigated.

2.3.1 Dependence of Cumulative Production on Conductivity

Figure 2.13 shows 1 year, 5 year, 10 year and 20 year cumulative productions as a function of the hydraulic fracture conductivity for different propped lengths in a 200 nD non-naturally fractured reservoir. All four charts show similar trends: the cumulative production increases with the conductivity at a decreasing rate. Given a propped length, there is a certain conductivity beyond which the production is insensitive to the change of the conductivity. The cutoff point is defined as the critical conductivity for the given propped length at the given production time. Once the cutoff point of the hydraulic fracture conductivity is achieved, pumping more proppants to increase the conductivity is suboptimal because the increase of the proppant cost will outweigh the productivity benefits. At the same production time, the critical conductivity increases with the propped length. It is because that higher conductive capacity is needed to transport the fluid out from the fracture tip as the hydraulic fracture penetrates deeper into the reservoir. For the same propped length, the critical conductivity decreases with the production time. The reason is that, as the production time increases, reservoir pressure decreases and the escaping rate of gas from the reservoir into the hydraulic fracture decreases. So lower fracture flow capacity (conductivity) is needed to transport less gas out of the fracture as the drawdown pressure decreases.

Based on Figure 2.13, 1 year, 5 year, 10 year and 20 year relative cumulative productions versus the hydraulic fracture conductivity for different propped lengths are plotted in Figure 2.14. The relative production is the production of a certain conductivity fracture divided by the production of an infinite conductivity hydraulic fracture. Comparing different lines, it is noted that the production is more sensitive to the hydraulic fracture conductivity at the longer propped length and shorter production time. By setting a cutoff line in these charts (red dashed line in the first chart), the critical conductivity at the given cutoff value can be determined. For example, if the cut-off value is 97%, the critical conductivity is 22.8 md-ft for 300 ft propped length and is 86 md-ft for 600 ft propped length for 1 year production.

2.3.2 Critical Conductivity Chart

By setting a cutoff line to the relative cumulative production curves (e.g. Figure 2.14), the critical conductivity for all propped lengths (200-700 ft) and different production time (1, 5, 10, 20 year) in a 200 nD shale are obtained and plotted in Figure 2.15. There are two trends observed: (1) the critical conductivity increases with propped length at a decreasing rate in a semi-log plot; (2) the critical conductivity of different propped lengths decreases with production time at a similar rate. The critical conductivity chart clearly reflects the sensitivity of the hydraulic fracture productivity to its conductivity; higher the critical conductivity is, more sensitive the productivity is to the fracture conductivity. This chart can either provide guidelines to choose the right proppants and concentrations for treatment design or provide reference information to design new proppants. One thing that should be kept in mind is that the critical conductivity illustrated in this chart is a dynamic conductivity of the induced hydraulic fracture, which considers the non-Darcy flow effect and time effect (proppant diagenesis, closure stress change etc.). To make the chart more applicable, a safety factor (Duenckel et al., 2012) should be multiplied to convert the dynamic conductivity values to the baseline values.

Figure 2.16 is the critical conductivity chart for a 20 nD non-naturally fractured reservoir. It is noted that the critical conductivity is decreased by 1.3-3.4 times as the reservoir permeability is reduced by 10 times. The decrease is larger for shorter propped length and shorter production time.

2.3.3 Effects of Natural Fracture Properties on Critical Conductivity

When the reservoir is naturally fractured, the conductive capacity of the reservoir is improved, and the stimulation should also be altered to achieve the optimal production. Figure 2.17 compares the pressure distributions after different production time of a non-naturally fractured 200 nD reservoir and the same reservoir with natural fractures perpendicular to the hydraulic fracture. The hydraulic fracture is infinite conductive with a propped length of 600 ft. The natural fractures have the uniform conductivity of 0.1md-ft and spacing of 50 ft. It shows that natural fractures highly speed up the drainage of the reservoir at the initial time (1 year). But the impact decreases with time. After 10 years, both non-naturally fractured and naturally fractured reservoirs are fully depleted and exhibit similar pressure distributions. Figure 2.18 compares the critical conductivity of 300 ft and 600 ft propped lengths of the non-naturally fractured reservoir and the naturally fractured reservoir. The critical conductivity of the naturally fractured reservoir (dashed lines) is higher than that of the non-naturally fractured reservoir (solid lines) initially. As the production time increases, the critical conductivity of the naturally fractured reservoir drops faster than that of the non-naturally fractured case. After 2000 days, the critical conductivity of the naturally fractured reservoir is lower than that of the non-naturally fractured reservoir. The possible reason is that the naturally fractured reservoir is depleted faster due to its higher effective reservoir permeability, leading to a faster decrease of the gas flow rate from the matrix into the hydraulic fracture as time passes. So the demand of the HF flow capacity for naturally fractured reservoir decreases faster accordingly.

Similarly, Figures 2.19 and 2.20 illustrate the comparison of the pressure fields and critical conductivity between naturally and non-naturally fractured reservoirs for a 20 nD case. The properties of the natural fractures are the same as those in the previous example. Comparing Figures 2.19 and 2.17, it is noted that natural fractures have larger impacts on the reservoir with lower matrix permeability. After 20 years, the non-naturally fractured reservoir is still under a pressure of 2000 psi, while the naturally fractured reservoir is already fully depleted. In Figure 2.20, the critical conductivity of the naturally fractured reservoir (dashed lines) decreases faster than that of the non-naturally fractured reservoir (solid lines) because of the faster depletion of the reservoir. However, since the depletion is much slower because of a decrease of the matrix permeability to one tenth, the critical conductivity of the naturally fractured reservoir is still larger than that of the non-naturally fractured reservoir after 20 years.

Overall, critical conductivity decreases with production time because of the decrease of the drawdown pressure with reservoir depletion. The decrease is faster for reservoirs with natural fractures than those without natural fractures. Initially, the critical conductivity is higher for naturally-fractured reservoirs. For higher matrix permeability (200 nD), the critical conductivity of the naturally fractured reservoir can decrease to lower than that of the non-naturally fractured reservoir. For lower matrix permeability (20 nD), the critical conductivity of the naturally fractured reservoir is always larger than that of the non-naturally fractured reservoir throughout 20 years production life.

In actual fields, natural fracture conductivity and spacing could vary from place to place and from treatment to treatment. Large uncertainties of these two parameters lead us to conduct further sensitivity study in the next section to investigate how the variation of natural fracture properties would impact the critical conductivity.

2.3.3.1 Critical Conductivity vs. NFC

Figures 2.21 and 2.22 illustrate how critical conductivity changes with NFC for reservoirs with 200 nD matrix permeability and 20 nD matrix permeability, respectively. Natural fracture spacing is fixed as 50 ft. The NFC varies from 0.001 md-ft to 10 md-ft. For 1 year production, the critical conductivity increases slightly with NFC when NFC < 0.001 md-ft. The increase of the critical conductivity becomes fast when 0.001 md-ft < NFC < 0.1 md-ft. The increase slows down when NFC > 0.1md-ft. The plots of 5 year, 10 year and 20 year show a different trend: the critical conductivity is first constant when NFC < 0.001 md-ft, decreases when 0.001 md-ft < NFC < 0.1 md-ft, and then becomes almost constant again when NFC > 0.1 md-ft. The increase of the critical conductivity with NFC in the first year is because the increase of the flow capacity of the reservoir resulting from the increase of NFC. The decrease of the critical conductivity with NFC in 5 - 20 year is because that, as production time increases, the critical conductivity decreases faster for higher NFC due to the faster decrease of the drawdown pressure. For a relative high matrix permeability of 200 nD, the largely reduced drawdown pressure in the long term may lead to a negative correlation between the critical conductivity and NFC. For both short and long-production terms, the critical conductivity is not sensitive to NFC when NFC < 0.001 md-ft because NFC is so low that the reservoir depletion is not sensitive to the alteration of NFC. When NFC > 0.1 md-ft, the change of the critical conductivity with NFC also slows down because NFC is infinite conductive compared with the matrix permeability. Comparing different propped lengths at the same production time, they all show similar curve shapes.

Figure 2.22 shows the critical conductivity versus NFC at different propped lengths and production time for 20 nD matrix permeability. Different from the previous 200 nD case, the critical conductivity in this case increases with NFC for 1 year, 5 year, and 10 year production time. The increase is slow when NFC < 0.001 md-ft, fast when 0.001 md-ft < NFC < 0.01 md-ft, and slow again when NFC > 0.01 md-ft. After 20 years, the critical conductivity becomes insensitive to NFC. Since the matrix permeability is decreased by 10 times, the critical conductivity is more sensitive to NFC compared with the previous case. Besides, since the reservoir is depleted much more slowly due to a lower matrix permeability, the positive correlation between critical conductivity and NFC can be established for a longer time (>10 years). Because NFC is too low to affect the reservoir depletion when NFC < 0.001 md-ft, and is too high compared with 20 nD matrix permeability when NFC > 0.01 md-ft, the change of the critical conductivity with NFC is slight in these two ranges.

To conclude, the increase of the NFC leads to two contrasting effects: (1) higher effective permeability (flow capacity) of the reservoir, which leads to a higher critical conductivity at the same drawdown, and (2) faster decrease of the drawdown due to faster depletion, which leads to a faster decrease of the critical conductivity with production time. At initial time when the reservoir pressure is high, the first effect dominates the second one. The critical conductivity is positively correlated with NFC. As time increases, the second effect gradually becomes dominant, the correlation becomes less positive (20 nD) or negative (200 nD). There are lower and upper bounds of NFC. The lower and upper bounds are 0.001 md-ft and 0.1 md-ft for matrix permeability of 200 nD, and 0.001 md-ft and 0.01 md-ft for matrix permeability of 20 nD. Below the lower bound NFC is too low to impact the reservoir depletion, while above the upper bound NFC is relatively high to the matrix. Thus, the impact of the NFC on the critical conductivity is small when NFC is outside the two bounds.

2.3.3.2 Normalized Critical Conductivity vs. NFC

All critical conductivity results in Figures 2.21 and 2.22 minus the critical conductivity of the corresponding non-naturally fractured reservoirs. The subtractions are further divided by the critical conductivity of the non-naturally fractured reservoirs to obtain the normalized critical conductivity. Figures 2.23 and 2.24 show the normalized critical conductivity versus NFC at different propped lengths and production times for matrix permeability of 200 nD and 20 nD, respectively. In both figures, the normalized critical conductivity curves of all five propped lengths (300ft - 700ft) converge to a single curve for one year production. As the production time increases, the convergence becomes worse, which might be attributed by the more and more influx coming from the outside non-stimulated zone. The convergence is better in the 20 nD case than in the 200 nD case. The trends of the normalized curves are consistent with the trends observed in the corresponding non-normalized results.

For 200 nD case (Figure 2.23), the normalized critical conductivity is almost constant when NFC < 0.003 md-ft, and increases with NFC at a decreasing rate when NFC > 0.003 md-ft for 1 year production. For 5 to 20 year productions, the normalized critical conductivities are almost zero when NFC < 0.003 md-ft, and decrease with NFC when NFC > 0.003 md-ft. The curves become flat again at 1 md-ft, 0.2 md-ft and 0.1 md-ft for 5 year, 10 year and 20 year, respectively. Comparing different propped lengths, the relative decrease of the critical conductivity with NFC during 5 - 20 years is more significant when the propped length is longer.

For 20 nD case (Figure 2.24), all converged curves at different production time exhibit similar trends, which increase slowly when NFC < 0.001 md-ft, then sharply when 0.001 md-ft < NFC < 0.01 md-ft. Once NFC is above 0.01 md-ft, the increase of the normalized critical conductivity slows down (≤ 10 years) or becomes zero (20 years). Compared with Figure 2.23, the values of the relative change due to the NFC change become larger, representing an increased sensitivity of the critical conductivity to NFC as matrix permeability decreases.

2.3.3.3 Critical Conductivity vs. NFSPC

In addition to natural fracture conductivity (NFC), natural fracture intensity is another important parameter deciding the reservoir flow capacity. A similar study is conducted on the impact of the natural fracture spacing (NFSPC) or natural fracture intensity on the critical conductivity.

Figures 2.25 and 2.26 illustrate how critical conductivity changes with the natural fracture spacing for matrix permeability of 200 nD and 20 nD, respectively. Natural fracture conductivity is fixed as 0.1 md-ft. The NFSPC varies from 25 to 200 ft. In Figure 2.25, for the 1 year production, the critical conductivity decreases with NFSPC at a decreasing rate. For 5 year, 10 year and 20 year productions, the critical conductivity increases with NFSPC at a decreasing rate. The possible reason is similar to before. In the first year when the reservoir is not fully depleted yet, the flow capacity of the reservoir is the bottleneck of the production. So the critical conductivity is positively correlated with the reservoir flow capacity. Higher is the NFSPC, lower is the flow capacity, and hence, lower critical conductivity is needed. As the NFSPC further increases, the impact of the natural fractures on the flow capacity of the reservoir decreases and the sensitivity of the critical conductivity to the NFSPC also decreases. As the production time increases, the reservoir with a smaller NFSPC is depleted faster, leading to a faster decrease of the critical conductivity. After five years, it is the drawdown pressure rather than the flow capacity that controls the influx from the matrix into the hydraulic fracture. So the reservoir with a larger NFSPC, which has a larger drawdown pressure, will have a higher critical conductivity.

Figure 2.26 shows the critical conductivity versus the NFSPC at different propped lengths and production time for 20 nD matrix permeability. Considering that the matrix permeability is reduced by 10 times, the reservoir is depleted much more slowly as compared with the 200 nD matrix permeability case. So the critical conductivity has a negative correlation with the NFSPC at most of the production time: the critical conductivity decreases with the NFSPC at a decreasing rate from 1 to 5 years and decreases with the NFSPC at NFSPC > 50 ft from 10 to 20 years.

2.3.3.4 Normalized Critical Conductivity vs. NFSPC

Similar to section 2.3.3.2, all critical conductivities in Figures 2.25 and 2.26 are normalized by the critical conductivity of the non-naturally fractured reservoirs and are plotted against the NFSPC, as shown in Figures 2.27 and 2.28. The trends observed in the normalized critical conductivity plots are consistent with the trends of the corresponding non-normalized results. Comparing the normalized plots at different production time, curves of all propped lengths converge to a single curve at early time (1 year for 200 nD & 1, 5 year for 20 nD) and diverge as time increases. The divergence is caused by the influx from outside the stimulated zones. Comparing Figures 2.27 and 2.28, the values of the relative change due to the NFSPC change is larger in Figure 2.28, representing an increased sensitivity of the critical conductivity to NFSPC as matrix permeability decreases from 200 nD to 20 nD.

2.3.4 Effects of Other Parameters on Critical Conductivity

Besides natural fracture properties, there are other parameters that affect the critical conductivity results. This chapter discusses some of them listed below,

- Hydraulic fracture spacing;
- Gas desorption;
- Water recovery;
- Different types of reservoir fluids;
- Flowing BHP.

According to the linear superposition theory, the propped height does not affect the critical conductivity predictions by ignoring the end effect at the fracture head connecting to the wellbore.

In the following study, the base case has matrix permeability of 200 nD, NFC of 0.1 md-ft, NFSPC of 50 ft, hydraulic fracture spacing (HFSPC) of 100 ft, BHP of 500 psi, and 100% gas (sg: 0.55).

2.3.4.1 Effect of HFSPC

Figure 2.29 compares the critical conductivity results predicted by the model with a HFSPC of 200 ft (dashed line) and the results from the based model with a HFSPC of 100 ft (solid line). It shows that the critical conductivity increases as HFSPC increases. Figure 2.30 plots the relative difference ((Test Case – Base Case)/ Base Case) of the critical conductivity between the two cases against the propped length at different production time. When HFSPC is increased from 100 to 200 ft, the critical conductivity increases by 40 % for 1-year production, and by almost 100% for 5-20 year productions. It is noted that the long time relative increase of the critical conductivity is roughly equal to the relative increase of the HFSPC. The possible reason is that HFSPC represents the drainage boundary, which governs the long-term production where the (pseudo) steady state flow develops.

2.3.4.2 Effect of Gas Desorption

Figure 2.31 compares the critical conductivity results of the model without considering gas desorption (dashed line) and the results of the base model with considering gas desorption (solid line). It shows that the critical conductivity is lower when the gas desorption is not considered. Figure 2.32 plots the relative difference of the critical conductivity between the two cases against the propped length at different production time. During the first year, the relative decrease of the critical conductivity is around 18-19% by assuming no gas desorption. After 5 years, the relative decrease is 30-40%. Gas desorption affects the long term critical conductivity more than the short term critical conductivity, because the ratio of the desorbed gas to the free gas becomes larger as the reservoir pressure decreases and the production time increases.

2.3.4.3 Effect of Water Recovery

In the base case, the model is assumed to be a dry gas model without water flowing. But in most actual conditions, a large amount of water invades into the reservoir during fracturing. The water would flow back with the producing gas, which might be harmful to the production. To investigate the water impact, a water recovery model is built by setting the matrix water saturation of 0.3 and natural fracture water saturation of 0.9 in the drainage area within the fracture propagation length. The water saturation in the outside area is still set as a residual water saturation of 0.2. Figure 2.33 compares the critical conductivity results predicted by the model after considering the water recovery (dashed line) with the results from the base model without considering the water recovery (solid line). Figure 2.34 plots the relative difference of the critical conductivity between the two cases against the propped length at different production time. It shows that the critical conductivity is increased by 25-40% when considering the water recovery issue. The effect is a little bit higher for shorter lengths and longer production time. The reason of the increase of the critical conductivity due to the water recovery is different for different production time. For the initial term when water producing rate is high (>100 bbl/D), the well production is highly dependent on the water recovery rate. And larger hydraulic fracture conductivity can improve the water-gas two-phase flow. As the water producing rate decreases with time (<10 bbl/D), the well production is mainly dependent on the gas rate. There are more gas trapped in the water saturated reservoir than in the dry reservoir after long production time according to the gas mass balance (total gas mass is the same for both cases). So the long-term critical conductivity is also larger for the reservoir with water recovery.

2.3.4.4 Effect of Reservoir Fluid Type

In the base case, the reservoir is assumed to be a dry gas reservoir filled with 100% methane. Other than dry gas, the unconventional reservoir fluids could be gas condensate, wet gas, or light oil, depending on the maturity of the hydrocarbons at different bearing temperatures and pressures. In Figure 2.35, the critical conductivity results from an oil case (dashed line) are plotted against the critical conductivity results from the base dry gas case (solid line). It shows that changing from gas to oil leads to an increase in the critical conductivity. The reason is that, when the reservoir fluids become more viscous (from gas to oil), the transport of the hydrocarbon fluid inside the hydraulic fracture becomes more difficult, increasing the demand of high hydraulic fracture conductivity. Figure 2.36 plots the relative difference of the critical conductivity between the two cases against the propped length at different production time. The relative increase of the critical conductivity by changing gas to oil is larger for longer production time. The average relative increase is 2 for 1 year production and 8 for 10-20 year productions. For long term productions (10-20 years), the relative increase of the critical conductivity is larger for longer propped lengths. The relative increase of the critical conductivity is changed from 5.4 to 9.8 as the propped length increases from 200 ft to 700 ft for 20 year production.

2.3.4.5 Effect of BHP

Figure 2.37 compares the critical conductivity generated at different BHPs. The solid lines are the base case with a BHP of 500 psi (drawdown ΔP=2800 psi). The dashed lines are the case with a higher BHP of 1000 psi (ΔP=2300 psi). It illustrates that the critical conductivity decreases with the increasing flowing BHP because the increase of the BHP leads to a reduced drawdown pressure and a faster transition from the transient flow to the boundary dominant. The relative critical conductivity difference chart (Figure 2.38) shows that the relative change of the critical conductivity caused by the change of the BHP is higher for a longer production period or a longer propped length.

2. 4 CONCLUSIONS

This chapter built a “discrete natural fracture” reservoir model with one fourth of a planar hydraulic fracture perpendicularly intersected by uniformly distributed natural fractures. A comprehensive sensitivity study including over 1000 cases is conducted on the model. Based on the study, the minimum conductivity (critical conductivity) required to fully stimulate the reservoir for different propped lengths and different production time is obtained and plotted in a critical conductivity chart. The effect of reactivated natural fracture properties (NFC & NFSPC) on the critical conductivity is investigated. Along with the natural fracture properties, other parameters, such as cluster spacing, gas desorption, water reservoir, reservoir fluid type and flowing BHP, also affect the critical conductivity. Their effects are also discussed.

Some key results are listed below:

- For each propped length and production time, there is a critical conductivity beyond which production is insensitive to the conductivity.
- For a certain reservoir, the critical conductivity increases with propped length and decreases with production time. The decrease is faster for reservoirs with higher flow capacity.
- In the typical Marcellus condition (k_m=200nD), the critical conductivity is 4-38 md-ft for 200-700 ft propped lengths of five years production, which, even multiplied by a sand safety factor (3-5), is still much less than the baseline conductivity of the commonly used sand.
- Natural fractures increases the short-term (1 year) critical conductivity but decreases the medium and long-term critical conductivity (5-20 year) for the reservoir with matrix permeability of 200 nD, while it increases the critical conductivity of all production terms (1-20 year) for the reservoir with matrix permeability of 20 nD.
- The increase of the critical conductivity due to natural fractures becomes smaller (or negative) with time.
- The critical conductivity is insensitive to the natural fracture conductivity lower than 0.001 md-ft or spacing larger than 100 ft, because natural

factures with ultra-low conductivity or intensity have limited impacts on reservoir depletion.

- If the natural fracture is infinitely conductive with respect to the matrix (0.1md-ft for 200 nD or 0.01 md-ft for 20 nD), the critical conductivity also does not change with natural fracture conductivity.
- The critical conductivity is positively correlated with hydraulic fracture spacing (cluster spacing), water saturation, and gas desorption, while it is negatively correlated with flowing BHP.
- In the typical Marcellus condition, oil has critical conductivity 3 - 10 times larger than gas for 1 - 20 year productions.
- Unlike the earlier works (Mayerhofer et al. 2006, Warpinski et al. 2008, Cipolla et al. 2008) illustrating how production changes with the stimulation parameters, the parametric study conducted in this chapter obtains the cutoff conductivity value for the primary fracture to achieve the near maximum production and how this value is affected by reactivated natural fracture properties and other parameters. The reservoir simulation model is limited to the 2D bi-wing planar fracture scenario and dry gas reservoirs. Further work can be done to extend the work to complex fracture networks or other reservoir fluid types (gas condensate, wet gas, or oil).

Nomenclature

FCD, dimensionless conductivity, no unit

t_{DXf}, dimensionless time, no unit

J, productivity index, no unit

k, permeability, md

w, fracture width, inch

μ, viscosity, cp

z, gas compressibility factor, no unit

T, reservoir temperature, ^{o}F

β_f, turbulence coefficient, ft^{-1}

γ_g, the gas specific gravity, no unit

P, the reservoir pressure, psi

r_e, the drainage radius, ft

Gs, the gas released from the rock, scf/ton

V_L, the Langmuir volume, scf/ton

P_L, the Langmuir pressure, psi,

L_f, fracture length/ propped length, ft

NFC, natural fracture conductivity, md-ft

HFSPC, hydraulic fracture spacing, ft

NFSPC, natural fracture spacing, ft

Φ_g, the potential of the gas phase, psi

β, the non-Darcy flow coefficient, no unit

ϕ, porosity, no unit

S_g, gas saturation, no unit

ΔP, drawdown pressure, psi

BHP, bottomhole pressure, psi

$\sigma_{\min}$, minimum horizontal stress, psi

v_{term}, terminal settling velocity, m/s

g, gravity acceleration, m/s^2

d, the particle diameter, m

ρ, density, kg/m^3

Subscripts

hf, hydraulic fracture

nf, natural fracture

s, solid particles

w, water

g, gas

f, fluid

e, drainage area

well, wellbore

m, matrix

prop, propped fracture

References

Agarwal, R.G., Carter, R.D., and Pollock, C.B. 1979. Evaluation and Performance Prediction of Low-permeability Gas Wells Stimulated by Massive Hydraulic Fracturing. JPT: 362-72.

Cinco L.H., Samaniego V.F., and Dominguez A.N. 1978. Transient Pressure Behavior for a Well with Finite-Conductivity Vertical Fracture. Soc. Pet. Eng. J.: 253-64.

Cipolla, C.L., Warpinski, N.R., Mayerhofer, M.J., Lolon, E.P., and Vincent, M.C. 2008. The Relationship Between Fracture Complexity, Reservoir Properties, and Fracture-Treatment Design. Paper SPE 115769 presented at the SPE Annual Technical Conference and Exhibition held in Denver, Colorado, USA, Sep. 21-24.

Cipolla, C.L., Lolon, E.P., Erdle, J.C., and Rubin, B. 2009a. Reservoir Modeling in Shale-Gas Reservoirs. Paper SPE 125530, presented at the SPE Eastern Regional Meeting, Charleston, West Virginia, USA, Sep. 23-25.

Cipolla, C.L., Lolon, E.P., Mayerhofer, M.J., and Warpinski, N.R. 2009b. The Effect of Proppant Distribution and Un-Propped Fracture Conductivity on Well Performance in Unconventional Gas Reservoirs. Paper SPE 119368 presented at the SPE Hydraulic Fracturing Technology Conference held in The Woodlands, Texas, USA, Jan. 19-21.

Cohen, C.E., Abad, C., Weng, X., England, K., Phatak, A., Kresse, O., Nevvonen, O., Lafitte., V., and Abivin, P. 2013. Optimum Fluid and Proppant Selection for Hydraulic Fracturing in Shale Gas Reservoirs: a Parametric Study Based on Fracturing –to-Production Simulations. Paper SPE 163876 presented at the SPE Hydraulic Fracturing Technology Conference, The woodlands, Tx, USA, Feb. 4-6.

Cohen, C.E., Xu, W., Weng, X., and Tardy, P.M.J. 2012. Production Forecast After Hydraulic Fracturing in Naturally Fractured Reservoir: Coupling a complex Fracturing Simulator and a Semi-Analytical Production Model. Paper SPE 152541 presented at the SPE Hydraulic Fracturing Technology Conference and Exhibition held in The Woodlands, Texas, USA, Feb. 6-8.

Duenckel, R., Conway, M.W., Eldred, B., and Vincent, M.C. 2012. Proppant Diagenesis - Integrated Analyses Provide New Insights into Origin, Occurrence, and Implications for Proppant Performance. SPE Production & Operations, 27 (2): 131-144.

Evans, R.D. and Civan, F. 1994. Characterization of Non-Darcy Multiphase Flow In Petroleum Bearing Formations. Report, U.S. DOE Contract No. DE-AC22-90BC14659.

Fisher, M.K., Wright, C.A., Davidson, B.M., Goodwin, A.K., Fielder, E.O., Buckler, W.S., and Steinsberger, N.P. 2005. Integrating Fracture-Mapping Technologies

To Improve Stimulations in the Barnett Shale. SPE Production & Facilities 20(2): 85-93.

Fredd, C.N., McConnell S.B., Boney C.L., and England K.W. 2001. Experimental Study of Fracture Conductivity for Water-Fracturing and Conventional Fracturing Applications. Paper SPE 74138 presented at the 2000 SPE Rocky Mountain Regional/Low Permeability Reservoirs Symposium and Exhibition, Denver, Colorado, March 12-15.

Gale, J.F.W., Reed, R.M., and Holder, J. 2007. Natural Fractures in the Barnett Shale and Their Importance for Hydraulic Fracturing Treatments. AAPG Bulletin 91 (4): 603-22.

Jacot, R.H., Bazan, L.W., and Meyer, B.R. 2010. Technology Integration - A Methodology to Enhance Production and Maximize Economics in Horizontal Marcellus Shale Wells. Paper SPE 135262 presented at the SPE Annual Technical Conference and Exhibition, Florence, Italy, Sep. 19-22.

Khan, A.M. 2013. Multi-Frac Treatments in Tight Oil and Shale Gas Reservoirs: Effect of Hydraulic Fracture Geometry on Production and Rate Transient. Thesis of Master of Science in Engineering. University of Texas at Austin.

Laubach, S.E., Olson, J.E., and Gale J.F.W. 2004. Are Open Fractures Necessarily Aligned With Maximum Horizontal Stress? Earth and Planetary Science Letters 222: 191-5.

Mayerhofer, M.J., Lolon, E.P., Youngblood, J.E., and Heinze, J.R. 2006. Integration of Microseismic Fracture Mapping Results With Numerical Fracture Network Production Modeling in the Barnett Shale. Paper SPE 102103 presented at the SPE Annual Technical Conference and Exhibition held in San Antonio, Texas, USA, Sep. 24-27.

Mcguire, W.J. and Sikora, V.J. 1960. The Effect of Vertical Fractures on Well Productivity. Trans., AIME 219: 401-03.

Meyer, B.R. and Lucas, W.B. 2011. A Discrete Fracture Network Model for Hydraulically Induced Fractures: Theory, Parametric and Case Studies. Paper SPE 140514 presented at the SPE Hydraulic Fracturing Technology Conference held in The Woodlands, Texas, USA, Jan. 24-26.

Olson, J.E. and Wu, K. 2012. Sequential versus Simultaneous Multi-zone Fracturing in Horizontal Wells: Insights from a Non-planar, Multi-frac Numerical Model. Paper SPE 152602 presented at the SPE Hydraulic Fracturing Technology Conference held in The Woodlands, Texas, USA, Feb. 6-8.

Olson, J.E., Bahorich, B., and Holder, J. 2012. Examining Hydraulic Fracture-Natural Fracture Interaction in Hydrostone Block Experiments. Paper SPE 152618 presented at the SPE Hydraulic Fracturing Technology Conference held in The Woodlands, Texas, USA, Feb. 6-8.

Rubin, B. 2010. Accurate Simulation of Non-Darcy Flow in Stimulated Fractured Shale Reservoirs. Paper SPE 132093 presented at the SPE Western Regional Meeting, Anaheim, California, USA, May 27-29.

Tannich, J.D. and Nierode, D.E. 1985. The Effect of Vertical Fractures on Gas Well Productivity. Paper SPE 15902, presented at the SPE Annual Technical Conference and Exhibition, New Orleans, Louisiana, October 5-8.

Thompson, J.M., M'Angha, V.O., and Anderson, D.M. 2011. Advancements in Shale Gas Production Forecasting – A Marcellus Case Study. Paper SPE 144436 presented at the SPE Americas Unconventional Gas Conference and Exhibition, The Woodlands, Tx, USA, June 14-16.

Tinsley, J.M., Williams Jr., J.R., Tiner, R.K., and Malone, W.T. 1969. Vertical Fracture Height - Its Effect on Steady-State Production Increase. JPT, AIME 246: 633-38.

Wang, W., Olson, J.E., and Prodanović, M. 2013. Natural and Hydraulic Fracture Interaction Study Based on Semi-Circular Bending Experiments. Paper SPE 168714 presented for presentation at the Unconventional Resources Technology Conference held in Denver, Colorado, USA, Aug. 12-14.

Warpinski, N.R., Mayerhofer, M.J., Vincent, M.C., Cipolla, C.L, and Lolon, E.P. 2008. Stimulating Unconventional Reservoirs: Maximizing Network Growth While Optimizing Fracture Conductivity. Paper SPE 114173 presented at the SPE Unconventional Reservoirs Conference held in Keystone, Colorado, USA, Feb. 10-12.

Weng, X., Kresse, O., Cohen, C., Wu, R., and Gu, H. 2011. Modeling of Hydraulic Fracture Network Propagation in a Naturally Fractured Formation. Paper SPE 140253 presented at the SPE Hydraulic Fracturing Technology Conference and Exhibition held in The Woodlands, Texas, USA, Jan. 24-26.

Yu, W. and Sepehrnoori, K. 2013. Optimization of Multiple Hydraulically Fractured Horizontal Wells in Unconventional Gas Reservoirs. Paper SPE 164509 presented at the SPE Production and Operations Symposium held in Oklahoma City, Oklahoma, USA, Mar. 23-26.

Zhang, J. Kamenov, A., Zhu, D., and Hill, A.D. 2013. Laboratory Measurement of Hydraulic Fracture Conductivities in the Barnett Shale. Paper SPE 163839 presented at the SPE Hydraulic Fracturing Technology Conference held in The Woodlands, Texas, USA, Feb. 4-6.

Table 2.1: Simulation input values for parametric study (Marcellus Dry Gas).

Reservoir Properties				Completion Parameters	
Pr_{pore} (psi)	3300	E (psi)	2E6	L_{well} (ft)	5000
σ_{min} (psi)	4500	ν	0.25	Well Spc (ft)	2000
Temp (^{o}F)	130	P_L (psi)	468	Frac Spc (ft)	100, 200
φ	8%	V_L (scf/lb)	0.0425	H_{prop} (ft)	150
H_{pay}(ft)	150	ρ_{rock} (g/cc)	2.6	L_{prop} (ft)	*s.s.*
k_m (nD)	20, 200	S_{wi}	20%	$Cond_{prop}$ (md-ft)	*s.s.*
K_v/k_h	0.1	S_{gi}	80%		
C_{por} (1/psi)	6E-6	Methane	100%	BHP (psi)	500

Table 2.2: Parametric (hydraulic fracture conductivity & propped length) study matrix.

L_{prop} (ft) HFC (md-ft)	200	300	400	500	600	700
1						
5						
10						
20			Total 60 sets			
50						
100						
250						
500						
750						
1000						

Table 2.3: Reactivated natural fracture properties for parametric study.

NFSPC (ft) NFC (md-ft)	25	50	100	200
0				
0.001				
0.01				
0.1				
1				
10				

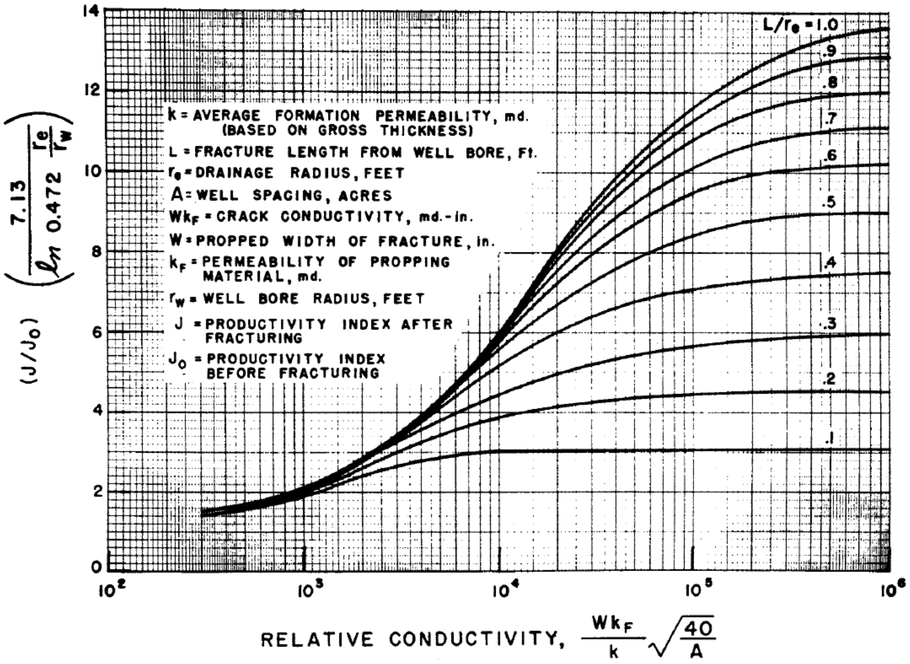

Figure 2.1: McGuire and Sikiora's producing-rate folds-of-increase curves (McGuire and Sikiora, 1960).

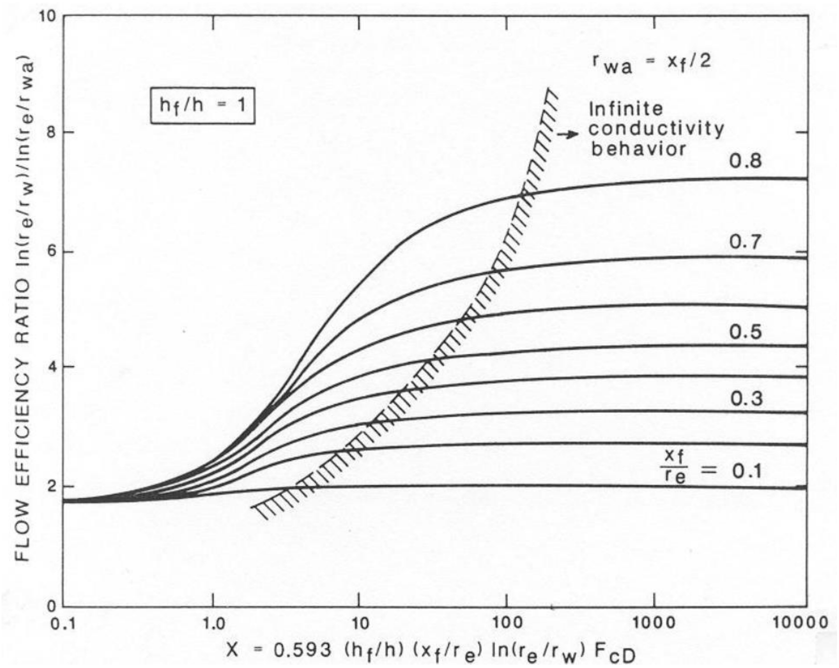

Figure 2.2: Tinsley's producing-rate folds-of-increase curves (Tinsley et al., 1969).

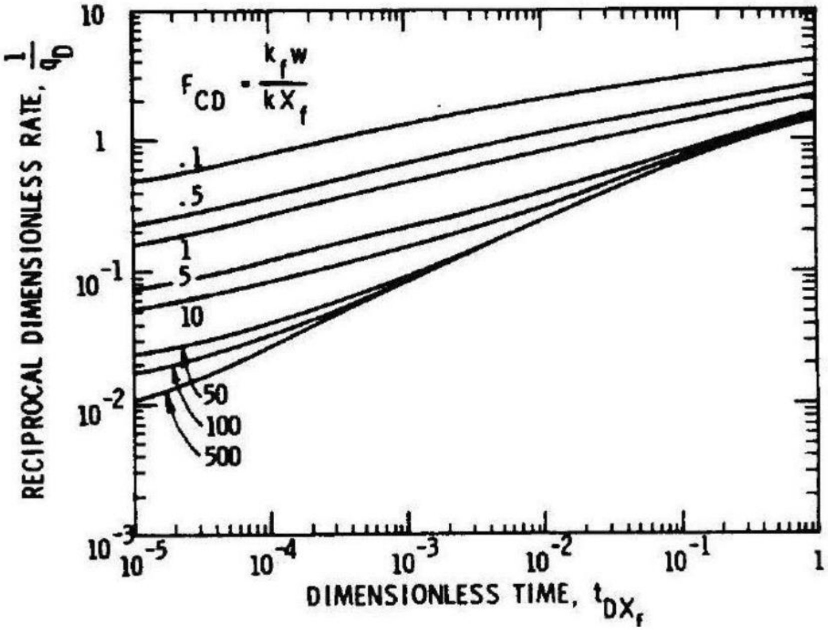

Figure 2.3: Agarwal's type curves with propped vertical fractures at transient flow (Agarwal et al., 1979).

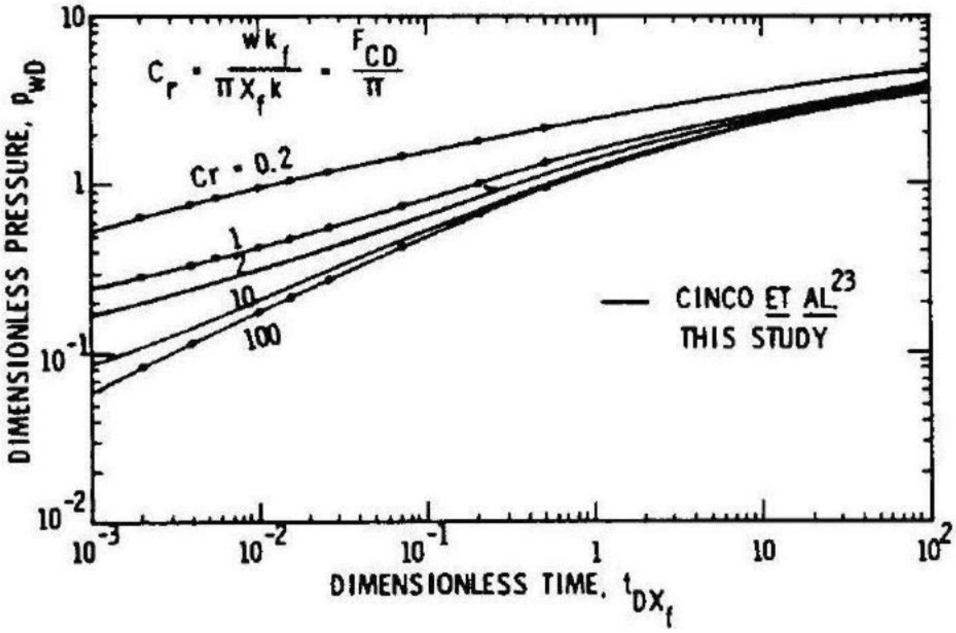

Figure 2.4: Cinco's type curves with propped vertical fractures at transient flow (Cinco et al., 1978).

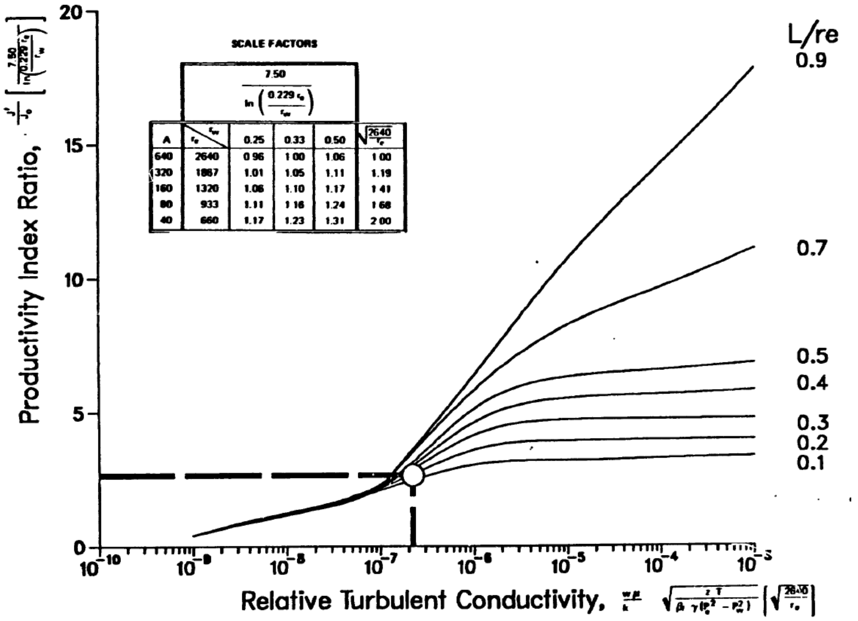

Figure 2.5: Tannich and Nierode's type curves for gas wells (base case) (Tannich and Nierode, 1985).

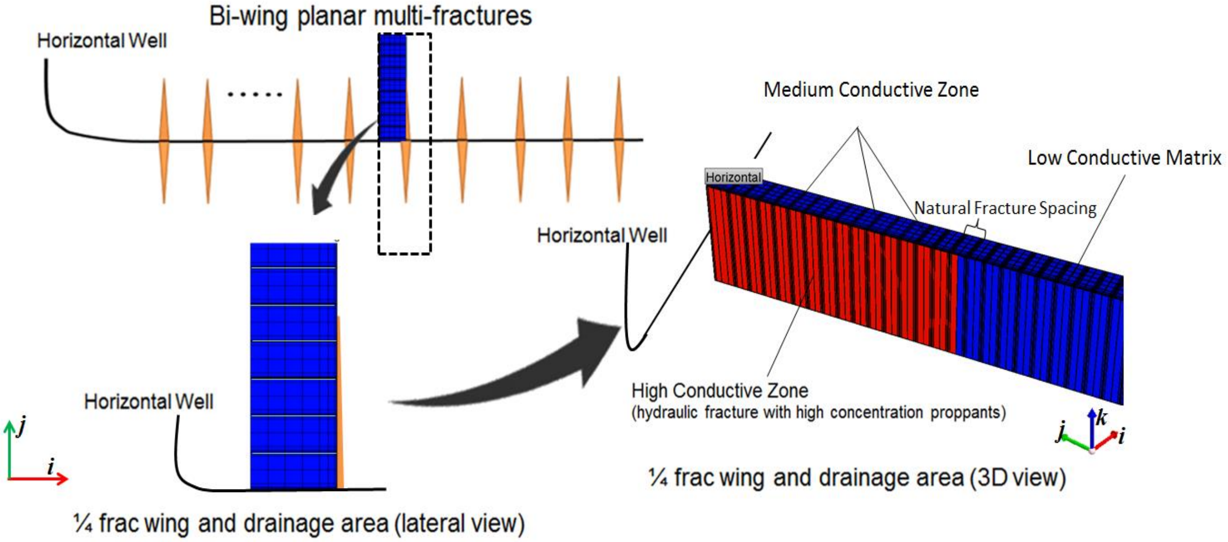

Figure 2.6: The reservoir simulation model of the one fourth of the fracture and the corresponding drainage area.

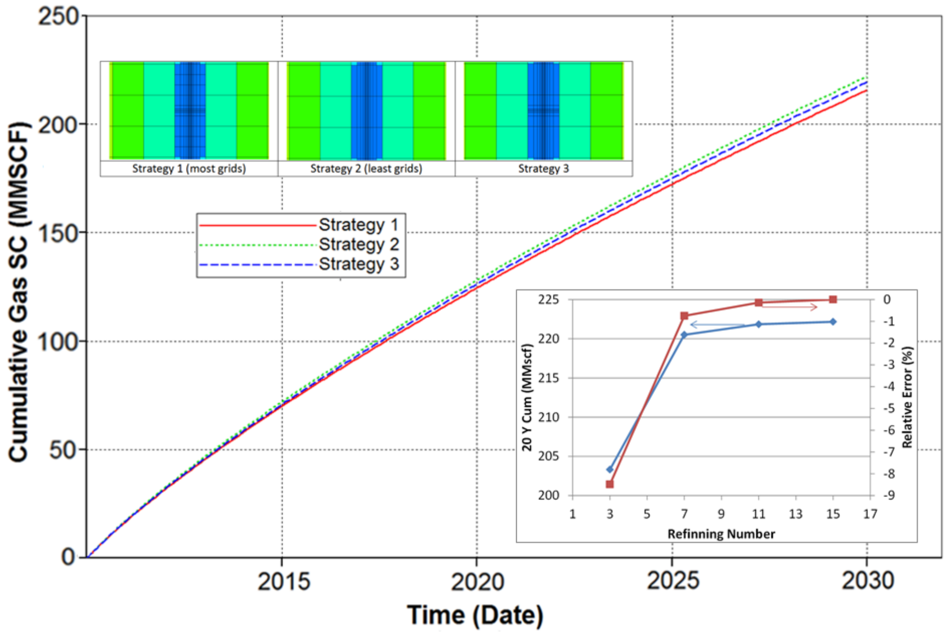

Figure 2.7: The validation of grid refinement strategy.

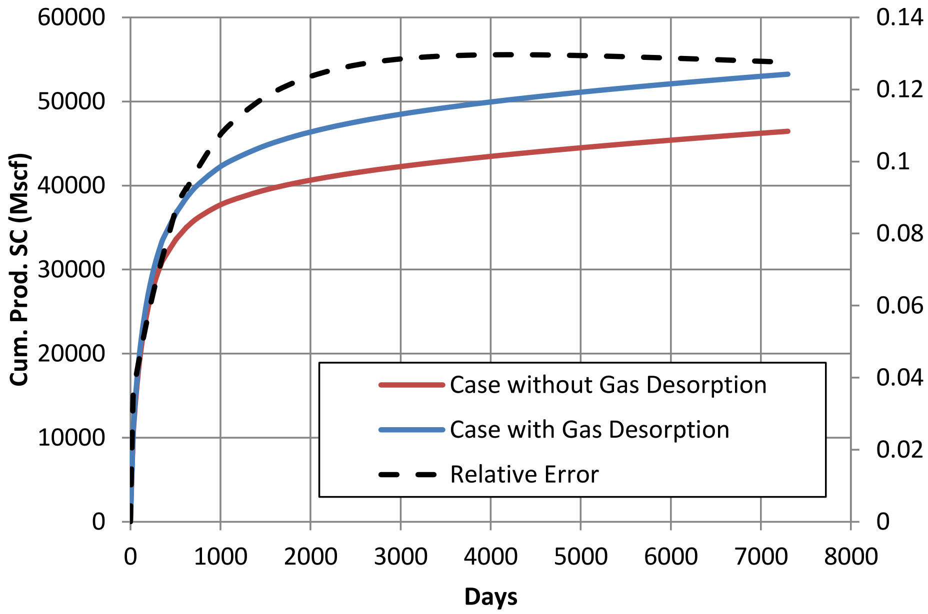

Figure 2.8: Gas Desorption vs. Non Gas Desorption (Lf: 400ft, HFC: 1000 md-ft, NFSPC: 50ft, NFC: 0.1md-ft).

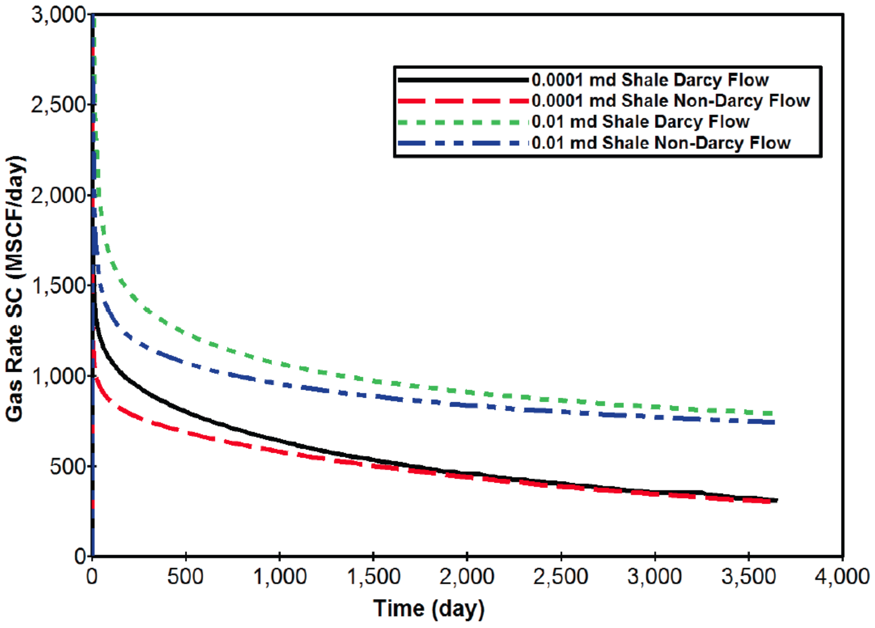

Figure 2.9: Darcy Flow vs. Non-Darcy Flow (Rubin, 2010).

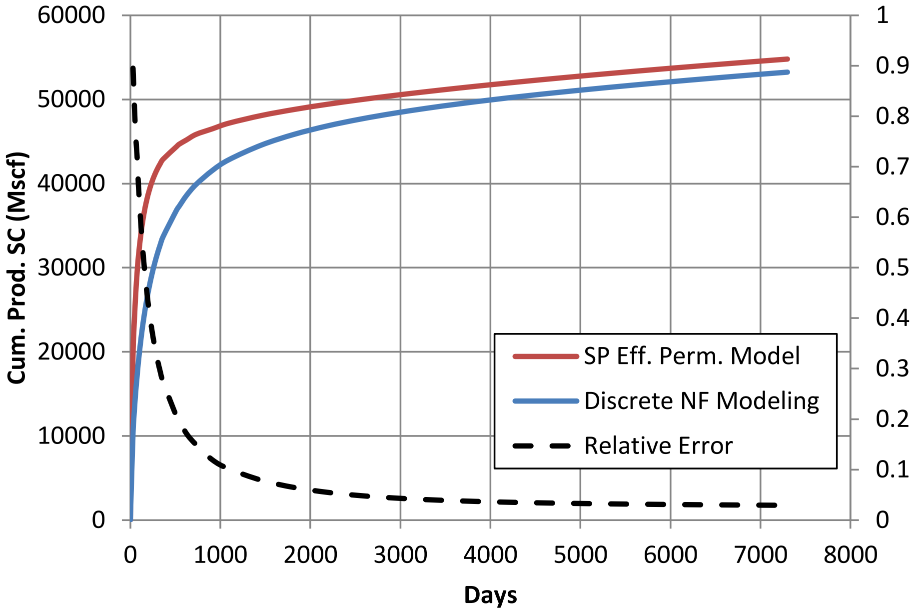

Figure 2.10: Single Porosity Effective Perm. Model vs. Discrete Natural Fracture Model (Lf: 400ft, HFC: 1000 md-ft, NFSPC: 50ft, NFC: 0.1md-ft).

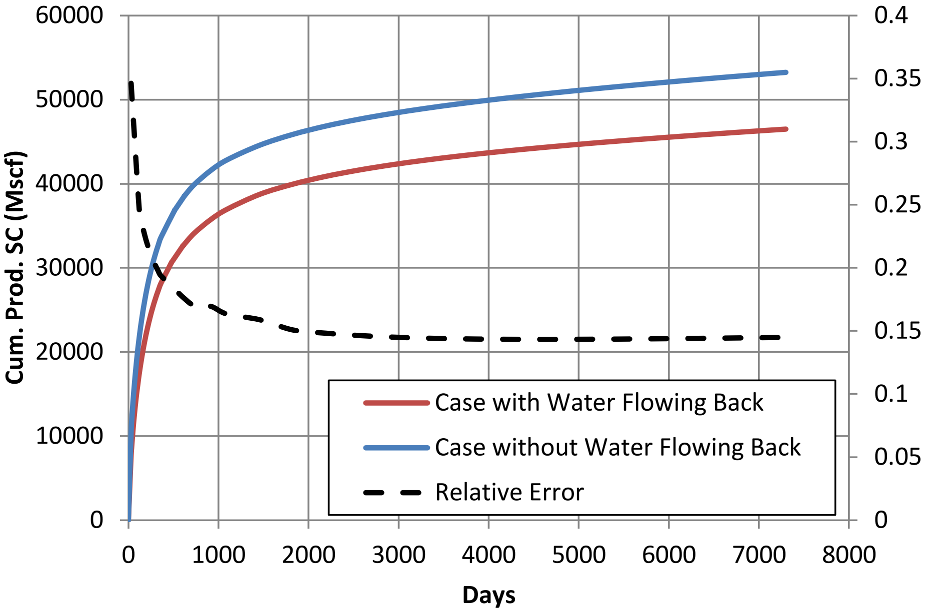

Figure 2.11: Water Flowing-back vs. Dry Gas (Lf: 400ft, HFC: 1000 md-ft, NFSPC: 50ft, NFC: 0.1md-ft).

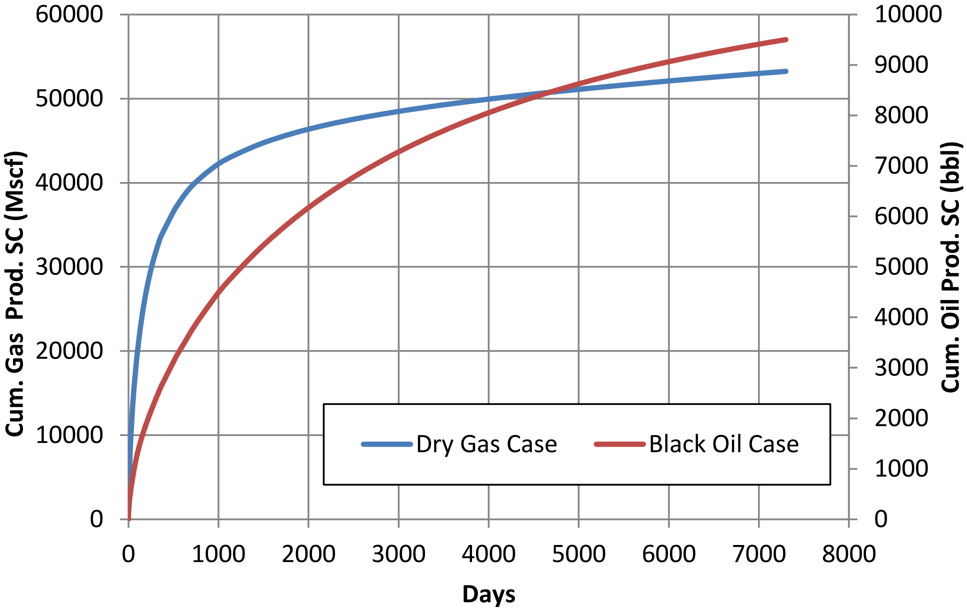

Figure 2.12: Black Oil vs. Dry Gas (Lf: 400ft, HFC: 1000 md-ft, NFSPC: 50ft, NFC: 0.1md-ft).

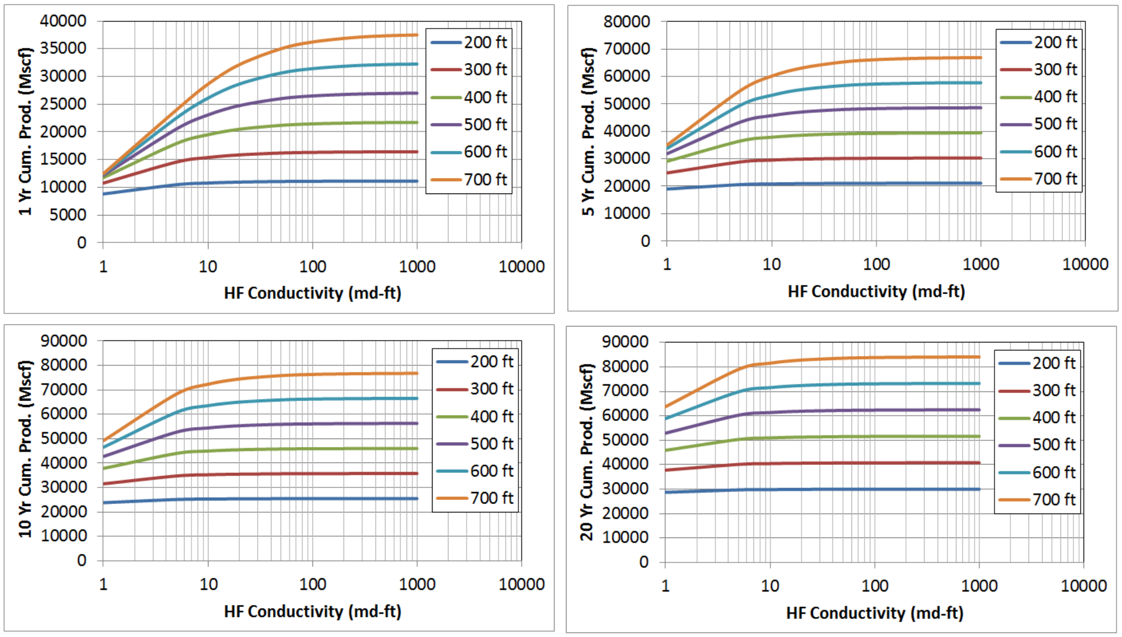

Figure 2.13: Cumulative Productions vs. HF Conductivity at different production time (200 nD, no NF).

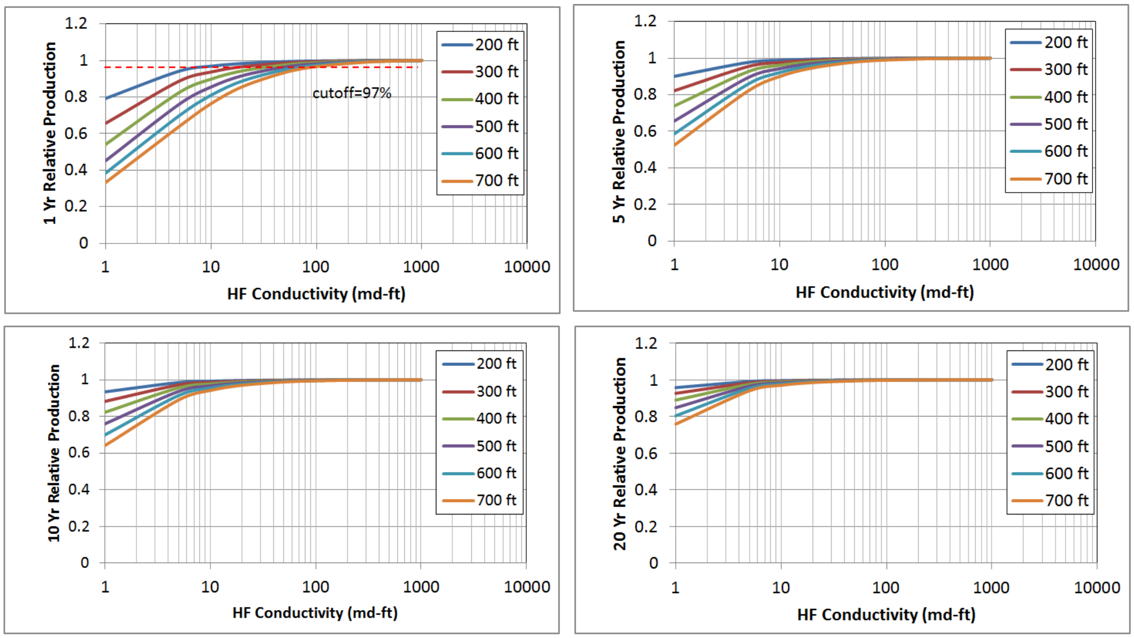

Figure 2.14: Relative Cum. Prod. vs. HF Conductivity at different production time (200 nD, no NF).

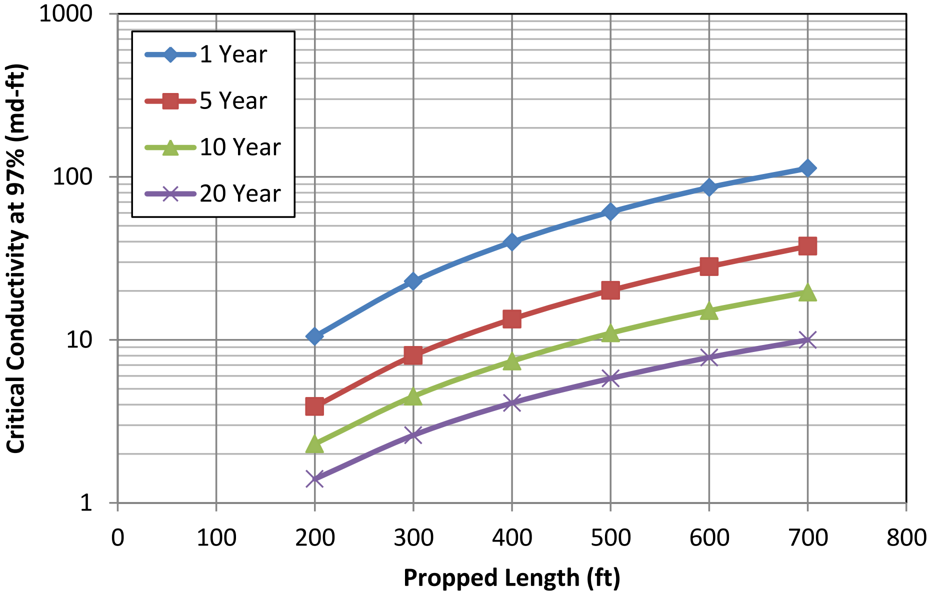

Figure 2.15: Critical Conductivity vs. Propped Length for different production time (200 nD, no NF).

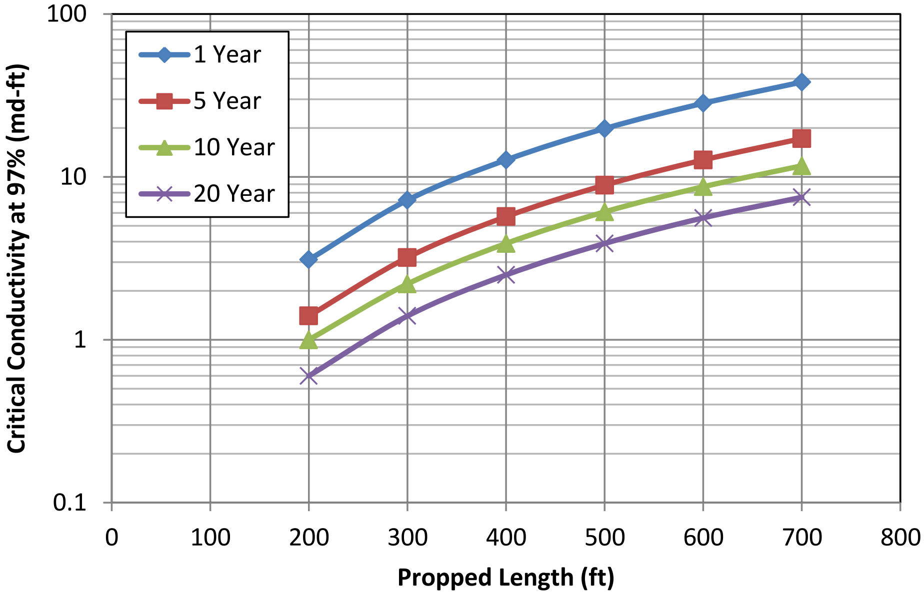

Figure 2.16: Critical Conductivity vs. Propped Length for different production time (20 nD, no NF).

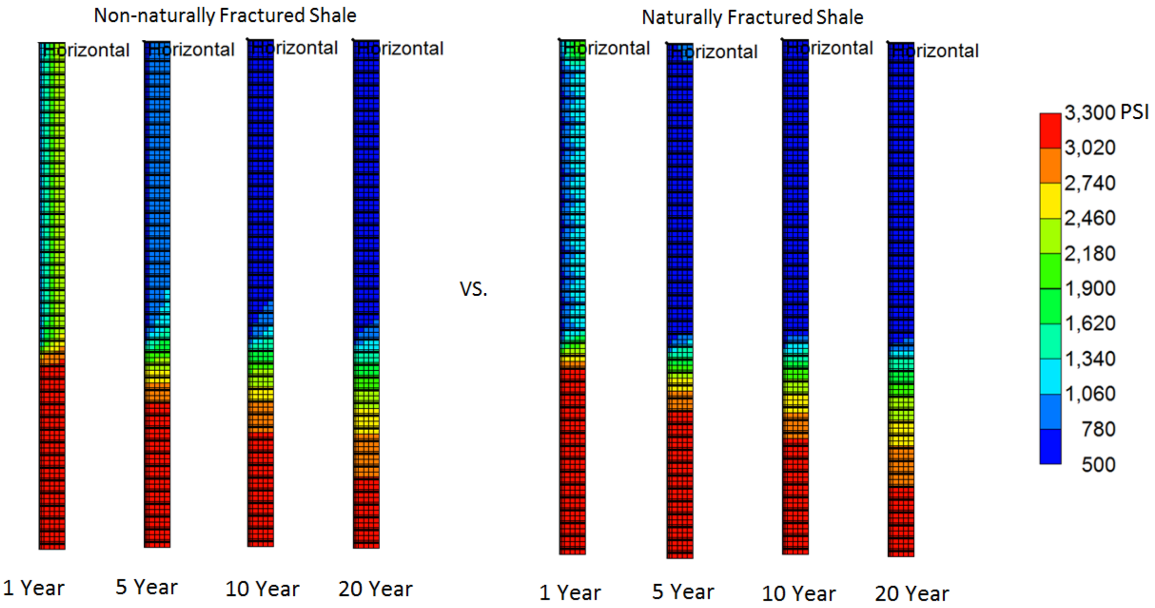

Figure 2.17: Pressure fields after different production time for non-naturally fractured and naturally fractured shale reservoirs (k_m=200 nD).

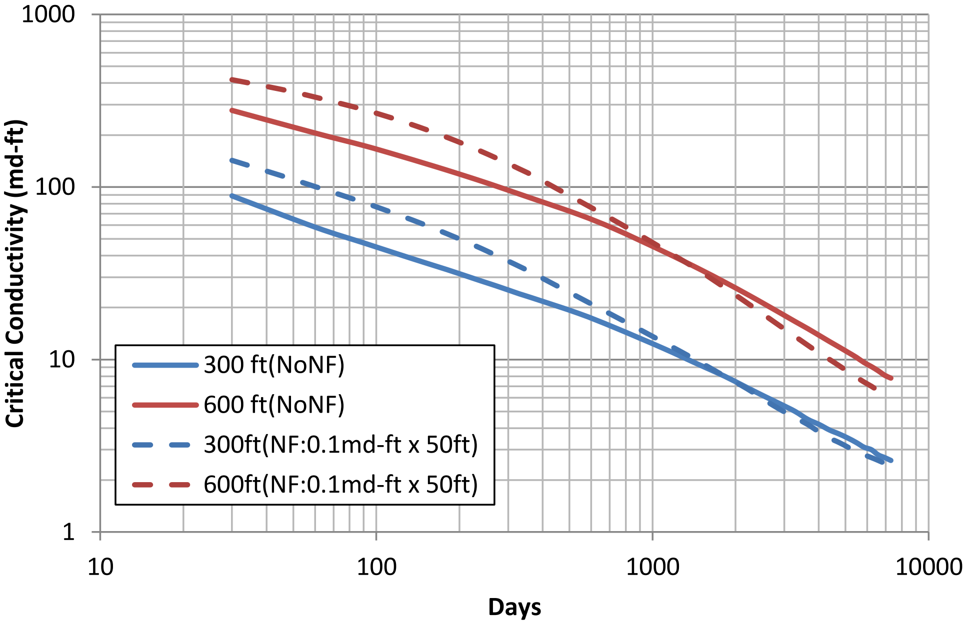

Figure 2.18: Critical Conductivity vs. Production Time for 200 nD matrix with and without natural fractures.

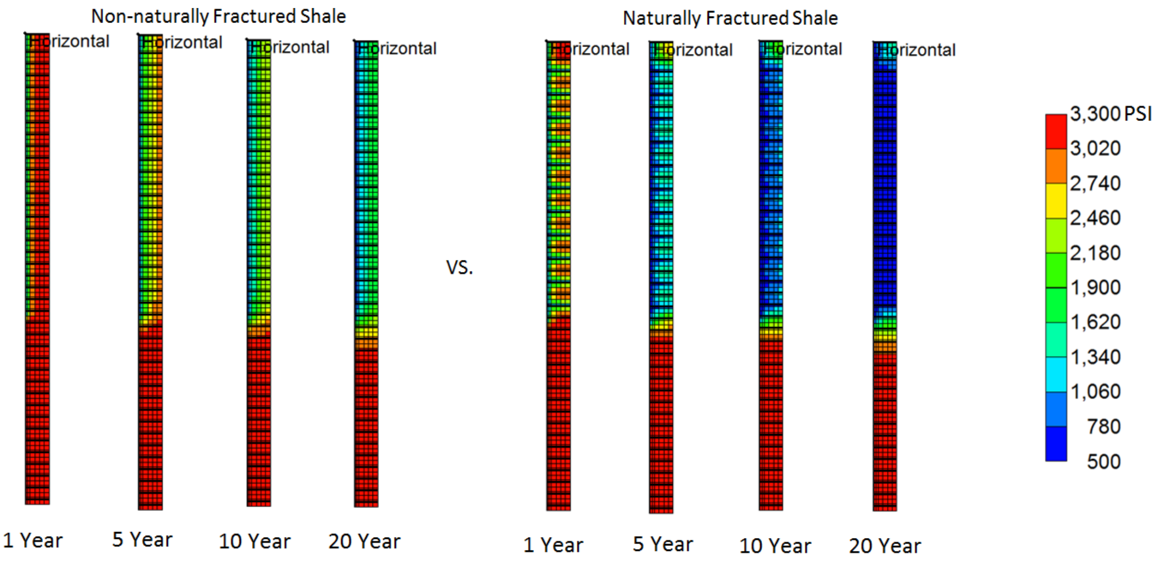

Figure 2.19: Pressure fields after different production time for non-naturally fractured and naturally fractured shale reservoirs (k_m=20 nD).

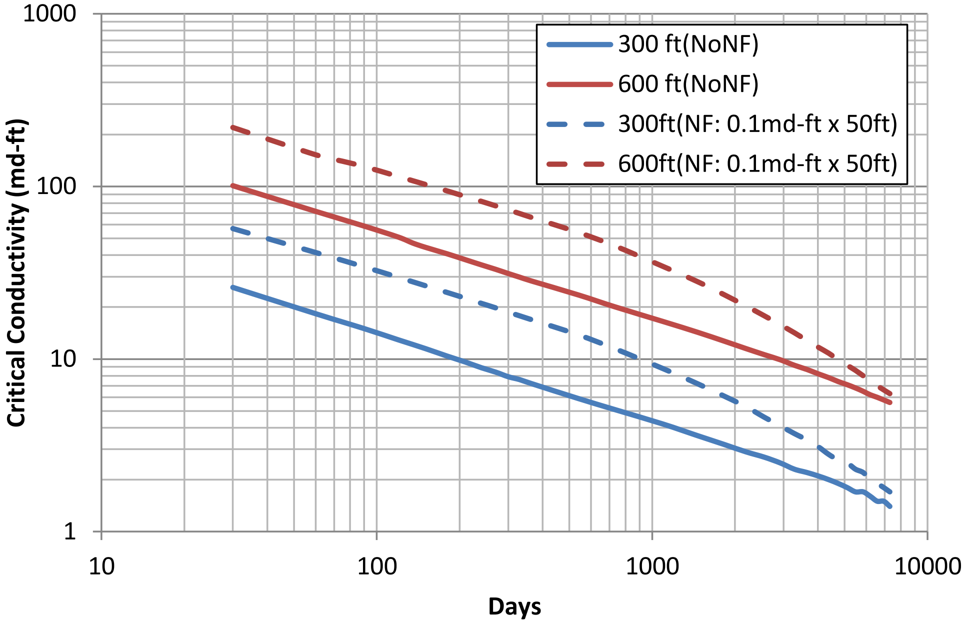

Figure 2.20: Critical Conductivity vs. Production Time for 20 nD matrix with and without natural fractures.

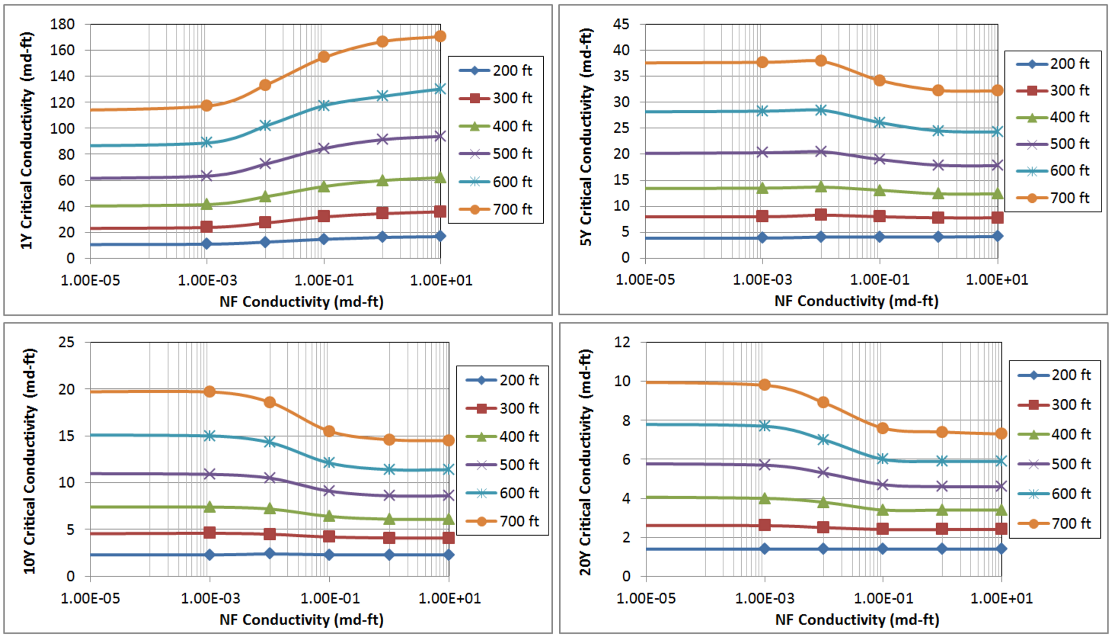

Figure 2.21: Critical Conductivity vs. NFC at different propped lengths and production time (k_m=200 nD).

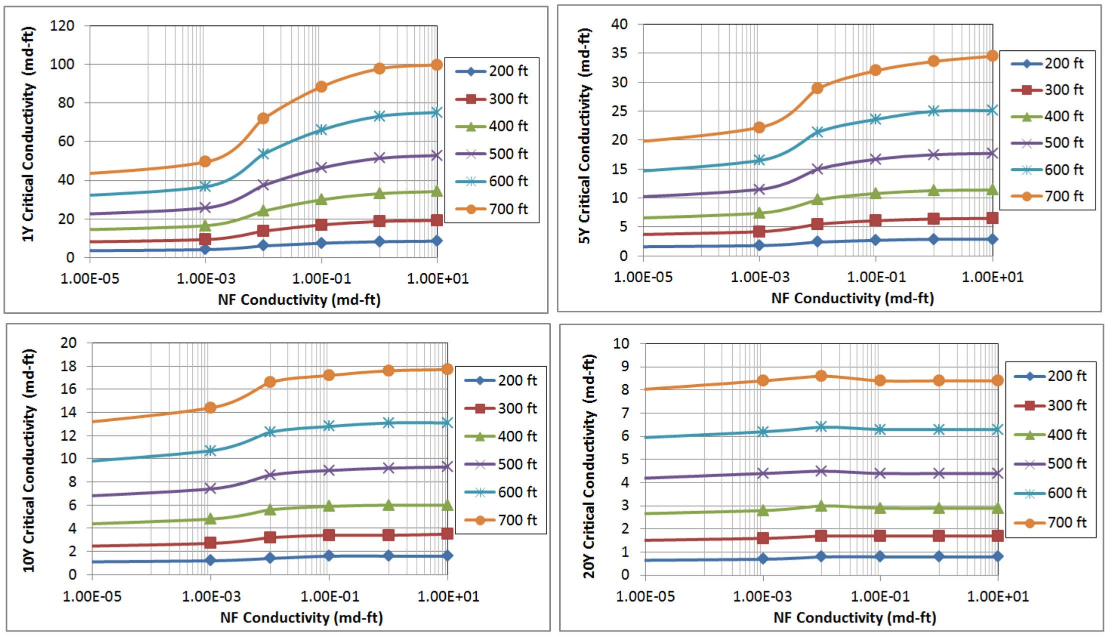

Figure 2.22: Critical Conductivity vs. NFC at different propped lengths and production time (k_m=20 nD).

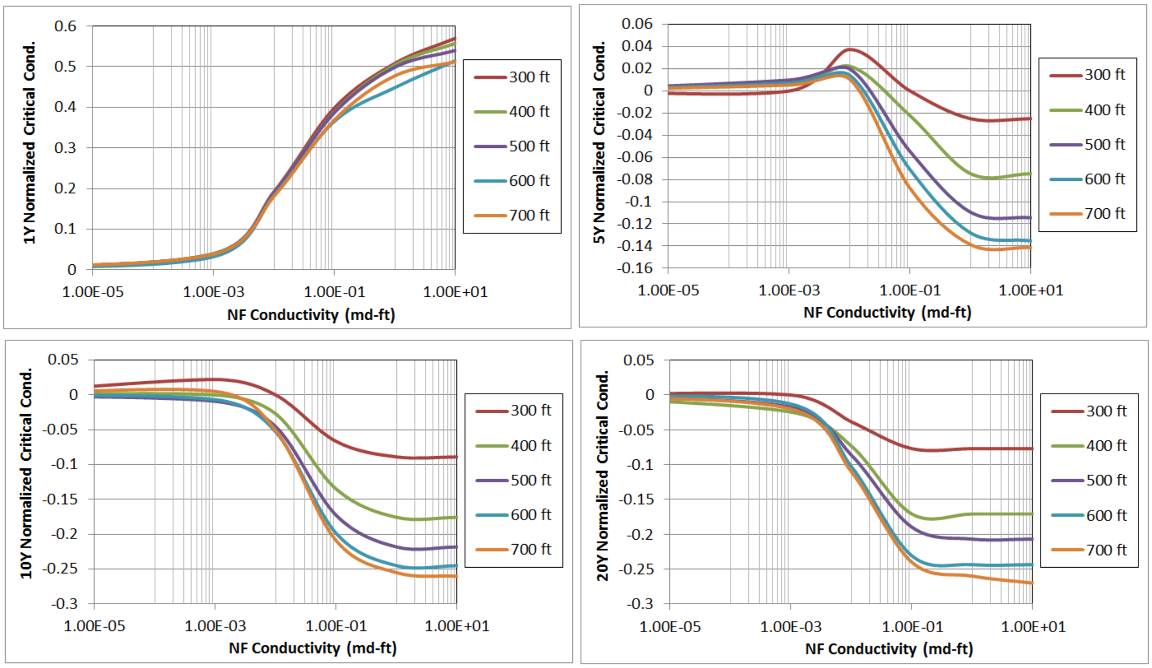

Figure 2.23: Normalized Critical Conductivity vs. NFC at different propped lengths and production time (k_m=200 nD).

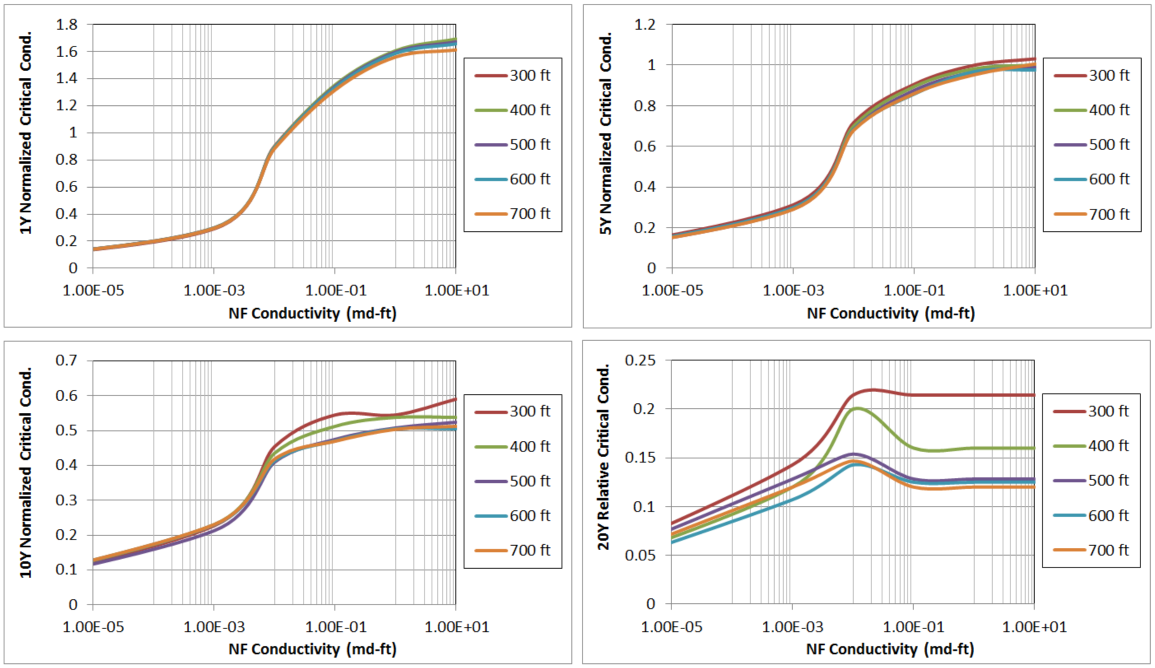

Figure 2.24: Normalized Critical conductivity vs. NFC at different propped lengths and production time (k_m=20 nD).

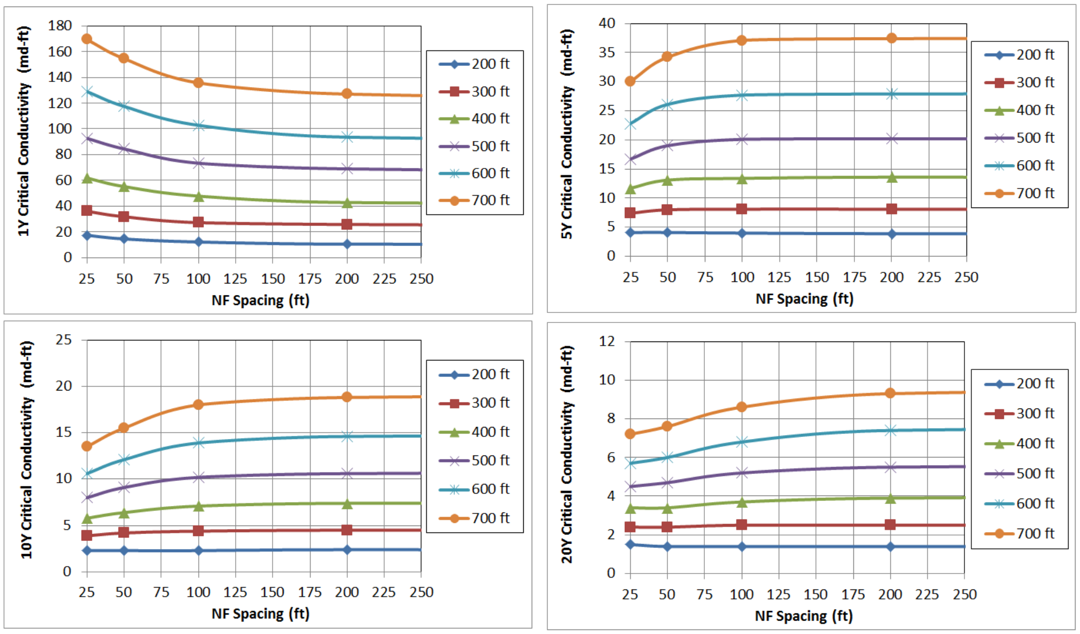

Figure 2.25: Critical Conductivity vs. NFSPC at different propped lengths and production time (k_m=200 nD).

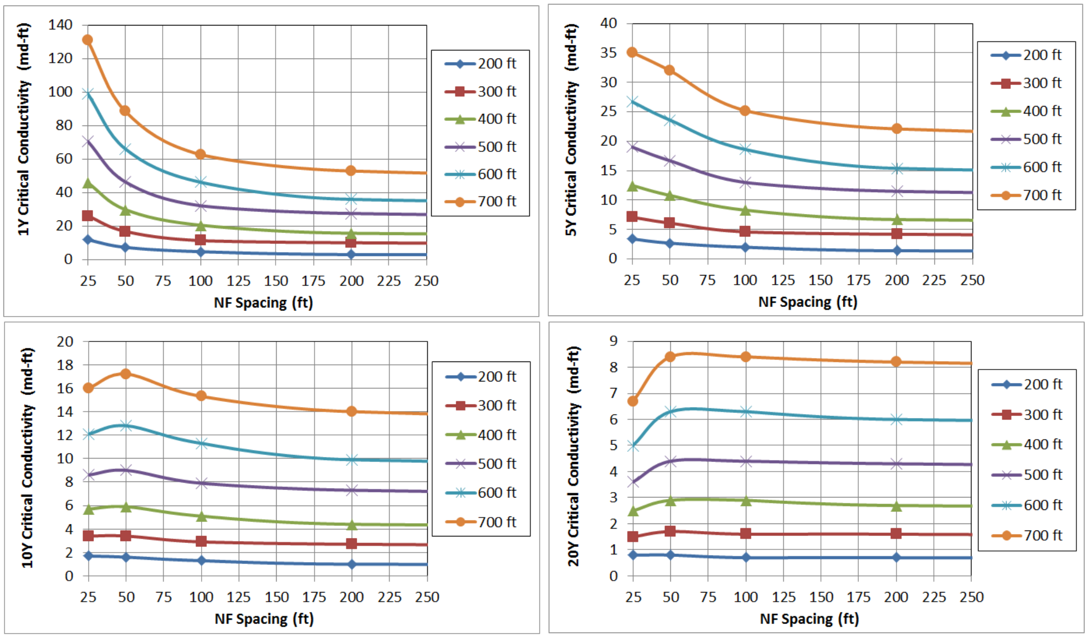

Figure 2.26: Critical Conductivity vs. NFSPC at different propped lengths and production time (k_m=20 nD).

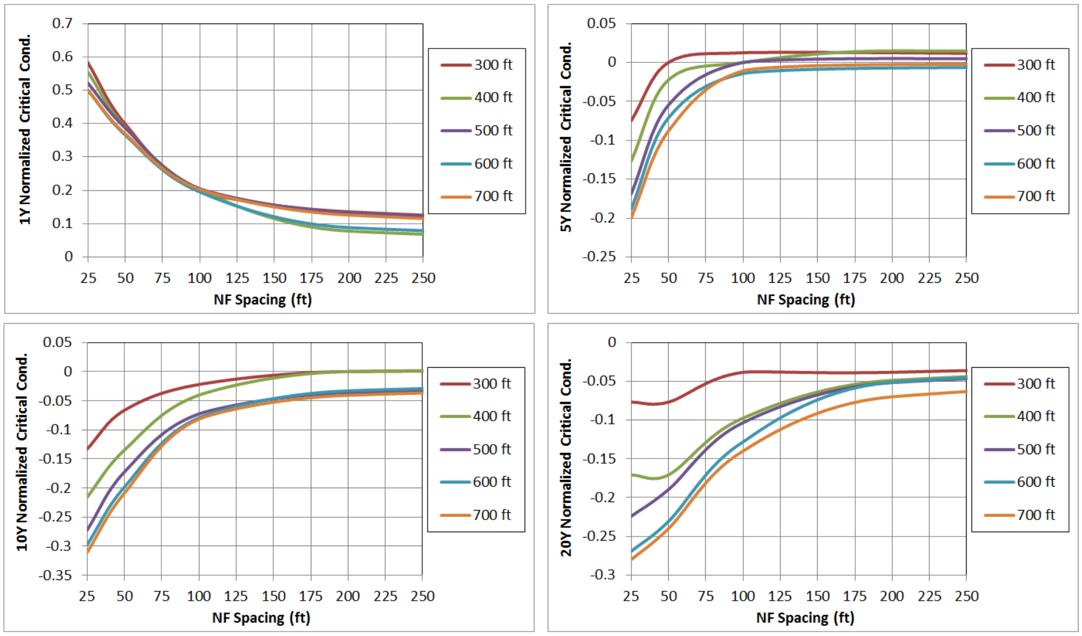

Figure 2.27: Normalized Critical Conductivity vs. NFSPC at different propped lengths and production time (k_m=200 nD).

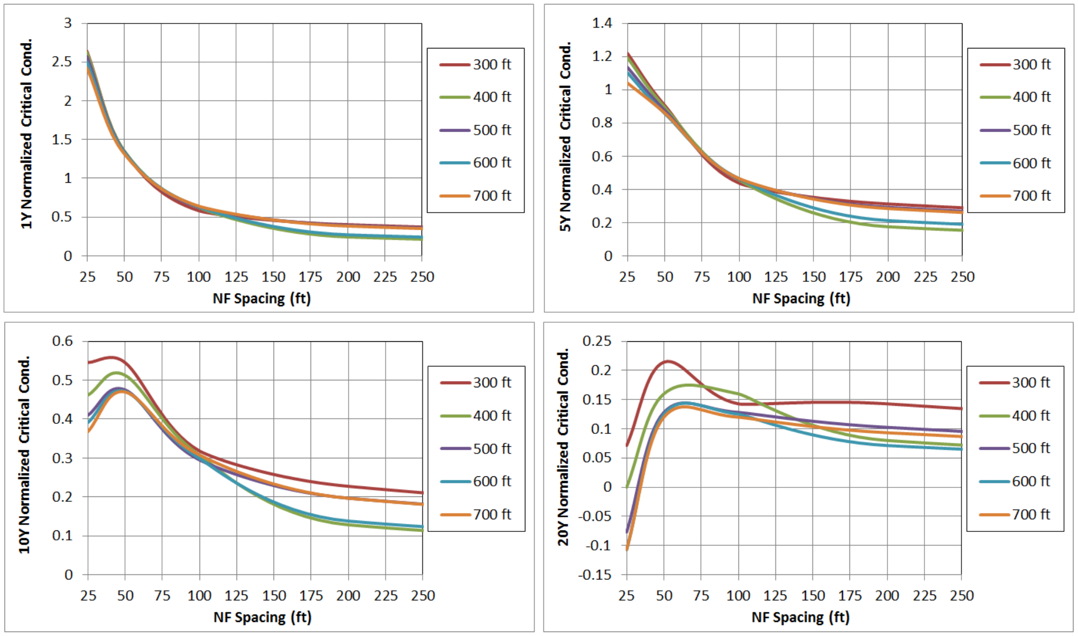

Figure 2.28: Normalized Critical Conductivity vs. NFSPC at different propped lengths and production time (k_m=20 nD).

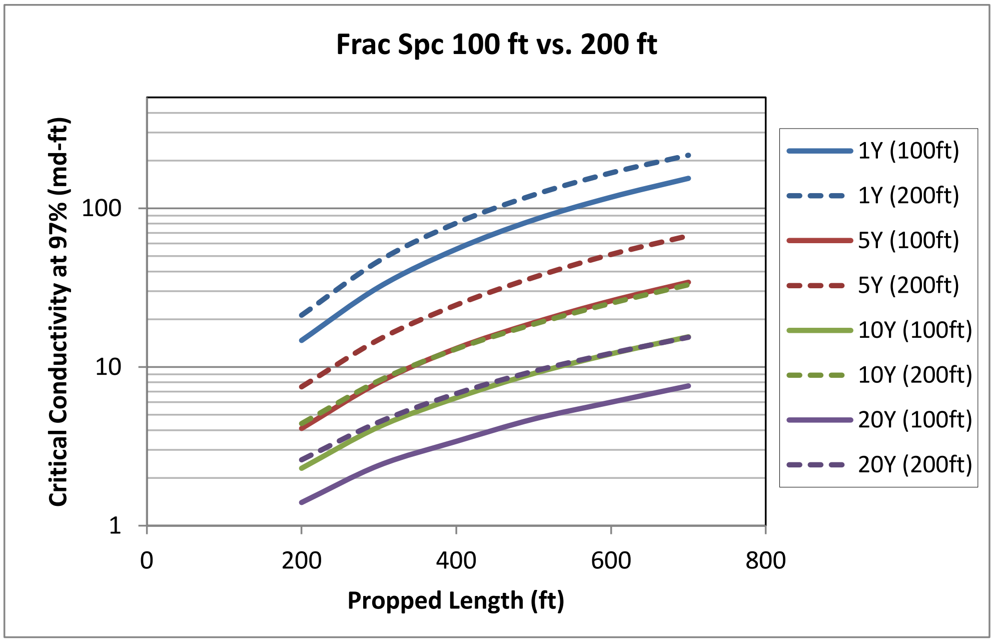

Figure 2.29: Comparison of critical conductivity at different hydraulic fracture spacing.

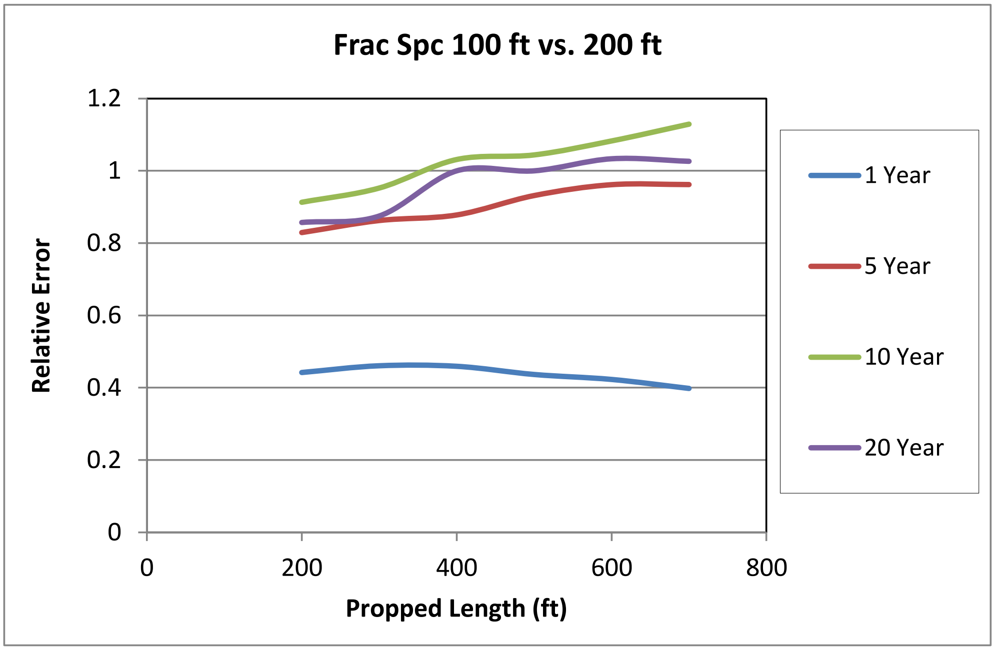

Figure 2.30: Relative error of critical conductivity caused by hydraulic fracture spacing.

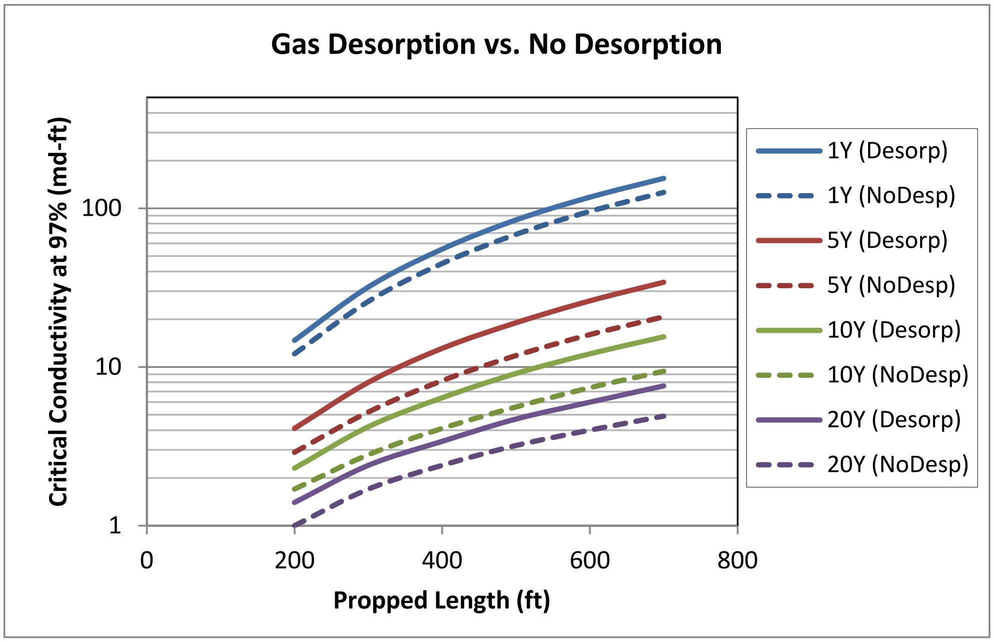

Figure 2.31: Comparison of critical conductivity with and without considering gas desorption.

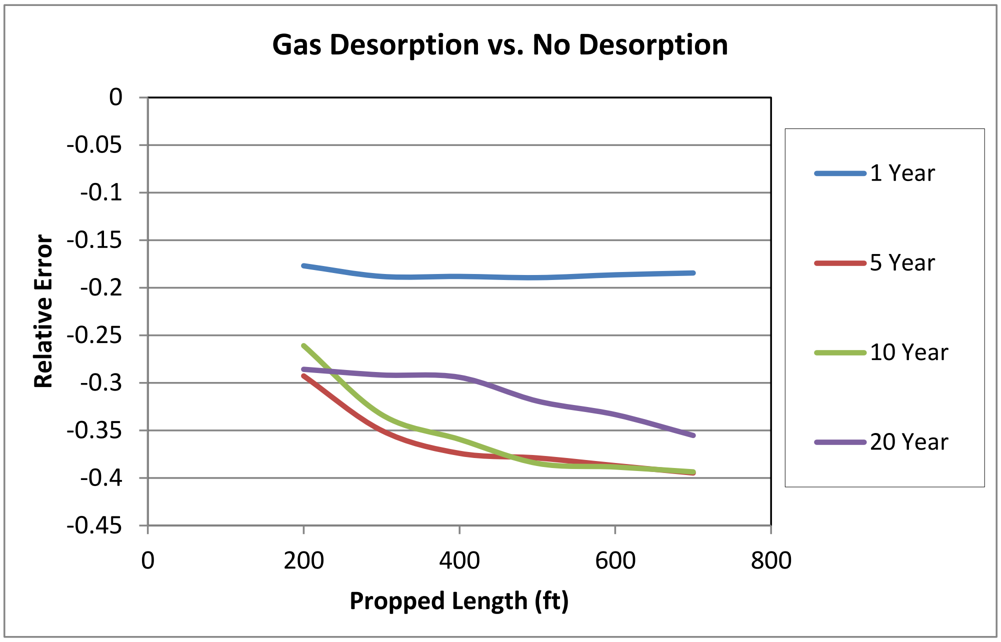

Figure 2.32: Relative error of critical conductivity caused by gas desorption.

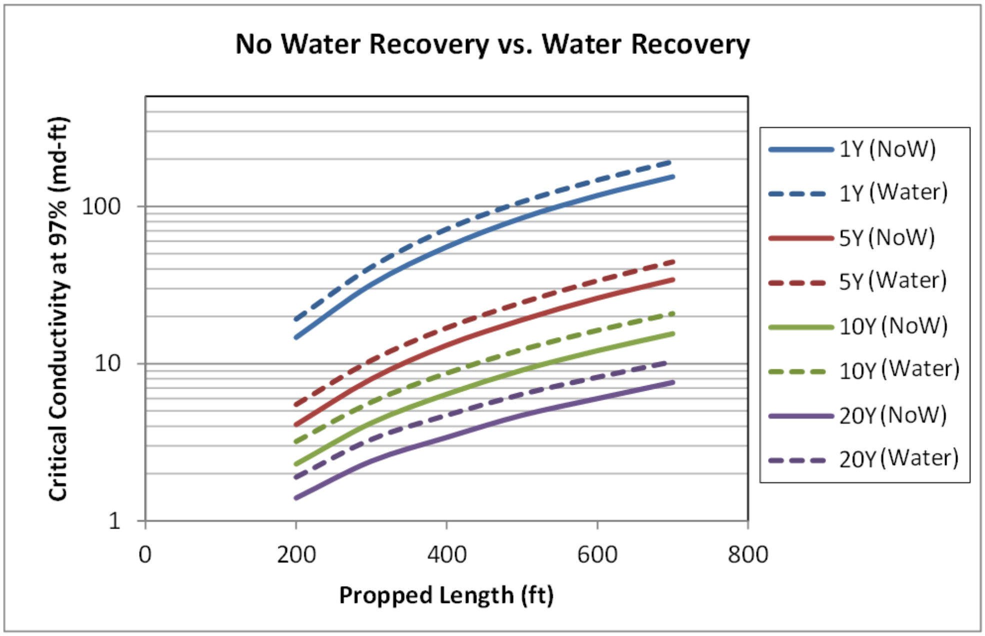

Figure 2.33: Comparison of critical conductivity with and without considering water recovery.

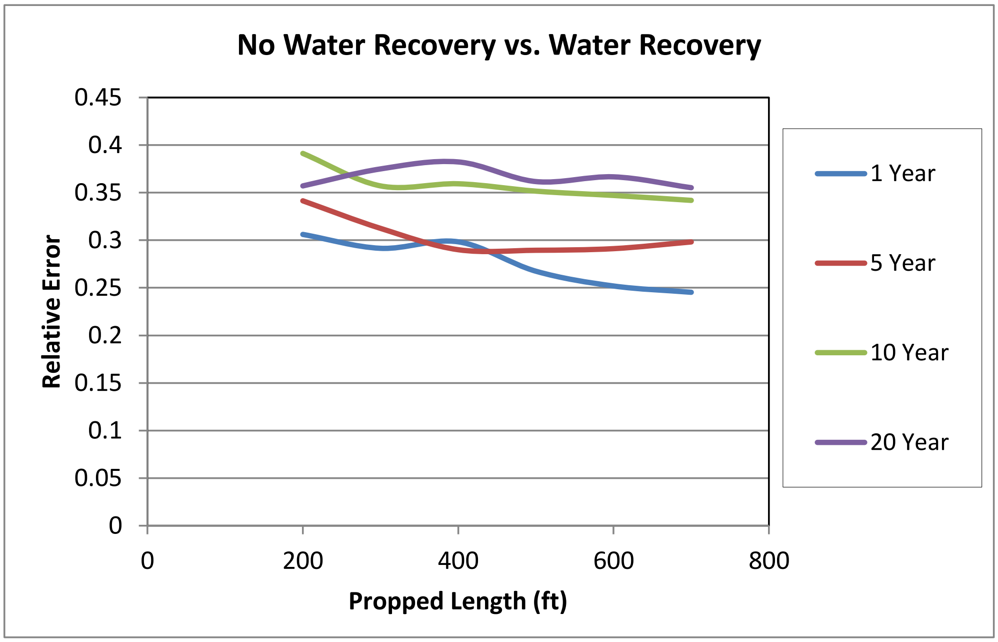

Figure 2.34: Relative error of critical conductivity caused by water recovery.

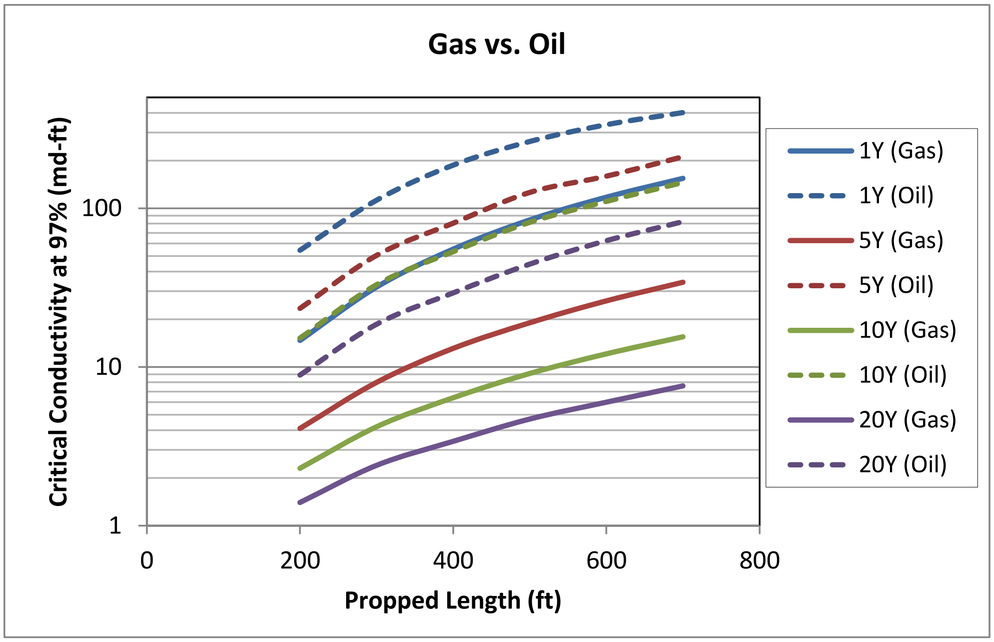

Figure 2.35: Comparison of critical conductivity of different reservoir fluid types.

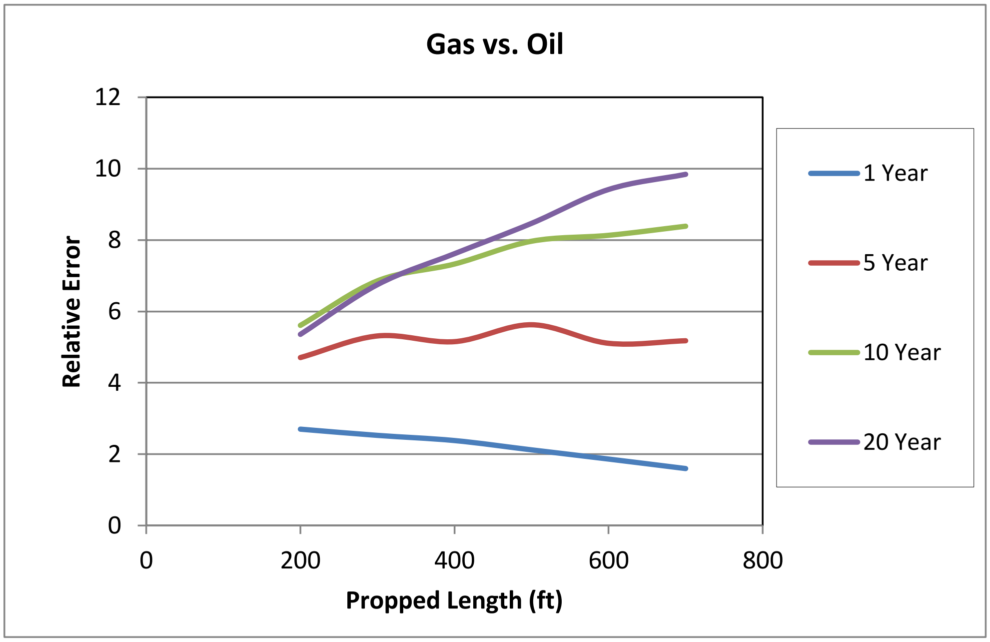

Figure 2.36: Relative error of critical conductivity caused by the change of the reservoir fluid type.

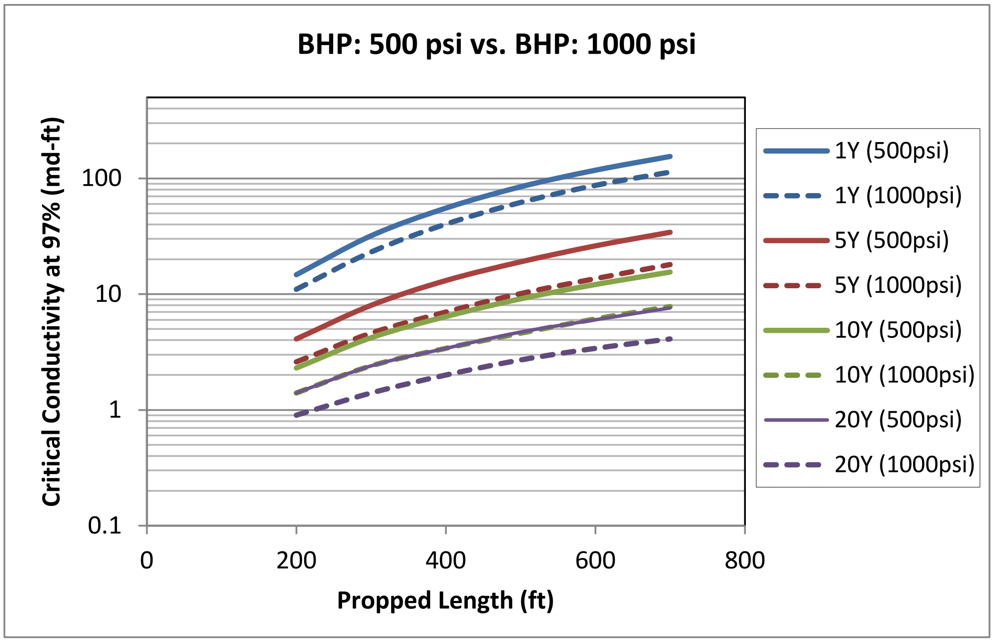

Figure 2.37: Comparison of critical conductivity at different flowing BHPs.

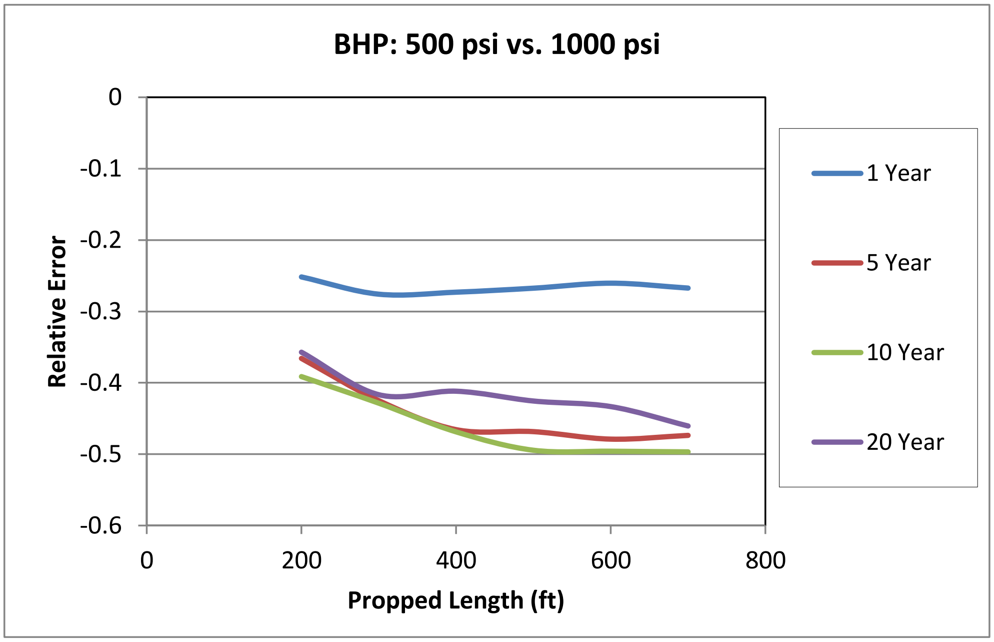

Figure 2.38 Relative error of critical conductivity caused by the increase of the BHP.

Chapter 3: Modeling of Fracture Propagation, Proppant Transport and Fracture Productivity

To investigate the impact of the proppant and fracturing fluid properties on fracture productivity, a fracture modeling simulator is developed to predict the fracture geometry and proppant distribution. The 2D fracture propagation model is built based on the PKN (Perkins-Kern-Nordgren) model. Proppant distribution is obtained by solving a separate proppant transport equation. These predicted results are input into a state-of-the-art reservoir simulator (CMG) to estimate the resulting fracture productivity.

This chapter first reviews the current fracture modeling, then introduces the formulations and algorithm implemented in our fracture modeling simulator, and finally discusses some preliminary results.

3.1 REVIEW OF EXISTING FRACTURE MODELS

Various models have been developed in the past to describe the fracture opening during hydraulic fracturing, such as two-dimensional fracture models (Khristianovitch and Zheltov, 1955, Perkins and Kern, 1961, Geertsma and Klerk, 1969, Nordgren, 1972, Abé et al., 1976), pseudo three-dimensional models (Settari and Cleary, 1986), and fully three-dimensional models (Gu and Leung, 1993, Sousa et al., 1993). Perkins and Kern (1961) developed a two-dimensional fracture propagation model by assuming that fracture height is fixed and much smaller than the fracture length. Plane strain is considered in the vertical direction perpendicular to the direction of fracture propagation. The other assumptions include neglected fracture toughness, elliptical cross-section, and constant pressure along the vertical direction. Later Nordgren (1972) improved this model by adding fluid loss term; this model is commonly known as the PKN model. Another classical 2D model is the KGD model developed by Khristianovitch and Zheltov

(1955) and Geertsma and de Klerk (1969). It assumes that flow rate and pressure are constant along the majority of the fracture length, except for a small region close to the fracture tip. In this model, plane strain is assumed to be in the horizontal direction, which holds true if fracture height is much greater than fracture length. When the fracture height is comparable with the fracture length, there is another more appropriate 2D model, known as the Penny-shaped or radial model (Abé et al., 1976). In this model, the fracture propagates in a given plane, and the geometry of the fracture is symmetric with respect to the point at which fluids are injected. The above 2D models are simple, fast, good approximations, but they are not able to simulate both vertical and lateral propagation.

The pseudo-3D (P3D) models, evolving from the 2D PKN model, assume that the height grows with time and varies along the propagation direction (Settari and Cleary, 1986). Additionally, a vertical fluid flow component is added in flow equations in P3D models. More complex fully 3D models are developed to simulate fractures of arbitrary shape and orientation in the heterogeneous reservoir by solving a set of coupled equations governing the deformation of a 3D rock and the 2D fluid flow in the fracture (Gu and Leung, 1993, Sousa et al., 1993). They are mathematically more rigorous, but expensive to run.

Recently, Friehauf and Sharma (2009) developed the first compositional 2D hydraulic fracturing model (EFRAC-2D) for energized fracturing. In this model, an energy balance is added to track the temperature change in the wellbore and the fracture. An equation of state is implemented to calculate the amount and composition of each phase based on the fluid pressure, temperature, and composition. This new model reduces to the PKN model when incompressible fluid and isothermal systems are used. Ribeiro and Sharma (2013) extend the 2D simulator to 3D, named as EFRAC-3D. Compared with EFRAC, the simulator in this dissertation does not consider the temperature impact on foam fracturing. Besides, instead of including a wellbore flow, a constant inlet flow rate constraint is applied at the entrance of the fracture.

StimPlan is a planar 3D fracture software developed by Mike Smith and coworkers at NSI Tech. The numerical solution of model equations is obtained by combination of finite element method (for rock deformation) and finite difference method (for fluid flow within fracture). It has several features including, vertical change of stratigraphy, stress shadow simulation, natural fracture leak-off, and integration with log data, Microseismic data, pressure history matching and reservoir simulation. FracPro is another famous planar 3D fracture software. It has the similar features as StimPlan. However, both simulators are not open source software. We cannot add or modify equations inside the simulators (e.g. incorporating API conductivity results or fluid rheological model). Thus, in current study, we developed a research simulator, which can include different constitutive models from the lab study.

3.2 FORMULATION APPLIED IN CURRENT FRACTURE MODELING

In this section, the geomechanics equation, fluid flow equation, proppant transport equation and their differential forms are introduced. Following that, the algorithm to solve the derived non-linear partial equation system for fracture width, fracture length, velocity field, pressure field, and proppant concentration distribution is discussed.

3.2.1 Fracture Propagation Equations for Incompressible Fluids

In the current study, fracture propagation is solved based on the PKN model. It is a 1D model. The model assumes that (1) the fracture height is constant and independent of fracture length, (2) the fracture fluid pressure is constant in the vertical cross-sections perpendicular to the propagation orientation, (3) 2D plane-strain deformation only occurs in the vertical plane, and (4) the cross-section takes the elliptic shape with maximum width in the center of the height (Perkins and Kern, 1961),

$$w(x,z)=\frac{(1-\nu)}{G}(h_{hf}{}^{2}-4z^{2})^{1/2}(P[x]-\sigma_{h\min}) \tag{3.1}$$

where v is Poisson's ratio of rock formation with no unit, G is shear modulus of rock formation in kPa, h_{hf} is fracture height in m, P is the fracture pressure in kPa, σ_{hmin} is minimum horizontal stress in kPa, and z is the position along the fracture height in m. The maximum width is given as,

$$w_{\max}(x)=\frac{(1-\nu)h_{hf}}{G}(P[x]-\sigma_{h\min}) \tag{3.2}$$

The average width is the maximum width multiplied by π/4. The equations above are based on the linear elastic model. If the deformation is more plastic, which is most likely found in ductile shale formations (i.e. Haynesville Shale), the widths are underestimated by the linear elastic model. Given a fixed injection volume, the fracture length and height are overestimated.

The fluid pressure gradient along the propagation direction in a narrow, elliptical flow channel for Newtonian fluid (laminar flow) is

$$\frac{\partial(P-\sigma_{h})}{\partial x}=-\frac{64}{\pi h_{hf}w_{\max}{}^{3}}\mu q \tag{3.3}$$

where q is the volumetric flow rate in m^3/min (Perkins and Kern, 1961). For the power law fluid flowing between parallel walls, the flow equation (Gidley et al., 1989) is

$$\frac{\partial(P-\sigma_{h})}{\partial x}=-2K'\left(\frac{2n'+1}{3n'}\right)^{n'}\left(\frac{6q}{h_{hf}}\right)^{n'}\frac{1}{w^{(2n'+1)}} \tag{3.4}$$

where n' and K' are the power-law consistency index and power-law flow behavior index, respectively. The major technical drawback of the equation above is overestimation of the flow resistance at low flow rates, unless a cutoff, like the Sprigg's model (Bird, 1965), is used. For simplification, non-Newtonian fluid is taken as Newtonian fluid by replacing the Newtonian fluid viscosity with an apparent viscosity in Equation 3.3. Assuming the power law flow behavior, the apparent viscosity is given as

$$\mu_{ap} = K'\gamma^{n'-1} \tag{3.5}$$

The volume balance (Nordgren, 1972) is

$$\frac{\partial q}{\partial x} + \frac{\pi h_{hf}}{4}\frac{\partial w_{\max}}{\partial t} + q_{lk} = 0 \tag{3.6}$$

where the first term is the convective (flux) term, the second term is the time derivative term and the third term is the leakage term. The volume leak-off rate is given as

$$q_{lk} = \frac{2h_{hf}K_{lk}}{\sqrt{t-\tau(x)}} \tag{3.7}$$

where K_{lk} is the leak-off coefficient in m/min$^{1/2}$ which will be discussed in details in the next section, $\tau(x)$ is the starting time of leakage at the x position in min (Gidley et al., 1989).

Elimination of ΔP and q from Eq. 3.6 based on Eq. 3.2 and 3.3 provides a nonlinear partial-differential equation in terms of $w_{max}(x,t)$:

$$\frac{G}{64h_{hf}(\nu-1)}\frac{\partial}{\partial x}\left(\frac{1}{\mu}\frac{\partial w_{\max}{}^{4}}{\partial x}\right) + \frac{\partial w_{\max}}{\partial t} + \frac{8K_{lk}}{\pi\sqrt{t-\tau(x)}} = 0 \tag{3.8}$$

subject to the initial condition $w(x,0)=0$, and boundary conditions $w(x,t)=0$ for $x>L$ and

$$\frac{\pi G}{256\mu(\nu-1)}\frac{\partial w_{\max}(0,t)^4}{\partial x}=q_{inj} \tag{3.9}$$

for x=0. In the second boundary condition (Eq. 3.9), q_{inj} is the injection flow rate at the fracture entrance in m^3/min.

Eq. 3.8 can be differentiated and solved numerically by using a central finite differencing scheme (Nordgren, 1972). Integration of Eq. 3.8 with respect to time from t_m to t_{m+1} and with respect to x from $x_{i-1/2}$ to $x_{i+1/2}$ yields the following equation

$$\begin{aligned}&C_{diff}\frac{\Delta t}{2\Delta x}\left\{\left(\frac{1}{\mu}\frac{\partial w_{\max}{}^4}{\partial x}\right)_{i+1/2}^{m+1}-\left(\frac{1}{\mu}\frac{\partial w_{\max}{}^4}{\partial x}\right)_{i-1/2}^{m+1}+\left(\frac{1}{\mu}\frac{\partial w_{\max}{}^4}{\partial x}\right)_{i+1/2}^{m}-\left(\frac{1}{\mu}\frac{\partial w_{\max}{}^4}{\partial x}\right)_{i-1/2}^{m}\right\}\\&+\left(w_{\max,i}^{m+1}-w_{\max,i}^{m}\right)+\frac{16K_{lk}}{\pi}\left(\sqrt{t_{m+1}-\tau_i}-\sqrt{t_m-\tau_i}\right)=0\end{aligned} \tag{3.10}$$

where $C_{diff} = G/64/h_{hf}/(\nu-1)$.

The extended form of the equation above is

$$\begin{aligned}&C_{diff}\frac{\Delta t}{2\Delta x^2}\left\{\begin{array}{l}\dfrac{1}{\mu_{i+1/2}^{m+1}}\left(w_{\max,i+1}^{m+1\ 4}-w_{\max,i}^{m+1\ 4}\right)-\dfrac{1}{\mu_{i-1/2}^{m+1}}\left(w_{\max,i}^{m+1\ 4}-w_{\max,i-1}^{m+1\ 4}\right)\\+\dfrac{1}{\mu_{i+1/2}^{m}}\left(w_{\max,i+1}^{m\ \ 4}-w_{\max,i}^{m\ \ 4}\right)-\dfrac{1}{\mu_{i-1/2}^{m}}\left(w_{\max,i}^{m\ \ 4}-w_{\max,i-1}^{m\ \ 4}\right)\end{array}\right\}\\&+\left(w_{\max,i}{}^{m+1}-w_{\max,i}{}^{m}\right)+\frac{16K_{lk}}{\pi}\left(\sqrt{t_{m+1}-\tau_i}-\sqrt{t_m-\tau_i}\right)=0\end{aligned} \tag{3.11}$$

To solve this non-linear equation, we write

$$w_{\max,i}{}^{m+1}=w_{\max,i}{}^{m}+\Delta w_{\max,i}{}^{m} \tag{3.12}$$

and take

$$\left(w_{\max,i}{}^{m+1}\right)^4\approx\left(w_{\max,i}{}^{m}\right)^4+4\left(w_{\max,i}{}^{m}\right)^3\Delta w_{\max,i}{}^{m} \tag{3.13}$$

Substituting Eq. 3.13 in Eq. 3.11, we obtain,

$$\begin{aligned}&\frac{C_{diff}\Delta t}{2\Delta x^2}\left\{\begin{array}{l}\dfrac{1}{\mu_{i+1/2}^{m+1}}\left({w_{\max,i+1}^{m}}^4+4{w_{\max,i+1}^{m}}^3\Delta {w_{\max,i+1}}^{m}-{w_{\max,i}^{m}}^4-4{w_{\max,i}^{m}}^3\Delta {w_{\max,i}}^{m}\right)\\ -\dfrac{1}{\mu_{i-1/2}^{m+1}}\left({w_{\max,i}^{m}}^4+4{w_{\max,i}^{m}}^3\Delta {w_{\max,i}}^{m}-{w_{\max,i-1}^{m}}^4-4{w_{\max,i-1}^{m}}^3\Delta {w_{\max,i-1}}^{m}\right)\\ +\dfrac{1}{\mu_{i+1/2}^{m}}\left({w_{\max,i+1}^{m}}^4-{w_{\max,i}^{m}}^4\right)-\dfrac{1}{\mu_{i-1/2}^{m}}\left({w_{\max,i}^{m}}^4-{w_{\max,i-1}^{m}}^4\right)\end{array}\right\}\\ &+\Delta {w_{\max,i}}^{m}+\frac{16K_{lk}\left(\sqrt{t_{m+1}-\tau_i}-\sqrt{t_m-\tau_i}\right)}{\pi}=0\end{aligned} \tag{3.14}$$

Rearranging the equation above, a linear tri-diagonal system is obtained,

$$\begin{aligned}&\frac{C_{diff}\Delta t}{2\Delta x^2}\frac{4{w_{\max,i+1}^{m}}^3}{\mu_{i+1/2}^{m+1}}\Delta {w_{\max,i+1}}^{m}+\frac{C_{diff}\Delta t}{2\Delta x^2}\frac{4{w_{\max,i-1}^{m}}^3}{\mu_{i-1/2}^{m+1}}\Delta {w_{\max,i-1}}^{m}+\left[1-\frac{C_{diff}\Delta t}{2\Delta x^2}\left(\frac{4{w_{\max,i}^{m}}^3}{\mu_{i+1/2}^{m+1}}+\frac{4{w_{\max,i}^{m}}^3}{\mu_{i-1/2}^{m+1}}\right)\right]\Delta {w_{\max,i}}^{m}\\ &=-\frac{C_{diff}\Delta t}{2\Delta x^2}\left[\begin{array}{l}\dfrac{1}{\mu_{i+1/2}^{m+1}}\left({w_{\max,i+1}^{m}}^4-{w_{\max,i}^{m}}^4\right)-\dfrac{1}{\mu_{i-1/2}^{m+1}}\left({w_{\max,i}^{m}}^4-{w_{\max,i-1}^{m}}^4\right)\\ +\dfrac{1}{\mu_{i+1/2}^{m}}\left({w_{\max,i+1}^{m}}^4-{w_{\max,i}^{m}}^4\right)-\dfrac{1}{\mu_{i-1/2}^{m}}\left({w_{\max,i}^{m}}^4-{w_{\max,i-1}^{m}}^4\right)\end{array}\right]-\frac{16K_{lk}\left(\sqrt{t_{m+1}-\tau_i}-\sqrt{t_m-\tau_i}\right)}{\pi}\end{aligned} \tag{3.15}$$

Since the viscosity term in the above equation is time dependent, initially the viscosity of the previous time step is adopted. Once Δw is calculated, the viscosity is updated by using the new w. Several iterations are taken until Δw converges.

3.2.2 Fracture Propagation Equations for Compressible Fluids

If the fracturing fluid is compressible, the volume balance equation is no longer valid. A mass balance equation should be used instead,

$$\frac{\partial \rho q}{\partial x}+\frac{\pi h_{hf}}{4}\frac{\partial \rho w_{\max}}{\partial t}+\rho q_{lk}=0 \tag{3.16}$$

where ρ is the density of the compressible phase, which is dependent on the pressure and temperature. Foam is a two-phase fluid, which includes an incompressible liquid phase and a compressible gas phase. The two phases should obey the mass balance separately,

$$\frac{\partial \rho_l q(1-Q)}{\partial x}+\frac{\pi h_{hf}}{4}\frac{\partial \rho_l w_{\max}(1-Q)}{\partial t}+(1-Q)\rho_l q_{lk,l}=0 \tag{3.17}$$

,

$$\frac{\partial \rho_g qQ}{\partial x}+\frac{\pi h_{hf}}{4}\frac{\partial \rho_g w_{\max}Q}{\partial t}+Q\rho_g q_{lk,g}=0 \tag{3.18}$$

where Q (0-1) is the gas volume percentage of the total foam volume, which is known as foam quality.

The liquid phase mass balance (Eq. 3.17) has a similar differentiation form as its volume balance equation,

$$\begin{aligned}
&\frac{C_{diff}\Delta t}{2\Delta x^2}\frac{4{w^m_{\max,i+1}}^3}{\mu^{*m+1}_{i+1/2}}\Delta {w_{\max,i+1}}^m+\frac{C_{diff}\Delta t}{2\Delta x^2}\frac{4{w^m_{\max,i-1}}^3}{\mu^{*m+1}_{i-1/2}}\Delta {w_{\max,i-1}}^m+\left[1-Q_i^{m+1}-\frac{C_{diff}\Delta t}{2\Delta x^2}\left(\frac{4{w^m_{\max,i}}^3}{\mu^{*m+1}_{i+1/2}}+\frac{4{w^m_{\max,i}}^3}{\mu^{*m+1}_{i-1/2}}\right)\right]\Delta {w_{\max,i}}^m \\
&=\left(Q_i^{m+1}-Q_i^m\right)w^m_{\max,i}-\frac{C_{diff}\Delta t}{2\Delta x^2}\left[\begin{array}{l}\frac{1}{\mu^{*m+1}_{i+1/2}}\left({w^m_{\max,i+1}}^4-{w^m_{\max,i}}^4\right)-\frac{1}{\mu^{*m+1}_{i-1/2}}\left({w^m_{\max,i}}^4-{w^m_{\max,i-1}}^4\right)\\+\frac{1}{\mu^{*m}_{i+1/2}}\left({w^m_{\max,i+1}}^4-{w^m_{\max,i}}^4\right)-\frac{1}{\mu^{*m}_{i-1/2}}\left({w^m_{\max,i}}^4-{w^m_{\max,i-1}}^4\right)\end{array}\right] \\
&-\frac{16{K_{lk,li}}^{m+1/2}\left(1-Q_i^{m+1/2}\right)\left(\sqrt{t_{m+1}-\tau_i}-\sqrt{t_m-\tau_i}\right)}{\pi}
\end{aligned} \tag{3.19}$$

where μ^* is the modified viscosity of liquid phase,

$$\mu^{*m+1}_{i\pm1/2}=\mu^{m+1}_{i\pm1/2}/(1-Q^{m+1}_{i\pm1/2}) \tag{3.20}$$

For the gas phase, it is assumed that the gas obeys the ideal gas law. Besides, the temperature impact on the gas properties is neglected here. So the energy balance equation is not needed to solve for the temperature change of the fracturing fluid. The differentiated form of Eq. 3.18 is

$$\begin{aligned}
&\frac{C_{diff}\Delta t}{2\Delta x^2}\frac{4{w^m_{\max,i+1}}^3}{\mu**^{m+1}_{i+1/2}}\Delta {w_{\max,i+1}}^m+\frac{C_{diff}\Delta t}{2\Delta x^2}\frac{4{w^m_{\max,i-1}}^3}{\mu**^{m+1}_{i-1/2}}\Delta {w_{\max,i-1}}^m+\left[Q_i^{m+1}-\frac{C_{diff}\Delta t}{2\Delta x^2}\left(\frac{4{w^m_{\max,i}}^3}{\mu**^{m+1}_{i+1/2}}+\frac{4{w^m_{\max,i}}^3}{\mu**^{m+1}_{i-1/2}}\right)\right]\Delta {w_{\max,i}}^m \\
&=\left(\frac{P_i^m}{P_i^{m+1}}Q_i^m-Q_i^{m+1}\right)w^m_{\max,i}-\frac{C_{diff}\Delta t}{2\Delta x^2}\left[\begin{array}{l}\frac{1}{\mu**^{m+1}_{i+1/2}}\left({w^m_{\max,i+1}}^4-{w^m_{\max,i}}^4\right)-\frac{1}{\mu**^{m+1}_{i-1/2}}\left({w^m_{\max,i}}^4-{w^m_{\max,i-1}}^4\right)\\+\frac{1}{\mu**^{m}_{i+1/2}}\left({w^m_{\max,i+1}}^4-{w^m_{\max,i}}^4\right)-\frac{1}{\mu**^{m}_{i-1/2}}\left({w^m_{\max,i}}^4-{w^m_{\max,i-1}}^4\right)\end{array}\right] \\
&-\frac{16P_i^m {K_{lk,gi}}^{m+1/2}Q_i^{m+1/2}\left(\sqrt{t_{m+1}-\tau_i}-\sqrt{t_m-\tau_i}\right)}{P_i^{m+1}\pi}
\end{aligned} \tag{3.21}$$

where $\mu**$ is the modified viscosity of gas phase,

$$\mu**^{m+1}_{i\pm1/2}=\left(P_i^{m+1}\mu^{m+1}_{i\pm1/2}\right)/\left(P^{m+1}_{i\pm1/2}Q^{m+1}_{i\pm1/2}\right) \tag{3.22}$$

The total mass balance can be achieved by solving the Eqs. 3.19 and 3.21. Compared with incompressible fluid, three parameters: viscosity, pressure and quality, are updated in each iteration until Δw converges.

3.2.3 Leak-off Modeling

The leak-off coefficient in Eq. 3.8 is a combination of three types of linear flow mechanisms, which are effluent viscosity and relative permeability effects, C_v, reservoir-fluid viscosity/compressibility effects, C_c, and wall-building effects, C_w (Howard and Fast, 1970). The first two coefficients are determined by the reservoir properties and fracturing fluid viscosity. The third coefficient accounts for the fluid flow rate through the filter cake generated by the filtration process when particulate or polymer in solution is pressurized against the fracture face. Figure 3.2 shows that, during the initial period, the leak-off rate is mainly governed by the first two effects. As the filter cake is built up with time, the third effect gradually dominates the fluid loss.

Constant-pressure injection of a viscous fracturing fluid into a porous medium under linear flow is expressed as (Howard and Fast, 1970)

$$C_v = 0.0469\sqrt{\frac{k_f \Delta P \phi}{\mu_f}} \tag{3.23}$$

in ft/min$^{1/2}$, where k_f is the formation permeability to leak-off effluent in Darcies, ΔP is difference in pressure between fluid at formation face and initial pore pressure of formation in psi, φ is formation porosity, and μ_f is the viscosity of Newtonian fracturing fluid or apparent viscosity of non-Newtonian fracturing fluid in cp. For foams, there are two ways to calculate the fluid-loss coefficient. The simplest way is to assume that the two phases are leaking at the same rate. So the foam quality does not change due to the leak-off. The fracturing fluid viscosity in the equation above is the local foam apparent viscosity. The second way is to calculate the leak-off rate of the two phases separately. Compared with the first way, the second way is closer to the real condition, but the leak-off rates of two phases need to be determined by experiments in advance. For a high permeability reservoir, the assumption adopted by the first way is acceptable. For ultra-low permeability shale reservoirs, the second way is better, because the loss of gas phase into the formation is much lower than that of liquid phase due to the extremely high capillary pressure.

Both the compressibility and viscosity of the existing reservoir fluid also affect the leak-off rate and is governed by the following relation (in ft/min$^{1/2}$) (Howard and Fast, 1970)

$$C_c = 0.0374\Delta P\sqrt{\frac{k_{mrf} c_t \phi}{\mu_{mrf}}} \tag{3.24}$$

where k_{rmf} is the formation permeability to mobile reservoir fluid in Darcies, ΔP is difference in pressure between fluid at formation face and initial pore pressure of formation in psi, c_t is the total formation compressibility in psi^{-1}, φ is formation porosity, and μ_{rmf} is the viscosity of mobile formation fluid at reservoir conditions in cp. The third coefficient C_w is determined from the slope of later time cumulative leak-off volumes vs. square root of time (shown in Fig. 3.2) (Gidley et al., 1989).

Williams (1970) and Williams et al. (1979) developed the total leak-off coefficient that combines the three effects together,

$$C_t = \frac{2C_c C_v C_w}{C_v C_w + \left[C_v^2 C_w^2 + 4C_c^2\left(C_v^2 + C_w^2\right)\right]^{1/2}} \tag{3.25}$$

In the current study, there is almost no polymer additive in the fracturing fluid, so the third effect is ignored. If only the first two effects are accounted for the fluid leak-off, the leak-off coefficient is given as

$$K_{lk} = C_{vc} = \frac{2C_v C_c}{C_v + \left(C_v^2 + 4C_c^2\right)^{1/2}} \tag{3.26}$$

3.2.4 Proppant Transport Equations

In current modeling, it is assumed that proppants do not impact the flow field and fracture geometry. But proppant concentration can affect the apparent viscosity of the total slurry. Since proppants travel at a velocity different from that of the fluid because of gravity, wall retardation, and proppant concentration retardation, a separate mass balance equation of solid is adopted to track the proppant flow, i.e.,

$$\frac{d\left[wc_p\right]}{dt}+\frac{d\left[v_x k_{retx} w c_p\right]}{dx}+\frac{d\left[-v_{set} k_{retz} w c_p\right]}{dz}=0 \tag{3.27}$$

$$ic: c_p(\partial\Omega_{tip},t)=c_{inj}$$

$$bc: \frac{\partial c_p}{\partial x}(\partial\Omega_{toe},t)=0; \frac{\partial c_p}{\partial z}(\partial\Omega_{bond},t)=0$$

where w is the average width, c_p is the proppant volume concentration, v_{set} is the settling velocity of the proppant calculated by Stokes Law, v_x is the horizontal velocity of the fluid obtained by solving mass balance equations 3.17 and 3.18, k_{retx} is the horizontal retardation factor considering the proppant concentration effect and the wall effect, k_{retz} is the vertical retardation factor considering inertial effect, wall effect and concentration effect. SI units are adopted for all parameters in this section.

Both of the retardation factors are predicted by the empirical correlations developed from the experiments (Gadde et al., 2004, Liu, 2006). The horizontal retardation factor k_{retx} is mainly governed by two effects, which are fracture walls and proppant concentrations. The correlation below is used to calculate the factor (Liu, 2006),

$$k_{retx}=1+\left(\frac{d_p}{w_{cor}}\right)-2\left(\frac{d_p}{w_{cor}}\right)^2 \tag{3.28}$$

where d_p is the proppant diameter, and w_{cor} is the effective width corrected by considering the effects of wall and proppant concentration (Liu, 2006),

$$\frac{1}{{w_{cor}}^2}=\frac{1}{w^2}+a\left(\frac{1}{d_p^2}-\frac{1}{w^2}\right){c_p}^b \tag{3.29}$$

where w is the true local fracture width, c_p is the proppant concentration (≤ 0.65), and *a, b* are empirical parameters determined by experiments. In this study, *a*=1.411, *b*=0.8. The vertical retardation factor k_{retz} is calculated by multiplying independent correction factors for the inertial, proppant concentration and fracture walls (Liu, 2006),

$$k_{retz} = f(\mathrm{Re})\, f(c)\, f(w) \tag{3.30}$$

Equations 3.31-3.33 (Liu, 2006) are correction factors for the inertial effect, proppant concentration, and fracture walls, respectively,

$$f(\mathrm{Re}) = \frac{0.3736\mu_f^{0.57}}{\rho_f^{0.29}\left(\rho_p - \rho_f\right)^{0.29} d_p^{0.86}} \tag{3.31}$$

$$f(c_p) = -5.918{c_p}^3 + 8.8477{c_p}^2 - 4.7891c_p + 1 \tag{3.32}$$

$$f(w) = 0.563\left(\frac{d_p}{w}\right)^2 - 1.563\left(\frac{d_p}{w}\right) + 1 \tag{3.33}$$

Assuming that there is no vertical convection flow, the finite difference form of the Equation 3.27 is given by,

$$\begin{aligned} &\frac{w^{n+1}(i,j)c^{n+1}(i,j) - w^n(i,j)c^n(i,j)}{\Delta t} \\ &= \frac{k_{retx}{v_x}^{n+1}(i-1,j)w^{n+1}(i-1,j)c^n(i-1,j) - k_{retx}{v_x}^{n+1}(i+1,j)w^{n+1}(i+1,j)c^n(i+1,j)}{2\Delta x} \\ &+ \frac{k_{retz}{v_{set}}^{n+1}w^{n+1}(i,j-1)c^n(i,j-1) - k_{retz}{v_{set}}^{n+1}w^{n+1}(i,j+1)c^n(i,j+1)}{2\Delta z} \end{aligned} \tag{3.34}$$

Rearranging the above equation, we have,

$$\begin{aligned}&\Delta x\Delta z w^{n+1}(i,j)c^{n+1}(i,j)\\&=\Delta x\Delta z w^{n}(i,j)c^{n}(i,j)\\&+\frac{\Delta z\Delta t k_{retx}{v_x}^{n+1}(i-1,j)w^{n+1}(i-1,j)}{2}c^{n}(i-1,j)-\frac{\Delta z\Delta t k_{retx}{v_x}^{n+1}(i+1,j)w^{n+1}(i+1,j)}{2}c^{n}(i+1,j)\\&+\frac{\Delta x\Delta t k_{retz}{v_{set}}^{n+1}w^{n+1}(i,j-1)}{2}c^{n}(i,j-1)-\frac{\Delta x\Delta t k_{retz}{v_{set}}^{n+1}w^{n+1}(i,j+1)}{2}c^{n}(i,j+1)\end{aligned} \tag{3.35}$$

Once the proppant concentration is obtained, the slurry viscosity is updated by the following equation (Brouwers, 2010),

$$\mu_{slurry}=\mu_f\left(\frac{1-c_p}{1-c_p/c_1}\right)^{\frac{a_1\cdot c_1}{1-c_1}} \tag{3.36}$$

where μ_{slurry} is the apparent slurry viscosity, μ_f is the viscosity of the fracturing fluid, c_p is the proppant volume fraction, c_1 is the random close packed volume fraction, and a_1 is the first-order virial coefficient. For hard sphere suspensions at low shear rates, c_1=0.64, a_1=2.5. Here, the slurry is taken as a homogeneous fracturing fluid. After the slurry viscosity is calculated from the proppant concentration, the slurry viscosity, μ_{slurry}, is used in the place of the fracturing fluid viscosity, μ_f, in the fluid flow equations to calculate the fracture propagation in next time step.

3.2.5 The Solution Algorithm of Current Simulator

The partial differential equations 3.19, 3.21 and 3.35 are solved numerically for net pressure, flow rate, foam quality, fracture width, and proppant concentration. Figure 3.2 shows a flowchart of the fracture modeling simulator.

The simulator is built in a modular fashion so that each module can be easily validated and improved. In the data input module, all data required for modeling, such as reservoir properties, completion parameters, and numerical parameters, is input. In the second module, the nonlinear partial differential equations 3.19 and 21 are solved in a semi-explicit-implicit scheme. In a given time step, the equations 3.19 and 21 are first solved implicitly for fracture width with the data from the last time step. The new widths are used to update the flow rates, pressures, foam qualities, and foam viscosities. The equations 3.19 and 21 are solved implicitly again with the updated coefficients μ^{*m+1} and μ^{**m+1}. The process is repeated until the fracture width of the new step converges. Once the fracture geometry (w_{hf} and l_{hf}), pressure field, flow rate field and foam properties are obtained for the new time step, the judgment is made on proppant injection. If there is proppant injected at the inlet into the fracture, the simulation moves to the next module where the proppant mass balance equation 3.35 is solved for proppant concentration distribution. The new proppant volume concentration is used to update the slurry viscosity of the next time step through equation 3.36. The whole time loop is run until the end of the pumping schedule. The last module is used to convert the fracture geometry and proppant concentration distribution into the format that can be accepted by the state-of-the-art reservoir simulator, i.e. CMG, to further predict the productivity of the fracture.

The common pumping schedule includes three phases, which are initial pad injection, slurry injection and shut-in. It is realized in the simulator by setting zero proppant injection for the initial pad period, setting non-zero proppant injection for the slurry period and setting zero injection flow rate for shut-in period.

3.3 MODEL VALIDATION

In this section, the fracture model is first verified by the analytical solutions for incompressible, Newtonian fluid. Then the impacts of the friction loss and leak-off on the foam quality, foam viscosity and resulting fracture geometry are discussed. Finally, proppant transport results modified by the empirical retardation factors are compared with the non-modified results for water and high quality foams.

3.3.1 Model Verification with Analytical Solutions for Incompressible Fluids

To verify the current model, the numerical results are compared with the analytical results of PKN model (Perkins and Kern, 1961, Nordgren, 1972, Gidley et al., 1989) under no leakage and high leakage conditions, respectively. To make the comparison applicable, all assumptions made by analytical solutions are applied to the current numeric model. The assumptions include one dimensional fracture propagation, linear elastic rock deformation, constant injection rate, single-phase, Newtonian, and incompressible fluid flow. Some important parameters used in the verification model are listed in Table 3.1.

The equations for fracture length and maximum fracture width for constant injection rate under no leakage condition are (Perkins and Kern, 1961, Nordgren, 1972),

$$L_{hf}\left(t\right)=0.68\left(\frac{Gq_{inj}^{3}}{\left(1-\nu\right)\mu_{f}{h_{hf}}^{4}}\right)^{1/5}t^{4/5} \tag{3.37}$$

$$w_{\max}\left(0,t\right)=2.5\left(\frac{\left(1-\nu\right)\mu_{f}q_{inj}^{2}}{Gh_{hf}}\right)^{1/5}t^{1/5} \tag{3.38}$$

The shape of the fracture then takes the form (Gidley et al., 1989)

$$w_{\max}\left(x,t\right)=w_{\max}\left(0,t\right)\left(1-x/L_{hf}\right)^{0.25} \tag{3.39}$$

The equations for fracture length and maximum fracture width for constant injection rate under high leakage condition are (Gidley et al., 1989),

$$L_{hf}\left(t\right)=\frac{1}{\pi}\frac{q_{inj}\sqrt{t}}{h_{hf}C_{cv}} \tag{3.40}$$

$$w_{\max}\left(0,t\right)=4\left(\frac{2}{\pi^3}\right)^{1/4}\left[\frac{\mu_f\left(1-\nu\right)q_{inj}^2}{Gh_{hf}C_{cv}}\right]^{1/4}t^{1/8} \tag{3.41}$$

Since there is leakage during fracturing, the resulting fracture should be narrower than that of the non-leak-off case. Thus, the exponential factor should be larger than 0.25. The best match yields an exponential factor of 0.35. The shape of the fracture is

$$w_{\max}\left(x,t\right)=w_{\max}\left(0,t\right)\left(1-x/L_{hf}\right)^{0.35} \tag{3.42}$$

Figures 3.4 and 3.5 compare the numeric results with the analytical results for two leak-off conditions, respectively. For the leak-off model, the leak-off coefficient for water loss to 0.05 md dry gas matrix is calculated to be 0.00125 ft/min$^{1/2}$.The fluid injection time is varied from 15 minutes to 60 minutes. It shows that the numerical (red lines) and analytical (blue lines) results based on the same assumptions match well with each other at different injection times.

3.3.2 Validation of Foam Fracturing Modeling

Foam quality is affected by both pressure decrease along the propagation direction and the fluid loss into the formation. The quality change leads to a change of the foam rheology and hence the fracture geometry. Besides, pressure can directly affect the property of the gas phase (e.g. gas density and bubble texture) and hence the rheology of the foams as well as the fracture geometry.

In this section, fracturing treatments with 60-80 % quality foams are simulated to illustrate the effect of the friction loss and fluid loss on the foam quality and fracture geometry. Foam rheology is from Chapter 5. Table 3.2 shows the selected key parameters for three cases of foam fracturing simulation. The first case assumes that both gas phase and liquid phase leak into a high permeability shale (10 μD) at the same rate. The second case assumes that only liquid phase leaks into a low permeability shale (1 μD). The third case is a reference case to the second one, which assumes that both gas and liquid phase leak to the same reservoir at the same rate. Other reservoir properties are from Table 3.1.

3.3.2.1 The Pressure Impact on Foam Fracturing

In the first case, the reservoir permeability is 10 μD. It is assumed that the leak-off rates of both phases of foams are the same, which is a reasonable approximation for high permeability reservoirs. The foam is viewed as a homogeneous fluid. The effluent viscosity in Eq. 3.23 is replaced by an apparent viscosity of the foam. Based on the assumption, leakage has no impact on foam quality. Thus only the decrease of the net pressure due to the friction loss affects the foam quality. The equation below is adopted to calculate the foam quality of the new time step affected by the net pressure,

$$Q_i^{m+1} = \frac{\Delta t q_{i-1/2}^m Q_{i-1}^m \left(P_{i-1}^m / P_i^m\right) - \Delta t q_{i+1/2}^m Q_i^m + \left(V_i^m - V_{leak,i}^m\right) Q_i^m}{V_i^m - V_{leak,i}^m + \Delta t q_{i-1/2}^m \left(1 - Q_{i-1}^m + Q_{i-1}^m P_{i-1}^m / P_i^m\right) - \Delta t q_{i+1/2}^m} \tag{3.43}$$

where Δt is the time interval, q is the volume flow rate, Q is the foam quality, and V is the cell volume.

Figure 3.6 plots the pressure distributions along the fracture propagation direction for different quality foams in 10 μD shales. The minimum horizontal stress is 1100 psi in the left plot and 4500 psi in the right plot. It is noted that the fracture pressure decreases with the fracture propagation direction due to the friction loss. The pressure decreasing rate increases with the distance. At the fracture tip, the pressure equals to the minimum horizontal stress, leading to a zero net pressure. The decrease of the fracture pressure is more significant for higher quality foams because of their larger apparent viscosity. The pressure change affects the foam quality, and hence the foam rheology and the leak-off rate. Figure 3.7 shows the resulting quality change along the fracture propagation direction for three foams under two minimum horizontal stresses. Foam quality increases with the propagation distance at an increasing rate. The quality change due to the friction loss is more significant for the shale with lower minimum horizontal stress. Figure 3.8 compares the fracture dimensions (width and length) predicted by models considering pressure impact (solid lines) and models without considering pressure impact (dashed lines) under two minimum horizontal stresses. For the 1100 psi case, it shows that the decreasing fracture pressure along the propagation direction finally leads to a wider and shorter fracture. The pressure impact is larger for higher quality foams. As minimum horizontal stress increases to 4500 psi, the pressure change due to friction loss has negligible effect on fracture geometry. The reason is that pressure change is relatively low to the minimum horizontal stress in this case. For our foam fracturing simulations in later study, pressure impact is always included in the model.

3.3.2.2 The Leak-off Impact on Foam Fracturing

In the second case, the reservoir permeability is 1 μD and the minimum horizontal stress is 4500 psi. Other parameters are similar to the previous. This study assumes that only water phase leaks into the formation with a leak-off coefficient modified to

$$C_{vc,wp} = \left(1 - Q_{foam}\right) C_{vc,w} \tag{3.44}$$

The effluent permeability in the equation above is multiplied by $k_{r(1-S_{gr})}$*(1-Q_{foam})/(1-S_{gr}) according to the two-phase relative permeability curve (Fig. 3.9). The third case is the reference case by making the same leak-off assumption as the first case, which is no leak-off impact on foam quality (assuming equal leak-off rate for both phases). Figure 3.10 compares the foam quality distributions predicted by two leak-off models. For low permeability reservoirs, assuming the same leak-off rates for both liquid and gas phases underestimates the foam quality. The underestimation grows as foam propagates deeper into the fracture. Comparing different foams, the underestimation of the foam quality is more significant for lower quality foams. This quality underestimation caused by assuming equal leak-off rate for both phases finally leads to a longer fracture length and a smaller fracture width (shown in Figure. 3.11). Comparing Figures 3.10 and 3.11, the different leak-off assumptions have lower impact on the predictions of fracture geometries than foam qualities. Overall, although the fractures are narrower and longer by assuming equal leak-off rates for both gas and liquid phases, the difference of the fracture geometries predicted by difference leak-off models is not as large as we expected. As the shale permeability decreases to below 1 μD, the effect of leak-off is further decreased. And the difference of the two leak-off assumptions will be also decreased. It should be noted that the assumption of equal leak-off rates of gas/liquid phases made in case 1 & 3 and no gas leak-off assumption made in case 2 are two extreme situations. The actual leak-off status is most likely in the middle. Furthermore, the first leak-off model (C_{vg}=C_{vl}) is not a bad assumption to fracture geometry predictions, especially when the foam is dry and the reservoir permeability is lower than 1 μD. To simplify our studies and make consistent comparisons, the first leak-off model, which treats foam as a homogeneous fluid leaking into the formation, will be used to model foam leak-off for 0.1 - 10 μD shales in the following chapters.

3.3.3 Proppant Settling Predicted by Stokes Law vs. Modified Stokes Law

By solving the nonlinear partial differential equations 3.19 and 3.21, the 1D fracture width, pressure, and flow rate profiles are all obtained simultaneously. To predict the 2D proppant distribution, the 1D results are expanded to 2D. The 2D width distribution along the vertical direction follows the elliptical cross-section assumption made by PKN model. For simplicity, the line velocity along the fracture propagation direction is assumed to be constant vertically. The assumption is not bad when the fracture height is much larger than the width. The proppant velocity equals to the fluid velocity multiplied by a horizontal retardation factor, which accounts for the wall effect and concentration effect. The settling velocity can be either predicted by the Stokes law or a modified Stokes law. Stokes law is established for a single spherical proppant settling in an unbounded Newtonian fluid at a laminar settling rate. For high settling rate, small fracture width, and highly concentrated slurry, a vertical retardation factor is used to modify the Stokes law by taking into account of the inertial effect, wall effect, and concentration effect. The modified settling rate is usually much smaller than the original settling rate because of the three effects mentioned above. Figures 3.12 and 3.13 compare the average proppant areal concentration over the fracture height versus fracture length predicted by Stokes law with and without multiplying the vertical retardation factor. The corresponding 2D areal concentration distributions are also shown besides the curves. Figure 3.12 shows the results of a water-sand (20 mesh) case, and Figure 3.13 shows the results of a 75% quality foam-sand (20 mesh) case. For the water-sand case, the vertical retardation factor significantly decreases the sand settling rates and leads to a larger expansion of the sand bed along the fracture propagation direction. For the foam case, the vertical retardation factor does not have much impact on the proppant distribution. The reason is that the three retardation effects (wall, concentration and inertial effect) are highly reduced in a higher viscosity proppant laden fluid because it has much wider fractures (low width effect), constant low proppant volume concentration (low concentration effect), and ignorable proppant settling rate (no inertial effect).

3.4 COUPLING FRACTURE MODELING WITH RESERVOIR SIMULATOR

Once the fracture geometry and proppant distribution are predicted by the fracture modeling simulator, the results are combined with the API proppant conductivity test results to obtain the conductivity distribution. Following that, a date conversion module is run to reformat the data to the accepted forms by a state-of-the- art reservoir simulator CMG IMEX. Then, the reformatted conductivity distribution is input into the reservoir simulation model built in Chapter 2 along with the respective porosity and non-Darcy flow parameter. In addition to that, the total leak-off volume of the water is used to update the water saturation of the drainage zone after fracturing. The gas productivity and producing rate of the target fracture are obtained by running the reservoir model. Figure 3.14 illustrates each step combined in an optimization loop. In the later chapters, the optimization loop is used to optimize the pumping schedule for our foams and light weight proppants under different reservoir conditions.

3.5 CONCLUSIONS

This chapter introduced the basic equations and their discretized forms used to numerically modeling fracture propagation and proppant transport within the propagating fracture. The fracture propagation modeling is based on the PKN model. The mass balance is adopted instead of volume balance to track the gas phase of the foams. Besides, foam rheology as a function of pressure and quality is used to simulate the friction-loss impact on the ultimate predictions of fracture dimensions. Furthermore, two foam leak-off models are proposed and their impacts on foam quality and fracture dimensions are discussed.

The proppant concentration is tracked with a separate mass balance equation. In the equation, the horizontal traveling rate is the average proppant laden fluid flow rate multiplied by a horizontal retardation factor considering wall and concentration effects.

The proppant setting rate is the Stokes setting rate modified by a vertical retardation factor which accounts for wall, concentration and inertial effects. Compared with Stokes law, the modified Stokes law predicts a lower and more expanded sand bed in the water, while it predicts similar proppant distribution in high quality foams.

A fracture modeling simulator is developed based on the theoretical equations to predict the fracture geometry and proppant distribution. The simulator is verified with analytical solutions of incompressible, Newtonian fluid under no leak-off and high leak-off conditions. The simulator is built in a modular fashion. The major modules are data input module, fracture geometry solver, proppant transport solver, and data output/linking to CMG module. Each element can be updated or improved independently. The program is written in Matlab codes, which are easy to understand and modify for future researchers. By using the last module, the predicted fracture geometry and proppant distribution after fracture closure can be easily incorporated into a reservoir simulator to further predict the fracture productivity. We utilize these numerical models to generate the multiple simulation cases in the following chapters.

Compared with the commercial fracture simulators (e.g. StimPlan and Fracpro), the fracture simulator developed in this chapter is based on a 2D planar bi-wing fracture model. It cannot simulate natural fracture growth, stress interference from neighboring fractures, and complex stratigraphy. However, it is efficient for parametric studies to evaluate the application of ULWPs and PPFs in shale fracturing by including the empirical correlations for ULWP conductivity and PPF rheology.

Nomenclature

v, Poisson's ratio of rock, no unit

G, shear modulus of rock formation, kPa

h_{hf}, hydraulic fracture height, m

σ_{hmin}, minimum horizontal stress, kPa

w, hydraulic fracture width, m

P, pressure, kPa

q, volume flow rate, m^3/min

μ, fluid viscosity, kPa·min

K', power-law consistency index, Pa·s$^{n'}$

n', power-law flow behavior index, no unit

γ, shear rate, s^{-1}

μ_{ap}, apparent viscosity, Pa·s

q_{lk}, volume leak-off rate, m^3/min

K_{lk}, leak-off coefficent, m/min$^{1/2}$

Q, foam quality, no unit

C_v, effluent leak-off coefficient, m^3/min

k_f, formation permeability, Darcy

ϕ, porosity, no unit

C_c, res. fluid leak-off coefficient, m^3/min

c_t, total formation compressibility, psi^{-1}

ΔP, net pressure, psi

C_w, wall-building coefficient, m^3/min

C_{vc}, combination of C_v and C_c, m^3/min

c_p, proppant volume concentration, no unit

k_{retx}, horizontal retardation factor, no unit

k_{retxz}, vertical retardation factor, no unit

L_f, hydraulic fracture length, m

d_p, proppant diameter, m

ρ, density, kg/m^3

q_{inj}, injection rate, m^3/min

Subscripts

max, maximum width

hf, hydraulic fracture

m, time step

i, grid cell number

g, gas phase of foam

l, liquid phase of foam

p, proppant

f, fracturing fluid

foam, foam

lk, leak-off

References

Abé, H., Mura, T., and Keer, L. 1976. Growth-rate of a Penny-shaped Crack in Hydraulic Fracturing of Rocks. J. Geophys. Res., 81 (35): 6292-98.

Bird, R.B. 1965. Polymer Fluid Dynamics. Selected Topics in Transport Phenomena, Chemical Engineering Progress Symposium Series 58. 61, Chap. 6.

Brouwers, H.J.H. 2010. Viscosity of a Concentrated Suspension of Rigid Monosized Particles. Phys. Rev. E, 81 (05): 1402-12.

Friehauf, K. and Sharma, M.M. 2009. A New Compositional Model for Hydraulic Fracturing with Energized Fluids. SPE Production & Operations, 24 (4): 562-72.

Gadde, P.B., Liu Y., Norman J., Bonnecaze R., and Sharma M.M. 2004. Modeling Proppant Settling in Water-Fracs. Paper SPE 89875. In: Proceedings of the 2004 SPE Annual Technical Conference and Exhibition, Houston, September 26-29.

Geertsma, J. and de Klerk, F.A. 1969. A Rapid Method of Predicting Width and Extent of Hydraulically Induced Fractures. J. Pet. Tech., 21: 1571-81.

Gidley, J.L., Holditch, S.A., Nierode, D.E., and Veatch Jr., R.W. 1989. Recent Advances in Hydraulic Fracturing. SPE Monograph 12, Society of Petroleum Engineers, Richardson, TX.

Gu, H. and Leung, K.H. 1993. 3D Numerical Simulation of Hydraulic Fracture Closure with Application to Minifracture Analysis. JPT, p: 206-11.

Howard, G.C. and Fast, C.R. 1970. Hydraulic Fracturing, Monograph Series, SPE, Richardson, 2, 55.

Khristianovitch, S.A. and Zheltov, Y.P. 1955. Formation of Vertical Fractures by Means of Highly Viscous Fluids. In: Proceeding of the 4th World Petroleum Congress, Rome, Italy. 2:579-86.

Liu, Y. 2006. Settling and Hydrodynamic Retardation of Proppants in Hydraulic Fractures. Dissertation of Doctor of Phylosophy. University of Texas of Austin.

Nordgren, R.P. 1972. Propagation of a Vertical Hydraulic Fracture. Society of Petroleum Engineering Journal, 253: 306-14.

Perkins, T.K. and Kern, L.R. 1961. Widths of Hydraulic Fractures. J. Pet. Tech., 13: 937-49.

Ribeiro, L.H. and Sharma, M.M. 2013. A New 3D Compositional Model for Hydraulic Fracturing with Energized Fluids. SPE Prod. & Operations, 28(3): 259-67.

Settari, A. and Cleary, M.P. 1986. Development and Testing of a Pseudo-three dimensional Model of Hydraulic Fracture Geometry. SPE Prod. Eng., 1 (6): 449-66.

Sousa, J.L.S., Carter, B.J., and Ingraffea, A.R. 1993. Numerical Simulation of 3D Hydraulic Fracture Using Newtonian and Power-law Fluids. Int. J. Rock Mech. Min. Sci. & Geomech. Abstr., 30: 1265-71.

Williams, B.B. 1970. Fluid Loss from Hydraulically Induced Fractures. JPT, AIME 249: 882-88.

Williams, B.B., Gidley, J.L., and Schechter, R.S. 1979. Acidizing Fundamentals. Monograph Series, SPE, Richardson, TX (1979) 6.

Table 3.1: Reservoir property input for incompressible fluid fracturing verification.

Pr_{pore} (psi)	3300	E (psi)	2E6
σ_{min} (psi)	4500	ν	0.25
Temp (^oF)	130	P_L (psi)	468
φ	8%	V_L (scf/lb)	0.0425
H_{pay}(ft)	150	ρ_{rock} (g/cc)	2.6
k_{ml} (μD)	1-10	S_{wi}	20%
k_{mv} (μD)	0.1-1	S_{gi}	80%
C_{por} (1/psi)	6E-6	Methane	100%

Table 3.2: Selected input parameters for foam fracturing modeling.

Three Foam Modeling Cases		Injected Q_{foam}	Pad Time (min)	q_{inj} (m^3/min)	k_m (μD)	σmin (psi)
Case 1	High Perm. Res. (C_{vg}=C_{vw}=C_{vfoam})	60-80%	60	1.2	10	1100, 4500
Case 2	Low Perm. Res. (C_{vg}=0)	60-80%	60	1.2	1	4500
Case 3	Low Perm. Res. (C_{vg}=C_{vw}=C_{vfoam})	60-80%	60	1.2	1	4500

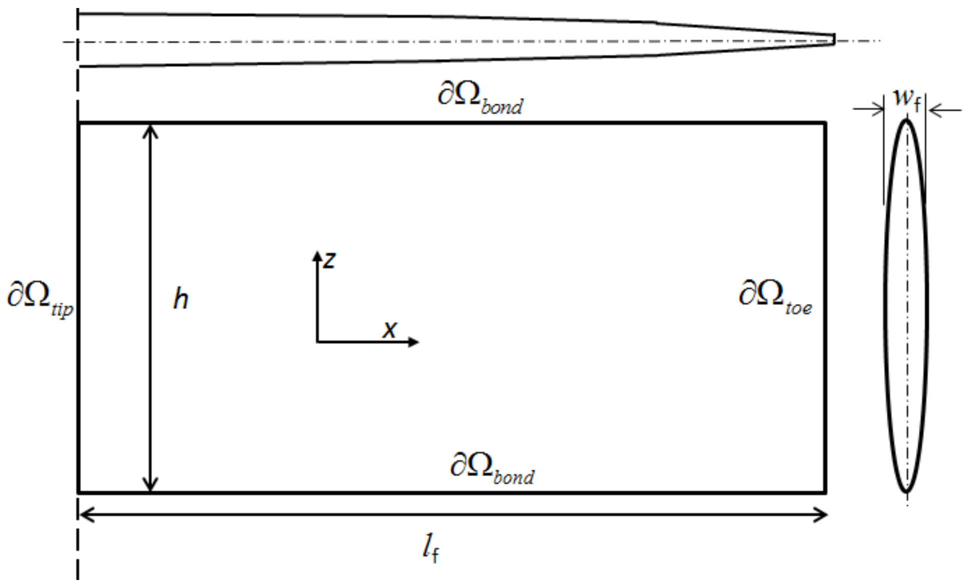

Figure 3.1: Schematic of the fracture model (PKN).

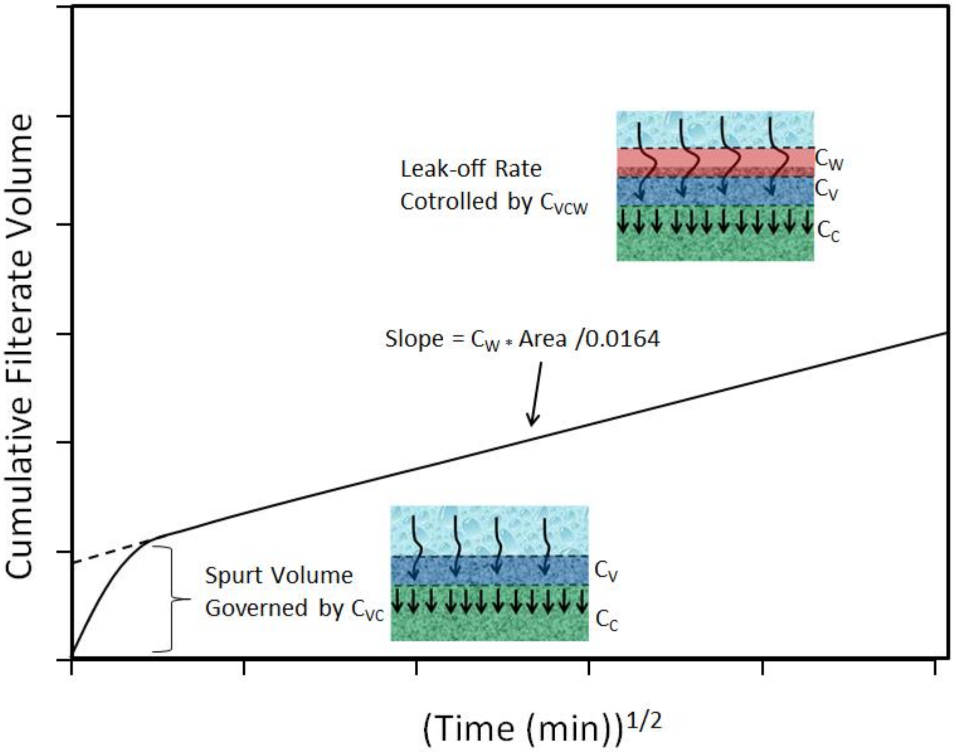

Figure 3.2: Different leak-off periods and the corresponding governing parameters.

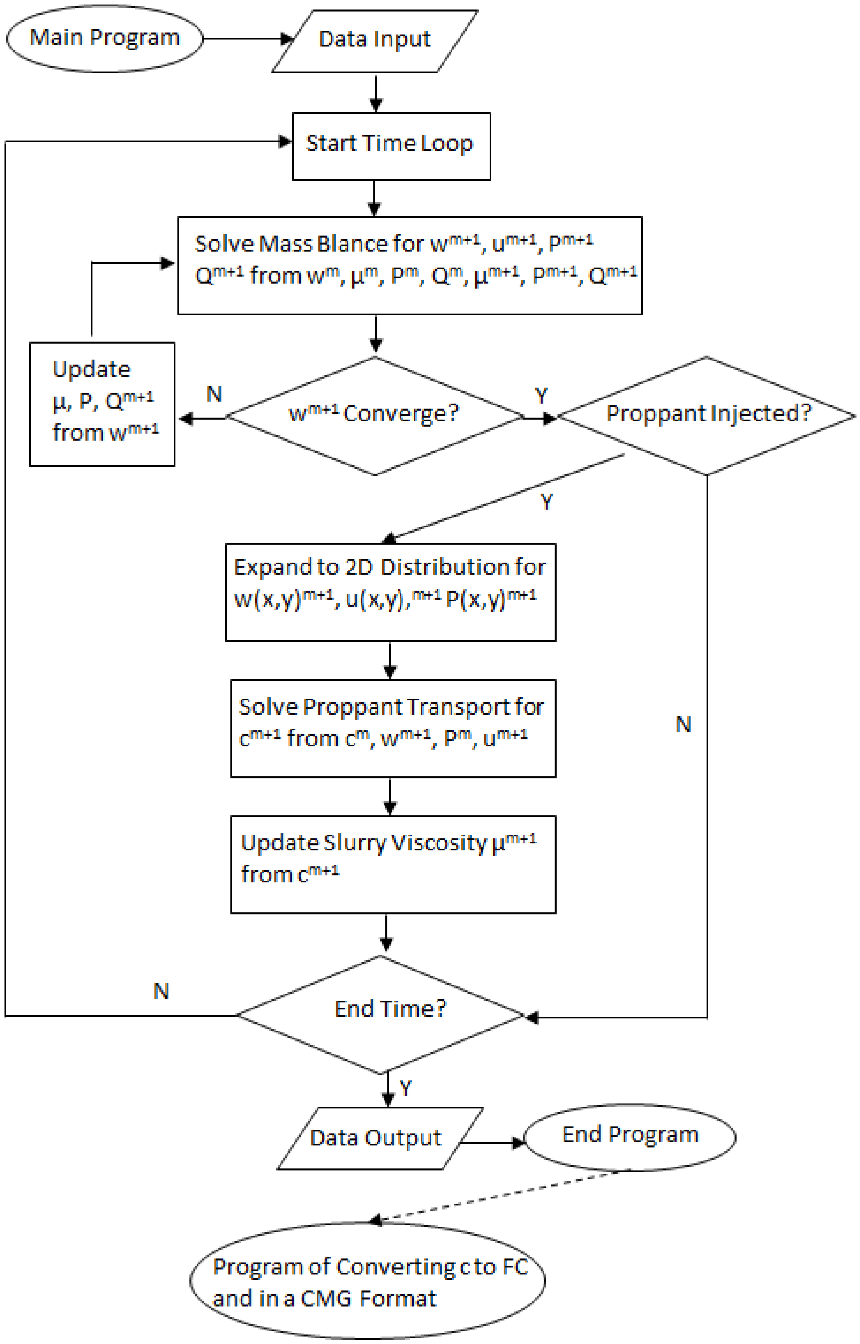

Figure 3.3: Flowchart for fracture modeling.

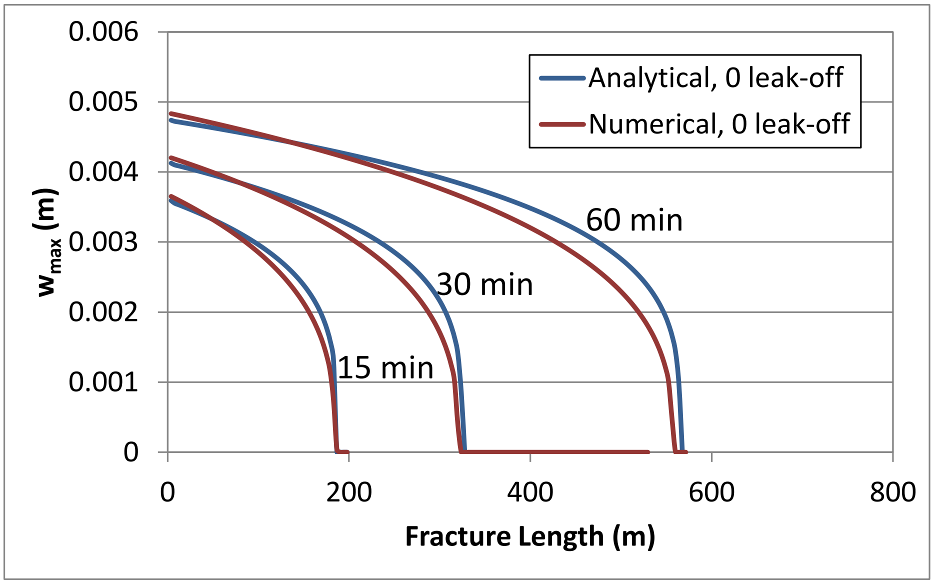

Figure 3.4: Comparison of predicted fracture dimensions from analytical and numerical models (no leak-off).

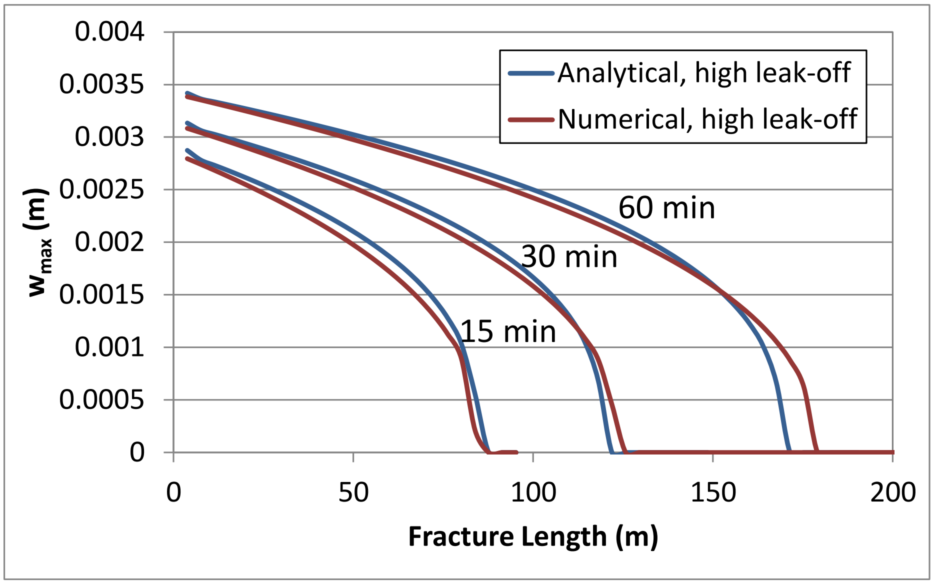

Figure 3.5: Comparison of predicted fracture dimensions from analytical and numerical models (high leak-off).

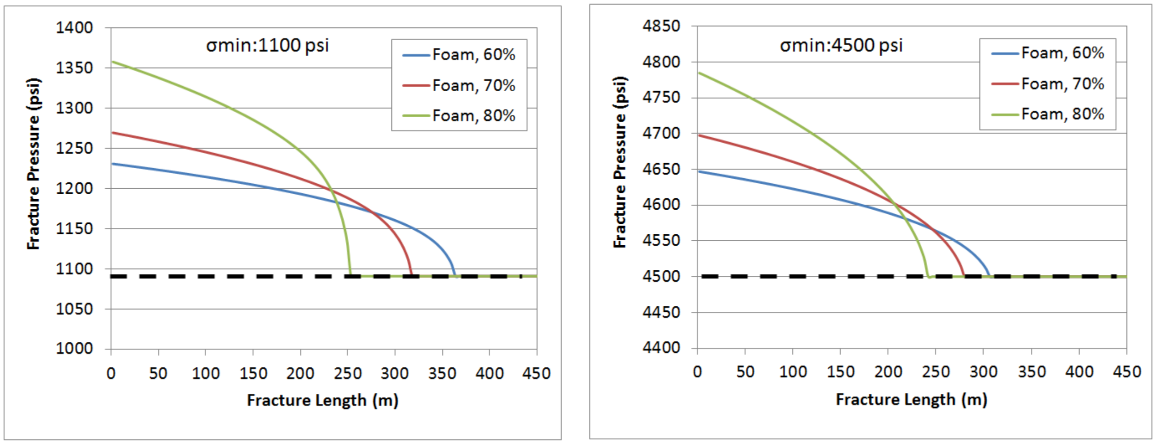

Figure 3.6: Pressure distribution along the propagation direction for different foam qualities at 10 μD.

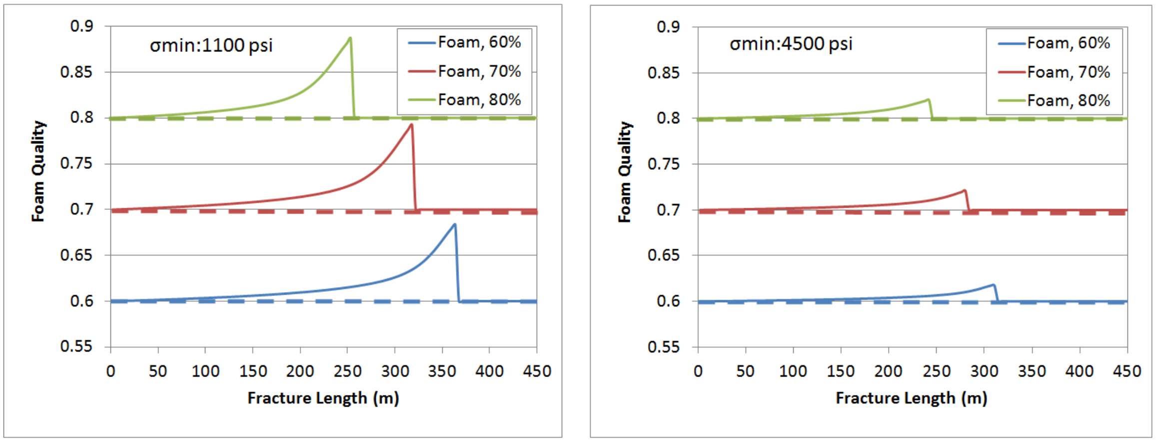

Figure 3.7: Foam quality distribution along the propagation direction for different foam qualities at 10 μD.

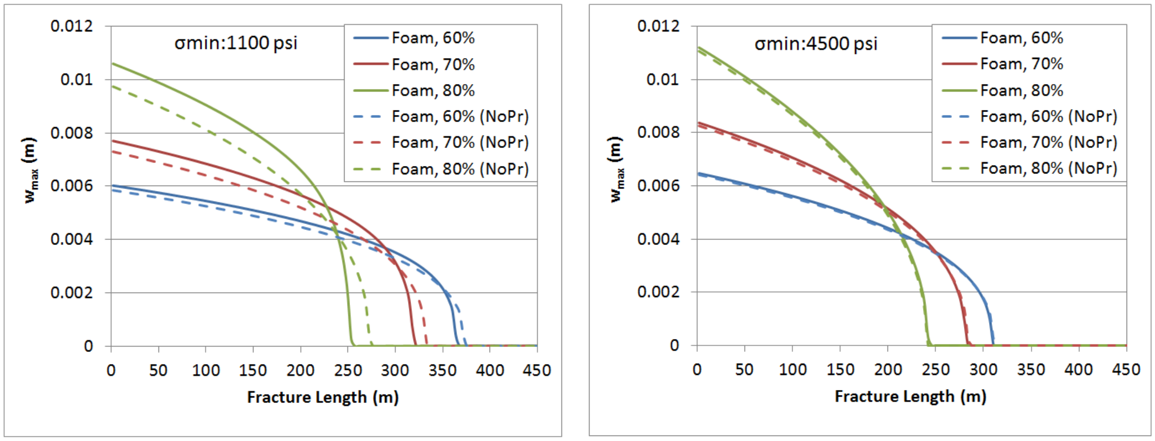

Figure 3.8: Maximum fracture width distribution for different foam qualities (solid line: modeling with pressure impact, dashed line: no pressure impact).

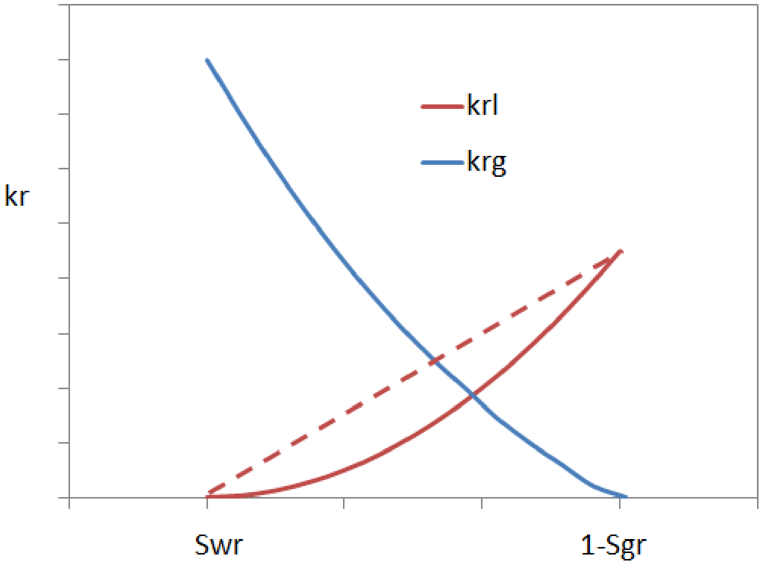

Figure 3.9: Relative permeability curve for water-gas two-phase flow.

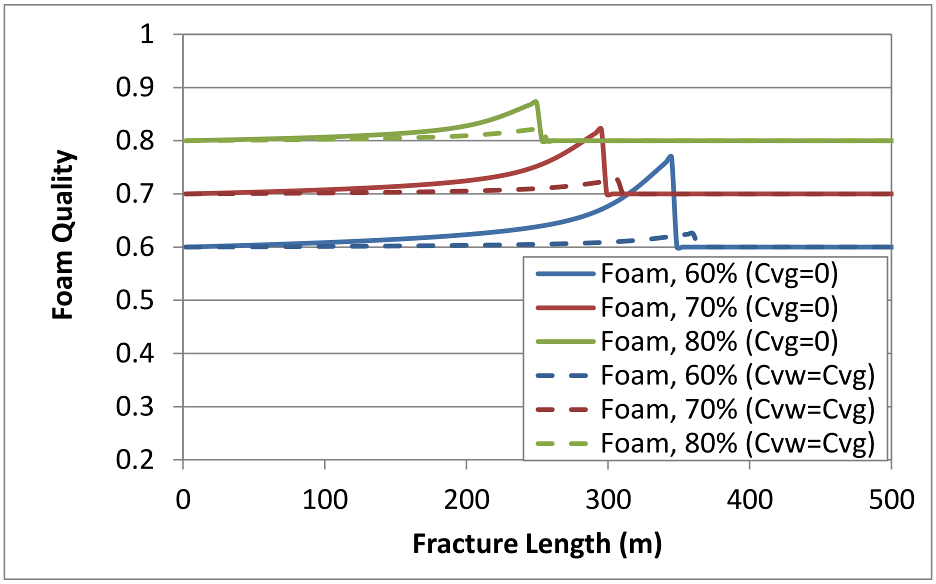

Figure 3.10: Foam quality distribution along the propagation direction for different foam qualities with different leak-off assumptions at 1 μD.

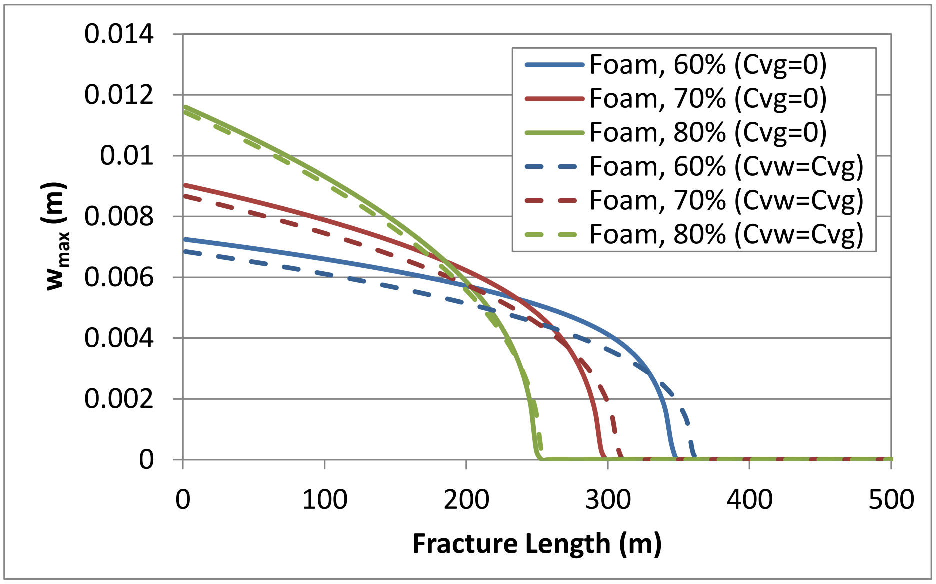

Figure 3.11: Maximum fracture width distribution along the propagation direction for different foam qualities with different leak-off assumptions at 1 μD.

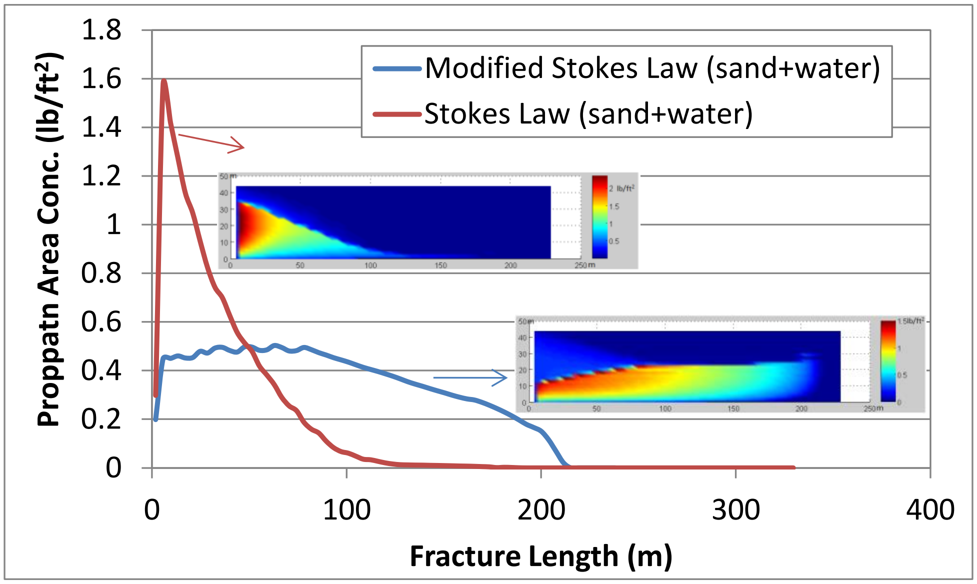

Figure 3.12: Proppant distribution in water frac predicted by Stokes Law vs. Modified Stokes law.

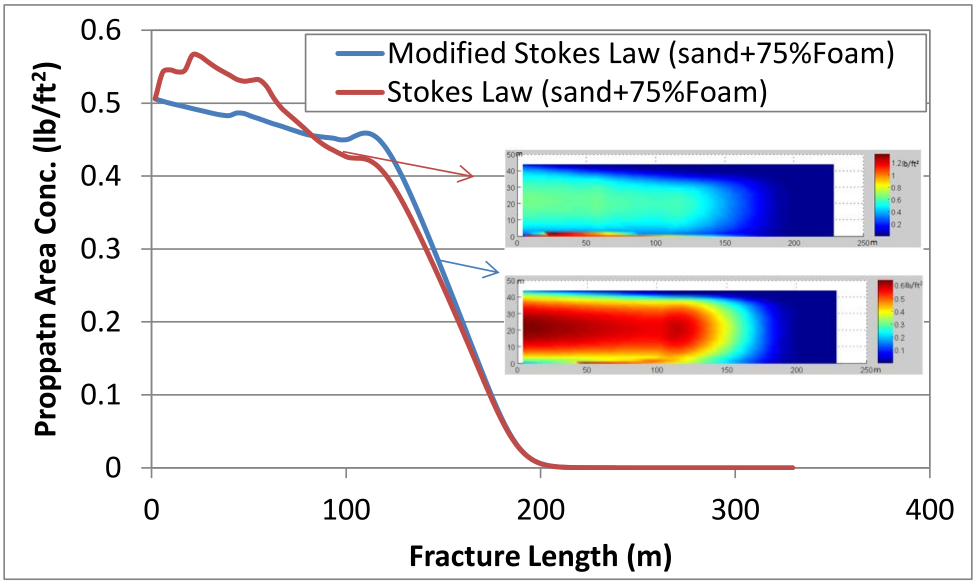

Figure 3.13: Proppant distribution in foam (75%) frac predicted by Stokes Law vs. Modified Stokes law.

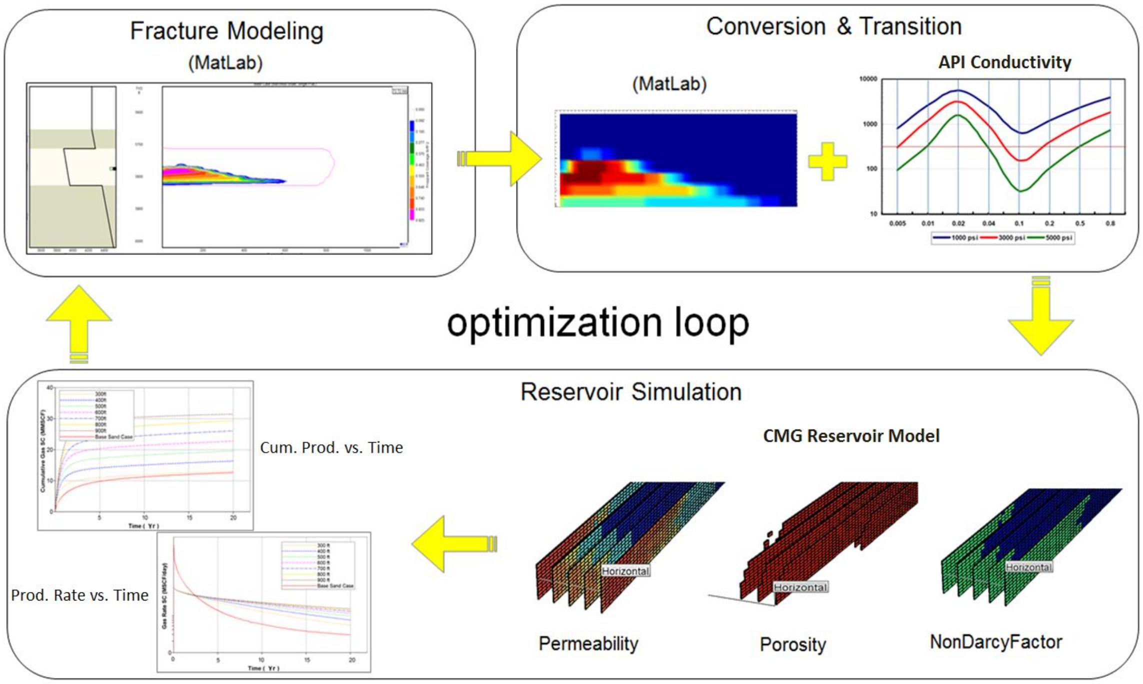

Figure 3.14: The schematic figure of the optimization loop.

Chapter 4: Experiment and Simulation Study of Ultra-Light Weight Proppants and Their Application in Shale Gas Fracturing

This chapter discusses properties and applications of the three ultra-light weight (ULW) proppants. The physical properties, mechanical properties and conductivity of the ULW proppants have been tested by several experiments. Based on their properties, the critical conductivity chart and reservoir simulation model built in Chapter 2 combined with the fracturing model developed in Chapter 3 are used to evaluate the application of these ULW proppants in shale fracturing. This study aims at understanding the impact of the ULW proppants on the conventional slickwater-sand treatment and then optimizing pumping schedule to maximize the performance of the well stimulated by the ULW proppants.

4.1 BACKGROUND AND MOTIVATION

Hydraulic fracturing is a stimulation technique to create high conductivity conduits between wellbores and ultra-low permeability reservoirs by injecting a pressurized fluid mixed with proppants into the subsurface. Proppants are solid particles preventing the created fractures from closure after the hydraulic pressure is relieved (Economides and Martin, 2007). The proppant laden fluids most often used are either gelled fluids, which favor enhanced fracture width, or slickwater fluids, which favor enhanced fracture length (Biot and Medlin, 1985).

Slickwater has become the most popular fracturing fluid for shale reservoirs in recent time because it creates long and skinny fractures and it is relatively cheap (Warpinski et al., 2005). Other advantages of using slickwater are easier to implement, lower gel residues and better fracture containment. The problem with slickwater is the high settling rate of common proppants, e.g. sand, which results in propped fractures much smaller and shorter than the original cracked fractures (Mahoney et al., 2013, Gadde and Sharma, 2005). Use of gels can help in proppant transport but introduce extra permeability damage to the formation and proppant pack by blocking the micro or nano-scale pores with large polymer molecules (Fredd et al., 2000). It is known that hydraulic fracture deliverability is largely defined by the propped area that exhibits sufficient conductivity contrast to the reservoir (Brannon and Starks II, 2008). So the low proppant transport efficiency may reduce the benefits of using slickwater, leading to sub-optimal production rates (Bulova et al., 2006).

To overcome the settling issue, one way is to use lighter proppants, which can be transported further by a less complex fracturing fluid. ULWPs are newly created proppants, which are lighter than conventional proppants (SG: 1-2), but strong enough to withstand reservoir stresses (Mahoney et al., 2013, Brannon and Starks II, 2009, Gaurav et al., 2010, 2012). Some of them are made by light materials like polymer (Brannon and Starks II, 2009, Gaurav et al., 2010, 2012), or polymer alloy (MonoProp from Halliburton). Some of them are heavy hard materials coated by light materials, such as resin (Brannon and Starks II, 2009, Gaurav et al., 2010, 2012) , or hydrogels (Mahoney et al., 2013), to decrease the nominal specific gravity. Another example is IBU Prop Lite, which is manufactured by IBU-Tec advanced materials AG consisting of a specially coated core material. They can also be made by creating a large amount of pores inside the stronger materials such as porous ceramics (Gaurav et al., 2010, 2012). Table 4.1 lists the important properties of all the light weight proppants mentioned above. In terms of transportability, these proppants show more promise with slickwater than conventional sand, ceramic, or sintered bauxite (S.G. 3.6). Besides, typical shale fracturing processes are extremely water intensive. Once the stimulation treatment is completed, there are other issues with the disposal of the recovered fracturing fluid. The ULWPs also provides us an option of using foams, thereby reducing the water consumption and disposal.

However, most ULWPs cannot provide as much conductivity as conventional proppants due to their weaker strengths. Furthermore, if the same volume of ULWPs and sand are pumped, ULWPs would form a thinner pack than sand because they cover more areas. These two factors lead to much lower fracture conductivity generated by the ULWP treatment compared with the conventional sand treatment. Another disadvantage of ULWP is the more complex manufacturing process and hence higher proppant cost. For example, LiteProp108 has a price of \$5.5/lb (\$360/ft^3, Brannon and Starks II 2008). As a contrast, sand price is \$0.24/lb or \$40/ft^3.

Considering the low conductivity and high cost of the ULWP treatment, it is necessary to study the strength and conductivity of ULWPs under different reservoir conditions and determine the optimal pumping strategy to maximize economic benefits based on the tested proppant properties (experimental results obtained in this chapter), the reservoir properties (critical conductivity chart created in Chapter 2) and the modeling/simulation study (parametric study by using simulator tools developed in Chapter 2, 3).

4.2 REVIEW OF EXISTING LIGHT PROPPANT STUDY

Since the earliest treatments over 60 years ago, many different materials have been used as proppants. Currently, the most commonly used proppants include various sands, ceramics, and sintered bauxite, due to their cheap cost and sufficient strength to withstand various reservoir closure stresses and temperatures. Generally speaking, the strength of a proppant increases with its density (Rickards, 2003). However, increase of proppant density directly leads to increasing settling rate and reduced propped area for equal amounts of injected proppants. Excessive settling also leads to proppant bridging before the desired stimulation is achieved. Rickards et al. (2003) from BJ Services first introduced two newly developed ULW proppants. One is a porous ceramic coated by resin with a specific gravity of 1.75, while another is ground walnut hull coated with resin with a specific gravity of 1.25. The resin coating significantly increases the strength and crush resistance, by protecting the inner brittle materials from crushing, helping to combat embedment, and preventing the liberation of fines. Figure 4.1 compares the calculated Stoke's settling rate of different proppants with the 20/40 mesh size in 2% KCl brine. ULWP-1.25 and ULWP-1.75 settle down 75% and 33% more slowly than sand. Meyers Mfrac was used to compare the fracture geometry and proppant placement of the ULWPs with those of conventional sand. Figure 4.2 shows that ULWPs covers higher and longer fracture areas with a smaller propped width. Wood et al. (2003) from the same company conducted conductivity tests on the two ULWPs in a standard API conductivity cell. According to Figure 4.3, both proppants show very good conductivity within their designated applicability range of closure stress with an enhanced strength led by resin coating.

Brannon et al. (2004), through the lab tests and field experiences, demonstrated how the convergence of these new light proppants with old theory of partial monolayer (PML) can produce economic profits. Over fifty years ago, Darin and Huitt (1960) first introduced the concept of partial monolayers which is shown in Figure 4.4. Their reasoning for the high conductivity of a partial monolayer was attributed to possibility of flow through open spaces around the sparsely distributed solid particles. However, issues such as inability to obtain uniform coverage with a partial monolayer, insufficient proppant strength to support the load, loss of fracture width due to proppant embedment and potentially deleterious non-Darcy flow effects in the relatively narrow propped fracture, made the concept inapplicable until light and strong ULWPs were developed. Figure 4.5 shows that lab measured conductivities of partial monolayers with ULW-1.25 are comparable with its multi-layers from 1000 to 6000 psi. By using the ULWPs, partial monolayer can be achieved with a near infinite conductivity with respect to the low permeability formation, which is indicated by observed extraordinary stimulation from wells treated with low concentrations of the ULWPs.

Brannon and Starks II (2008) from BJ Services introduced another ULWP. It is a heat-treated, thermoplastic nano-composite with an apparent specific gravity of 1.05. The proppant can be employed with slickwater to yield nearly neutrally buoyant proppant slurry, and efficiently minimize proppant settling. The tested conductivity of a 14/40 mesh ULW-1.05 at concentrations ranging from 0.01 to 0.8 lb/ft^2 is shown in Figure 4.6. The shapes of the curves constructed from the lab data are very similar to those modeled by Darin and Huitt (1960), which shows a peak conductivity at partial monolayer concentration. Considering the much higher cost of ULWP than conventional sand, parametric study by using fracture modeling was conducted to design the treatment using ULWP. An index, known as Return-On-Fracturing-Investment (ROFI), was defined to measure the economic success of stimulated wells. It is the stimulated well performance relative to the stimulation cost. The paper compared the ROFI implications of partial monolayer designs using ULWPs and typical packed designs using conventional proppants, which is shown in Figure 4.7. Among all the cases, the treatment design using large size ULW injected at PML demonstrated the most favorable combination of costs, fracture deliverability, productivity, and profitability (ROFI).

Gaurav et al. (2010, 2012) conducted comprehensive experiment study on the physical properties (Riley Sphericity, elasticity, strength, and conductivity) of three kinds of ULWPs supplied by BJ Services. ULW-1 is polymeric and has the smallest density and largest elasticity. ULW-2 is a resin coated and impregnated ground walnut hull, which demonstrates higher density and less elasticity than ULW-1. ULW-3 is a porous ceramic coated by resin, which has the largest density and brittleness. ULW-3 has conductivity comparable with conventional sand, while ULW-1 and -2 have much poorer conductivity. The author of this dissertation participated in some of the experimental work, such as strength test and conductivity test. In this dissertation, some of the important experimental results in Gaurav et al. (2010, 2012) are illustrated and utilized to evaluate the performance of the ULWPs in shale fracturing.

Mahoney et al. (2013) introduced a self-suspending proppant. It is normal sand coated with a thin layer of a high-molecular-weight hydrogel polymer. When introduced into water, the polymeric coating swells to many times the original size (3 times shown in Figure 4.8), causing an inhibition of settling. Conventional breakers are used to break the hydrogel and release the proppant into the fracture after transport.

This chapter focuses on the three kinds of ULWPs provided by BJ Services. These three ULWPs cover a wide range of specific gravity and represent the three typical manufacturing methods. The experimental works done by Gaurav et al. (2010, 2012) are reviewed and discussed. Based on the experimental results, empirical correlations are derived. The empirical correlations are incorporated in the fracturing and reservoir simulation models developed in the previous chapters to study the impacts of the three ULWPs on the propped area, conductivity, productivity and ROFI of conventional slickwater-sand treatment in shale reservoirs. Finally, based on a comprehensive parametric study, both the optimum pumping schedule and acceptable price range for the ULWPs are determined to yield better stimulation performance and economics than sand.

4.3 EXPERIMENTAL STUDY OF ULWPS

In this section, three kinds of ULWPs are tested for evaluating their mechanical properties and conductivity. ULW-1 is polymeric proppant with a specific gravity of 1.08 and mesh size 14/40. ULW-2 is resin coated and impregnated ground walnut hull with a specific gravity of 1.25 and mesh size 14/30. ULW-3 is resin coated porous ceramic with a specific gravity of 1.75 and mesh size 20/25. All these proppants are supplied by BJ Services Company. Based on the test results, empirical correlations are developed for ULWP deformability and conductivity, which are used in the following modeling and simulation.

4.3.1 Approach and Methodology

4.3.1.1 Equipment and Process for Testing Mechanical Properties

The strength of individual particles as well as their bulk packs was tested both at room temperature (77 ^{o}F) and high reservoir temperature (203 ^{o}F) in a strength test tool. The equipment is shown in Figure 4.9. It has three major parts: top piston, bottom piston and cylindrical sleeve. Test samples are placed inside the cylindrical sleeve above the bottom piston. The whole set is made from aluminum. But the surfaces of the pistons exposure to proppants are made with tool steel to prevent embedment of proppants. The equipment together with samples is placed in a Humboldt press machine. In the machine, the level of the top piston can be adjusted to achieve a certain strain, and the resultant stress is recorded.

After the strength test, the crush test was performed in the same equipment. A maximum stress level of 15000 psi was applied to the proppant packs for two minutes. The end product of the crush test was screened through appropriate sieves to see how much proppant was crushed into comparatively finer particles.

4.3.1.2 Equipment and Process for Testing Proppant Conductivity

The long-term conductivity tests were performed following guidelines specified in ISO 13503-5. All the conductivity tests were done at 203 ^{o}F and varied closure stresses ranging from 1000 to 6000 psi. The fluid used for test was DI water with a viscosity of 0.316 cP at the temperature. The back pressure was maintained at 400 psi. The flow rate is controlled to be in the Darcy regime (Re<10, Bird and Stewart).

The API conductivity system is shown in Figure 4.10. The most important part of the system is the API conductivity cell. It has the similar construction to the equipment of strength test, which includes top piston (with a metal shim), rectangular sleeve and bottom piston (with a metal shim). There are five ports around the sleeve. The two at the ends are inlet and outlet flow ports. The other three ones in the side are pressure ports. The cell is placed in a pressure system to be pressurized and the whole set along with an accumulator is put in an oven maintained at high reservoir temperature. Outside the oven, a pump is used to drive the DI water from the accumulator into the API conductivity cell at a specified flow rate. When the fluid flows through the proppant pack, the pressure difference is recorded through two separate differential pressure transducers connected to pressure ports. Using Darcy’s law, the permeability of the proppant pack can be calculated. To obtain the conductivity, the width of the proppant pack is also needed. The width of the pack at various stresses is measured according to the guidelines outlined in ISO 13503-5. The metal shims are used to mimic the fracture face to confine the proppant packs in the API conductivity cell. It can be a good approximation that if the target reservoir is a hard shale, such as the Barnett, where proppant embedment can be ignored. For soft shales, replacing metal shims with actual core cuts is highly recommended for considering embedment effect on conductivity.

Two major difficulties were encountered in the conductivity test. One is leakage of the API conductivity cell, which leads to an overestimation of permeability. The rubber O-rings in the top and bottom piston were not sealed perfectly. To overcome this problem, high temperature resistant thin rubber gaskets are applied between the metal shims and the pistons. The rubber sheets provide an improved seal by being expanded to fill all gaps inside the cell once the closure stress is applied. With the effort, the entire fluid flow can be well confined between the metal shims. The second problem is the big measurement error in fracture width, especially when testing the partial monolayer width. To minimize measurement errors, each width test was repeated for several times by different persons. For a partial monolayer, whose thickness is smaller than the stainless steel tubing (1/16") inserted in the pack, the tubing is flattened with a threaded screw. However, this may cause the tubing at the outlet port to be plugged by proppant fines, leading to zero flow rate and a dramatically high pressure.

4.3.2 Experimental Results

4.3.2.1 Physical Properties

Figure 4.11 illustrates the three ULWPs in the normal scale and the magnified scale. ULW-1 is a perfect sphere with a dark color, ULW-2 is extremely angular with a brown color, and ULW-3 is intermediately spherical with a yellow color. Figure 4.12 shows the sieve size distribution obtained from sieve size analysis on 80 grams of each proppant type following the guidelines of ISO 13503-2. For ULW-1 and ULW-3, nearly 80% of proppants have the sieve size of 25. ULW-2, due to its irregular shape, has a wider distribution than ULW-1 and ULW-3. The mean value is around 20. The proppants were then placed at the top of a column of fluid and a handy-cam was used to monitor the downward movement. The settling velocity of proppants (three ULWPs and sand) in water does not follow Stokes law because the Reynolds number is larger than unity (10-300). Instead, it agrees well with the Happel correlation, which is valid for Reynolds number between 2 and 500. In the next step, the proppants were mixed with 0.1wt% anionic surfactant foam with a foam quality larger than 90%. None of the proppants fell through the foam.

4.3.2.2 Mechanical Properties

The strength test was first conducted on proppant pack of each type of proppant to a closure stress level of up to 15000 psi at room temperature and reservoir temperature. Figure 4.13 compares the stress-strain curves of three ULWPs at 203 ^{o}F. Each curve represents average values of four repeated tests. After completion of the test, the proppant pack was maintained at 15000 psi for two minutes and then placed in a sieve box for crush test. The weight percentage of fines formation for each proppant is shown in the legend of Figure 4.13. From the initial linear elastic behavior regime, the Young's modulus of each proppant pack is obtained. Young's modulus of ULW-1, -2 and -3 are 22500 psi, 18000 psi and 40000 psi, respectively. Comparing all three proppants, ULW-1 and ULW-2 share the similar stress-strain trend and similar Young's modulus, while ULW-3 has a more rigid behavior. Young's modulus of a proppant pack is mainly determined by the elasticity of an individual particle and the pore elasticity. One possible reason to explain that the ULW-2 pack is more deformable than ULW-1 is that the particle of ULW-2 is more irregular and less sorted, leading to larger pore elasticity than that of ULW-1. The big difference between ULW-3 and ULW-1, -2 can be explained by following strength test on individual particles of each type. Comparing their crush test results, ULW-1, due to its deformable nature, formed a negligible amount of fines (<1%). ULW2 is also highly ductile with 1.5% fines formed. ULW3 is the most brittle, with almost 30% of the original amount broke into fines. The same tests are repeated at room temperature. It is found that with decrease in temperature, ULW-1 and -2 tend to be less deformable and form more fines, while ULW-3 becomes less brittle with a reduction of fines formed. Young's modulus of proppant pack is not quite dependent upon temperature.

The multi-layer conductivity is highly dependent on the strength and crush test results of the pack, while the partial monolayer conductivity is mainly determined by the mechanical behavior of an individual particle. The pack strength test was followed by a strength test of a single proppant particle. Figure 4.14 shows the applied load and the resulting deformation for individual particles of three types at 203 ^oF. Each curve represents average values of five samples. ULW-1 deforms with increasing stress without getting crushed. The deformation slowed down as stress increased. It is due to the deformable nature of the polymer material. Compared with ULW-1, ULW-2 was less deformable and there was a failure point at load of 25 lbf. ULW-3 is the least deformable with a failure point at load less than 5 lbf, due to the brittleness and hard nature of the ceramics. All tests were repeated under room temperature, showing a decrease in elasticity with temperature for ULW-1 and -2, and an increase in brittleness for ULW-3.

4.3.2.3 Conductivity

The long term conductivity of the proppant pack as well as the partial monolayer was measured at closure stress ranging from 1000-6000 psi, and temperature of 203 ^oF, following the guidelines of ISO 13503-5. Proppant concentrations chosen for the test were from 0.05 lb/ft^2 to 1 lb/ft^2, covering partial monolayer to multilayer. Figures 4.15, 4.16 and 4.17 show the preliminary results for ULW-1, -2 and -3, respectively. For ULW-1 and -2, a partial monolayer ($\leq$ 0.07 lb/ft^2) provides as much conductivity as multilayer (≥ 0.1 lb/ft^2). For ULW-3, conductivity increases monotonically with concentration. However, its partial monolayer still has conductivity comparable to or larger than the conductivity of other two ULW proppants.

Difference of mechanical properties leads to difference of conductivity. From previous study, ULW-1 and -2 shared a similar deformability. So their conductivity behaviors are also similar, with two common features: 1. Partial monolayer performs as efficiently as multilayer; 2. Conductivity at partial monolayer to multilayer is much lower than conventional sand or ULW-3 (for example: 1-10 md-ft at a closure stress from 4000 to 6000 psi). The low conductivity may be attributed to the high deformability of the two proppants. Under large confining stress, proppant may be deformed and expanded to fill the void spaces around the particles for fluid to flow through. The largely decreased pore volumes and pack widths are the major killers to conductivity. ULW-3 is much less deformable but much more brittle, which makes it behave like conventional sand in conductivity. Its low conductivity at partial monolayer is attributed to its low failure point. In partial monolayer, the effective load upon each particle might exceed the limit that ULW-3 can withstand, leading to a large decrease of the fracture width due to crush.

The published conductivity data from the literature is shown in Figures 4.5 and 4.6. The conductivity of ULW-1 measured by Brannon and Starks II (2008) is 800-1100 md-ft at 0.8 lb/ft^2, 3-5000 psi, and 150 ^{o}F, which is much higher than the value (10-15 md-ft) we measured at the similar concentration and closure stress but a higher temperature (200 ^{o}F). The possible reasons for the discrepancy are (1) ULW-1 becomes more deformable under high temperature, leading to a reduction of pore volumes and hence conductivity, (2) There may be a difference in materials of our ULW-1 and the one tested in the literature. The same reasons are applied for the different ULW-2 conductivity values measured by Rickards et al. (2003), Brannon (2004) and us.

4.3.3 Empirical Equations Development

In this section, empirical equations for proppant deformation and conductivity are developed, which will be utilized in following fracture modeling and reservoir simulation study.

4.3.3.1 Empirical Equations for ULWPs Deformability

Figure 4.18 illustrates the deformation of an individual particle under an increasing load for different ULWPs according to their load-deformation behaviors shown in Fig. 4.14. As load increases, ULW-1 becomes more and more flat and extended. The process is continuous and no failure happens. The decreasing width and void spaces around the particles are mainly responsible for the reduction of the conductivity. ULW-2 has a similar deformation process before failure. Above a load of 25 lbf per particle, walnut hulls break out of resin coatings and form scattered smaller pieces. Fracture width and conductivity of the partial monolayer suddenly drops. ULW-3 does not deform too much due to the rigid nature of ceramics. Above 4.5 lbf per particle, it breaks into small pieces and fracture width suddenly drops.

Empirical equations for deformability of ULWPs are developed based on Figure 4.14. For ULW-1 (blue line), the load increases with deformation at an increasing rate without failure. Below 1 lbf, linear elastic behavior is assumed. Above 1 lbf, deformation is linearly correlated with the logarithm of the load with an R square of 0.989. The empirical equation for deformability of ULW-1 is

$$\begin{cases} \Delta D(inch) = 0.000948F(lbf) & F < 1lbf \\ \Delta D(inch) = 0.011522\log(F(lbf)) + 0.000742 & F \geq 1lbf \end{cases} \tag{4.1}$$

where ΔD is the proppant deformation in inches, F is the according force applied upon proppant in lbf. For ULW-2 (red line) and ULW-3 (green line), there are failure points at

25 lbf and 4.5 lbf, respectively. Below failure points, load and deformation are linearly correlated with each other. Empirical equations are only developed for the regime prior to the failure point. The empirical equation for ULW-2 is

$$\Delta D(inch) = 0.000613F(lbf) \qquad F < 25lbf \tag{4.2}$$

, while the empirical equation for ULW-3 is

$$\Delta D(inch) = 0.000434F(lbf) \qquad F < 4.5lbf \tag{4.3}$$

The empirical equations will be used in the following study to develop empirical equations of conductivity.

4.3.3.2 Empirical Equations for ULWPs Conductivity

Proppant conductivity is a measure of the flow capacity of the fluid through a porous medium. In hydraulic fracturing, the fracture conductivity determines the flowing rate of the gas through the fracture, and is defined as the product of the fracture width and the permeability of the proppant pack within the fracture. It is dependent on the fracture closure stress, the rock stiffness and the parameters related to proppant including proppant concentration, size, and strength.

In the case of a fracture with a multilayer pack of propping agent, the Kozeny-Carman relation can be used to estimate the permeability (Carman, 1937). The relation is expressed as,

$$k = \frac{\phi^3}{CS^2(1-\phi)^2} \tag{4.4}$$

, where φ is the porosity, C is the Kozeny-Carman constant, and S is the area of particle surface per unit volume of packed space. C can be assigned a value of 5 for unconsolidated rigid sphere bed (Carman, 1937).

Darin (Darin and Huitt, 1960) introduced empirical equations to predict the partial monolayer system under the embedment condition,

$$kW_f \sim \frac{W_f}{{S_P}^2} \frac{\phi^3}{(1-\phi)^2} \tag{4.5}$$

Compared with Equation 4.4, S is replaced by S_p, which is the total wetted surface area per unit volume of particles. The fracture width is determined by conducting embedment experiment with proppant and core cuts.

In current study, proppant conductivity is assumed to be linearly correlated with proppant areal concentration in multilayer scenario. In partial monolayer scenario, conductivity is positively correlated with porosity and fracture width. Since metal shims are used for the conductivity test, embedment has no impact on partial monolayer conductivity. According to Equations 4.1-4.3, the product of porosity φ and partial monolayer thickness w_{pml} is plotted against proppant areal concentration for three ULWPs at different closure stresses in Figure 4.19-4.21. From the figures, three conductivity zones can be defined. For ULW-1, zone I is any partial monolayer concentration below 0.029 lb/ft^2, where flow capacity increases with increasing areal concentration. Zone II is any partial monolayer concentration between 0.029 and 0.095 lb/ft^2, where flow capacity decreases with increasing areal concentration. Zone III is any multilayer concentration above 0.095 lb/ft^2, where flow capacity is assumed to be positively correlated with proppant areal concentration. For ULW-2, the areal concentration boundary between zone II and III is 0.13 lb/ft^2. The areal concentration boundary between zone I and II are 0.026, 0.032, 0.045, and 0.057 lb/ft^2 under 1000, 2000, 4000, and 6000 psi, respectively. It is noted that, in zone I, there is an areal concentration below which flow capacity suddenly drops. It is determined by the failure point of ULW-2. Similarly, for ULW-3, the areal concentration boundary between zone II and III is 0.153 lb/ft^2. The areal concentration boundary between zone I and II are 0.023, 0.047, 0.094, and 0.135 lb/ft^2 under 1000, 2000, 4000, and 6000 psi, respectively. Different from ULW-1 and -2, the failure point is the division of zone I and II for ULW-3.

Based on the conductivity zones defined by Figures 4.19-21 and experimental data (Figs. 4.15-17), empirical equations are developed for predicting conductivity from proppant areal concentration for different proppants. Example results are shown below at a closure stress of 4000 psi. In each equation, *Y* is *log (conductivity, md-ft)*, *X* is *log (areal concentration, lb/ft^2)*.

Empirical conductivity correlations for ULW-1 are

$$\begin{gathered} Y = 0.9322X + 2.6089 \quad \sim \quad zone\ I \\ Y = -0.9322X - 0.2634 \quad \sim \quad zone\ II \\ Y = 0.7515X^3 + 1.7181X^2 + 1.4183X + 1.1847 \quad \sim \quad zone\ III \end{gathered} \tag{4.6}$$

Conductivity results predicted by the correlations (solid line) above are plotted along with the experiment results (square dots) in Figure 4.22. It shows that empirical equations can predict the conductivity pattern well in the whole concentrations ranging from partial monolayer to multilayer.

Empirical conductivity correlations for ULW-2 are

$$\begin{aligned} &Y = k_{zoneI} * X + 4.9983 \quad \sim \quad zone\ I \\ &Y = -2.6988X - 2.2688 \quad \sim \quad zone\ II \\ &Y = 1.2754X + 1.1930 \quad \sim \quad zone\ III \end{aligned} \tag{4.7}$$

where the slope in zone I is 2.6988 above the failure point and 4.7229 below the failure point. The larger slope below the failure point denotes a faster decay of conductivity due to the plastic deformation of proppants. Another thing that should be noted is that in zone III (multilayer), the slope is close to 1. It suggests that conductivity is almost linearly correlated with concentration, which agrees well with our initial assumptions. Similarly, Figure 4.23 plots the correlation predictions (solid line) and experiment results (square dots) together. A good match is observed.

For ULW-3, experiment results do not exhibit obvious divisions for three zones as shown in Figure 4.21. But we know that proppant started crushing at a concentration below 0.094 lb/ft^2. Thus, we assume a linear correlation of conductivity with concentration above 0.094 lb/ft^2 and a polynomial correlation to describe the fast decrease of conductivity with decreasing concentration below 0.094 lb/ft^2:

$$\begin{aligned} &Y = \text{-}11.486X^2\text{-}23.579X - 10.523 \quad \sim \quad zone\ I, II \\ &Y = 1.4099X + 3.0254 \quad \sim \quad zone\ III \end{aligned} \tag{4.8}$$

Figure 4.24 illustrates a good match between the correlation predictions (solid line) and experiment results (square dots) for ULW-3.

In the next section, fracture modeling and simulation are applied to evaluate the fracturing efficiency and economic efficiency of ULWPs based on their conductivity patterns developed in this section. As a comparison, a type of commonly used sand is adopted to generate reference cases. In this study, API conductivity test for sand was not performed as what we did for ULW-1-3. Different types of sands with different mesh sizes may yield totally different conductivity patterns and settling rates. To make it comparable with ULWPs as well as to simplify the problem, the reference sand is assumed to have the same mesh size and conductivity as ULW-3, but a larger specific gravity of 2.65. The assumption is reasonable for research purpose because ceramic (silicate), which ULW-3 is composed of, has the similar mechanics nature to sand (SiO_2).

4.4 FRACTURE MODELING & SIMULATION STUDY OF ULWPS

This section incorporates the empirical conductivity correlations developed in the previous section into the fracture modeling, developed in Chapter 3, and the reservoir simulation model, built in Chapter 2, to evaluate the effects of ULWPs on the propped fracture area, conductivity distribution and hence the stimulated well performance.

Table 4.2 shows the reservoir properties (left column) and completion parameters (right column) for fracture modeling and reservoir simulation. Reservoir is assumed to be isotropic with no natural fractures. The reservoir permeability is varied from 0.1 - 10 μD. The pay zone has a thickness of 150 ft and is confined by upper and lower cap zones. To eliminate the boundary effect, well spacing is 3250 ft, which is twice as large as the maximum propped length. In this study, in order to minimize the complexities (e.g. fracture geometry, gel filter-cake, polymer damage) introduced by polymer viscosified fluids, the author elected to limit the study to non-gelled, slickwater fluids with a viscosity of 5-6 cp. Pumping rate for a single wing is constant at 0.02 m^3/s, which is around 20 bbl/min for each perforation cluster (two wings). As described in Chapter 2, the reservoir simulation is conducted on one fourth of the fracture and its corresponding drainage area.

Proppant type, proppant pumping volume concentration, reservoir permeability, and treatment time are varied to develop the respective fracture models for comparison, as provided in Table 4.3. In Table 4.3, study cases are divided into two main categories, which are long time treatment and short time treatment. The pumping schedule for long time treatment is 20 minutes pad injection, 40 minutes slurry injection, and 20 minutes shut-in. In the short time treatment, the time for all steps is decreased to half. In each category, there are three sub-categories accounting for three different reservoir permeabilities: 0.1, 1 and 10 μD. In each sub-category, three different proppants, ULW-1, -2 and -3, are studied at different injection volume concentrations raging from a PML concentration of 0.02 v/v to a multilayer concentration of 0.1 v/v. For reference, conventional sand with a multilayer concentration of 0.1 v/v is simulated for each sub-category. By comparing the ULWP treatments with the reference sand treatment, fracturing performances of three ULW proppants and their impacts on proppant placement efficiency, fracture productivity and return-on-fracturing investment (ROFI) have been evaluated.

4.4.1 Effects of ULWPs on Propped Area and Conductivity

Figures 4.25 and 4.26 illustrate the conductivity distributions for different proppants at a long time treatment on 0.1 and 10 μD reservoirs, respectively. Figures 4.27 and 4.28 illustrate the conductivity distributions for different proppants at a short time treatment on 0.1 and 10 μD reservoirs, respectively. The picture at the top of each figure is the reference case treated by conventional sand at 0.1 v/v (2.2 lb/gal) injection volume concentrations. Below are three columns for ULW-1, -2, and -3. In each column, proppant volume injection concentration increases from 0.02 v/v at the top to 0.1 v/v at the bottom. In each figure, comparing different proppants, sand treatment generates a sand bed with the largest conductivity of 64-1400 md-ft. The sand distribution is highly non-uniform, with more proppant not reaching the upper areas as it moves further from the wellbore into the reservoir. ULW-1 exhibits the best proppant placement efficiency: the largest propped area with a uniform conductivity around 1-15 md-ft. The propped area and conductivity generated by the partial monolayer are similar to those generated by the multilayer. ULW-2 has the second largest propped area and conductivity with 2-23 md-ft. It is noted that at low proppant injection concentration, ULW-2 has a poor propped area. As proppant injection concentration increases, propped area increases along with a low conductivity zone (yellow area) growing in the middle. The growth of the low conductivity zone is attributed to the proppant areal concentration transition from the partial monolayer to around the monolayer. The propped area and conductivity of ULW-3 increase with an increasing proppant injection concentration. At high proppant injection concentration (0.06-0.1 v/v), ULW-3 generates a proppant bed longer and larger than sand but shorter and smaller than ULW-1. The propped conductivity is larger than those of ULW-1 and -2, but smaller than that of sand.

Comparing Figures 4.25 and 4.26, or 4.27 and 4.28, high leakage in high permeability shales (10 μD) limits the growth of the proppant propagation distance, leading to a similar propped length for all four proppants. Under this condition, using ULW proppants can only improve the propped area, which benefits production more in short and medium-term than long-term. In Figures 4.26 and 4.27, ULW-1 has a larger propped area than sand at all proppant injection concentrations, and ULW-2 and -3 have larger propped areas than sand at an injection concentration above 0.04 v/v and 0.08 v/v, respectively.

4.4.2 Effects of ULWPs on Fracture Productivity

The first order parameters influencing productivity of a fractured well are the propped area, propped length and the associated conductivity. Short-term production is tied to propped area and conductivity, while long-term production is tied to propped length. According to 4.4.1, ULWPs can improve the propped length and area in low permeability shale reservoirs, and improve the propped area in high permeability shale reservoirs. The improvement depends on the proppant amount to inject. Generally, the higher the proppant injection concentration, the larger the propped area. However, the benefits provided by the light proppants in terms of propped area are offset by their diminished conductivity due to their weaker strength and higher elasticity. According to our study, ULW-1 and -2 have conductivity two orders of magnitude lower than the multilayer conductivity of ULW-3 and sand. The study in Chapter 2 shows that the minimum conductivity required to fully stimulate the propped fracture (critical conductivity) is larger at short production times, longer propped lengths and higher permeability reservoirs. For a 200 nD non-naturally fractured reservoir, the critical conductivity is above 10 md-ft for propped lengths above 200 ft within 1 year production, for propped lengths above 400 ft within 5 year production, for propped lengths above 500 ft within 10 year production, and for propped lengths above 700 ft within 20 year production. For a reservoir with permeability higher than 200 nD or with natural fractures, the critical conductivity can be larger than 10 md-ft. In the previous conductivity test, the conductivity of ULW-1 and -2 are found to be in the range of 1 - 10 md-ft, which might be below the critical conductivity in most of the shale fracturing conditions. Thus, the concern of using ULWPs (especially ULW-1 and -2) is the productivity improvement resulting from increased propped areas may be offset by the decrease of the conductivity.

To better understand the effect of ULWPs on fracture productivity, the conductivity distribution generated from fracture modeling is input into the reservoir simulation model developed in Chapter 2 to predict the resultant fracture productivity.

The normalized productivity, which is the productivity of different light proppant cases divided by that of the reference sand case under the same reservoir condition and treatment time, is plotted against production time. Figures 4.29, 4.30 and 4.31 show the results from a long time treatment in 0.1, 1 and 10 μD reservoirs, respectively. Figures 4.32, 4.33 and 4.34 show the results from a short time treatment in 0.1, 1 and 10 μD reservoirs, respectively. In each Figure, there are three sub-plots accounting for ULW-1, -2 and -3. In each sub-plot, there are five solid curves with different colors accounting for different proppant injection concentrations. The solid curves represent the ULWP fracture productivity normalized by sand fracture productivity. Values above one represent productivity gains of ULWPs over sand, while values below one represent productivity losses of using ULWPs instead of sand.

For ULW-1, the proppant injection volume concentration of 0.04 v/v yields the best productivity than other concentrations. The second best is 0.06 v/v. The worst is 0.02 and 0.1 v/v. As production time increases, the benefit of using ULW-1 increases. Because as the production time increases, the role that conductivity plays in stimulating the propped area decreases (refer to the critical conductivity charts in Chapter 2). So the conductivity disadvantage of using ULW-1 diminishes with increasing production time. As the reservoir permeability increases, the advantage of using ULW-1 decreases. Taking the proppant injection concentration of 0.04 v/v as an example, the fracture productivity of ULW-1 is 1.5-2.7 times as large as that of sand for a 0.1 μD reservoir, while the values decrease to 0.9-1.6 times for a 1 μD reservoir, and further decrease to 0.5-0.9 times for a 10 μD reservoir. It is because for low permeability reservoirs, propped area dominates the production. As reservoir permeability increases, conductivity becomes more important to production than the propped area. The previous comparison of the conductivity distribution shows that ULW-1 creates larger propped areas with much lower conductivity than sand. Thus, ULW-1 presents greater advantages over sand in lower permeability shale reservoirs. Overall, ULW-1 significantly outperforms sand in 0.1 μD shales, and has better production after 100 days than sand in 1 μD shales. For shale permeability higher than 10 μD, ULW-1 shows much poorer initial production and a similar long-term production as compared with sand. Comparing different treatment times, ULW-1 exhibits slightly better normalized productivity trends in the short-term treatment than the long-term for 1 and 10 μD reservoirs. The reason is that the shorter propped fracture in short-term treatment has lower conductivity requirement (refer to the critical conductivity charts in Chapter 2).

For ULW-2, it has similar normalized productivity trends to ULW-1. For each case, ULW-2 exhibits worse production performance than ULW-1, because of its larger settling rate. Proppant injection volume concentrations of 0.04 and 0.06 v/v yield the best productivity, while an injection concentration of 0.02 v/v generates a much lower productivity than all other concentrations. Overall, ULW-2 generates production profits over sand in a 0.1 μD reservoir, only long-term production profits (>1000 Days) in 1 μD, and no production profits in 10 μD. The optimum injection concentration for ULW-2 is above 0.02 v/v. ULW-2 performs better in the short-term treatment than the long-term treatment for reservoir permeability above 1 μD for the same reason as ULW-1.

ULW-3 shows a much different normalized productivity trends from ULW-1 and -2. The relative productivity is not as sensitive to the production time as ULW-1 and -2. For ULW-3, the productivity increases with increasing pumping concentration. By injecting sand and ULW-3 at the same volume concentration of 0.1 v/v, ULW-3 can generate a productivity 1.3-1.4 times as large as sand in 0.1 μD, 1.2-1.3 times as large as sand in 1 μD, and similar to sand in 10 μD. The productivity performance of ULW-3 is similar in both short-term and long-term treatments.

Conclusively, ULW-1,-2 and -3 have strong productivity advantages over sand in 0.1 μD reservoir. The optimum pumping volume concentration is 4% for ULW-1, is 4-6% for ULW-2, is 10% for ULW-3. If reservoir permeability is increased by 10 times, only ULW-1 shows better productivity than sand after 100 days. By cutting down the treatment time by half, ULW-2 also exhibits a better productivity than sand after 1 year. Further increasing the reservoir permeability to 10 μD, all ULWPs show worse or comparable productivity than sand. The productivity advantage of using ULWPs increases with production time. For higher permeability shale reservoirs (>1 μD), short treatment time is preferred for ULW-1 and ULW-2.

4.4.3 Effects of ULWPs on Return-On-Fracturing-Investment, "ROFI"

Through the study of 4.4.2, it is apparent that ULWPs can bring productivity benefits to conventional sand treatment, especially in low permeability shale reservoirs (0.1 μD). However, ULWPs are much more expensive than sand, leading to a highly increased treatment cost counteracting the productivity benefits. To understand the effects of ULWPs on the economics of stimulated wells, the Return-on-Fracturing-Investments (ROFIs) of ULWPs are calculated and compared with that of sand. ROFI is estimated by simply subtracting the fracturing treatment cost from the value of the stimulated production after certain production time,

$$ROFI = Production\,Value - Proppant\ Cost - Nonproppant\ Cost \tag{4.9}$$

Table 4.4 lists the treatment costs for different proppants for a long-term treatment. Fracturing treatment costs are highly variable, depending on equipment requirements, material costs, logistics, time, and pumping services availability. For the current effort, the treatment costs related to the slickwater materials, pumping equipment, and services have been bundled to be a value of \$2.5/gal of fluid volume employed. Sand price is assigned a value of \$40/ft^3. All three light proppants (ULW-1, 2, 3) have a price ranging from \$67/ft^3 to \$670/ft^3, with a mean value similar to the value \$360/ft^3 given in the literature (Brannon and Starks II 2008). As a contrast, the typical cost for sand proppant is about \$0.24/lb or \$40/ft^3. The proppant costs are proppant prices multiplied by the total proppant volumes employed in the treatment. Compared with the fixed bundled costs (cost of fluid, pumping & services), proppant costs can be one twentieth at partial monolayer pumping volume and \$67/ft^3 price or 3.4 times larger at multilayer pumping volume and \$670/ft^3 price. Drilling costs and later well maintenance fees are ignored in this study. According to the last section, ULWPs exhibits more significant productivity advantages over sand in 0.1 μD shale reservoirs than other two higher permeability reservoirs. So the ROFI study is only applied to the 0.1 μD permeability shale in this section.

Figures 4.35, 4.36 and 4.37 plot the Normalized ROFI against proppant injection volume concentration at different light proppant prices. In each figure, the left sub-plot is calculated based on 1-year production, and the right sub-plot is for 5-year production. Normalized ROFI is calculated as ROFI of the ULWPs divided by ROFI of the base sand case,

$$ROFI_{norm} = ROFI_{ULW-1,2or3} / ROFI_{Sand} \tag{4.10}$$

$ROFI_{norm}$ below one denotes a negative economic impact generated by ULWPs, while above one denotes a positive economic impact.

For ULW-1 (Fig. 4.35), both 1-year and 5-year ROFIs increase with proppant injection amount at a proppant injection volume concentration below 4%, and decreases with proppant injection amount at an injection concentration above 4%. So 4% v/v is the optimum injection volume concentration for ULW-1. At the optimum injection concentration, 1-year ROFI of ULW-1 is 2.8 to 3.5 times as large as that of base sand case at a ULW price of \$10/lb to \$1/lb, while the number is 2.85 to 3.1 for 5-year production. Comparing plots of different production years, ROFI of a 5-year production is less sensitive to the proppant price than that of a 1-year production

For ULW-2 (Fig. 4.36), similar trends are found in two normalized ROFI plots. The optimum proppant injection volume concentration is 4-6% v/v for both 1-year and 5-year productions. Based on 1-year production, above \$6.02/lb, ULW-2 can never generate better ROFI than sand no matter what pumping volume is applied. Below that price, a pumping concentration window can always be found for any prices below \$6.02/lb to generate a positive ROFI impact from ULW-2. The lower the price of ULW-2, the larger the concentration window. For 5-year production, the concentration window is roughly between 0.03-0.1 v/v for all ULW-2 prices. At the optimum volume injection concentration within the pumping concentration window, ULW-2 can generate a ROFI 1.1 to 1.6 times as large as sand at a price from \$5.16/lb to \$0.86/lb based on 1-year production, while it can generate a ROFI 1.27 to 1.6 times as large as sand at a price from \$8.6/lb to \$0.86/lb based on 5-year production.

For ULW-3 (Fig. 4.37), the ROFI increases monotonously with the proppant injection volume concentration. Compared with ULW-1 and -2, ULW-3 only shows better ROFI than sand at large proppant injection volume concentrations and low proppant prices. For example, at 1-year production, ULW-3 outperforms sand at injection concentrations above 0.04 v/v for the proppant price of \$0.62/lb, above 0.06 v/v for the price of \$1.24/lb, above 0.08 v/v for the price of \$1.86/lb, and above 0.1 v/v for the price of \$2.48/lb. As production time increases to five years, the concentration windows to generate positive ROFI impacts over sand are increased by different amounts for different proppant prices.

Overall, comparing all the three kinds of ULWPs, ULW-1 generates the best ROFI among the three proppants. It generates a better ROFI than sand for both short and medium-term productions. ULW-2 is the second best. It has a medium-term ROFI better than sand. Both ULW-1 and ULW-2 have their optimum design (best ROFI) at a partial monolayer concentration scenario, which is created by injecting proppants at a proppant volume injection concentration of 0.04-0.06 v/v. ULW-3 only outperforms sand at high injection concentrations and low prices. For 1 year production and 0.1 μD shale reservoirs, the acceptable maximum price is \$10/lb for ULW-1, \$6/lb for ULW-2, and \$2.5/lb for ULW-3. The maximum price increases as production time increases. Besides, with increase of production time or decrease of proppant price, a larger proppant injection concentration window can be applied for ULWP treatment design to generate better ROFI than sand treatment.

4.4.4 Effects of Mixing ULWPs with Sand on Net Present Value (NPV)

According to the previous study, ULWPs increase the propped area and propped length at the expense of conductivity and proppant cost. Conventional treatment of pumping high concentration sand creates a high conductivity sand bed at the bottom of the facture with a large amount of upper and deeper fractured zones lost to production after closure. By adding ULWPs into sand, both the high conductivity zone at the bottom and low conductivity zone at the upper and deeper zones can be kept, which benefits both short and long-term production. Besides, the amount of ULWPs can be highly reduced, which decreases the total treatment cost. In this section, a simplified NPV study is conducted to figure out the optimum amount of ULWPs added into the sand, which generates the best NPV. ULW-1 is taken as an example. The price of ULW-1 is set to be \$360/ft^3, or \$5.5/lb (Brannon and Starks II, 2008). Reservoir permeability is still 0.1 μD. The total pumping time is 1 hour.

NPV is calculated as increased production value by adding ULW-1 minus the extra cost introduced by ULW-1. If NPV is above zero, adding ULW-1 into conventional sand treatment can bring positive economic impacts. The NPV is further normalized by the equation below,

$$NPV_{norm} = NPV / Prod_{Sand} = (\Delta Prod_{ULW1} - Cost_{ULW1}) / Prod_{Sand} \tag{4.11}$$

To determine the optimum adding amount of ULW-1, a parametric study is conducted on the injection concentration of ULW-1, which varies from 0.0002 v/v to 0.04 v/v. If the sand injection concentration is fixed to be 0.1 v/v, the mixing ratio of ULW-1 to sand is varying from 1/500 to 1/2.5. The normalized NPV is obtained as a function of the added ULW-1 amount. Figure 4.38 (a) compares the conductivity distributions of cases with different amount of ULW-1 added into sand. At the bottom of the fracture, there is a wedge-shaped sand bed (red zone) with relatively infinite conductivity of 63-1456 md-ft. Above the sand bed, the fracture face is mainly covered by ULW-1. The conductivity of that zone increases with the increasing ULW-1 injection volume concentration, which is 0.005-0.12 md-ft at 0.0002 v/v injection concentration, 0.12-2.8 md-ft at 0.002 v/v injection concentration, and >2.8 md-ft at 0.02 v/v injection concentration. Compared with the conductivity distribution of the base sand case in Figure 4.25, addition of ULW-1 highly increases the propped area and propped length by covering the upper and deeper fractured zones with the lighter proppants.

According to Figure 4.38 (a), increasing ULW-1 injection volume concentration can largely increase the conductivity of the zone propped by ULW-1 and slightly increase the propped length. But the proppant cost is also increased. Figure 4.38 (b) plots the normalized NPV at different ULW-1 injection volume concentrations in a semi-log plot. Even after 1 month production, adding ULW-1 can bring positive NPV. Within 5 years production, the normalized NPV generated from adding ULW-1 increases with production time at a decreasing rate. The normalized NPV of 10 years is similar to that of 5 years. For all production times, the normalized NPV increases with the increasing ULW-1 injection volume concentration below a concentration of 0.01 v/v. Above that value, the normalized NPV increases slightly or begins decreasing. So the optimum injection concentration of ULW-1 appears to be 0.02-0.03 v/v. In the same plot, the normalized NPV generated by pumping pure ULW1 are also plotted as a function of ULW-1 injection concentration, which is shown as the dashed lines. Comparing the solid and dashed lines with the same color, mixing ULW-1 with sand generates much better economic gains than pure ULWP treatment because the mixing strategy creates a high conductivity sand channel at the bottom, which meets the initial high critical conductivity need. Conclusively, compared with the previous pure ULW-1 treatment, the treatment of mixing ULW-1 with sand can be a better strategy under the conditions that initial short-term production is important, the fracture length is long, or the reservoir permeability is relatively high.

4.5 CONCLUSIONS

This chapter first discusses the experimental results of the mechanical properties and long-term conductivity of three ultra-light weight proppants, ULW-1, -2 and -3. Based on the experiment results, the empirical correlations of the conductivity as a function of proppant areal concentration and closure stress are developed for the three proppants. The empirical conductivity correlations are applied in fracture modeling and reservoir simulation developed in previous chapters to evaluate the impacts of ULW proppants on propped area/length, propped conductivity, productivity, and ROFI of conventional slickwater-sand treatment. Finally, based on the parametric study, optimum pumping strategies for ULWPs have been designed for different reservoir conditions.

The light proppants are not used commonly in the field. The possible reasons are their high cost, low strength, and limited availability. Our study shows that, although ULWPs can be much more expensive than sand, they can be cost effective if they are pumped with slickwater at a partial monolayer concentration for shale reservoir with a critical conductivity equal or lower than the baseline conductivity of the ULWPs. Also, to achieve better economics than sand, their prices should be determined by the sensitivity study conducted in Chapter 4. For example, for 1 year production in 0.1 μD shales, the acceptable maximum price is \$10/lb for ULW-1, \$6/lb for ULW-2, and \$2.5/lb for ULW-3. The maximum price increases as production time increases. The productivity benefits of the ULWPs have been validated in several field case studies of partial monolayer fracturing treatments employing ULWPs (Brannon et al. 2004, Schein et al. 2004, Myers and Moody 2004, Posey and Strickland, 2005, Kendrick et al. 2005).

Some key conclusions are

- ULW-1 is the most deformable with the lowest effective Young's modulus; ULW-3 is the most brittle with the highest effective Young's modulus; ULW-2 has an intermediate Young's modulus and elasticity.
- Single particles of ULW-1 have no failure point, while ULW-2 has an average failure point at a load of 25 lbf and ULW-3 has an average failure point at a load of 4.5 lbf.
- The size, elasticity, and failure point of three light proppants determine their three conductivity-concentration boundaries: *zone I* (increasing conductivity

trend in partial monolayer), *zone II* (decreasing conductivity trend in partial monolayer) and *zone III* (multilayer conductivity linearly correlated with concentration).

- Under 4000 psi closure stress, the conductivity of ULW-1 and -2 is on the order of 1-10 md-ft in both partial monolayer and multilayer, while the conductivity of ULW-3 is over 10-100 times larger, which is comparable with sand conductivity.
- Conductivity distributions of different proppants predicted by fracture modeling show that, at the same volume injection concentration, ULW-1 covers the most areas with the smallest average conductivity; ULW-2 covers the second most areas with the second smallest average conductivity; ULW-3 covers the second least areas with the second largest average conductivity; sand covers the least areas with the largest average conductivity.
- For high permeability shale reservoirs (10 μD), high slickwater leakage limits the proppant travelling distance, leading to a similar propped length for all proppants.
- ULW-1,-2 and -3 have strong productivity advantages over sand in 0.1 μD reservoir. The optimum pumping volume concentration is 4% for ULW-1, is 4-6% for ULW-2, and is 10% for ULW-3. If reservoir permeability is increased by 10 times, only ULW-1 and ULW-2 shows better productivity than sand after 100 days and 1000 days, respectively. Further increasing the reservoir permeability to 10 μD, all ULWPs have comparable or worse productivity than sand.
- The productivity advantage of using ULW-1 and ULW-2 decreases with increasing reservoir permeability, while increases with increasing production

time, because lower critical conductivity is needed for lower permeability shales or longer production time.

- For shale reservoirs >1 μD, shorter treatment time is preferred for ULW-1 and ULW-2.
- ULW-1 generates the best ROFI among the three proppants, with a much larger ROFI than sand for both 1-year and 5-year productions; ULW-2 is the second best, with a 5-year ROFI better than sand; ULW-3 only outperforms sand at high injection concentration and low price.
- Both ULW-1 and ULW-2 have their optimum design (best ROFI) at a partial monolayer concentration scenario, with a proppant volume injection concentration of 0.04-0.06 v/v; the optimum injection volume concentration for ULW-3 is greater than 0.1 v/v.
- For 1 year production and 0.1 μD shale reservoirs, the acceptable maximum price is $10/lb for ULW-1, $6/lb for ULW-2, and $2.5/lb for ULW-3. The maximum price increases as production time increases.
- With increasing production time or decreasing proppant price, a larger injection concentration window of ULWPs can be applied for ULWP treatment design to generate better ROFI than sand.
- By adding ULWPs into sand, both the high conductivity zone at the bottom and low conductivity zone at the upper and deeper zones can be achieved, which benefits both short and long-term production.
- The simplified NPV study illustrates that the optimum injection concentration of mixing ULW-1 with 0.1 v/v sand is 0.02-0.03 v/v.

- Mixing ULW-1 with sand can be a better strategy under the conditions that initial cash flow is emphasized, the fracture length is relatively long, or the reservoir permeability is relatively high.
- In this chapter, experiments were conducted to determine the key properties of three ULWPs. And simulations were conducted to determine the efficiency of using ULWPs. Compared with the earlier work (Brannon and Starks II 2008, 2009), a wider range of proppant pumping concentrations and proppant prices were altered in the parametric study to figure out the optimum pumping concentration and acceptable price range for each ULWP. Besides, a pumping strategy of mixing ULWP with sand was proposed and evaluated for the different shale fracturing conditions. The study is limited to the planar bi-wing fracture scenario. Future work is recommended to evaluate the ULWP performance in complex primary-natural fracture networks.

Nomenclature

ΔD, proppant deformation, inch

F, load on single particle, lbf

k, proppant pack permeability, Darcy (cm^2)

ϕ, proppant pack porosity, no unit

C, Kozeny-Carman constant, no unit

S, particle surface area per unit volume of packed space, 1/cm

S_P, total wetted surface area per unit volume of particles, 1/cm

w_f, fracture width, inch

Y, log (conductivity, $k_f w_f$)

X, log (proppant areal concentration, lb/ft^2)

ROFI, return on fracturing investment, $

NPV, net present value, $

Subscripts

ULW-1, ultra-light weight proppant 1.08

ULW-2, ultra-light weight proppant 1.25

ULW-3, ultra-light weight proppant 1.75

sand, conventional sand

slw, slickwater

norm, normalized value by base case

References

Baihly, J., Altman, R., Malpani, R., and Luo, F. 2010. Shale Gas Production Decline Trend Comparison Over Time and Basins. Paper SPE 135555, presented at the SPE Annual Technical Conference and Exhibition, Florence, Italy, Sep. 19-22.

Biot, M.A. and Medlin, W.L. 1985. Theory of Sand Transport in Thin Fluids. Paper SPE 14468, presented at the SPE Annual Technical Conference and Exhibition, Las Vegas, Nevada, Sep. 22-25.

Brannon, H.D., Malone, M.R., Rickards, A.R., Wood, W.D., Randall Edgeman, J., and Bryant, J.L. 2004. Maximizing Fracture Conductivity with Proppant Partial Monolayers: Theoretical Curiosity or Highly Productive Reality? Paper SPE 90698, presented at the SPE Annual Technical Conference and Exhibition, Houston, Texas, USA, Sep. 26-29.

Brannon, H.D. and Starks II, T.R. 2008. The Impact of Effective Fracture Area and Conductivity on Fracture Deliverability and Stimulation Value. Paper SPE 116057, presented at the 2008 SPE Annual Technical Conference and Exhibition, Denver, Colorado, Sep. 21-24.

Brannon, H.D. and Starks II, T.R. 2009. Maximizing Return-On-Fracturing-Investment by Using Ultral-lightweight Proppants to Optimize Effective Fracture Area: Can Less Be More? Paper SPE 119385, presented at the SPE hydraulic fracturing technology conference, Woodlands, Texas, Jan. 19-21.

Bulova, M., Nosoca, K., Willberg, D., and Lassek, J. 2006. Benefits of the Novel Fiber-laden Low-viscosity Fluid Systems in Fracturing Low-permeability Tight Gas Formations. Paper SPE 102956, presented at the SPE Annual Technical Conference and Exhibition, San Antonio, Texas, Sep. 24-27.

Carman P.C. 1937. Fluid Flow Through a Granular Bed. Trans. Inst. Chem. Eng. 15: 150-6.

Coulter, G.R., Benton, E.G., and Thomson, C.L. 2004. Water Fracs and Sand Quantity: A Barnett Shale Example. Paper SPE 90891, presented at the SPE Annual Technical Conference and Exhibition, Houston, Texas, Sep. 26-29.

Darin, S.R. and Huitt, J.L. 1960. Effect of a Partial Monolayer of Propping Agent on Fracture Flow Capacity. Petroleum Transactions, AIME, 219: 31-37.

Economides, M.J. and Martin, T. 2007. Modern Fracturing, 1st Edition.

Fredd, C.N., McConnell, S.B., Boney, C.L., and England, K.W. 2000. Experimental Study of Hydraulic Fracture Conductivity Demonstrates the Benefits of Using Proppants. Paper SPE 60326, presented at the SPE Rocky Mountain Regional/Low-Permeability Reservoirs Symposium and Exhibition, Denver, Colorado, March 12-15.

Gadde, P.B. and Sharma, M.M. 2005. The Impact of Proppant Retardation on Propped Fracture Lengths. Paper SPE 97106, presented at the SPE Annual Technical Conference and Exhibition, Dallas, Texas, Otc. 9-12.

Gaurav, A. 2010. Ultra-Light Weight Proppants in Shale Gas Fracturing. Thesis of Master of Science in Engineering. University of Texas at Austin.

Gaurav, A., Dao, E.K. and Mohanty, K.K. 2010. Ultra-lightweight Proppants for Shale Gas Fracturing. Paper SPE 138319, presented at the tight gas completions conference, San Antonio, Texas, Nov. 2-3.

Gaurav, A., Gu, M. and Mohanty, K.K. 2012. Improvement of Fracturing for Gas Shales. RPSEA Final Report 07122-38, August.

Kendrick, D.E., Puskar, M.P., and Schlotterbeck, S.T. 2005. Ultralightweight Proppants: A Field Study in the Big Sandy Field of Eastern Kentucky. Paper SPE 98006, presented at the 2005 SPE Eastern Regional Meeting held in Morgantown, W.V., Sep. 14-16.

Mahoney, R.P., Soane, D., Kincaid, K.P., Herring, M., and Snider, P.M. 2013. Self-suspending Proppant. Paper SPE 163818, presented at the SPE hydraulic fracturing technology conference, Woodlands, Texas, Feb. 4-6.

Myers. R, Potratz, J., and Moody, M. 2004. Field Application of New Lightweight Proppant in Appalachian Tight Gas Sandstones. Paper SPE 91469, presented at the 2004 SPE Eastern Regional Meeting held in Charleston, West Virginia, USA, Sep. 15-17.

Posey, D. and Strickland, B. 2005. The Effect of Using a Lightweight Proppant in Treatment of a Low-Permeability, Dry Gas Reservoir: A Case Study. Paper SPE 97998, presented at the 2005 SPE Eastern Regional Meeting, Morgantown, West Virginia, Sep. 14-16.

Rickards, A.R., Brannon, H.D., Wood, W.D., and Stephenson, C.J. 2003. High Strength, Ultra-Lightweight Proppant Lends New Dimensions to Hydraulic Fracturing Applications. Paper SPE 84308, presented at the SPE Annual Technical Conference and Exhibition, Denver, Colorado, USA, Oct. 5-8.

Schein, G.W., Carr, P.D., Canan, P.A., and Richey, R. 2004. Ultra Lightweight Proppants: Their Use and Application in the Barnett Shale. Paper SPE 90838, presented at the SPE Annual Technical Conference and Exhibition, Houston, Texas, USA, Sep. 26-29.

Warpinski, N.R., Kramm, R.C. Heinze, J.R., and Waltman, C.K. 2005. Comparison of Single- and Dual- array Microseismic Mapping Techniques in the Barnett Shale. Paper SPE 95568, presented at the 2005 SPE Annual Technical Conference and Exhibition, Dallas, Texas, Oct. 9-12.

Wood, W.D., Brannon, H.D., Rickards, A.R., and Stephenson, C. 2003. Ultra-Lightweight Proppant Development Yields Exciting New Opportunities in Hydraulic Fracturing Design. Paper SPE 84309, presented at the SPE Annual Technical Conference and Exhibition, Denver, Colorado, USA, Oct. 5-8.

Table 4.1: Comparison of some typical light weight proppants.

	Material	Mesh Size	SG	Conductivity @ 4000 psi, 200F	Price
IBU Prop Lite[1] (IBU Tech.)	Coated Core Material	16/40	1.8	100 md-ft @ 1 lb/ft2	-
MonoProp[2] (Halliburton)	Thermoplastic alloy	-	1.08	5000-11000 md-ft @ 0.08-0.09 lb/ft2	-
SSP[3] (Marathon Oil)	Hydrogel Coated Sand	-	1.6	1500 @ 1 lb/ft2	-
LiteProp108 (Baker Hughes)	Polymer	14/40	1.08	15@ 1 lb/ft2	5.5 $/lb[4]
LiteProp125 (Baker Hughes)	RC Walnut	14/30	1.25	17@ 1 lb/ft2	-
LiteProp175 (Baker Hughes)	RC Ceramic	20/35	1.75	1000@ 1 lb/ft2	-

1. http://www.ibu-tec.de/fileadmin/editorial/drehrohr/datasheets/en/Datenblatt_IBUPropLite_ENG.pdf
2. http://www.halliburton.com/public/pe/contents/Data_Sheets/web/H/H06228.pdf
3. Brannon and Starks II, 2008
4. Mahoney et al. 2013

Table 4.2: Input of reservoir properties and completion parameters for parametric study of ULWP treatment.

Reservoir Properties				Completion Parameters	
Pr_{pore} (psi)	3300	E (psi)	2E6	L_{well} (ft)	5000
σ_{min} (psi)	4500	ν	0.25	Well Spc (ft)	3250
Temp (^oF)	130	P_L (psi)	468	Frac Spc (ft)	100, 200
φ	8%	V_L (scf/lb)	0.0425	H_{prop} (ft)	150
H_{pay}(ft)	150	ρ_{rock} (g/cc)	2.6	μ_{slw}(cp)	5.7
k_m (μD)	0.1-10	S_{wi}	20%	q_{inj} (m^3/s)	0.02
K_v/k_h	0.1	S_{gi}	80%		
C_{por} (1/psi)	6E-6	Methane	100%	BHP (psi)	500

Table 4.3: Cases for parametric study of ULWP treatment.

Case	k_m	Proppant Injection Volume Concentration				
Long Time Frac	20 min pad + 40 min slurry + 20 min shutin, 200ft Frac Spacing					
LTLKULW1_1-5	0.1 μD	0.02 v/v	0.04 v/v	0.06 v/v	0.08 v/v	0.1 v/v
LTLKULW2_1-5		0.02 v/v	0.04 v/v	0.06 v/v	0.08 v/v	0.1 v/v
LTLKULW3_1-5		0.02 v/v	0.04 v/v	0.06 v/v	0.08 v/v	0.1 v/v
LTMKULW1_1-5	1 μD	0.02 v/v	0.04 v/v	0.06 v/v	0.08 v/v	0.1 v/v
LTMKULW2_1-5		0.02 v/v	0.04 v/v	0.06 v/v	0.08 v/v	0.1 v/v
LTMKULW3_1-5		0.02 v/v	0.04 v/v	0.06 v/v	0.08 v/v	0.1 v/v
LTHKULW1_1-5	10 μD	0.02 v/v	0.04 v/v	0.06 v/v	0.08 v/v	0.1 v/v
LTHKULW2_1-5		0.02 v/v	0.04 v/v	0.06 v/v	0.08 v/v	0.1 v/v
LTHKULW3_1-5		0.02 v/v	0.04 v/v	0.06 v/v	0.08 v/v	0.1 v/v
Short Time Frac	10 min pad + 20 min slurry + 10 min shutin, 100ft Frac Spacing					
STLKULW1_1-5	0.1 μD	0.02 v/v	0.04 v/v	0.06 v/v	0.08 v/v	0.1 v/v
STLKULW2_1-5		0.02 v/v	0.04 v/v	0.06 v/v	0.08 v/v	0.1 v/v
STLKULW3_1-5		0.02 v/v	0.04 v/v	0.06 v/v	0.08 v/v	0.1 v/v
STMKULW1_1-5	1 μD	0.02 v/v	0.04 v/v	0.06 v/v	0.08 v/v	0.1 v/v
STMKULW2_1-5		0.02 v/v	0.04 v/v	0.06 v/v	0.08 v/v	0.1 v/v
STMKULW3_1-5		0.02 v/v	0.04 v/v	0.06 v/v	0.08 v/v	0.1 v/v
STHKULW1_1-5	10 μD	0.02 v/v	0.04 v/v	0.06 v/v	0.08 v/v	0.1 v/v
STHKULW2_1-5		0.02 v/v	0.04 v/v	0.06 v/v	0.08 v/v	0.1 v/v
STHKULW3_1-5		0.02 v/v	0.04 v/v	0.06 v/v	0.08 v/v	0.1 v/v

Table 4.4: Treatment volumes and costs for a single wing of a planar fracture.

	Fluid, m^3	Fluid Costs, $	Prop. Vol., m^3	Prop. Price, $/lb	Proppant Cost, $	Total Cost, $
ULW1	72	47,551	0.96	1-10	2286-22860	49837-70411
			1.92	1-10	4571-45710	52123-93261
			2.88	1-10	6857-68570	54408-116121
			3.84	1-10	9143-91430	56694-138981
			4.8	1-10	11429-114290	58980-161841
ULW2	72	47,551	0.96	0.86-8.6	2286-22860	49837-70411
			1.92	0.86-8.6	4571-45710	52123-93261
			2.88	0.86-8.6	6857-68570	54408-116121
			3.84	0.86-8.6	9143-91430	56694-138981
			4.8	0.86-8.6	11429-114290	58980-161841
ULW3	72	47,551	0.96	0.62-6.2	2286-22860	49837-70411
			1.92	0.62-6.2	4571-45710	52123-93261
			2.88	0.62-6.2	6857-68570	54408-116121
			3.84	0.62-6.2	9143-91430	56694-138981
			4.8	0.62-6.2	11429-114290	58980-161841
Sand	72	47,551	4.8	0.242	6786	54337

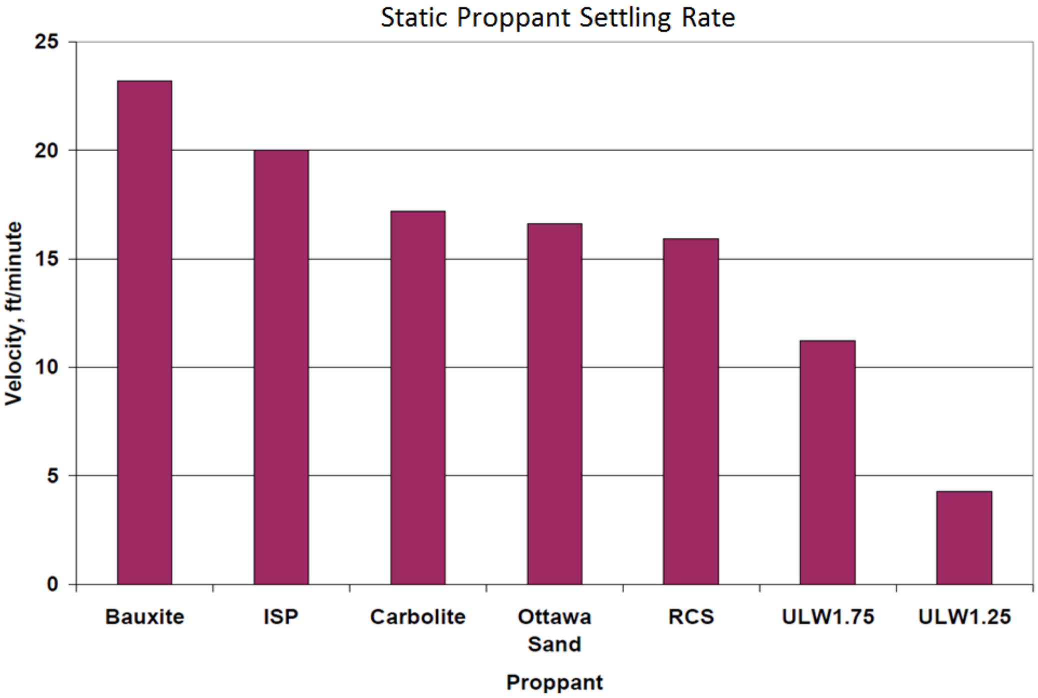

Figure 4.1: A comparison of static proppant settling rates in water (Rickards et al., 2003).

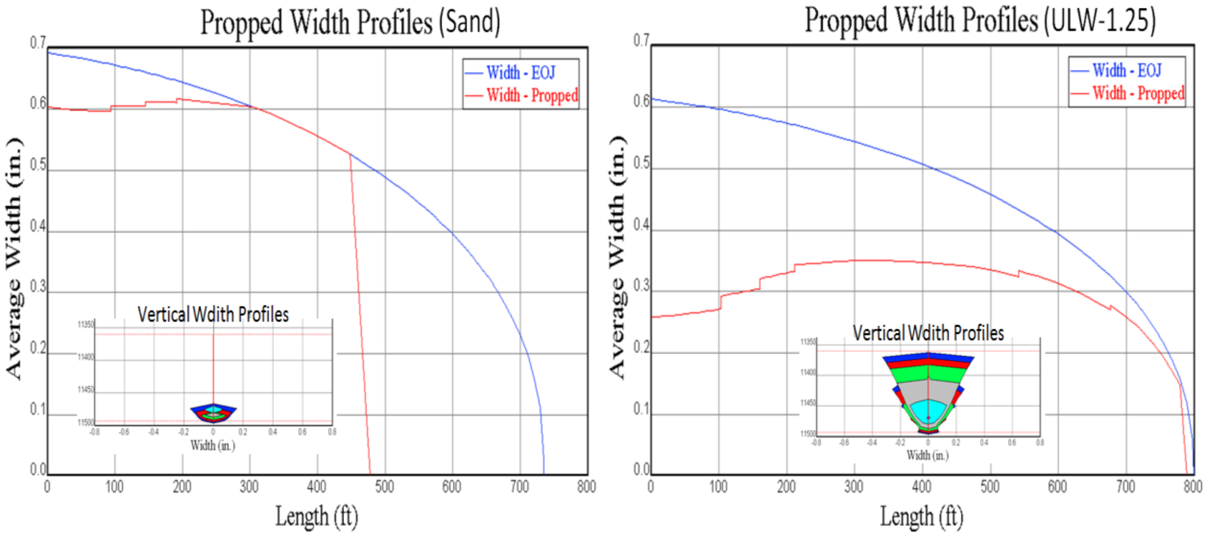

Figure 4.2: Mfrac graphs of the propped width profiles for Ottawa sand and ULW1.25 in a slickwater treatment at 80BPM (Rickards et al., 2003).

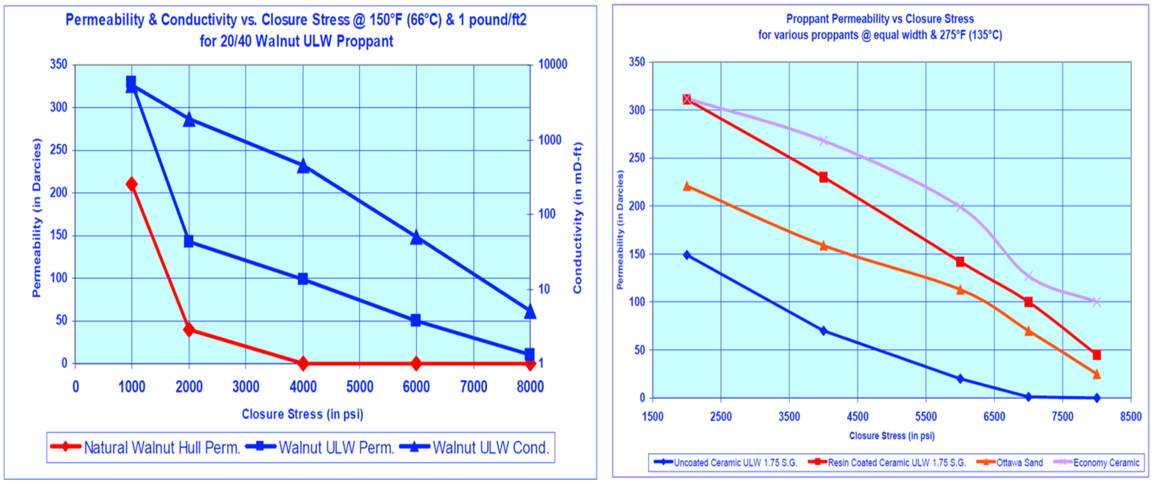

Figure 4.3: Permeability & Conductivity vs. Closure Stress @ 150 ^{o}F & 1 lb/ft^{2} for different resin coated and non-coated proppants (Wood et al., 2003).

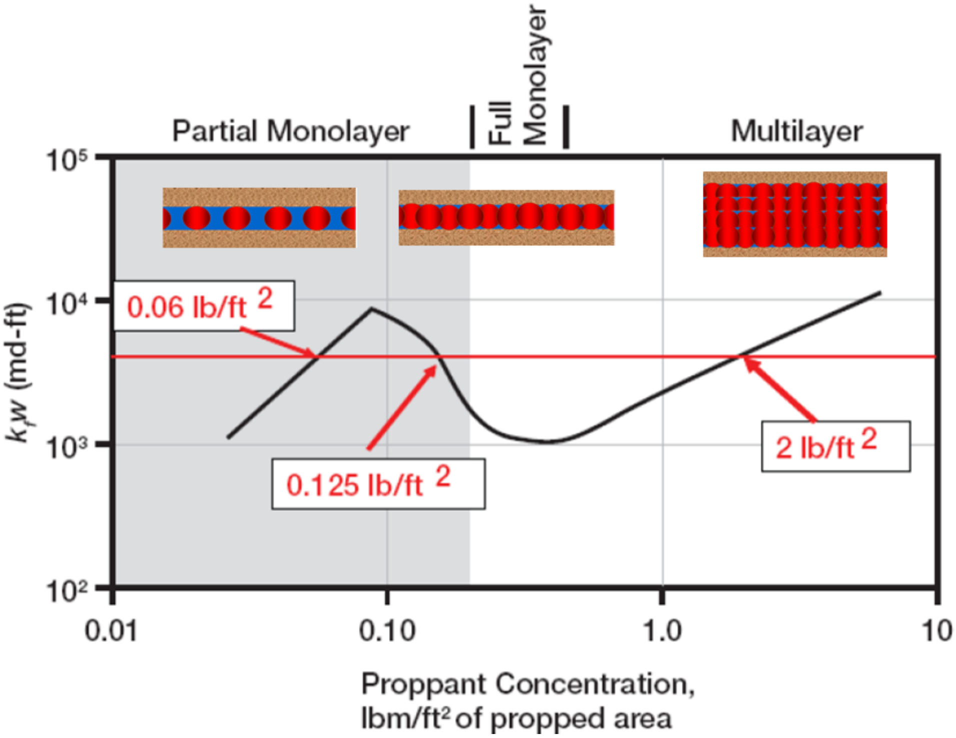

Figure 4.4: Fracture conductivity vs. 20/40 sand concentration at low temperature and closure stress (Darin and Huitt, 1960).

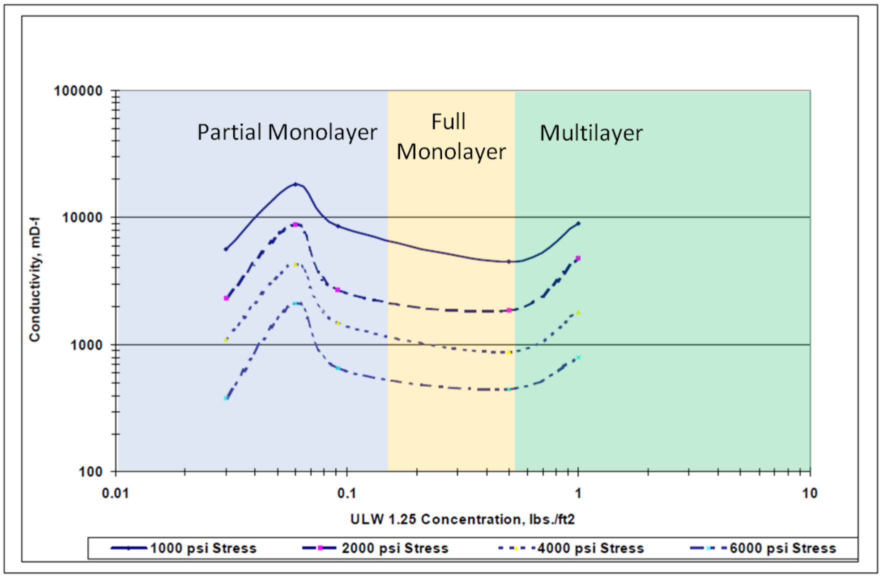

Figure 4.5: Conductivity of partial monolayer to multi-layers of 12/20 ULW-1.25 at various closure stresses and 100 ^{o}F (Brannon et al., 2004).

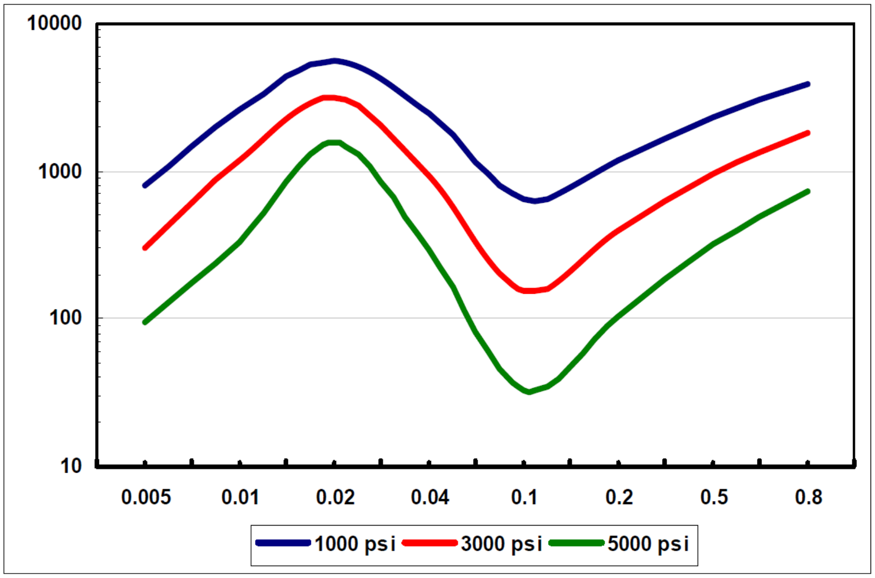

Figure 4.6: Conductivity vs. Proppant concentration for 14/40 ULW-1.05 at 150 ^{o}F, 1000-5000 psi closure stress (Brannon and Starks II, 2008).

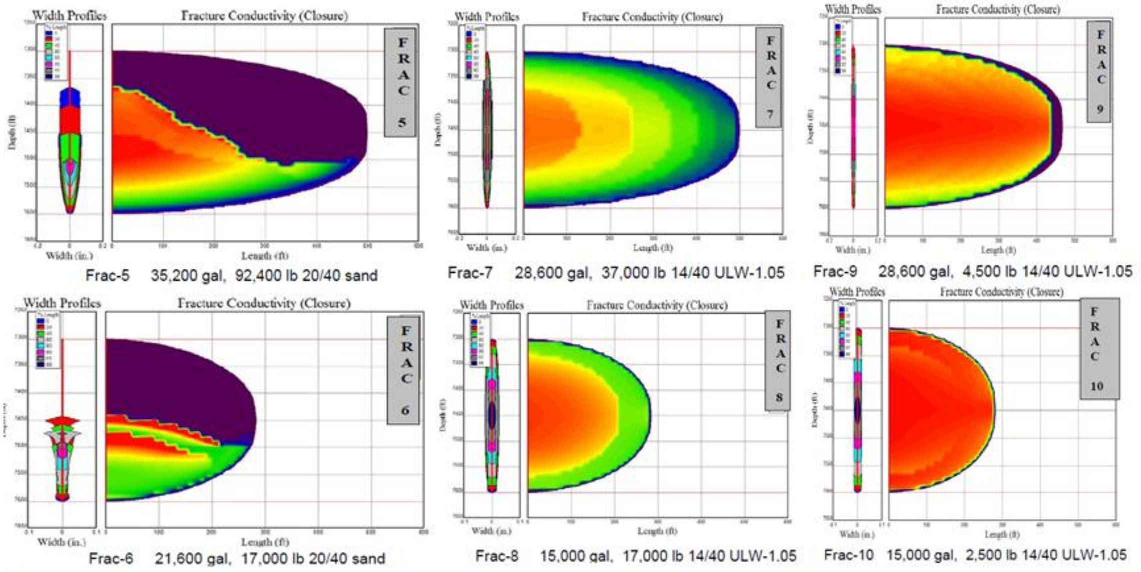

Frac-5 35,200 gal, 92,400 lb 20/40 sand

Frac-7 28,600 gal, 37,000 lb 14/40 ULW-1.05

Frac-9 28,600 gal, 4,500 lb 14/40 ULW-1.05

Frac-6 21,600 gal, 17,000 lb 20/40 sand

Frac-8 15,000 gal, 17,000 lb 14/40 ULW-1.05

Frac-10 15,000 gal, 2,500 lb 14/40 ULW-1.05

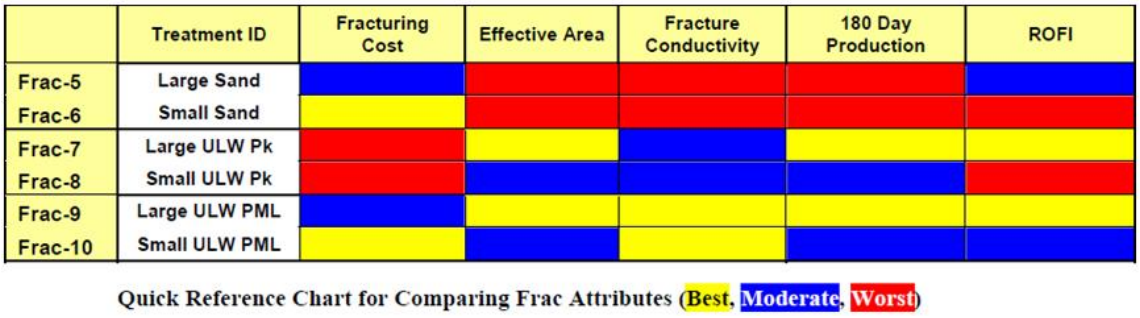

	Treatment ID	Fracturing Cost	Effective Area	Fracture Conductivity	180 Day Production	ROFI
Frac-5	Large Sand	🟦	🟥	🟥	🟥	🟦
Frac-6	Small Sand	🟨	🟥	🟥	🟥	🟥
Frac-7	Large ULW Pk	🟥	🟨	🟦	🟨	🟨
Frac-8	Small ULW Pk	🟥	🟦	🟦	🟦	🟥
Frac-9	Large ULW PML	🟦	🟨	🟨	🟨	🟨
Frac-10	Small ULW PML	🟨	🟦	🟨	🟦	🟦

Quick Reference Chart for Comparing Frac Attributes (🟨 Best, 🟦 Moderate, 🟥 Worst)

Figure 4.7: Comparison of different treatments of using sand and ULW-1.05 through fracture modeling (Brannon and Starks II, 2008).

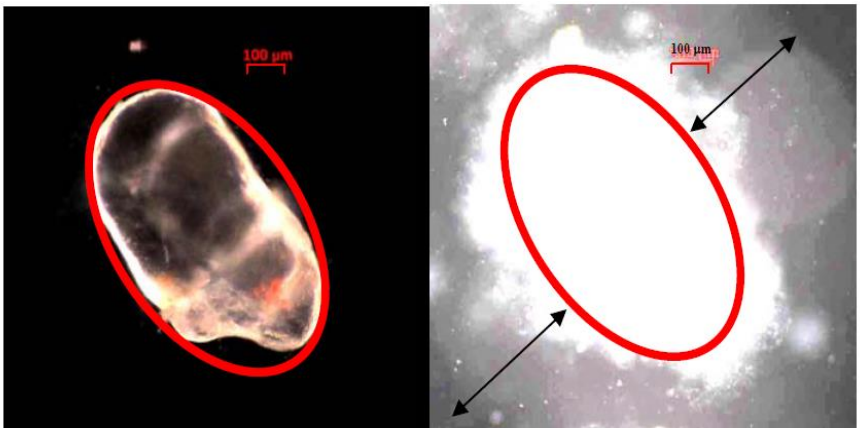

Figure 4.8: Light microscope images of 40/70 SSP grain at low and high brightness (Mahoney et al., 2013).

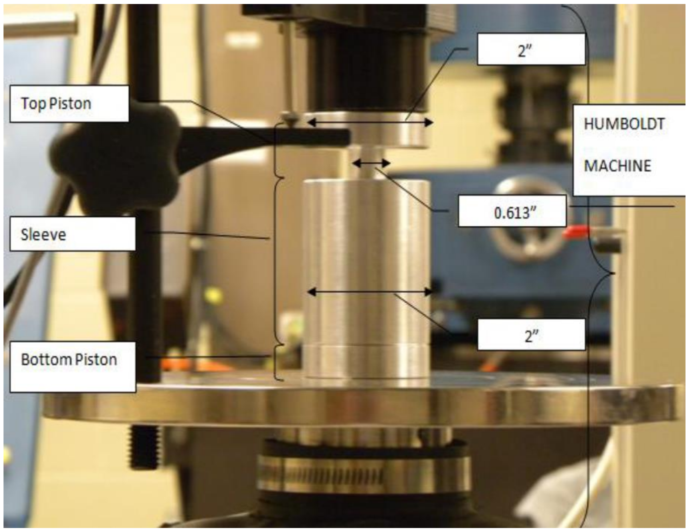

Figure 4.9: Equipment for proppant strength test.

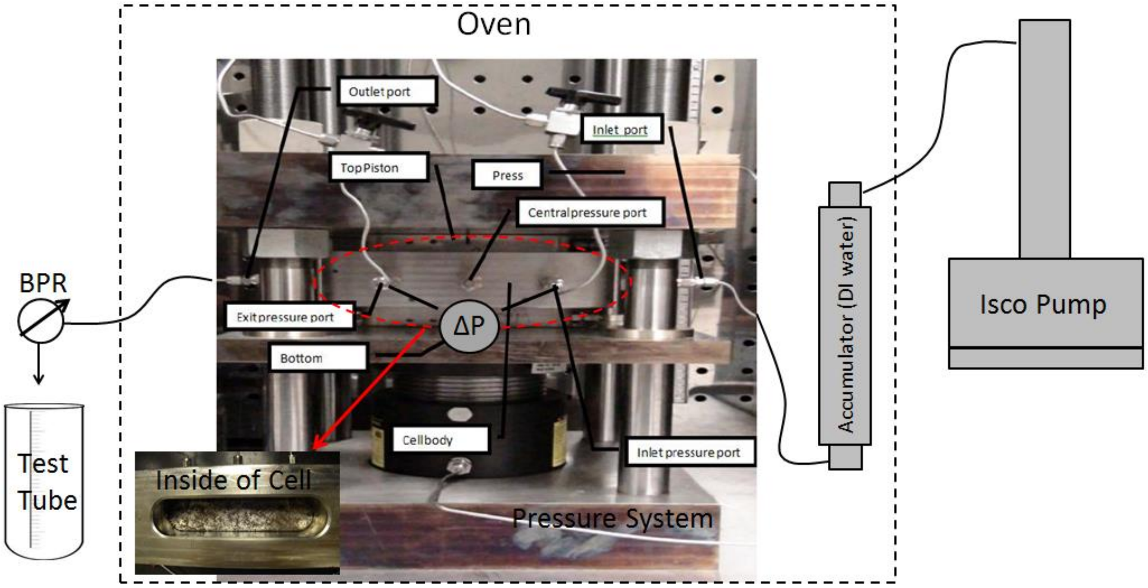

Figure 4.10: System for proppant API conductivity test.

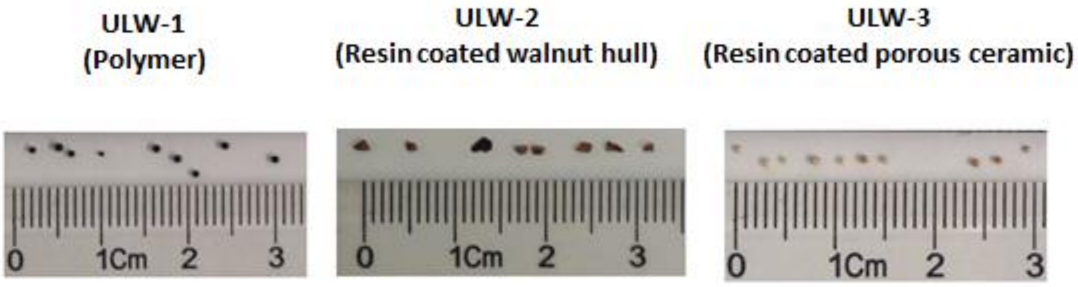

Dimension Comparison of three ULWPs

Close-up images of three ULWPs

Figure 4.11: Dimensions of three ULWPs and their close-up images.

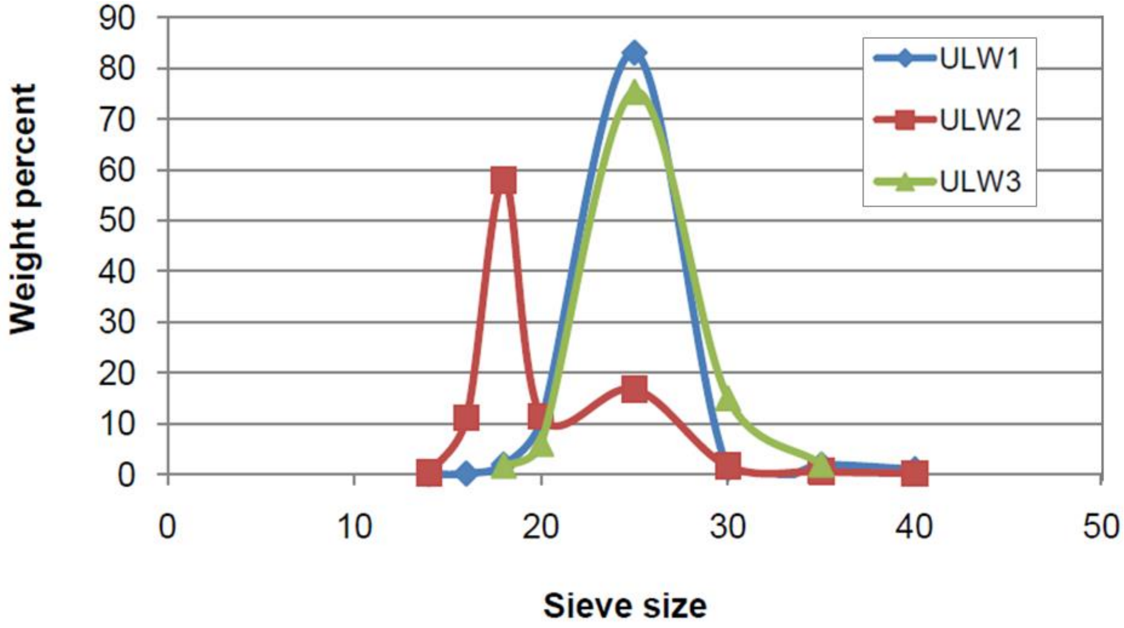

Figure 4.12: Sieve size distributions of the three ULWPs.

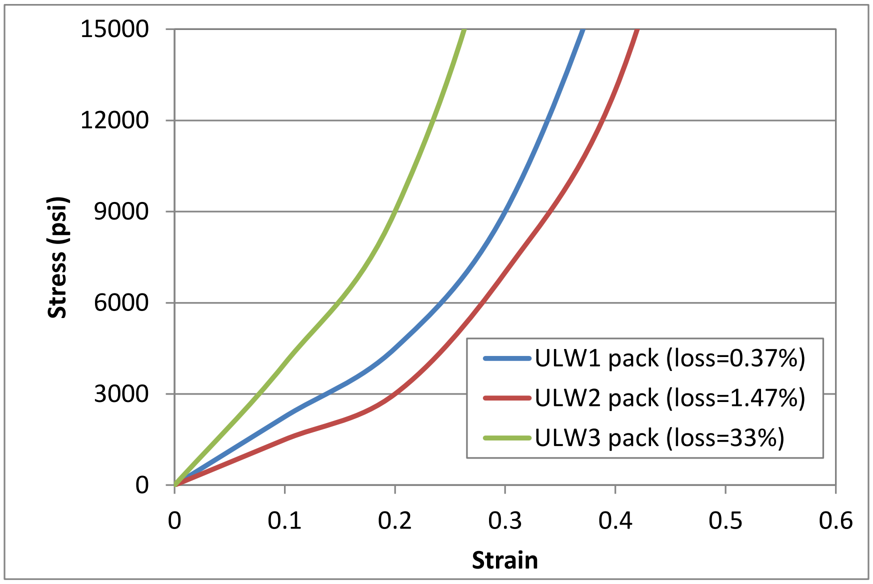

Figure 4.13: Stress vs. Strain for proppant packs of three ULWPs at 203 °F.

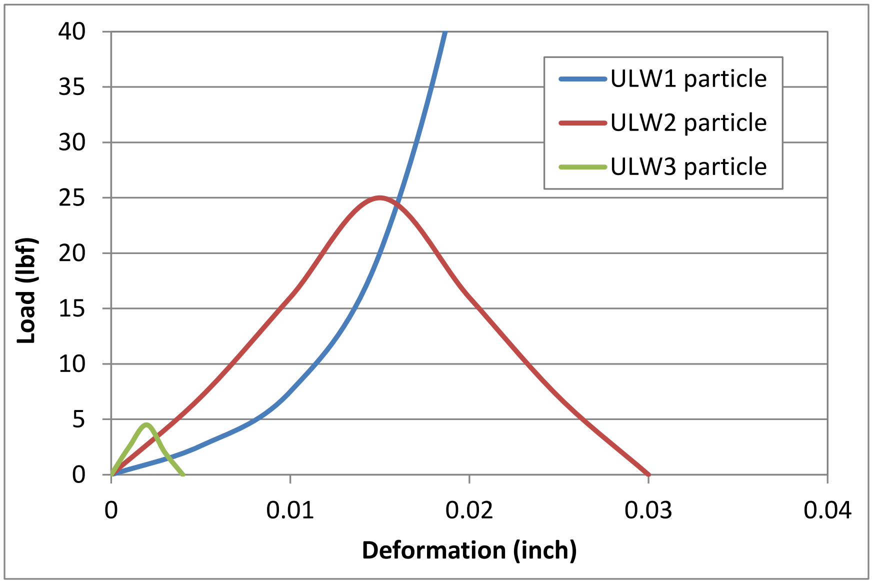

Figure 4.14: Strength test for single particle of three ULWPs at 203 °F.

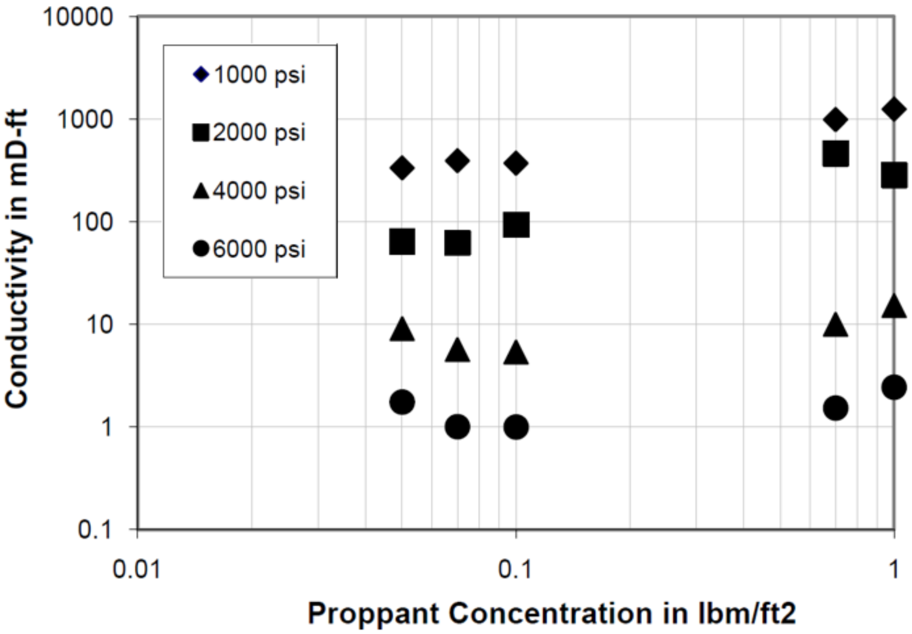

Figure 4.15: Conductivity vs. Areal Concentration for ULW-1 at 203 °F, 1000-6000 psi.

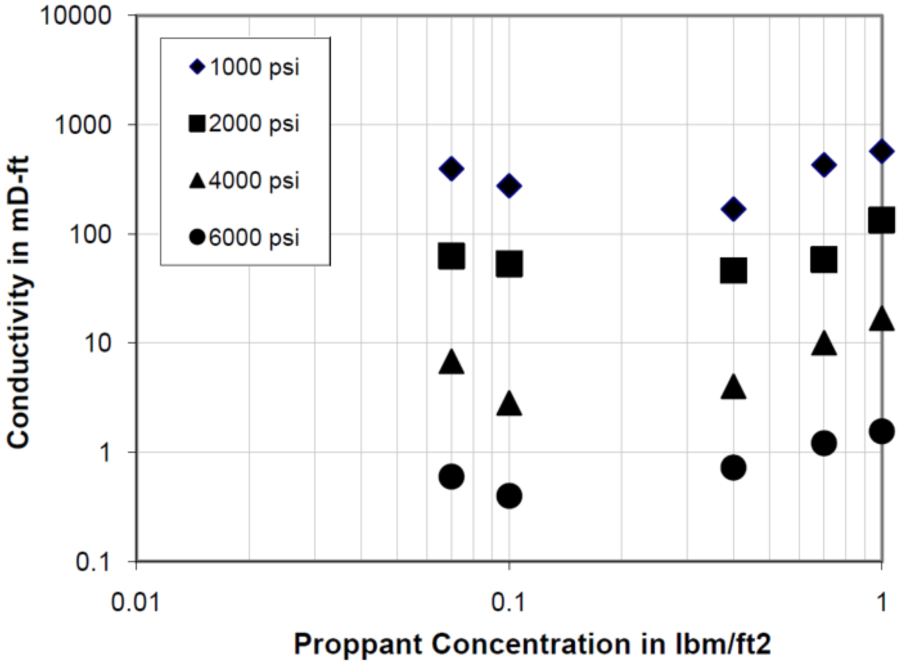

Figure 4.16: Conductivity vs. Areal Concentration for ULW-2 at 203 °F, 1000-6000 psi.

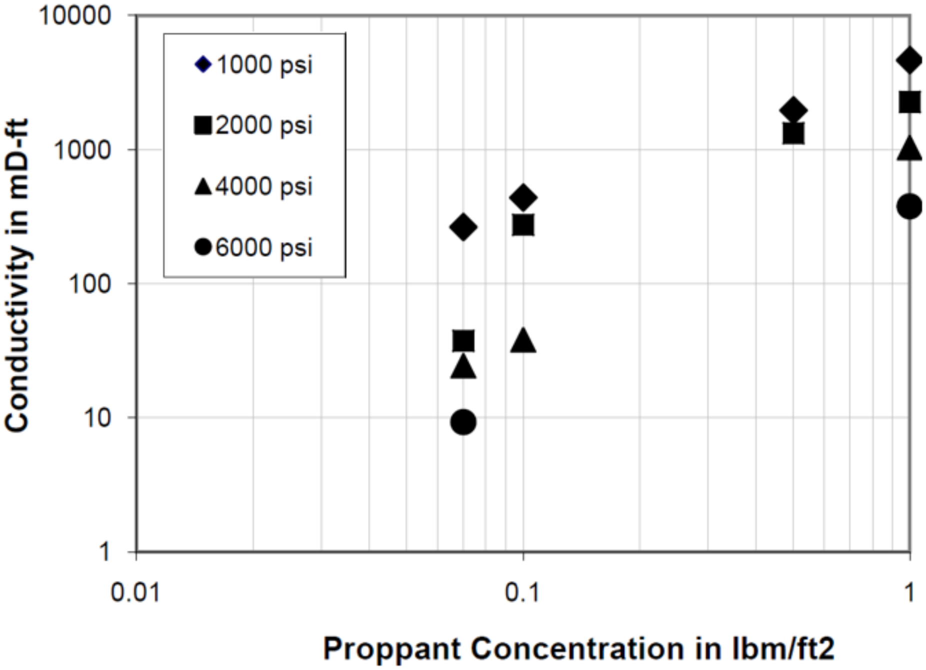

Figure 4.17: Conductivity vs. Areal Concentration for ULW-3 at 203 ^{o}F, 1000-6000 psi.

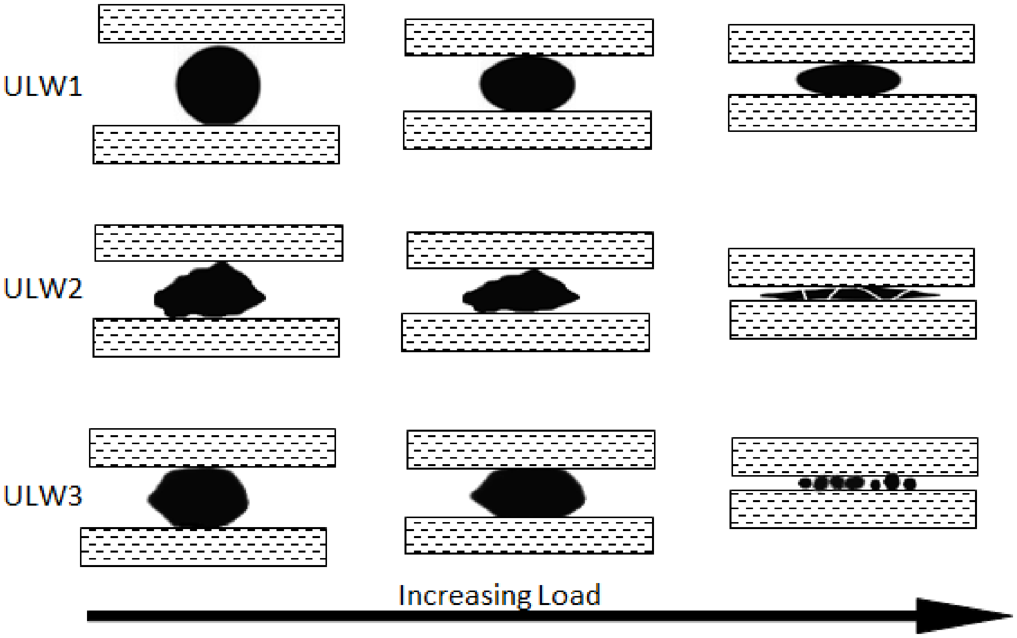

Figure 4.18: The schematic figure of the proppant deformation at increasing load for three ULWPs.

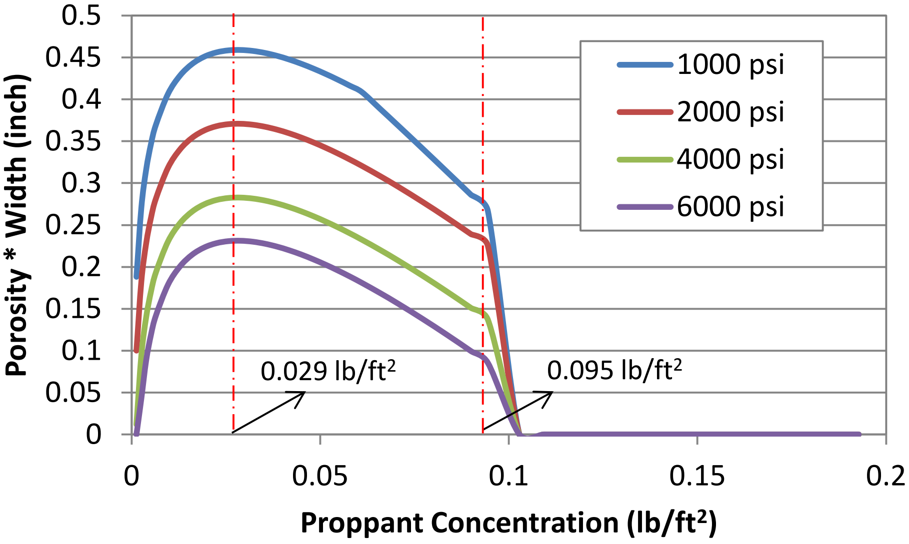

Figure 4.19: Fracture Flow Capacity vs. Areal Concentration for ULW-1 at partial monolayer concentration.

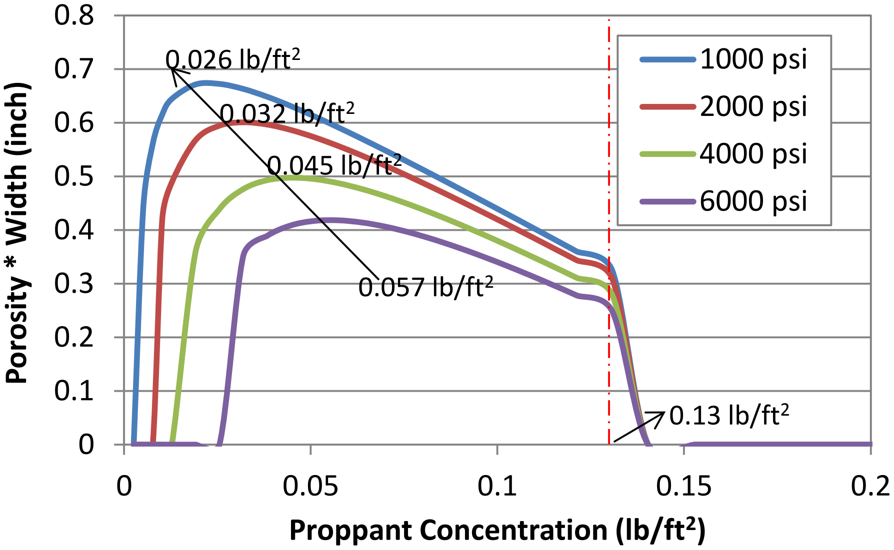

Figure 4.20: Fracture Flow Capacity vs. Areal Concentration for ULW-2 at partial monolayer concentration.

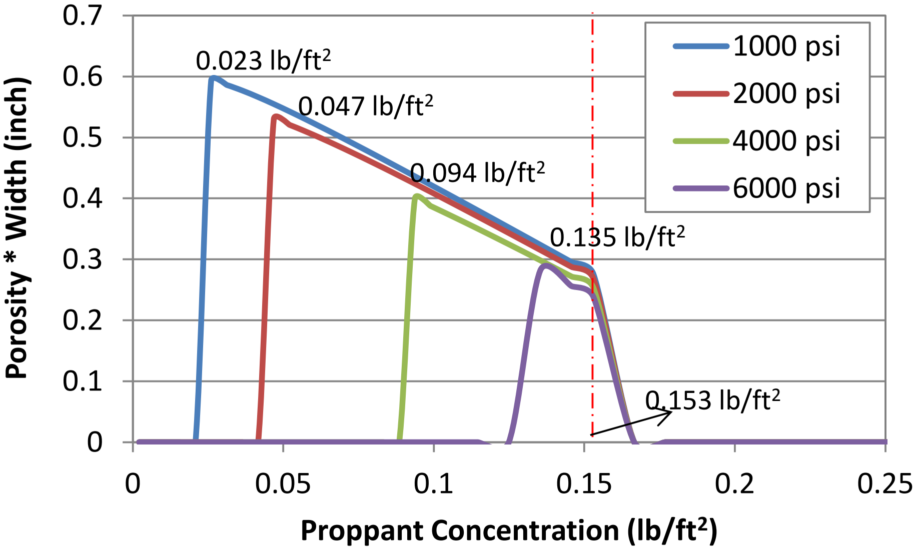

Figure 4.21: Fracture Flow Capacity vs. Areal concentration for ULW-3 at partial monolayer concentration.

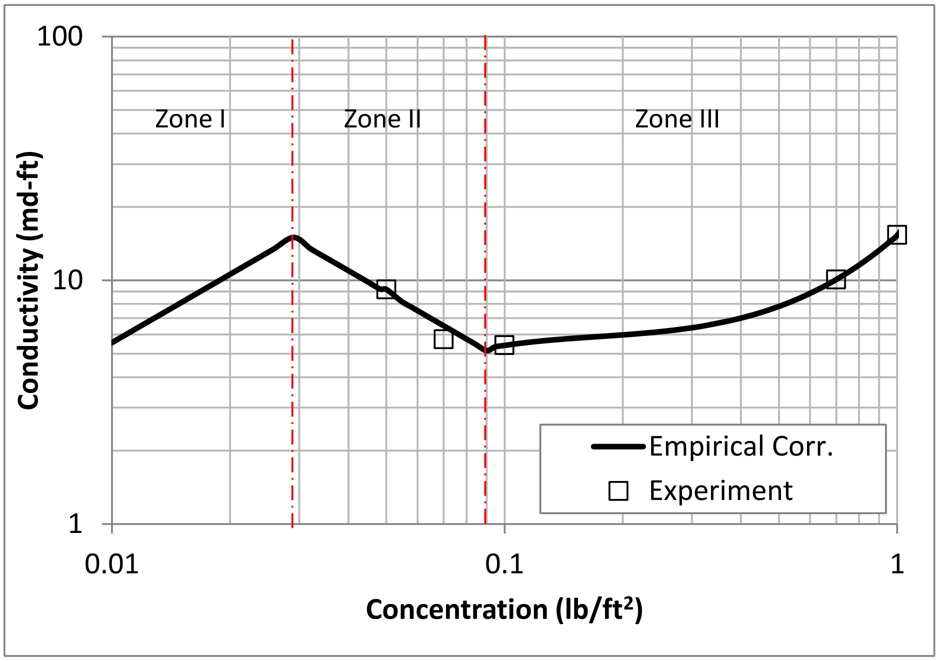

Figure 4.22: Conductivity predicted by empirical correlations and experimental results for ULW-1 at 203°F and 4000 psi.

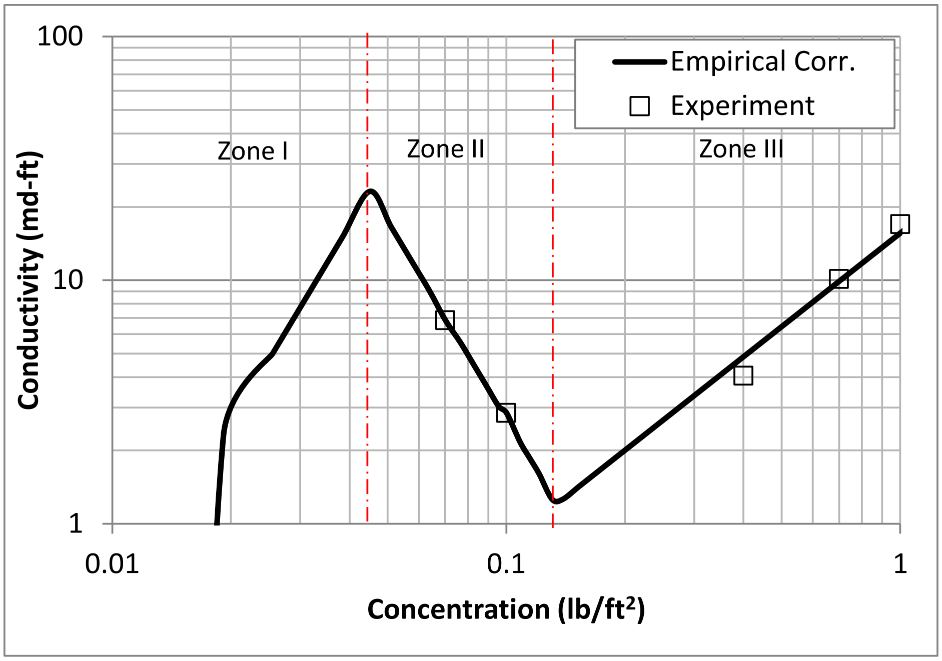

Figure 4.23: Conductivity predicted by empirical correlations and experimental results for ULW-2 at 203°F and 4000 psi.

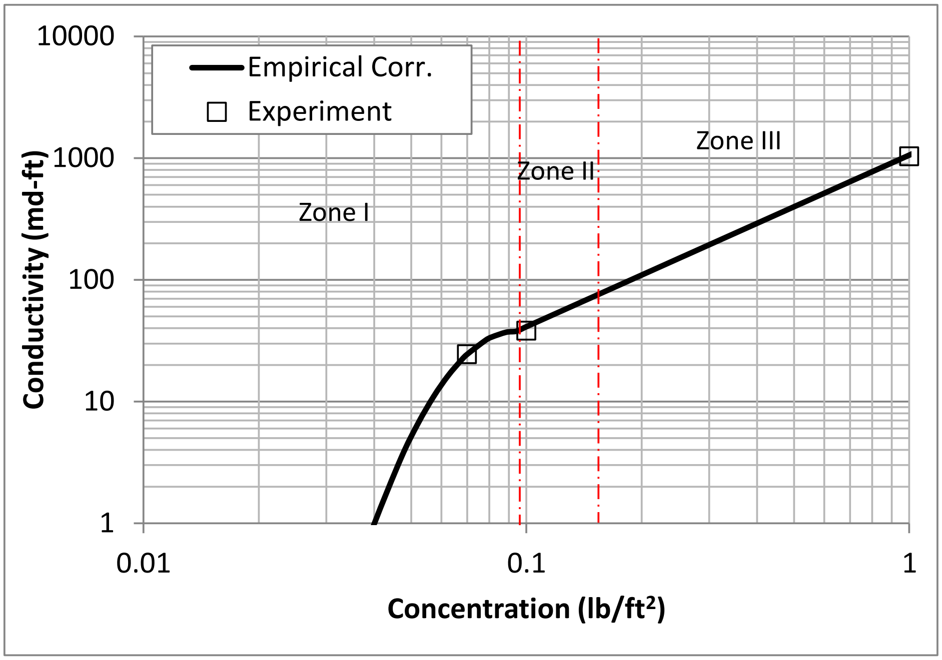

Figure 4.24: Conductivity predicted by empirical correlations and experimental results for ULW-3 at 203°F and 4000 psi.

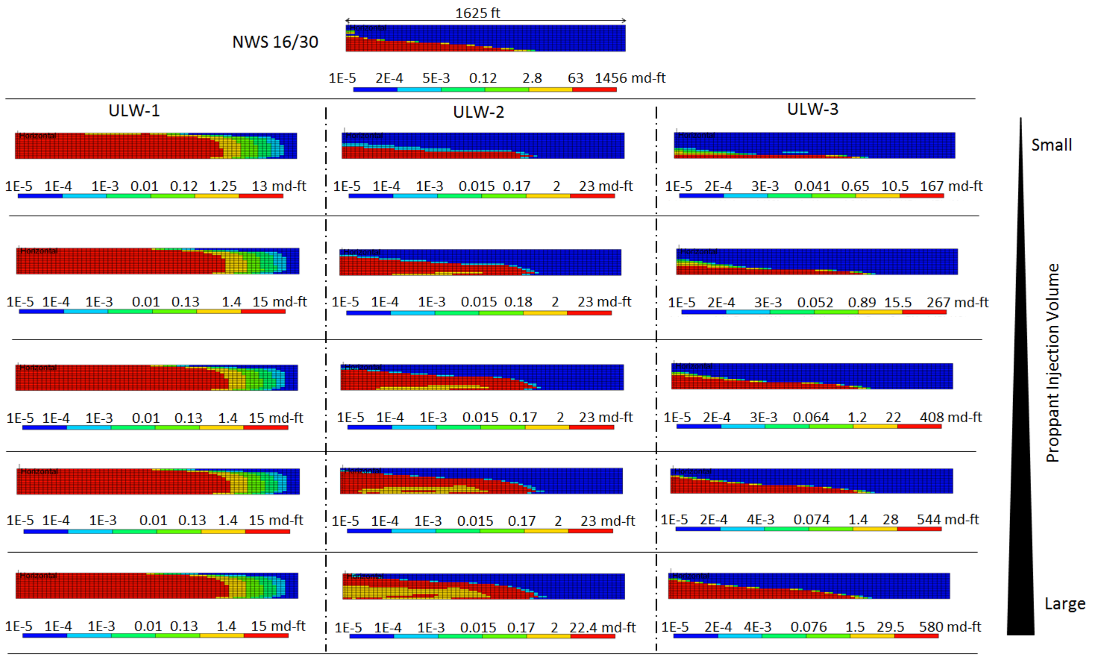

Figure 4.25: Conductivity distributions for different proppants in a long-time treatment and 0.1 µD shale.

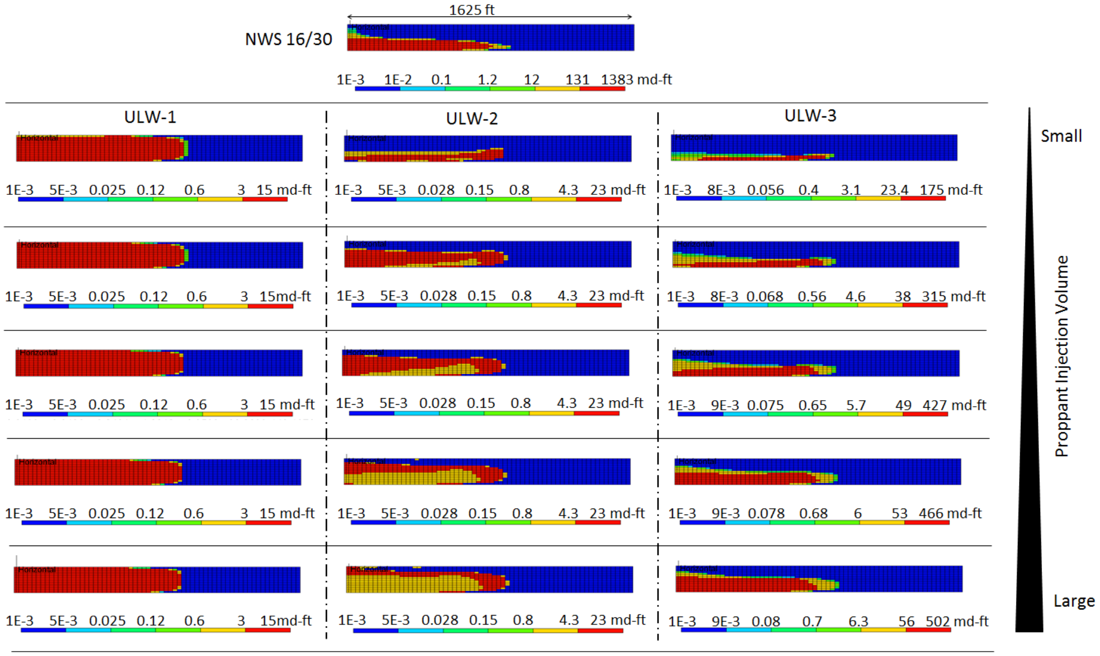

Figure 4.26: Conductivity distributions for different proppants in a long-time treatment and 10 µD shale.

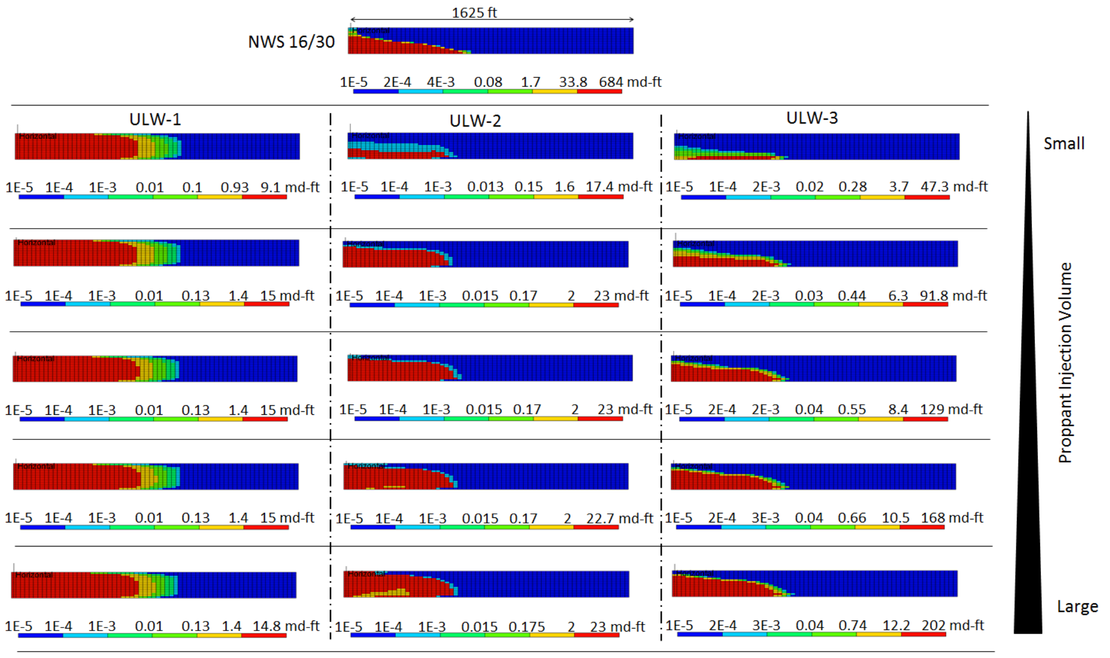

Figure 4.27: Conductivity distributions for different proppants in a short-time treatment and 0.1 μD shale.

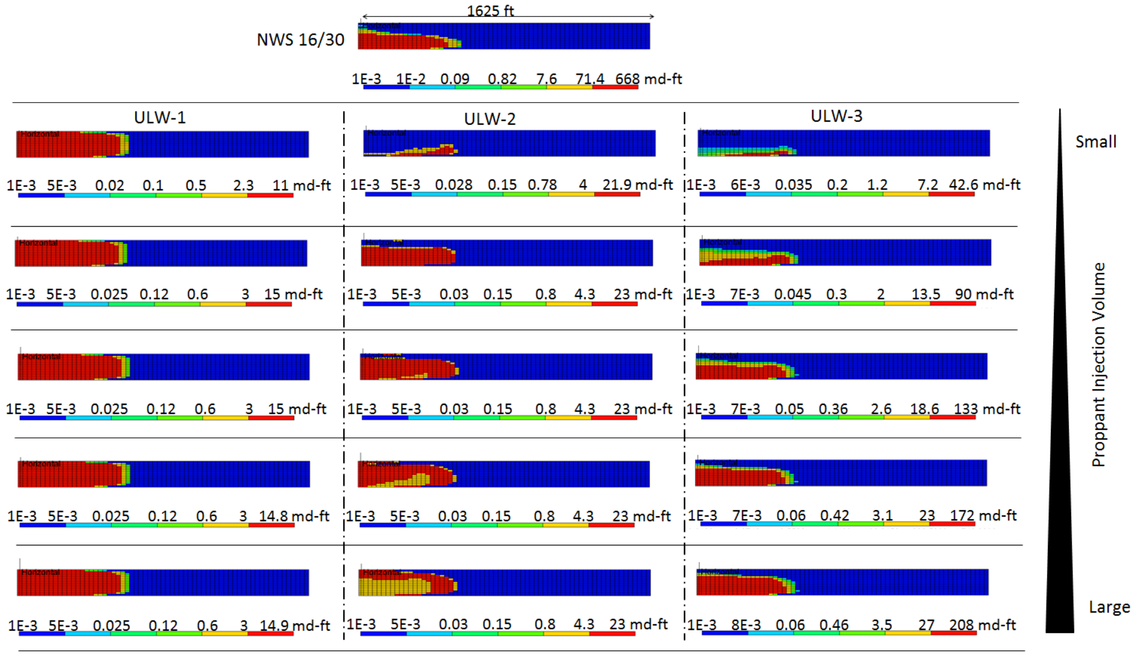

Figure 4.28: Conductivity distributions for different proppants in a short-time treatment and 10 μD shale.

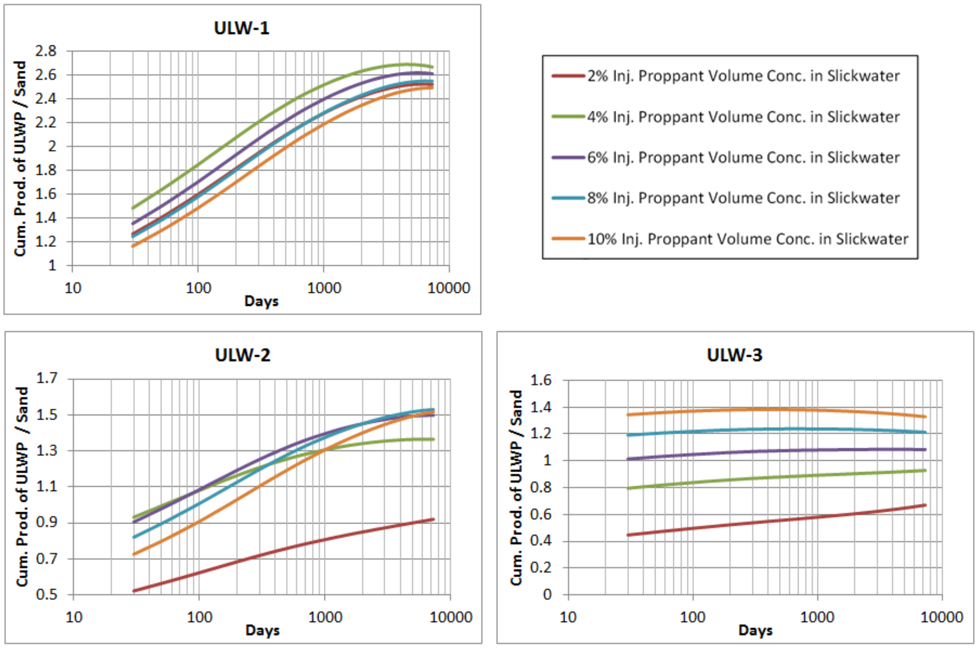

Figure 4.29: Normalized Productivity vs. Production Time for different proppants, long time treatment and 0.1 μD shale.

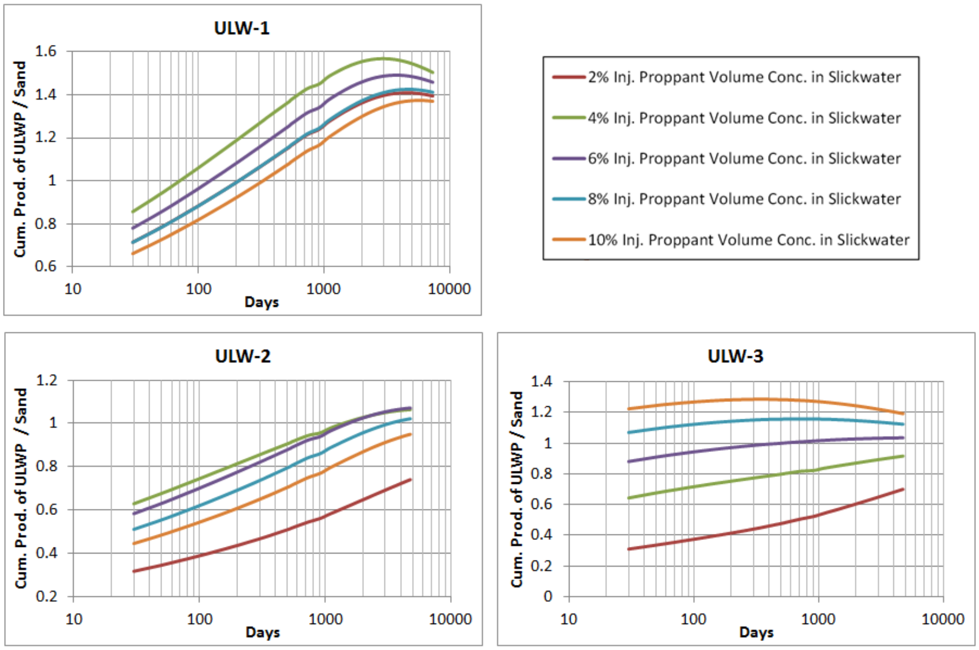

Figure 4.30: Normalized Productivity vs. Production Time for different proppants, long time treatment and 1 μD shale.

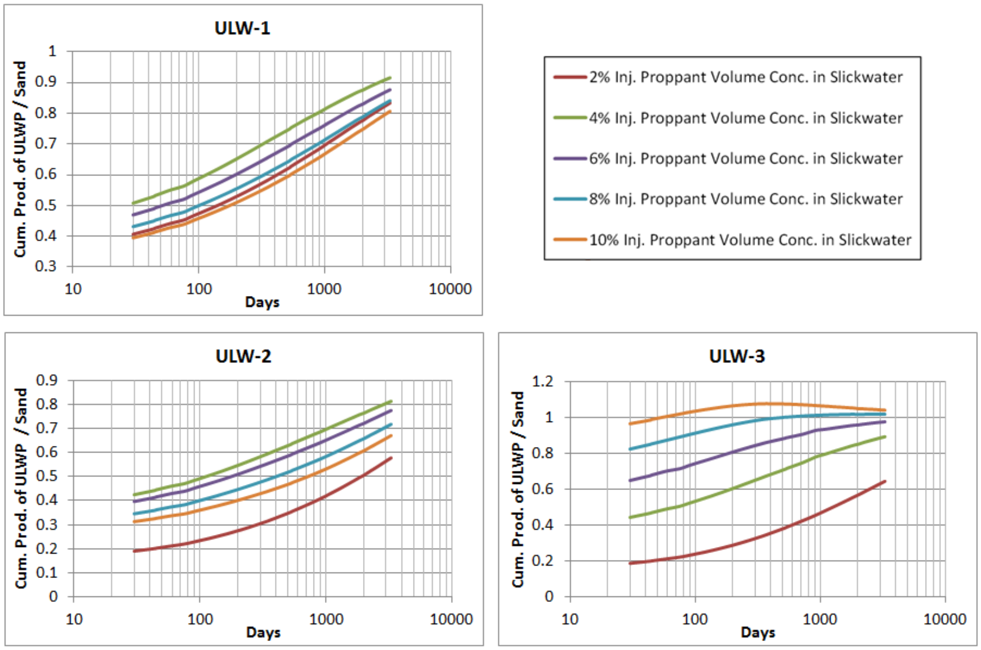

Figure 4.31: Normalized Productivity vs. Production Time for different proppants, long time treatment and 10 μD shale.

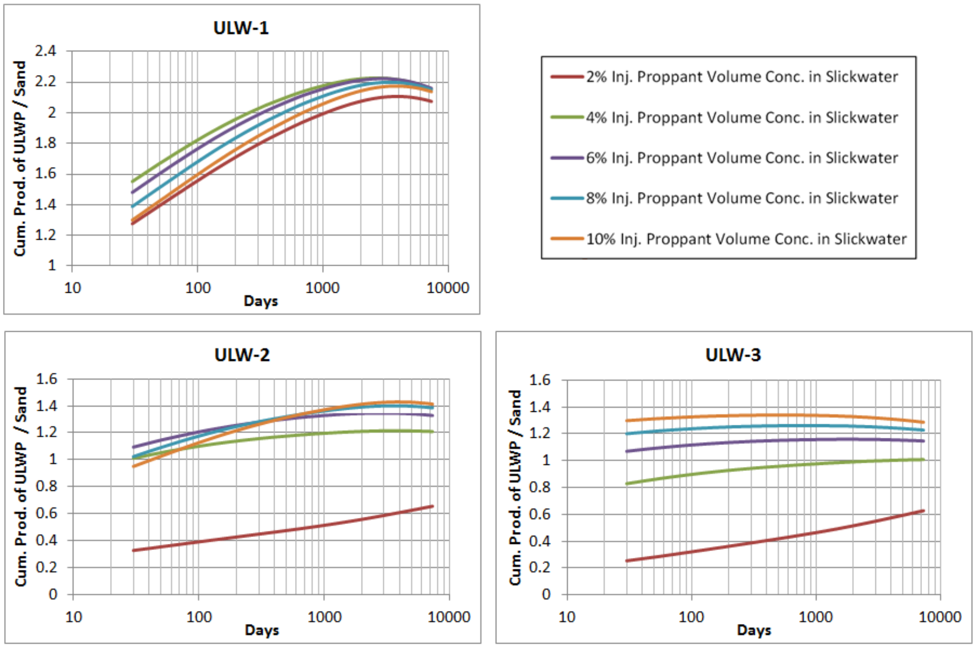

Figure 4.32: Normalized Productivity vs. Production Time for different proppants, short time treatment and 0.1 μD shale.

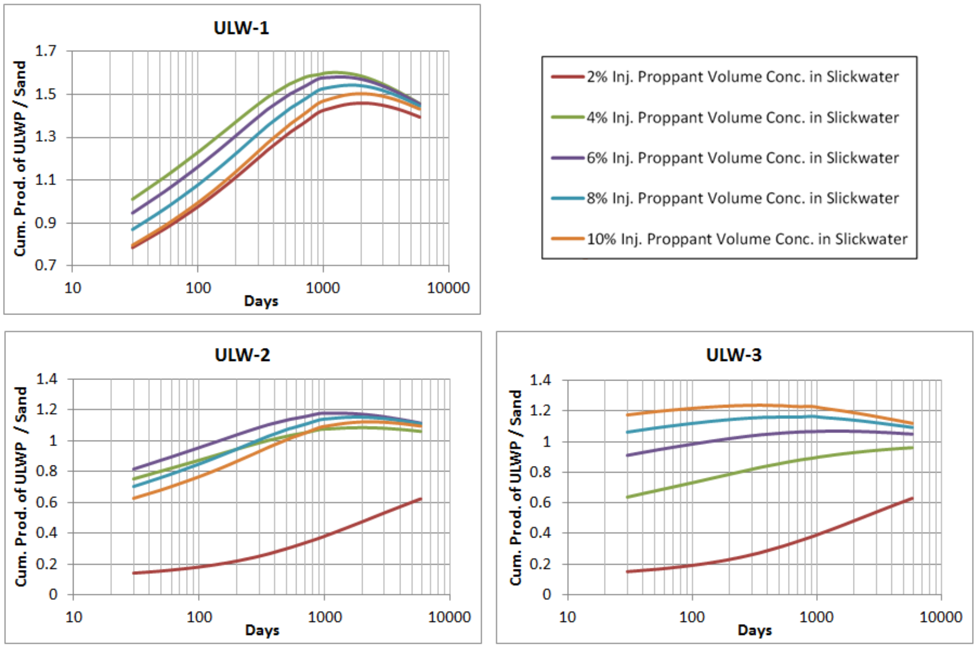

Figure 4.33: Normalized Productivity vs. Production Time for different proppants, short time treatment and 1 μD shale.

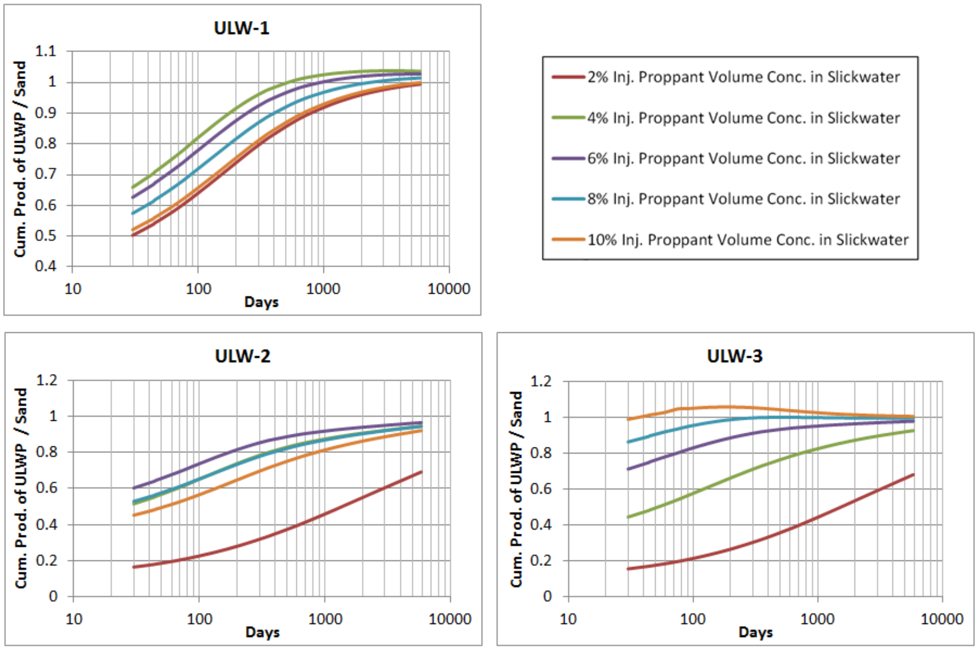

Figure 4.34: Normalized Productivity vs. Production Time for different proppants, short time treatment and 10 μD shale.

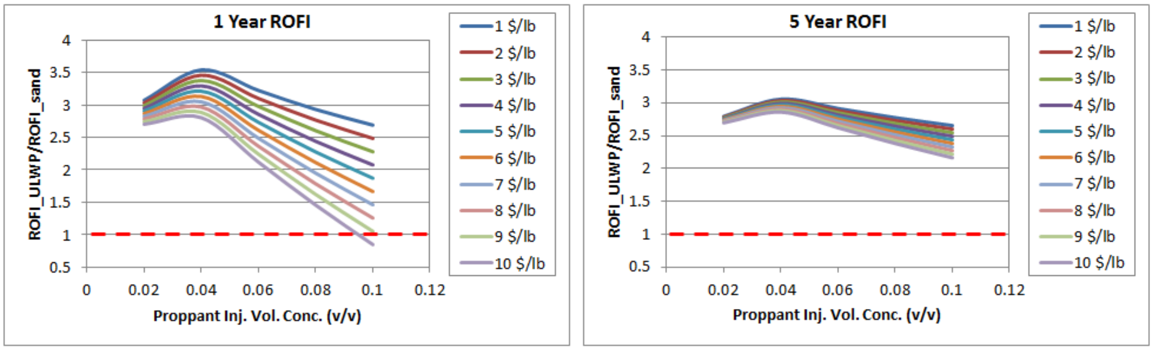

Figure 4.35: Normalized ROFI versus Proppant Injection Volume Concentration for ULW-1.

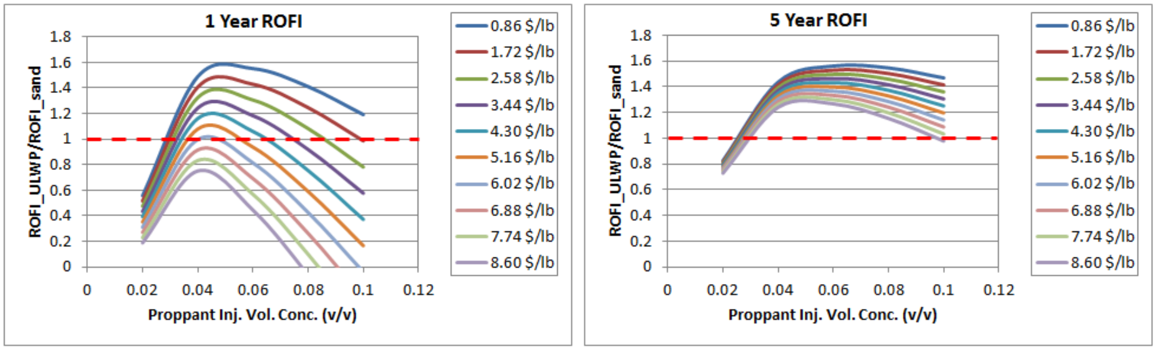

Figure 4.36: Normalized ROFI versus Proppant Injection Volume Concentration for ULW-2.

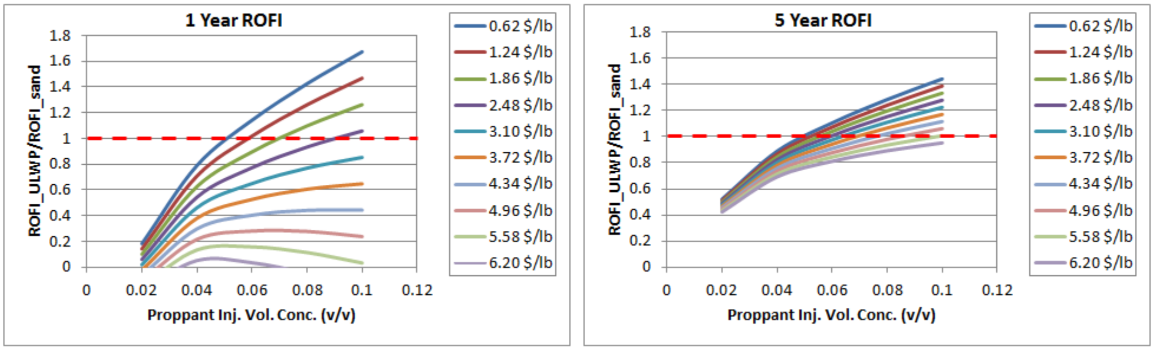

Figure 4.37: Normalized ROFI versus Proppant Injection Volume Concentration for ULW-3.

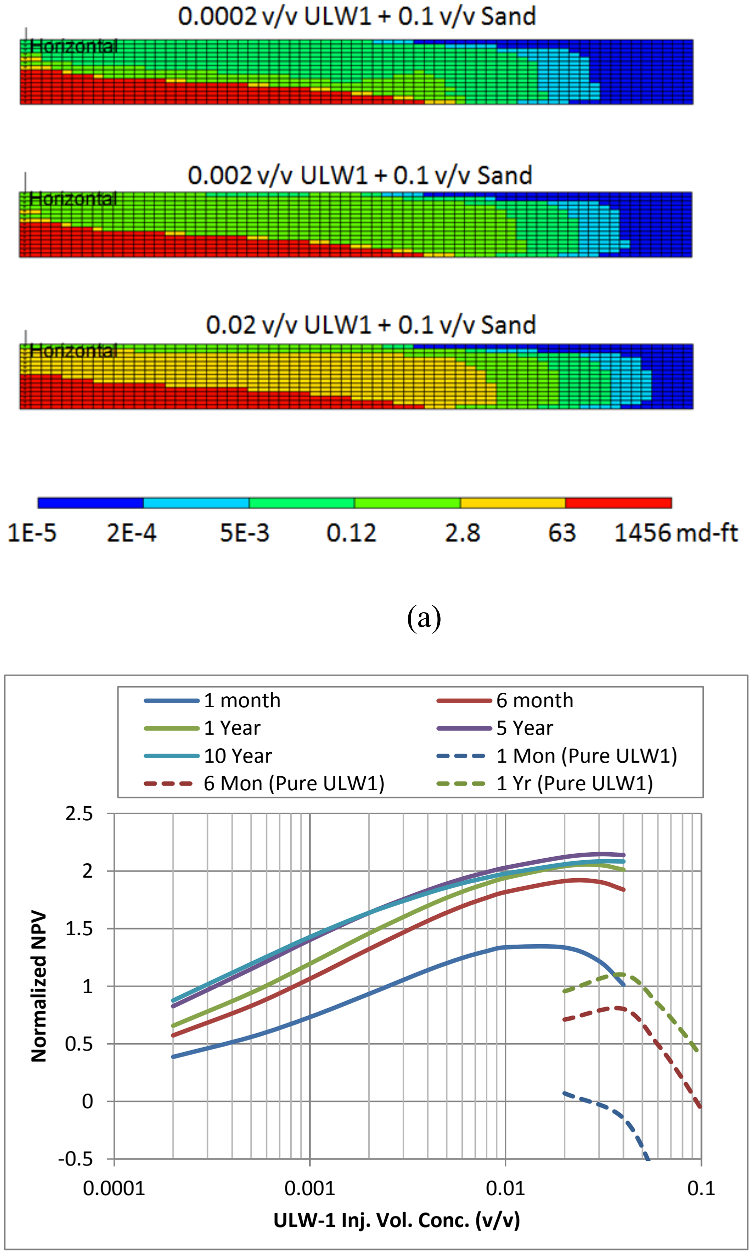

(a)

(b)

Figure 4.38: Normalized NPV (NPV/Prod. of Base Sand Case) generated from adding ULW1 at different volume concentrations in a sand treatment.

Chapter 5: Stability and Rheology Study of Polymer-Free Foam Fracturing Fluids

The previous chapter discusses the impact of ULWPs on conventional slickwater-sand hydraulic fracturing treatment in different shale reservoirs. This chapter and the next chapter will investigate another possible way of improving slickwater fracturing, which is using foams to facilitate sand transport, to cut down water consumption / disposal, and to increase fracture length/width with a better leak-off control. In this chapter, different kinds of polymer-free foams are developed, and their stability and rheology are investigated experimentally. Based on the experimental results, new correlations are developed to describe the aqueous foam rheology as a function of shear rate, quality, and pressure at the parameter range typical of hydraulic fracturing. The correlations will be incorporated in a fracture propagation simulator to evaluate the foam fracturing efficiency in the next chapter.

5.1 INTRODUCTION

5.1.1 Background and Motivation

The current fracturing treatment in shale gas reservoirs would pump large volumes of slickwater (water with a small amount of a drag-reducing polymer) along with well sorted, high mesh size (e.g. 30/50) sand at a high pumping rate. The reason slickwater fracturing fluids gain their popularity is that they are more effective in creating large, complex fracture networks at low costs. However, if conventional proppants, such as sand, are used in slickwater, they tend to settle down very quickly to the bottom of the fracture after travelling a small distance away from the wellbore, leaving lots of upper and deeper created surfaces closed and lost to production after surface pressure relieved (Brannon and Starks II., 2009; Cipolla et al., 2010; Warpinski et al., 2009).

The proppants can be placed farther away from the wellbore in a fracture if a more viscous fracturing fluid is used; There are usually two ways to increase the water viscosity. One way is to add polymers such as guar and guar derivatives (Gidley et al., 1989). However, in unconventional shale reservoirs, large polymer molecules can plug the small pores of the fracture surface and decrease the gas flow (Peles et al., 2002). The second way is to use foam-based fracturing fluids (Gidley et al., 1989). The cellular structure of foams can provide a high effective viscosity without forming polymer filter cake and plugging up the shale pores if polymers are avoided. Foams are usually generated from a base fluid made from a surfactant, a polymer stabilizer such as guar, HPG, or Xanthan gums, and other additives. Foams made from a surfactant foamer without polymers are known as polymer-free (or gel-free) aqueous foams. Foam stability and foam rheology the two most important properties for fracture-treatment design. Many experimental studies have been done for evaluating these two properties.

5.1.2 Review of Foam Stability Study

Foam structure is best preserved by using appropriate surfactants and external-phase viscosifiers. Addition of stabilizers can increase foam stability. Common stabilizers include the basic guar, HPG, and xanthan gums. By crosslinking polymers, foam stability can be further improved. Foam is destabilized through three pathways including drainage (Sarma et al., 1988), bubble coalescence (Kovscek and Radke, 1994), and disproportionation (gas diffusion from smaller bubbles to bigger ones) (Clark and Blackman, 1948, Lemlich, 1978). The first two mechanisms are usually dominant in causing foam destruction during a hydraulic-fracturing operation. Drainage is caused by gravity and capillary force, which could be reduced by increasing the foam quality and viscosifying the external phase (Sarma et al., 1988). Bubble coalescence is caused by lamella thinning and perturbation in liquid firms. Surfactant types and concentrations have a big impact on foam-coalescence rate (Rosen, 1989, Schramm, 1994).

A standard qualitative test for foam stability is the foam half-life test, which measures the time for a static foam column to collapse to half of its original height. Although it is a static, lab-scale test, it is simple and easy to conduct for evaluating the stability improvement effects of various viscosifiers and surfactants. Besides, it also helps to determine the proper chemical concentrations. Foam stability can also be measured dynamically. It is noted that high pressure and shear rate energy promote the stability of foams, while high temperature destabilizes the surfactants and accelerates the degradation of polymers to destabilize foams. These facts lead to a big difference between the dynamic stability and the static stability. Hutchins and Miller (2005) built a foam loop to mimic the shear condition, pressure, and temperature found in an actual fracturing condition in the field. The system was applied to evaluate foam stability with time and compare various foam formulations in foam fracturing. The results show that foam stability and bubble texture are affected by the additives, temperature, and pressure. The foams with fine and homogeneous bubble texture are more stable than those with coarse and heterogeneous texture.

5.1.3 Review of Foam Rheology Study

Foam rheology influences the tubing pressure drops, pump head, fracture geometry, proppant transport and fluid loss to the matrix. Foam rheology is affected by foam quality (gas volume percentage), bubble texture, foaming agent, viscosity of the liquid phase, pressure and temperature. A circulating loop rheometer is often adopted to characterize the foam rheology.

Hutchins and Miller (2005) investigated the rheology of foams containing polymers up to 400 ^{o}F and 2000 psi by using a circulating foam loop rheometer. The rheology was measured by monitoring the pressure drop across a 20-ft length of ¼-inch tubing maintained at temperature in an oven. Flow rate was continuously adjusted, to ensure a constant shear rate in the tubing, by the software using continuous mass-flowmeter input. A power law model was used to describe the rheological behavior of the foams. Results relating to CO_2 and N_2 polymer foams were discussed with emphasis on foam persistence, bubble size and population, and the rheological behavior with time. They found that the foams with fine and homogeneous bubble texture are more viscous than those with coarse and heterogeneous texture. Bonilla and Shah (2000), Sani et al. (2001), and Sudhakar and Shah (2002, 2003) utilized a similar circulating loop rheometer to investigate the rheology of Guar foams and Xanthan foams. Herschel-Bulkley (HB) model and power law model were adopted to correlate the viscosity data.

Harris and coworkers (Harris and Reidenbach, 1987; Harris, 1989; Harris, 1995; Harris, 1996; Reidenbach et al., 1986) have done a comprehensive study on polymeric foam rheology. They found that foam laminar flow behavior can be described by HB model with the foam behavior index, n, the same as that of the liquid phase and the foam consistency index, K, as a function of the liquid phase consistency index and foam quality (Reidenbach et al., 1986). Foams maintained their viscosity better than their base gel fluids under high temperatures. The high-temperature stability of foams depended more on surfactant type and concentration rather than polymer concentration (Harris and Reidenbach, 1987). Finer texture can be generated under higher shear rates, higher surfactant concentrations, and higher pressures (Harris, 1989). Gas types (N_2, CO_2) only affected foam stability, but not rheology (Harris, 1995). The foam viscosity can be increased by factors of 3 to 10 after cross-linking polymers in the liquid phase of foams (Harris, 1996).

5.1.4 Review of Theoretical Foam Rheological Models

In addition to the experimental study, different theoretical models have been developed for rheology of solid suspensions, emulsions and foams. In the low quality regime, the simplest model is a linear model that was proposed by Einstein (Einstein, 1906) for dilute suspensions assuming unimodal spheres and ignoring particle interactions. The ratio of the viscosity of the suspensions (emulsion or foams) to the viscosity of the continuous liquid phase, $H(Q)$ is estimated to be

$$H(Q) = 1 + \xi Q + o(Q^2) \tag{5.1}$$

where Q is the foam quality (gas volume fraction), and ξ is the Taylor coefficient (Taylor, 1932),

$$\xi = C\frac{0.4 + \mu_{\text{in}} / \mu_{ex}}{1 + \mu_{\text{in}} / \mu_{ex}} \tag{5.2}$$

where μ_{in} and μ_{ex} are internal and external viscosity, respectively. The shape factor C is 2.5 for spheres and larger for non-spherical suspensions. For low quality foams, bubbles are spherical and sparsely distributed in the fluid, and the viscosity ratio of the gas phase to the liquid phase is close to zero. So ξ is close to 1. The linear model is only valid for qualities lower than 10%. For higher qualities, the most widely used models are those proposed by Mooney (1951),

$$H(Q) = \exp(\frac{\xi Q}{1 - Q / Q_m}) \tag{5.3}$$

and Quemada (1977),

$$H(Q) = (1 - \frac{Q}{Q_m})^{-\xi Q_m} \tag{5.4}$$

where Q_m is the critical quality. The critical quality is found experimentally to be the random close pack limit (Lee, 1970) which is about 0.61 for spheres. Brouwers (2010) has proposed an analytical expression for suspension viscosity with a unimodal drop size,

$$H(Q) = (\frac{1-Q}{1-Q/Q_m})^{-\xi Q_m/(1-Q_m)} \tag{5.5}$$

As the quality increases, the discrete phase bubbles expand until they start to touch each other to form polyhedral structures with thin separating lamella. Within this quality regime, the rheology behavior is controlled by the foam structure and lamella properties. Princen and Kiss (1989) have proposed an empirical model to correlate the volume fraction, continuous phase viscosity, sauter mean diameter (SMD) and interfacial tension to the emulsion rheology, i.e.,

$$H(Q) = \frac{\tau_y}{\mu_{ex}\gamma} + 32\left(Q - 0.73\right)Ca^{-1/2} \tag{5.6}$$

where τ_y is the yield stress, μ_{ex} is the viscosity of the external phase, and γ is the shear rate . Ca is the capillary number, given as,

$$Ca = \frac{\mu_{ex} d_{sv} \gamma}{2\sigma} \tag{5.7}$$

with d_{sv} the SMD and σ the interfacial tension.

Herzhaft et al. (2005) measured the rheology for polymer-containing foam in a recirculating loop and compared the experimental results with several theories. Below a quality of 60%, the foam is Newtonian and the Taylor–Mooney (Mooney, 1951; Taylor, 1932) viscosity model for moderately concentrated emulsions matches experimental results. For high volume fraction foams ($\phi \geqslant 60\%$), the bubbles interfere with each other. The viscosity/shear stress curves of these foams show a severe shear-thinning behavior beyond an apparent dynamic yield stress. The flow behavior of high quality foams can only be predicted by the Princen and Kiss (1989) model which incorporates bubble size distribution and interfacial area.

5.1.5 Objective and Outline

Most of the studies above focused on the conventional fracturing foams with polymer additives as foam stabilizers. In our study, to avoid the polymer damage in ultra-low permeability shale reservoirs, polymer-free foams are developed based on the foam stability test and rheology test. A two-step bench-top static stability test is designed to screen out the best surfactant foaming agent and to study the effects of liquid composition, surfactant concentration, temperature and bubble texture on foam stability. The rheology of the aqueous foams is investigated in a circulating loop under a typical fracturing shear rate range of 100-1000 s^{-1}, reservoir temperature and pressure. Foam flow pressure drops are measured along with flow rates to generate the shear stress- shear rate rheology behaviors. And the effects of shear rate, foam quality, temperature, pressure, and chemical composition of the base fluid are investigated. The experiment data is compared with the theoretical models. Empirical correlations are developed for the rheology of polymer-free foams, which can be incorporated in the fracturing model developed in Chapter 3 to predict the fracture geometry and proppant distribution within the fractures.

5.2 METHODOLOGY

5.2.1 Static Foam Stability Test

The static foam stability test incudes two steps, *step1*: a qualitative test to fast screen out the best surfactant foaming agents, and *step2*: a quantitative test to study the effects of liquid composition, concentration, temperature and bubble size on foam stability.

In *step 1*, fourteen different surfactant foaming agents are put in the tubes with the same water level at the same activity concentration. All tubes are cap-sealed and vibrated at the same rate for a certain time to generate foam columns. Then, they are placed under camera to record the decay of foam columns with time. Figure 5.1 shows two example test results. Through *step 1*, best surfactant foaming agents with capacities of easily generating most stable foams are determined from the fourteen candidates.

In *step 2*, standard foam half-life time tests are conducted using the selected foaming agents. The experimental setup is shown in Figure 5.2. A calibrated glass tube, 63 cm in height and 1.52 cm in inner diameter, is sealed at one end by a rubber plug. A needle connected to a pressure regulator along with a N_2 gas cylinder is inserted through the rubber plug into the tube. A steady-state column of foam is generated by blowing N_2 gas into a surfactant solution at the bottom of the tube. By changing the gas injection rate and the needle size, uniform bubbles with different diameters can be produced. After a certain height is achieved, gas injection is stopped and the height of the foam column is measured with time. The time when the height reduces to its half is defined as half-life time of foam, which is a measure of the foam static stability. The whole setup can be placed in a water bath, which can be heated from room temperature to less than 100 ^{o}C. To evaluate the effects of parameters, such as liquid composition, concentration, quality, and temperature, on foam stability, we adjust one parameter at a time and measure the resulting change in foam stability. The test in *step 2* is divided into four groups. The first group of tests examines the effect of liquid composition, including several surfactants and one stabilizer. The stability of the foams produced from different surfactant solutions with the same concentration are measured and compared. Then, the stabilizer is added at different concentrations and the stability of foams is measured again. Following that, the effect of the length of the group [CH_2CH_2O] of the nonionic surfactant is also investigated. In the second group of tests, surfactants with different concentrations are used to produce foams and their half-life time results are collected and compared. In the third group of tests, the anionic surfactant solution with activity concentration of 0.1% is used to produce foams and the foam half-life time is measured at temperature from 20 to 80 ^{o}C. In the final group of tests, the cationic surfactant is used as the foaming agent. The foam columns with different bubble sizes and qualities are generated by changing the gas flow rate and the diameter of the gas injection port. Their half-life time results are collected and compared.

5.2.2 Foam Rheology Test (Foam Loop)

A circulating loop is built to generate foam at several quality, temperatures and pressures. Foam is circulated in the loop at several flow rates and corresponding pressure drops along a test section (diameter = 1.27 cm, length = 15.24 m) are measured by a differential pressure transducer. The whole loop is covered with thermal insulators, except one part that is coated with a heating jacket. The heating jacket can heat the circulating fluid up to a constant temperature around 155 ^{o}F. The pressure within the loop is set by a pressure regulator (PR) (connected to a gas cylinder) up to a pressure of 2000 psi. A transparent view cell is included to visually observe the foam texture. Figure 5.3

shows the schematic diagram of the circulating loop. Figure 5.4 shows the photograph of the loop.

The foam rheology measurement consists of the following steps:

1. The pipe is cleaned by pre-flushing with water and the surfactant solution.
2. The loop is filled with the surfactant solution by the gear pump. Then, the system is heated to the desired temperature.
3. The pump and the drainage valve are shut-off. A certain back pressure is applied by introducing the N_2 gas into the loop.
4. The surfactant solution is circulated in the loop, and the rheology of the base liquid is obtained.
5. N_2 gas is further introduced into the loop. The drainage valve is opened and the liquid phase is drained gradually through the back pressure regulator to the disposal tank until a desired quality is achieved.
6. Then the two-phase fluid mixture is circulated at about 1000 s^{-1} to obtain homogeneous foam, which usually takes not more than 10 minutes.
7. Following that, the flow rates are varied by adjusting the pump rotation speed and the corresponding pressure drops across the test section are recorded after the steady state is achieved.
8. The data are processed in a computer to obtain the shear stress and shear rate, which can be fit to different rheology models for flow behavior parameters, and further, the apparent viscosity.
9. After rheology test, foam is introduced into a high pressure visual cell and foam bubble texture is observed and recorded by a microscope.

All the steps above are repeated to investigate form rheology at different liquid compositions, foam qualities, pressures and temperatures. By conducting the same test with different pipeline diameters, the wall slippage effect can be eliminated. There is negligible slippage error in current tests, which is illustrated by Bonilla's experiment (Bonilla et al., 2000).

5.2.3 Rheology Determination

Foam quality is defined as the percentage of gas volume in the total volume of the foam, i.e.

$$Q = \frac{100 \times V_g}{V_g + V_l}\% \tag{5.8}$$

The wall shear stress is calculated from the pressure drop (ΔP) as

$$\tau_w = \frac{d\Delta P}{4L} \tag{5.9}$$

and the apparent wall shear rate is calculated from the flow rate ($v=4q/\pi d^2$) as

$$\gamma_{wa} = \frac{8v}{d} \tag{5.10}$$

where d and L are the inner diameter and the length of the test section. Assuming a power law fluid, the shear stress, τ is related to the shear rate, γ by

$$\tau = K\gamma^n \tag{5.11}$$

In Eq. 5.11, if shear stress is the wall shear stress τ_w, the shear rate should be the intrinsic shear rate at the wall γ_{wi}, which can be calculated as

$$\gamma_{wi} = \frac{(3n'+1)\gamma_{wa}}{4n'} \tag{5.12}$$

where n' is given by the slope of the log-log plot of wall shear stress τ_w and the apparent wall shear rate γ_{wa}, i.e.,

$$n' = \frac{d\log(\tau_w)}{d\log(\gamma_{wa})} \tag{5.13}$$

The power law index, n is equal to the parameter, n'. The consistency index K can be calculated as

$$K = K'/\left[\frac{(3n'+1)}{4n'}\right]^{n'} \tag{5.14}$$

where K' is the wall shear stress τ_w at γ_{wa} = 1 s^{-1}. The apparent viscosity of the fluid at any shear rate is given as

$$\mu_a = \frac{\tau_w}{\gamma_{wi}} = K\gamma_{wi}{}^{n-1} \tag{5.15}$$

The equations above are established under the conditions of incompressible fluid, fully developed laminar flow, and no-slip boundary.

Herschel-Buckley model,

$$\tau = \tau_0 + K\gamma^n \tag{5.16}$$

is used sometimes to describe foam rheology, but at a sufficiently high shear rate, the first term on the right hand side is negligible and it is equivalent to a power model (Eq. 5.11). The base foam fluids with only surfactant additives are Newtonian and their rheology is described by,

$$\tau_w = 8\rho v^2 \mathrm{Re}^{-1} \; for \quad \mathrm{Re} = \frac{dv\rho}{\mu} \le 2100 \tag{5.17}$$

and

$$\tau_w = 0.0395 \rho v^2 \mathrm{Re}^{-0.25} \quad for \quad \mathrm{Re} = \frac{d v \rho}{\mu} > 2100 \tag{5.18}$$

From Eqs. 5.10, 5.17 and 5.18, for laminar Newtonian flow

$$\tau_w \propto \gamma_{wa} \tag{5.19}$$

and for turbulent Newtonian flow

$$\tau_w \propto \gamma_{wa}{}^{1.75} \tag{5.20}$$

Because the exponent in Eq. 5.20 is greater than 1, a Newtonian fluid behaves like a shear thickening fluid due to turbulence.

5.3 RESULTS AND DISCUSSIONS FOR FOAM STABILITY TEST

5.3.1 Results for the Qualitative Test (*Step 1*)

In this study, one anionic surfactant (Anionic 1: Bio-terge AS 40), one series of nonionic surfactants (Nonionic 1: Tergitol-NP 10/30/50/70), eight cationic surfactants (Cationic 1-8: BTC series, Onyxide R series, Accosoft R 501, n-Decyl, n-Dodecyl), and one amphoteric surfactant (Amphoteric 1: Betaine) were used as foaming agent candidates. The stabilizer was glycerol (99%). No polymer additives were used in all foam base fluids. The qualitative tests were conducted to screen out the best foaming agents from the surfactant candidates listed above. Example 1 shown in Figure 5.1 is the result of the screening tests for the eight cationic surfactants. At 0 minute, the three BTC surfactants present the best foam generation capacity. After 30 minutes, BTC 1010 exhibits the best foam stability over other candidates. Similar test was conducted for nonionic surfactants with different lengths of the group [CH2CH2O], which shows that

NP70>50>10>30. Through the screening tests in *step1*, Anionic 1 (Bio-terge AS40), Cationic 1 (BTC 1010), and Nonionic 1 (Tergitol NP x) are selected as the best foaming agents.

5.3.2 Results for the Quantitative Test (*Step 2*)

In *step 2*, quantitative foam stability test (foam half-life time test) was conducted for the three selected foaming agents. There are four groups of tests focusing on the effects of liquid composition, foaming agent concentration, temperature and bubble size.

The first group of tests studies the effect of liquid composition on foam stability. Figure 5.5 shows the foam stability for the three surfactants Anionic 1, Cationic 1, and Nonionic 1 (NP30). All samples had a surfactant concentration of 1wt% and the same bubble size of around 2mm in diameter. The foam column was monitored as a function of time. The half-life time, defined as the time taken to reach half of the initial foam volume, was measured. The foam made with the surfactant Anionic 1 maintains its volume and has a half-life time much larger than 40 minutes. The volume of the foam made with the surfactant Cationic 1 decreases considerably in the first 40 minutes; the half-life is about 19 minutes. The foam made with the surfactant Nonionic 1 (NP30) collapses most quickly with a half-life of about 3 minutes. Thus the aqueous foam stability depends on the type of surfactant. The decline of foam volume is often discontinuous and contains several steps. This is because breakage of one foam bubble often leads to the breakage of many other neighboring bubbles. This may be due to the thinness of the lamella and perturbations created by the breakage of one bubble to other unstable lamellas. Because foams made with the nonionic surfactant are not very stable, glycerol is added to increase its stability. As shown in Figure 5.5, the foam collapse rate decreases with the increase in glycerol concentration. Glycerol concentration of 1.25%

and 2.24% can increase the half-life time of Nonionic 1 (NP30) foams from 3 minutes to 6 minutes and 22 minutes, respectively. Another experiment in this group is the investigation of the effect of hydrophilic length on foam stability. In this test, surfactants Nonionic 1 NP10, 30, 50 and 70 were used to make surfactant solutions with the active concentration of 1%. The NP number represents the number of units of ethoxy groups [CH_2CH_2O]. Figure 5.6 compares the foam stability for different NP numbers. The results suggest that, with the exception of NP10, foam stability is improved as the NP number increases. The possible reason is that longer hydrophilic chains stabilize the lamella and reduce the liquid drainage.

In the second group of tests, Anionic 1 was used at different surfactant concentrations in the foam base solvents. The foam columns were produced in the system shown in Figure 5.2. The evolution of foam volume with time was measured and plotted in Figure 5.7. The results indicate that the half-life time of the anionic foam is not very sensitive to the anionic surfactant concentration. However, comparing the collapse of foams with surfactant concentrations of 0.0165%, 0.024%, 0.05% and 0.1%, increasing anionic surfactant concentration delayed the decay of foams for periods greater than 400 minutes. Besides, it is noted that at the beginning of the foam collapsing process, there is a short period during which the height of the foam column changes very little. This period is defined as a drainage time zone, during which the liquid phase drains down from the top to the bottom of the foam column according to the liquid gravity and capillarity and thins the lamellae. Increasing the surfactant concentration or adding glycerol can extend this time period, and hence improve foam stability. Similar tests were also conducted on Nonionic 1 and Cationic. Both of them suggest a positive correlation between stability (half-life time) and surfactant concentration. The possible reason is that high concentration of the surfactant molecules can guarantee a good strength of the lamella film and retard the diffusion of the gas phase through the liquid film.

In the third group of tests, a water bath was used to keep the foam columns at a stable high temperature. It should be noted that gas expands as temperature increases. So we put the whole system including the gas pipelines in the water bath to pre-heat the gas before using it to generate foams. The Anionic 1 solution with a concentration of 0.1% was used. The results are plotted in Figure 5.8. The foam collapse rate increases with temperature. The half-life of the foam column drops down significantly as temperature increases. The decrease of the foam half-life with temperature slows down at high temperature. High temperature reduces liquid viscosity and increases liquid drainage. It also speeds up the evaporation of the liquid phase, weakening the liquid film. Furthermore, gas diffusion is also increased as the temperature increases.

In the last group of tests, foam half-life experiments were conducted to study the effects of bubble size and foam quality. Foam quality was changed by controlling the produced bubble size. We used gas injection needles of different sizes as well as different gas injection rates to get bubble sizes varying from 0.5 mm to 3 mm. Cationic 1 solution at a concentration of 0.1% was used to generate foam columns. Foam with smaller bubble size has lower qualities (e.g. 0.5mm: Q=95.7%, 1mm: Q=99.2%, 2mm: Q=99.7%, 3mm: Q=99.8%). Above diameter of 1 mm, foam quality is above 99% and changes very little. The time dependent volume of the four foam columns with different qualities and bubble sizes were measured and plotted in Figure 5.9. A smaller bubble size with a lower quality produces a more stable foam column. Limiting the comparison to the three higher quality foams, smaller bubble size leads to a better foam stability.

It should be kept in mind that all the above stability tests are under static condition with a room pressure, which cannot address the necessary conditions of temperature, pressure, and dynamic-flow conditions that can have remarkable influence on foam stability. In the following rheological study, foams were put in a circulating loop. Foam stability was tested under a dynamic condition with a test pressure up to 2000 psi. It was found that foam stability was increased under the shear condition and high pressure. No collapse was found over 30 minutes for all the foam candidates. The reason is that high pressure leads to uniform and fine bubble textures (shown in later bubble texture study) and shear rate helps create new bubbles from collapsed phases.

5.4 RESULTS AND DISCUSSIONS FOR FOAM RHEOLOGY TEST

5.4.1 Foam Base Fluids

In this section, the anionic surfactant Bioterge AS40 (39% active as supplied) was chosen for the study based on the previous stability test results and economic considerations. Another surfactant foaming agent of interest was the viscoelastic surfactant (VES) supplied by BJ Services. Glycerol (99% purity) was used as a stabilizer in some of the tests. Three foam base fluids were formulated: Fluid A: 0.5 wt% anionic surfactant in water, Fluid B: Fluid A + 2 wt% glycerol, Fluid C: 0.5 wt% viscoelastic surfactant in water. Nitrogen was used as the gas phase. The base fluid A and B are Newtonian fluids, which appear to be shear thickening fluids due to turbulence. The base fluid C has a viscoelastic surfactant, which forms entangled chains under low shear rate and becomes aligned chains at high shear rates. So it is shear thinning and follows Eq. 5.11 or 5.16 with a power law parameter n less than 1.

5.4.2 Preliminary Results of Shear Stress vs. Shear Rate

Foam flow experiment was conducted with the three surfactant formulations at different qualities, temperatures, pressures, and shear rates. Table 5.1 shows the range of test parameters. There were four surfactant formulations: A, B, C, and D. Formulation D is a reference case to formulation A, which has the same anionic surfactant as A, but at a lower concentration. Temperature was varied from 95 to 155 ^{o}F. The pressure was varied from 100 to 2000 psi. Foam quality was varied from 0 to 80%. The apparent wall shear rate was varied from 100 to 1100 s^{-1}. For each case, flow rate and pressure drop were measured from which the wall shear stress and apparent shear rate were calculated by Eqs. 5.9 and 5.10, respectively. Figure 5.10 shows wall shear stress versus apparent shear rate for foams A for different qualities at 95 ^{o}F. The shear stress increases with increasing shear rate at the same quality. The shear stress increases with increasing quality at the same shear rate. As the quality increases, the slope of the shear stress - shear rate curve decreases, in general. Qualities up to 80% were obtained for the fluid A and B. The data for fluid B, which is shown in Figure 5.11, is qualitatively similar to that of fluid A. The slope of the shear stress - shear rate curve is about 1.75 indicating that the flow is turbulent for the liquid flow (quality = 0%). At qualities below 50% and at higher shear rate range, the flow is also turbulent. For foam qualities between 50%-60%, the slope is close to 1, which suggests that the foam behaves like a Newtonian fluid and the flow is laminar in the whole shear rate range. But for foam qualities above 60%, the slope appears to be less than 1 indicating shear thinning non-Newtonian flow behavior.

For the fluid C, 0-60% qualities were successfully generated. Above 63% quality, the foam C becomes too viscous to be mixed and pumped in our flow loop. Figure 5.12 shows wall shear stress versus apparent shear rate for fluid C foams for different qualities at 95 ^{o}F. The slope of the shear stress-shear rate curve for the pure liquid has a slope less than 1, indicating shear thinning non-Newtonian behavior of the base fluid. The VES fluid has a viscoelastic surfactant which aggregates into cylindrical micelles, exhibiting high and non-Newtonian viscosity.

5.4.3 Effect of Shear Rate

The wall shear stress - apparent shear rate data were converted to apparent viscosity versus intrinsic shear rate plots using Eqs. 5.12-5.15. Figures 5.13-5.15 show the plots of apparent viscosity vs. intrinsic shear rate for foam A, B and C at different qualities and 95 ^{o}F. For foams A and B, the viscosity decreases with increasing shear rate for qualities above 60%, representing a shear thinning behavior. This decrease is larger for higher foam qualities. For low qualities (<50%), apparent viscosity increases slightly with the increase in shear rate. This increase in apparent viscosity is due to the turbulent flow at the shear rates above 300-400 s^{-1}. The turbulence increases the flow resistance and makes the foams behave like a shear thickening fluid. The low quality foams are dispersions of gas in water without much interaction between gas bubbles and the water flow is turbulent at high shear rates. The pattern of behavior is similar for foams A and B, because the base fluid is Newtonian for these two cases. Unlike foams A and B, foam C behaves like a shear-thinning fluid from low quality to high because of the shear-thinning nature of its liquid phase.

It is found that the low quality foams (20-30%) generated from formulations A and B possess higher apparent viscosities at shear rate below 500 s^{-1} and lower apparent viscosities at shear rate above 500 s^{-1}, as compared with their base fluids, as shown in Figures 5.13 and 5.14. That is because the bubbles dispersed in the base fluid retard the development of the turbulence at the high shear rate. This is a good property for the fracturing fluid, because during fracturing a low friction loss in the tubing facility (high shear rate zone) and a high proppant suspension viscosity in the fractures (low shear rate zone) are always desired.

5.4.4 Effect of Foam Quality

Besides the shear rate effect, the effect of increasing foam quality on the rheology of aqueous foam can also be investigated from Figures 5.13-5.15. The viscosity increases sharply with quality at the high quality regime. For example, for foam A at a low shear rate (100 s^{-1}), the viscosity increases from 1.5 cp to 8 cp at Q: 0-50% and from 8 cp to 85 cp at Q: 50-80%. At a high shear rate (1000 s^{-1}), the viscosity increases from 6 cp to 9.5 cp at the low quality regime, while from 9.5 cp to 45 cp at the high quality regime. This sudden increase of the viscosity above 50% quality is attributed to the transition from a loosely packed bubble regime to a closely packed bubble regime as quality increases.

5.4.5 Effect of Temperature

Figures 5.16-5.18 show the effect of temperature on foam apparent viscosities at 500 s^{-1} shear rate for fluids A, B and C, respectively. In general, the viscosity decreases with temperature. According to the figures, the temperature effects are more significant for high quality foams than for low quality foams. Increasing temperature causes deterioration of the foams by accelerating the liquid drainage in the lamellae; in some cases the surfactant solubility in the base solution can also decrease. The viscosity of the VES foam (C) decreases more than the viscosity of the regular surfactant foams (A, B) at high temperature. Figure 5.19 shows the apparent viscosity versus shear rate for base fluids B and C with temperature. The viscosity of the VES fluid (C) decreases with increasing temperature for a given shear rate, which is due to the degradation of the wormlike micelles of VES at high temperatures. The apparent viscosity for base fluid B hardly changes as the temperature increases. Thus, increasing the temperature destabilizes the foam C more than other foams A, B by thinning VES fluid more than the regular surfactant fluids.

5.4.6 Effect of Pressure

The pressure effect on the foam rheology is shown in Figure 5.20 for foam A at 500 s^{-1} shear rate and room temperature. For low quality foam (<50%), the effect of pressure is small, but for higher quality as pressure increases the apparent viscosity increases. The power law index, *n* and consistency index, *K* for foam A at different pressures are shown in the Table 5.2. For the foams with a quality below 50%, *K* and *n* change slightly as pressure increases. This change is more like a measurement error. When the quality is high, *K* and *n* are highly affected by pressure. Figure 5.21 shows that as pressure increases, the power law index, *n* decreases at a decreasing rate. Figure 5.22 shows that as pressure increases, the consistency index, *K* increases linearly. Pressure affects the foam rheology by increasing gas densities, slightly decreasing gas viscosity, and most importantly changing the foam bubble textures (e.g. size distribution and mean diameter) (Harris, 1989; Herzhaft et al., 2005). Our experiment results indicate that the pressure has negligible effect on foam rheology at low qualities (<50%) because droplets are sparsely distributed in continuous liquid phase with little interaction, but a significant one at high qualities (≥60%) because the foam bubble texture controls rheology.

5.4.7 Effect of Liquid Composition

Figure 5.23 concludes the apparent viscosity of foams produced from several base fluids and compares them with the viscosity of two conventional Guar foams from literature (Sudhakar and Shah, 2003). The condition is the same, with a pressure of 1000 psi, a temperature of 95 ^{o}F, and a shear rate of 200 s^{-1}. Comparing the results of foam A and foam D, increasing the surfactant concentration increases the foam viscosity, especially at high qualities. The increased surfactant concentration not only enhances the foam lamella stability, but also increases the total interfacial area of the foam structure. Adding glycerol also increases the foam viscosity by thickening the liquid phase. The polymer-free foams A and B are both less viscous than 0.24 wt% (20 lbs/1000 gallon) guar foams, while the VES foam C has an apparent viscosity similar to that of guar foams (between 0.24 -0.36 wt%). The formation of the wormlike micelles and their networks highly increase the viscosity of the liquid phase and the foam of fluid C.

5.4.8 Comparison with Theoretical Models

The experimental data are compared with the theoretical models (Eqs. 5.1-5.6) for the two foam quality regimes: a low foam quality regime (<60%) and a high foam quality regime (⩾60%). For low quality foams, bubbles are spherical and sparsely distributed in the continuous liquid phase (gray background), as shown in Figure 5.24 *a*. Because the viscosity ratio of the gas phase to the liquid phase is close to zero, ξ is close to 1 in Eq. 5.2. Figure 5.26 shows the experimental data of the viscosity ratio, $H(Q)$ in comparison with the theoretical models. All the models and the experimental data lie together in the quality range of 0-20%. As the quality further increases, the analytical model proposed by Brouwers (2010) agrees the best with the measured data, while the Quemada model (Quemada, 1977) is the second best. The linear model underestimates and the Mooney model (Mooney, 1951) overestimates.

As the quality increases, the bubble size increases and the lamella thickness decreases (Figure 5.24 *b*). Once they start to touch each other, polyhedral structures are formed with separating ultra-thin liquid layers (Figure 5.24 *c*). Within this quality regime, the rheology behavior is highly affected by the foam bubble textures and lamella properties. Assuming that foams and emulsions are similar, Eqs. 5.6 and 5.7 can, therefore, be applied to estimate the apparent foam viscosity, by replacing interfacial tension with surface tension. Furthermore, because the shear rate range in our experiments is above 100 s^{-1}, the first term of Eq. 5.6 can be negligible.

Figure 5.25 plots the bubble size distribution of Foam A at different foam qualities. The higher the foam quality, the broader the bubble size distribution and the larger the mean bubble size, which is consistent with the measurements of Herzhaft et al. (2005). The SMD is computed from the size distribution and plotted against the foam quality in the smaller box within the figure. The SMD (in mm) can be expressed as,

$$SMD = 2.28Q^2 - 3.11Q + 1.09 \tag{5.21}$$

for Q>60%. The surface tension is 34 mN/m for 0.5wt% and 38 mN/m for 0.1wt% anionic surfactant fluid, respectively. Figure 5.27 compares the apparent viscosity predicted by Eq. 5.6 with the measured values. The results show that the model has a good prediction for a 74% quality foam, while overestimates the viscosity for a 83% quality foam by 3 times. The discrepancy at higher qualities may be attributed to the broader drop size distribution, which deviates from the monosize assumption in the model.

5.4.9 Empirical Rheological Correlation Development

Having investigated the parameters that affect foam rheology, correlations are developed to estimate foam rheology under typical field conditions (shear rate, temperature and pressure) during fracturing. The power-law model parameters (*n* and *K*) are obtained for each experiment by fitting the experimental wall shear stress and rate; the results are presented in Table 5.3 along with the correlation coefficient, R^2. Based on this table, correlations are developed to estimate power-law (*n*) and consistency (*K*) indices for polymer-free foams.

Figures 5.27 and 5.28 show the power-law index (*n*) and the consistency index (*k*) as functions of quality for foam A at 1000 psi pressure and different temperatures. From the plots, it is observed that the rheology of the surfactant foam A depends on quality, but is not very sensitive to the temperature. The power-law index decreases with an increase in quality, while the consistency index increases exponentially with foam quality. These variations can be represented by the empirical correlations listed below (dashed lines in Figures 5.28 and 5.29):

$$n_0\left(Q\right)=1.54-1.64Q^2 \tag{5.22}$$

$$K_0\left(Q\right)=10^{\left(5.89Q^2+0.43Q-4\right)} \tag{5.23}$$

These correlations can be used to estimate the foam rheology for quality less than 60%. For higher quality, the influence of pressure needs to be considered. The effect of pressure on n and K can be captured by the following correlations

$$n\left(p,Q\right)=n_0\left(Q\right)+\left(0.21-0.89Q\right)\log(P/1000) \tag{5.24}$$

$$K\left(p,Q\right)=K_0\left(Q\right)+\left(8.6\times10^{-11}e^{21Q}\right)\left(P-1000\right) \tag{5.25}$$

where P is the pressure, and n_0, K_0, are power law parameters predicted by Eqs. 5.22 and 5.23. The pressure correlations are developed from the experimental data shown in Figures 5.21 and 5. 22.

Bonilla et al. (2000) have conducted foam rheology tests using different tubing sizes and found that the tubing size does not impact the foam rheology if the bubble size is much smaller than the tubing diameter. In this study, our bubble size of 10-100 µm is much smaller than typical hydraulic fracture width which is of an order of mm. So the PFF rheological models developed from the tubing flow test can be applied in fractures.

5.5 CONCLUSIONS

In this chapter, a two-step foam static stability test is designed to quickly screen out the best surfactant foaming agent and to study the effects of liquid composition, concentration, temperature and bubble size on foam stability. It is found that the foam stability depends on the surfactant used. Among the fourteen surfactants studied, the anionic surfactant Bio-terge AS 40 provides the best foam stability, with a half-life larger than one hour, which is sufficiently long for fracturing treatment. Addition of glycerol can improve the foam stability. Increasing the surfactant concentration causes an increase in foam stability for most cases, for the reason that more surfactant molecules could be absorbed on the surface of the liquid film to strengthen the film and to decrease gas diffusion through the film. High temperature decreases foam stability. Foam half-life decreases at a decreasing rate as temperature increases from room temperature to 80 degree C. Bubble size also affects foam stability. The foam column with a larger bubble size has a lower stability.

The rheology of three kinds of polymer-free foams (A: 0.5 wt% regular anionic surfactant, B: Fluid A + 2 wt% glycerol, C: 0.5 wt% viscoelastic surfactant) are studied in a circulating pipe rheometer. All three foams exhibit power-law rheological behavior. The regular surfactant foams (A and B) show shear thinning behavior at qualities above 60%, non-shear dependent behavior from 50% to 60% and shear thickening below 50% (due to turbulence). The VES foams show shear thinning at qualities less than 60%. Temperature lowers the viscosity of foams due to decrease in the liquid viscosity and increasing instability of the bubbles, but the temperature effect is small for foams A and B. Pressure increases foam viscosity; the impact increases with increasing foam quality and decreases with increasing pressure. The aqueous foams A and B are both less viscous than 0.24 wt% polymer (guar) foams, while the VES foam C has an apparent viscosity similar to that of 0.24-0.36 wt% guar foams. The model proposed by Brouwers agrees the best with the measured data for quality under 60%; the model proposed by Princen & Kiss for high quality does not match the experimental data. New correlations have been developed to describe the aqueous foam rheology as a function of shear rate, quality, and pressure at the parameter range typical of hydraulic fracturing. The correlations can be incorporated in a fracturing modeling simulator to evaluate the foam fracturing efficiency.

Overall, this chapter focused on studying a new type of foam, which does not include polymer additives. The stability and rheology of the polymer-free foam is evaluated by using the experimental systems similar to Hutchins and Miller (2005).The foam proppant transport study under the typical shear rate range and pressure range of fracturing is not conducted. Future experimental work can be done to better understand proppant settling in different quality foams at varied shear rate conditions and high pressures.

Nomenclature

H, viscosity ratio, no unit

Q, foam quality, no unit

ξ, Taylor coefficient, no unit

μ, viscosity, cp

τ, stress, pa

γ, shear rate, s^{-1}

Ca, capillary number, no unit

d_{sv}, sauter mean diameter, m

σ, interfacial tension, mN/m

V, single phase volume, m^3

d, tube diameter, m

ΔP, pressure difference, Pa

L, length of testing tube, m

n, flow behavior index, no unit

K, consistency index, Ns^n/m^2

ρ, fluid density, kg/m^3

v, flow rate, m/s

Re, Reynolds Number, no unit

NP, hydrophilic group number, no unit

Subscripts

in, internal phase

ex, external phase

g, gas phase of foam

l, liquid phase of foam

w, value at the wall

wa, apparent value at the wall

wi, intrinsic value at the wall

a, apparent value

References

Bonilla, L.F. and Shah, S.N. 2000. Experimental Investigation on the Rheology of Foams. Paper SPE 59752. Presented at the SPE/CERI Gas Technology Symposium, Alberta, Canada, Apr. 3-5.

Brannon, H.D. and Starks, T.R. 2009. Maximizing Return-on-fracturing-investment by Using Ultra-lightweight Proppants to Optimize Effective Fracture Area: Can Less Be More? Paper SPE 119385. Presented at the SPE Hydraulic Fracturing Technology Conference, The Woodlands, Texas, Jan 19-21.

Brouwers, H.J.H. 2010. Viscosity of a Concentrated Suspension of Rigid Monosized Particles. Phys. Rev. E. 81 051402.

Cipolla, C.L., Warpinski, N.R., Mayerhofer, M.J., Lolon, E.P., and Vincent, M.C. 2010. The Relationship Between Fracture Complexity, Reservoir Properties, and Fracture-treatment Design. SPE Production & Operations. 25 (4): 438-52.

Clark, N.O. and Blackman, M. 1948. The Degree of Dispersion of the Gas Phase in Foam. Faraday Soc. Than. 44: 1-7.

Einstein, A. 1906. Effect of Suspended Rigid Spheres on Viscosity. Ann. Phys. 19: 289–306.

Gidley, J.L., Holditch, S.A., Nierode, D.E., and Veatch Jr., R.W. 1989. Recent Advances in Hydraulic Fracturing. SPE Monograph 12, Soc. of Petr. Eng., Richardson, TX.

Harris, P.C. 1989. Effects of Texture on Rheology of Foam Fracturing Fluids. SPE Production Eng. 4 (3): 249-57.

Harris, P.C. 1995. A Comparison of Mixed Gas Foams with N_2 and CO_2 Foam Fracturing Fluids on a Flow Loop Viscometer. SPE Prod. & Faci. 10 (3): 197-203.

Harris, P.C. 1996. Rheology of Crosslinked Foams. SPE Prod. & Faci. 11 (2): 113-16.

Harris, P.C., and Reidenbach, V.G. 1987. High-Temperature Rheological Study of Foam Fracturing Fluids. J. of Petroleum Tech. 39 (5): 613-19.

Herzhaft, B., Kakadjian, S., and Moan, M. 2005. Measurement and Modeling of the Flow Behavior of Aqueous Foams Using a Recirculating Pipe Rheometer. Colloids and Surfaces A: Physicochem. Eng. Aspects. 263: 153-64.

Hutchins, R.D. and Miller, M.J. 2005. A Circulating-foam Loop for Evaluating Foam at Conditions of Use. SPE Production & Facilities. 20 (4): 286-94.

Kovscek, A.R. and Radke, C.J. 1994. Fundamentals of Foam Transport in Porous Media. Advances in Chemistry Series, Washington, DC. 242: 115-63

Lee, D.I. 1970. Packing of Spheres and Its Effect on the Viscosity of Suspensions. J. Paint Technology. 42: 579-87.

Lemlich, R. 1978. Predition of Changes in Bubble Size Distribution Due to Interbubble Gas diffusion in a Foam. Ind. Eng. Chem. Fundam. 17(2): 89-93.

Mooney, M. 1951. The Viscosity of a Concentrated Suspension of Spherical Particles. J. Colloid Sci. 6: 162-70.

Peles, J., Wardlow, R.W., Cox, G., Haley, W., Dusterhoft, R., Walters, H.G., and Weaver, J. 2002. Maximizing Well Production With Unique Low Molecular Weight Frac Fluid. Paper SPE 77746. Presented at the SPE Annual Technical Conference and Exhibition, San Antonio, Texas, Sep. 29 - Oct 2.

Princen, H.M. and Kiss, A.D. 1989. Rheology of Foams and Concentrated Emulsions IV. An Experiment Study of the Shear Viscosity and Yield Stress of Concentrated Emulsions. J. Colloid Interface Sci. 128: 176-86.

Quemada, D. 1977. Rheology of Concentrated Disperse Systems and Minimum Energy Dissipation Principle. Rheol. Acta. 16: 82-94.

Reidenbach, V.G. Harris, P.C., Lee, Y.N., and Lord, D.L. 1986. Rheological Study of Foam Fracturing Fluids Using Nitrogen and Carbon Dioxide. SPE Production Engineering. 1 (1): 31-41.

Rosen, M.J. 1989. Surfactants and Interfacial Phenomena. Second Edition. John Wiley & Sons, New York City 276-303.

Sani, A.M., Shah, S.N., and Baldwin, L. 2001. Experimental Investigation of Xanthan Foam Rheology. Paper SPE 67263. Presented at the SPE Production and Operations Symposium, Oklahoma City, Oklahoma, March 24-27.

Schramm, L.L. 1994. Foam Sensitivity to Crude Oil in Porous Media. Advances in Chemistry Series, Washington, DC. 242: 165-197.

Sita Ram Sarma, D.S.H., Pandit, J., and Khilar, K.C. 1988. Enhancement of Stability of Aqueous Foams by Addition of Water-Soluble Polymers- Measurements and Analysis, J. of Colloid and Interface Science. 124(1): 339-48.

Sudhakar, D.K. and Shah, S.N. 2002. New Empirical Friction Loss Correlation for Foam Fluids in Coiled Tubing. Paper SPE 74810. Presented at the SPE/ICoTA Coiled Tubing Conference and Exhibition, Houston, Texas, April 9-10.

Sudhakar, D.K. and Shah, S.N. 2003. New Rheological Correlations for Guar Foam Fluids. Paper SPE 88032. Presented at the SPE Production and Operations Symposium, Oklahoma City, Oklahoma, March 22-25.

Taylor, G.I. 1932. The Viscosity of a Fluid Containing Small Drops of Another Fluid. Proc. R. Soc. Ser. A. 138: 41-45.

Warpinski, N.R., Mayerhofer, M.J., Vincent, M.C., Cipolla, C.L., and Lolon, E.P. 2009. Stimulating Unconventional Reservoir: Maximizing Network Growth While Optimizing Fracture Conductivity. J. of Canadian Petro. Tech. 48 (10): 39-51.

Table 5.1: Foam base fluids and test matrix.

No.	Liquid phase	Temp (^oF)	Pressure (psi)	Quality (%)	Pipe Size (inch)	Mixing Shear (s^{-1})
A	0.5wt% AS[1] (39%[3])	95,125,155	1000	0-80	0.5	1000
B	0.5wt% AS[1] (39%[3])+ 2wt%Stabilizer(99%[3])	95,125,155	1000	0-80	0.5	1000
C	0.5wt% VES[2] (99%[3])	95,125,155	1000	0-80	0.5	1000
D	0.1wt% AS[1] (39%[3])	95	1000	0-80	0.5	1000

1. Anionic surfactant: Bio-terge AS 40;
2. Viscoelastic surfactant;
3. Surfactant Activity.

Table 5.2: Power law parameters for foam A at 95 °F.

Quality		200 psi	400 psi	600 psi	800psi	1000 psi	1400 psi	1700 psi
45%	n	1.16	1.24	1.24	1.25	1.24	-	-
	K(Ns^n/m^2)	2.72e-3	1.71e-3	1.74e-3	1.59e-3	1.86e-3	-	-
	μ_{ap}[1](cp)	7.34	7.49	7.80	7.52	7.99	-	-
59%	n	1.14	-	1.03	-	0.98	0.91	0.89
	K(Ns^n/m^2)	4.69e-3	-	1.15e-2	-	1.86e-2	2.85e-2	3.34e-2
	μ_{ap}[1](cp)	10.93	-	13.94	-	15.85	16.64	17.08
66%	n	1.07	-	0.89	-	0.84	0.80	-
	K(Ns^n/m^2)	9.12e-3	-	4.10e-2	-	6.35e-2	8.32e-2	-
	μ_{ap}[1](cp)	13.69	-	20.76	-	23.10	24.09	-
74%	n	0.91	-	0.71	-	0.65	0.62	-
	K(Ns^n/m^2)	3.28e-2	-	1.88e-1	-	3.74e-1	5.07e-1	-
	μ_{ap}[1](cp)	18.11	-	31.48	-	41.60	46.56	-
80%	n	0.85	-	0.59	-	0.49	0.45	-
	K(Ns^n/m^2)	1.14e-2	-	4.75e-1	-	1.19	1.77	-
	μ_{ap}[1](cp)	22.55	-	37.32	-	50.19	57.82	-

[1] Apparent viscosity is calculated under a typical fracturing shear rate of 500 s-1.

Table 5.3: Power law parameters for foams A, B and C at 1000 psi.

	T (°F)	Power Law Parameter	Quality (%)							
			0	25	30	50	60	70	75	80
A	95	n	1.60	-	1.25	1.07	0.88	0.64	-	0.53
		K(Ns^n/m^2)	1.00e-4	-	9.10e-4	5.75e-3	4.26e-2	3.98e-1	-	1.15
		R^2	0.998	-	0.996	0.994	0.999	0.999	-	0.998
	125	n	1.54	-	1.35	1.12	0.89	0.54	-	0.45
		K(Ns^n/m^2)	1.30e-4	-	4.50e-4	3.63e-3	3.55e-2	7.08e-1	-	1.68
		R^2	0.995	-	0.992	0.994	0.999	0.996	-	0.997
	155	n	1.52	-	1.39	1.16	0.91	0.51	-	0.42
		K(Ns^n/m^2)	1.40e-4	-	3.20e-4	2.13e-3	2.58e-2	8.58e-1	-	1.94
		R^2	0.997	-	0.992	0.996	0.999	0.999	-	0.998
B	95	n	1.63	1.34	-	1.14	0.79	0.61	0.57	0.55
		K(Ns^n/m^2)	8.00e-5	4.90e-4	-	4.03e-3	9.64e-2	5.45e-1	9.32e-1	1.36
		R^2	0.9990	0.9925	-	0.998	0.999	0.997	0.999	0.997
	125	n	1.56	1.43	-	1.24	0.78	0.46	0.45	0.44
		K(Ns^n/m^2)	1.30e-4	2.6e-4	-	1.79e-3	8.56e-2	1.47	1.70	2.27
		R^2	0.997	0.994	-	0.999	0.998	0.992	0.999	0.995
	155	n	1.53	1.51	-	1.23	0.78	0.45	0.41	0.40
		K(Ns^n/m^2)	1.50e-4	1.50e-4	-	1.36e-3	8.02e-2	1.45	2.03	2.76
		R^2	0.998	0.991	-	0.999	0.998	0.999	0.994	0.998
C	95	n	0.52	-	0.47	0.35	0.28	-	-	-
		K(Ns^n/m^2)	0.19	-	0.43	1.79	4.21	-	-	-
		R^2	0.992	-	0.991	0.997	0.999	-	-	-
	125	n	0.75	-	0.62	0.51	0.49	-	-	-
		K(Ns^n/m^2)	2.98e-2	-	0.12	0.62	0.98	-	-	-
		R^2	0.997	-	0.994	0.988	0.993	-	-	-
	155	n	0.92	-	0.91	0.74	0.63	-	-	-
		K(Ns^n/m^2)	8.24e-3	-	1.66e-2	7.91e-2	0.25	-	-	-
		R^2	0.999	-	0.999	0.999	0.992	-	-	-

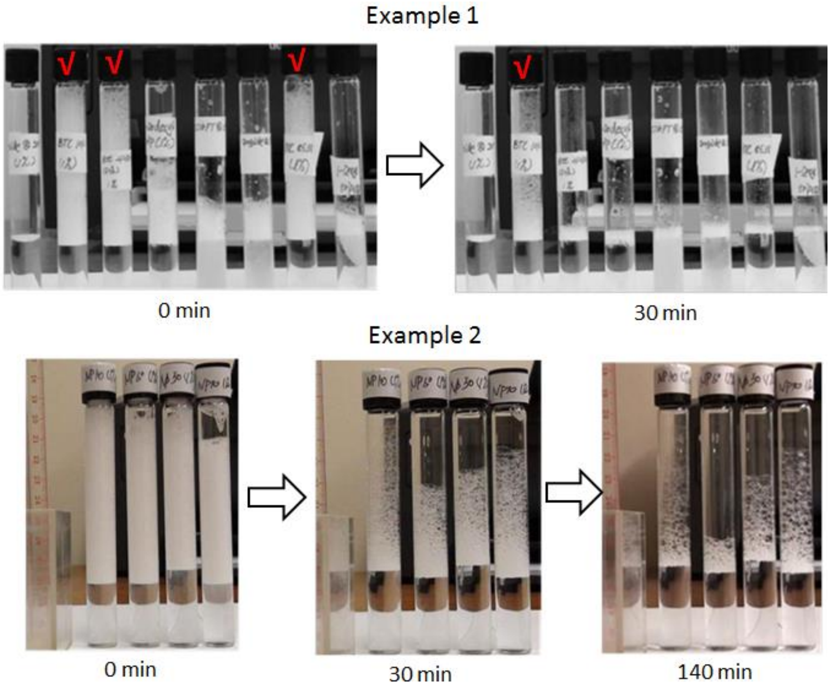

Figure 5.1: Testing example results from qualitative foam static stability test - *step 1*.

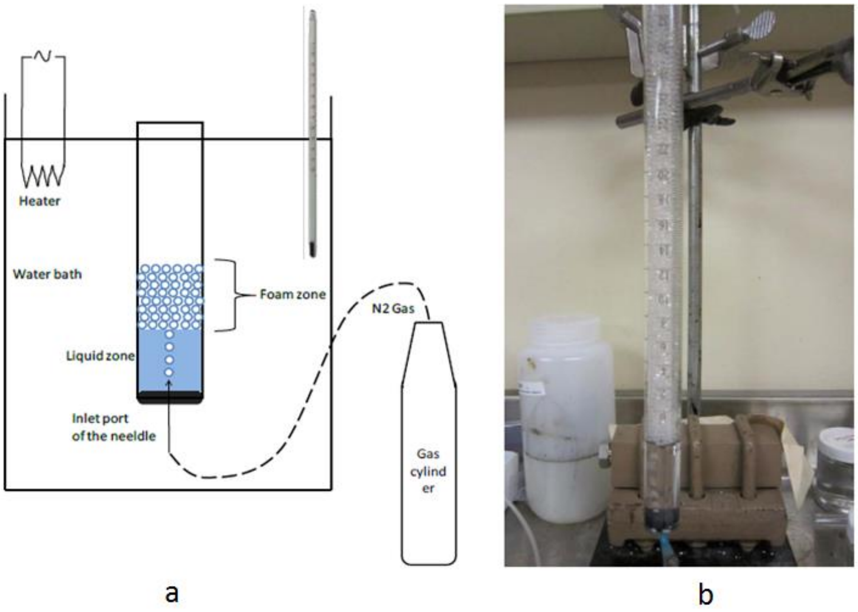

Figure 5.2: Setup for quantitative foam static stability test - *step 2* (a: schematic figure; b: photograph of real system).

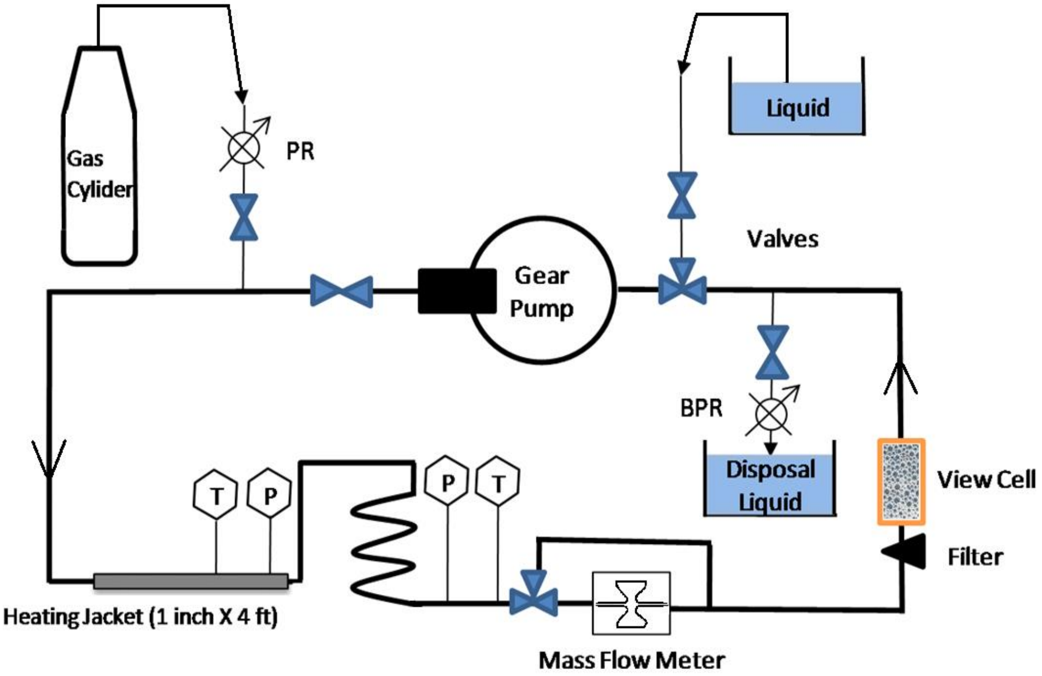

Figure 5.3: Schematic figure of the foam loop for foam rheology test.

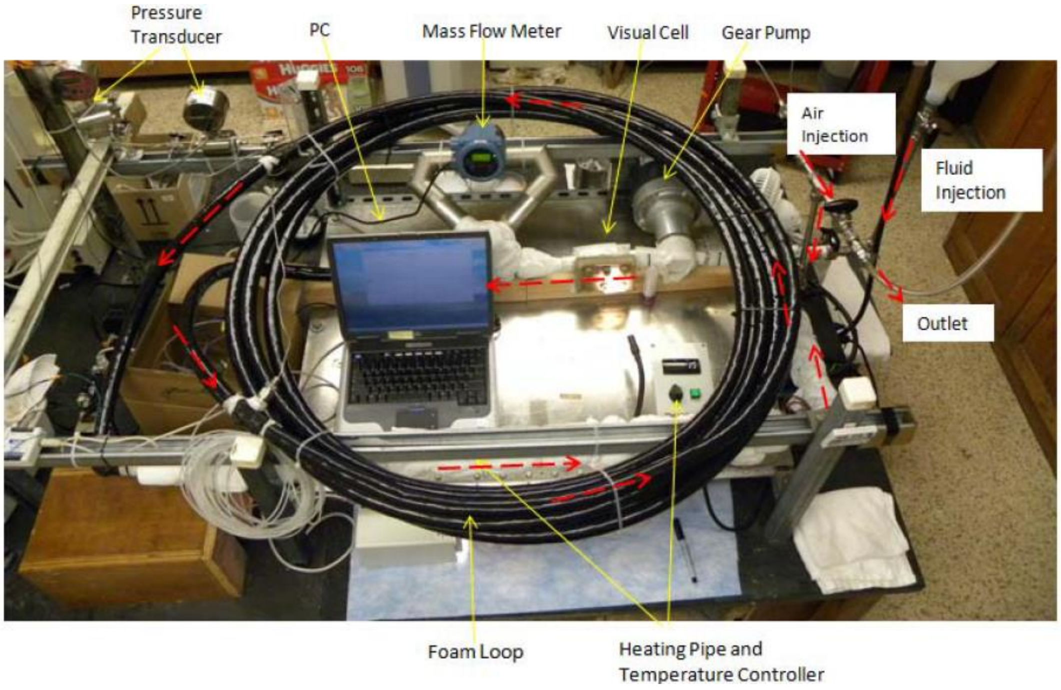

Figure 5.4: Photograph of the foam loop system.

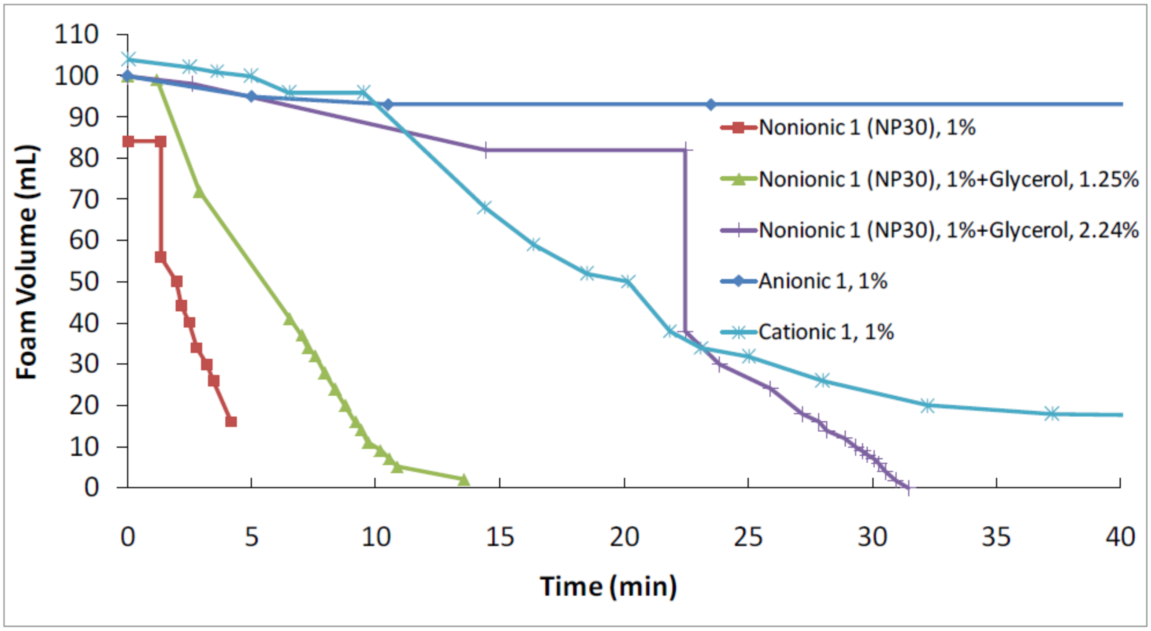

Figure 5.5: Foam stability for different liquid compositions (surfactant types and the addition of stabilizer: *Glycero*).

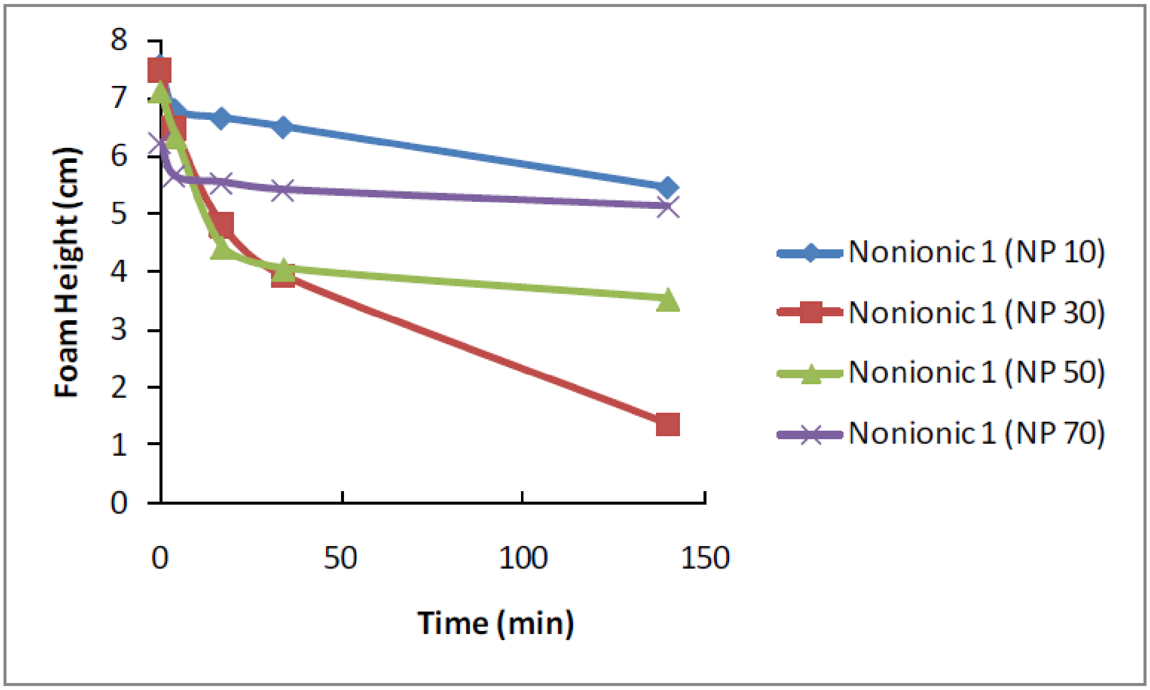

Figure 5.6: Foam stability for different NP numbers.

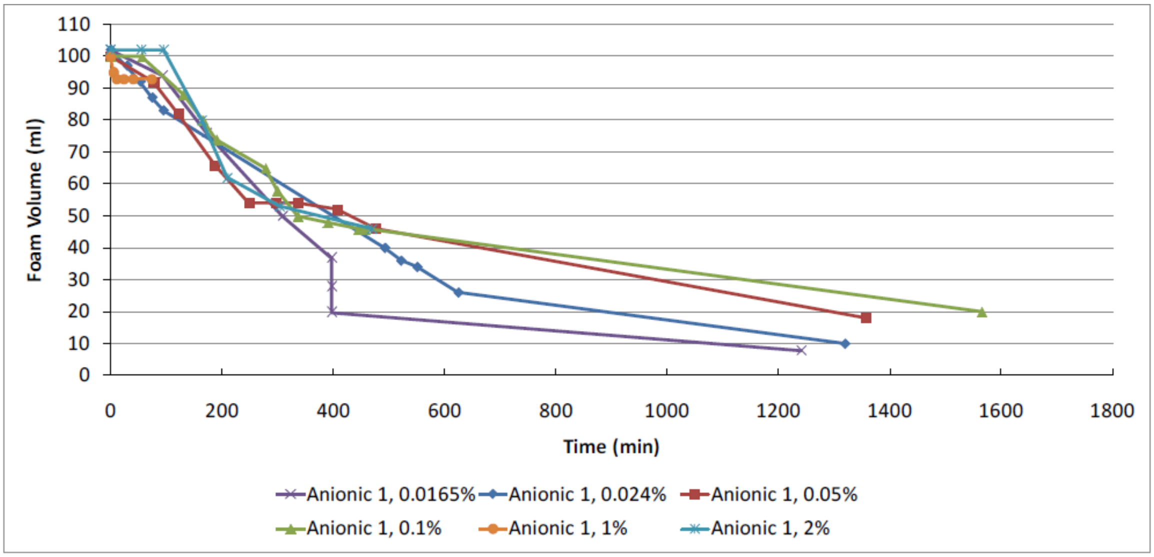

Figure 5.7: Foam stability for different surfactant concentrations.

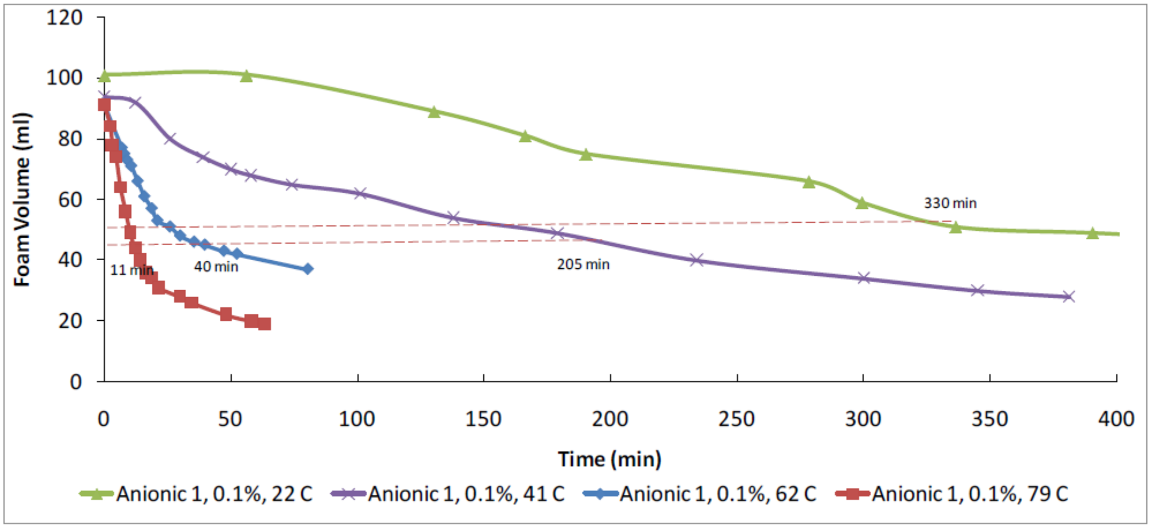

Figure 5.8: Foam stability for different temperatures.

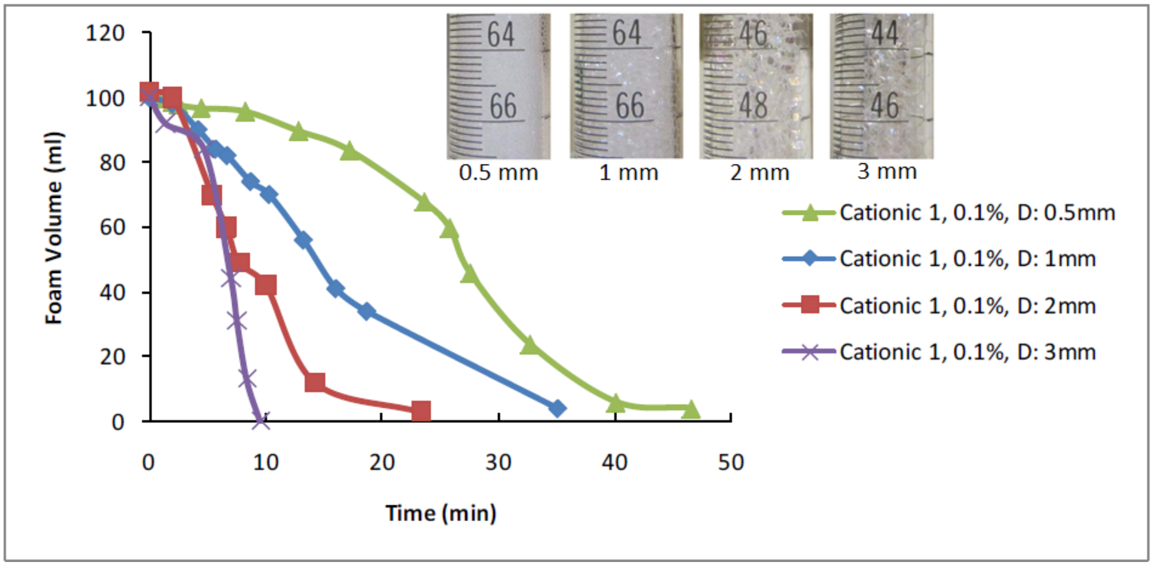

Figure 5.9: Foam stability for different bubble sizes.

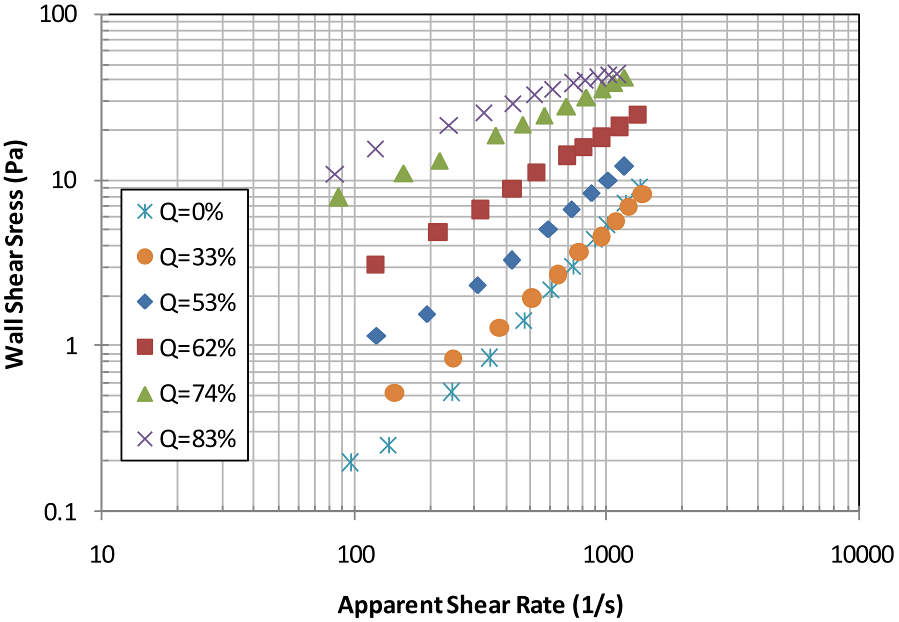

Figure 5.10: Wall Shear Stress vs. Apparent Shear Rate for foam A at 95 ^{o}F.

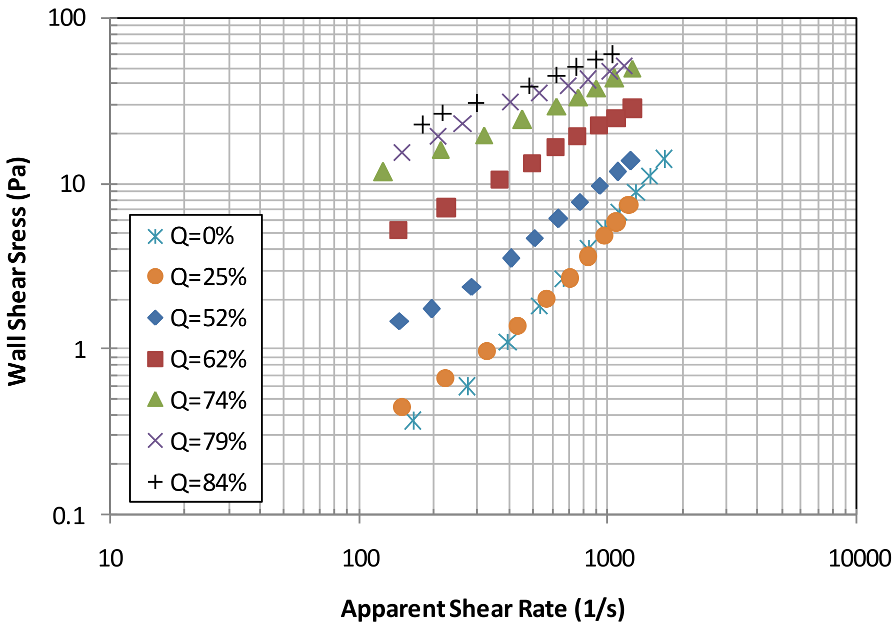

Figure 5.11: Wall Shear Stress vs. Apparent Shear Rate for foam B at 95 ^{o}F.

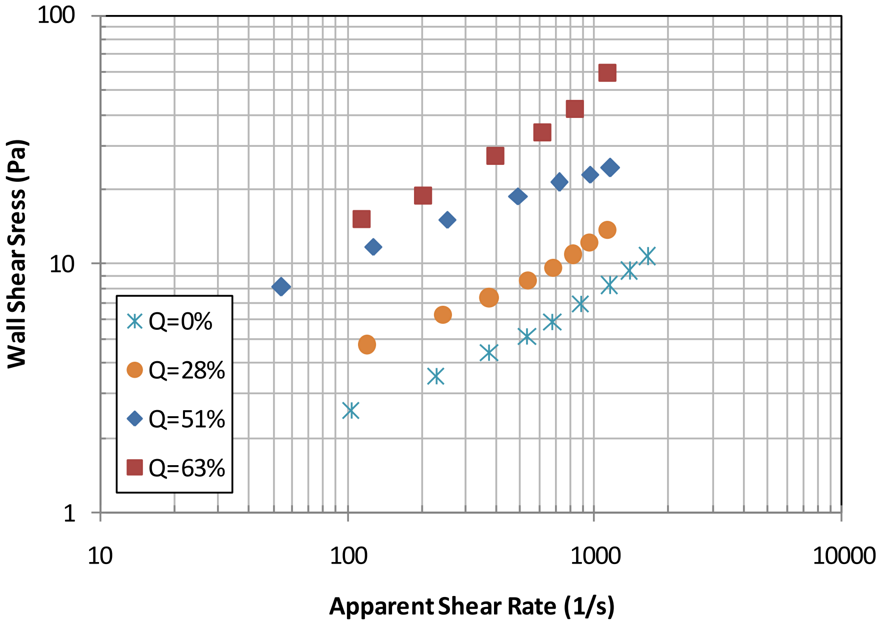

Figure 5.12: Wall Shear Stress vs. Apparent Shear Rate for foam C at 95 ^{o}F.

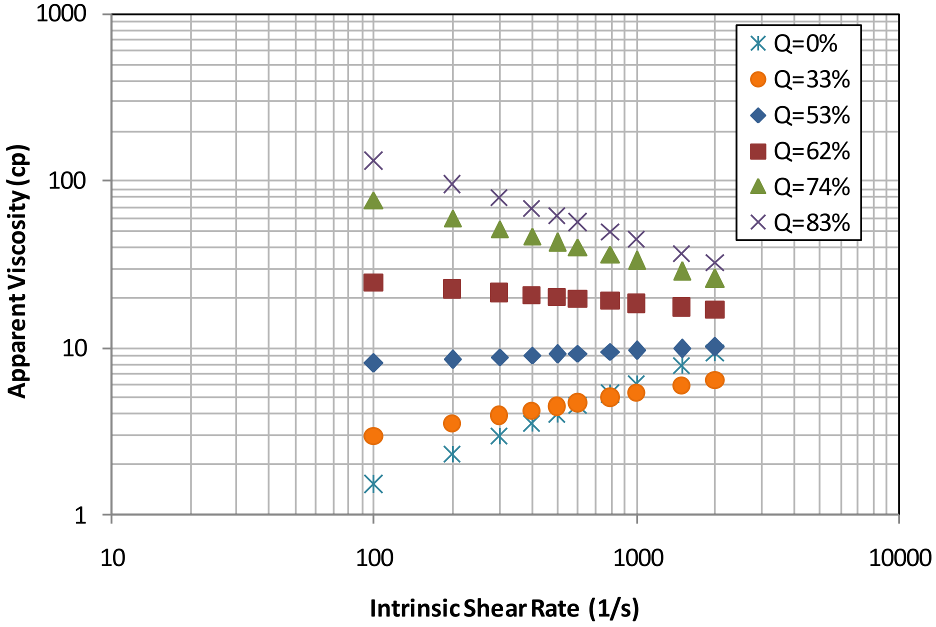

Figure 5.13: Apparent viscosity as a function of intrinsic shear rate for foam A at 95 °F.

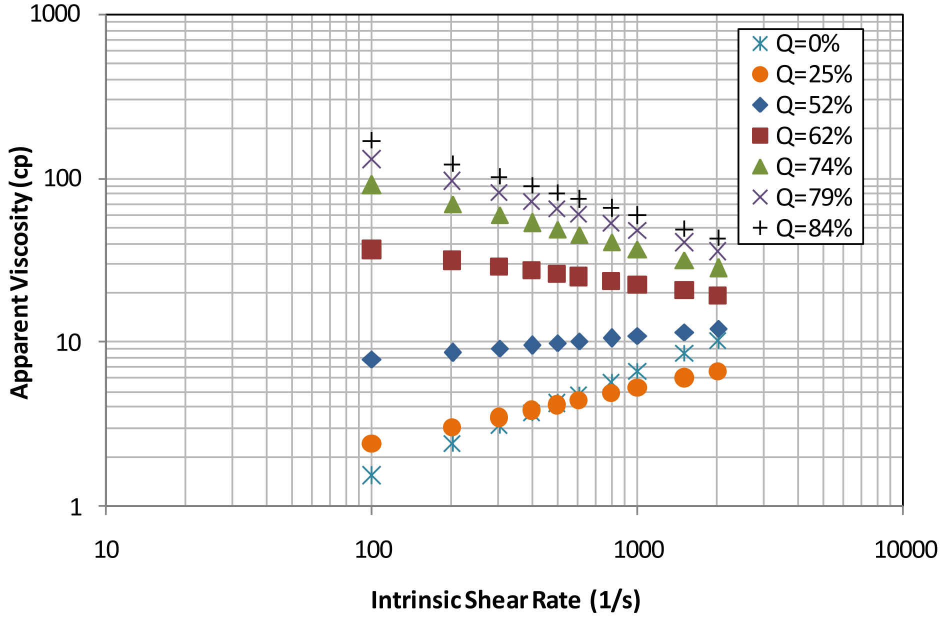

Figure 5.14: Apparent viscosity as a function of intrinsic shear rate for foam B at 95°F.

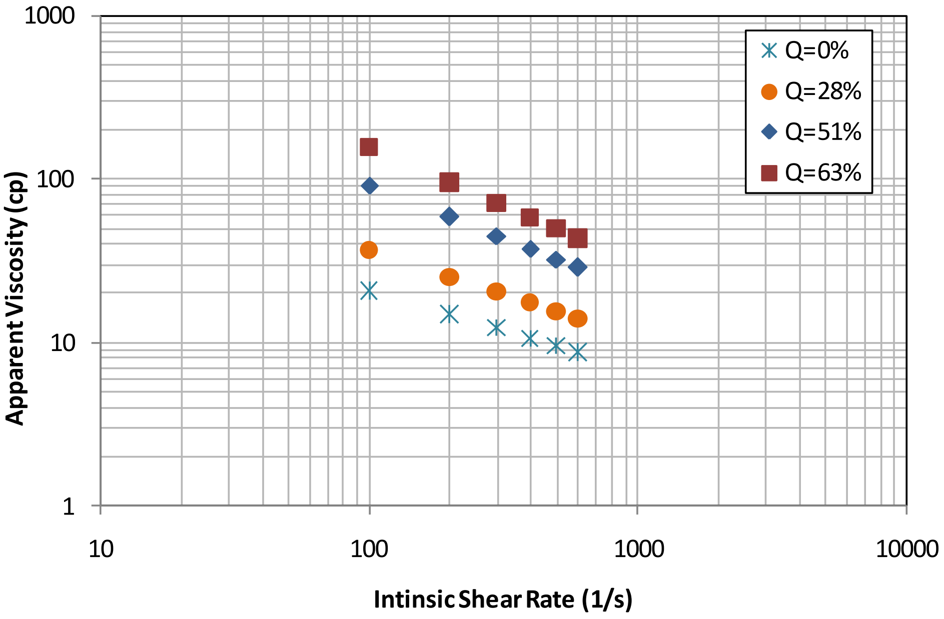

Figure 5.15: Apparent viscosity as a function of intrinsic shear rate for foam C at 95 °F.

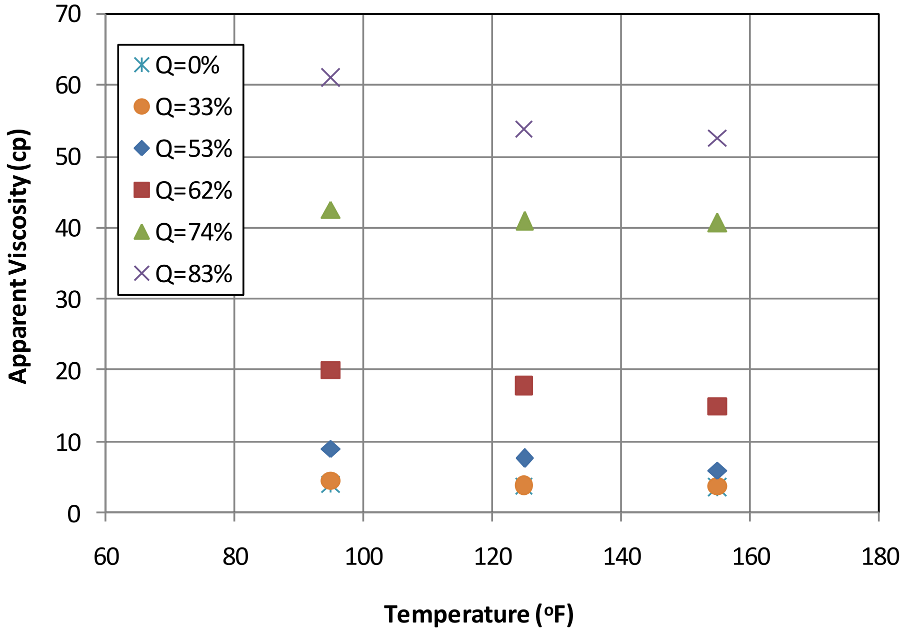

Figure 5.16: Effect of temperature on apparent viscosity for foam A at 500 s^{-1}.

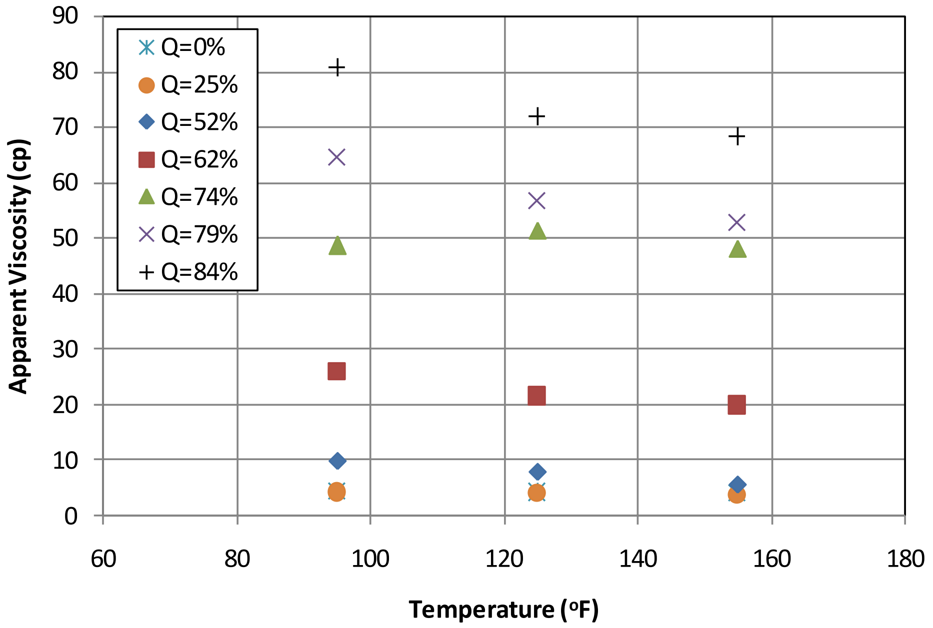

Figure 5.17: Effect of temperature on apparent viscosity for foam B at 500 s^{-1}.

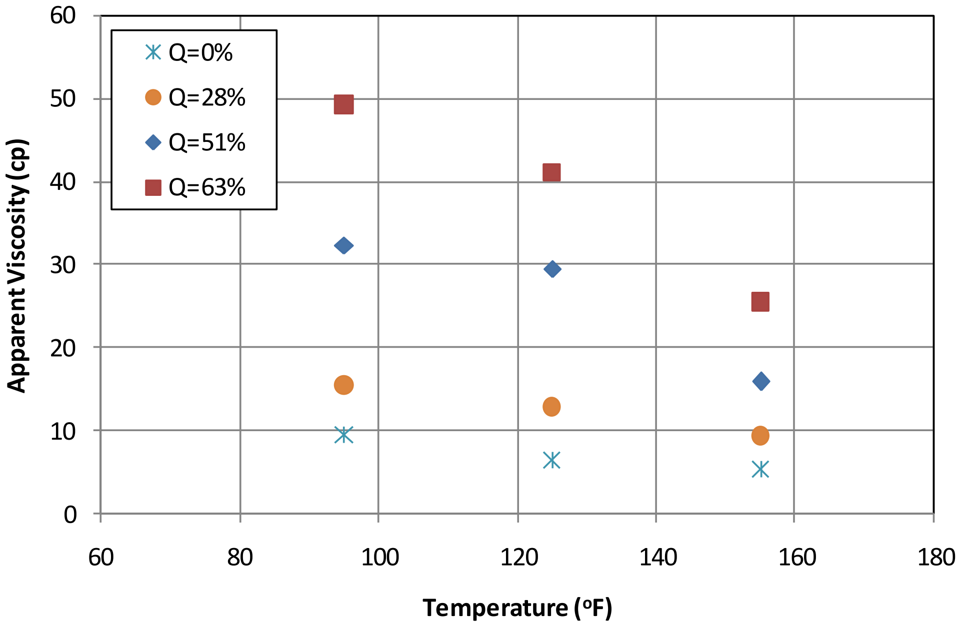

Figure 5.18: Effect of temperature on apparent viscosity for foam C at 500 s^{-1}.

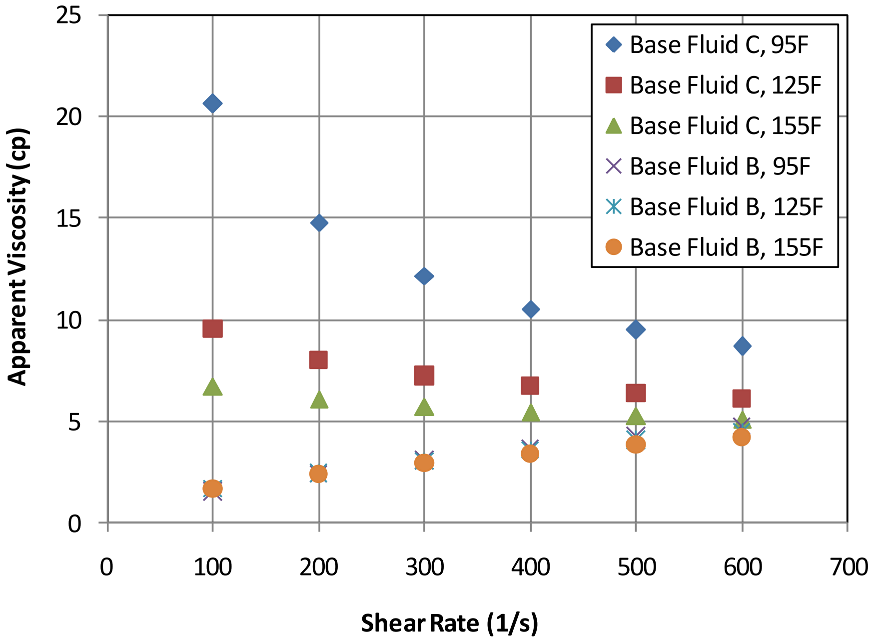

Figure 5.19: Apparent Viscosity vs. Shear Rate for foam base fluids B and C.

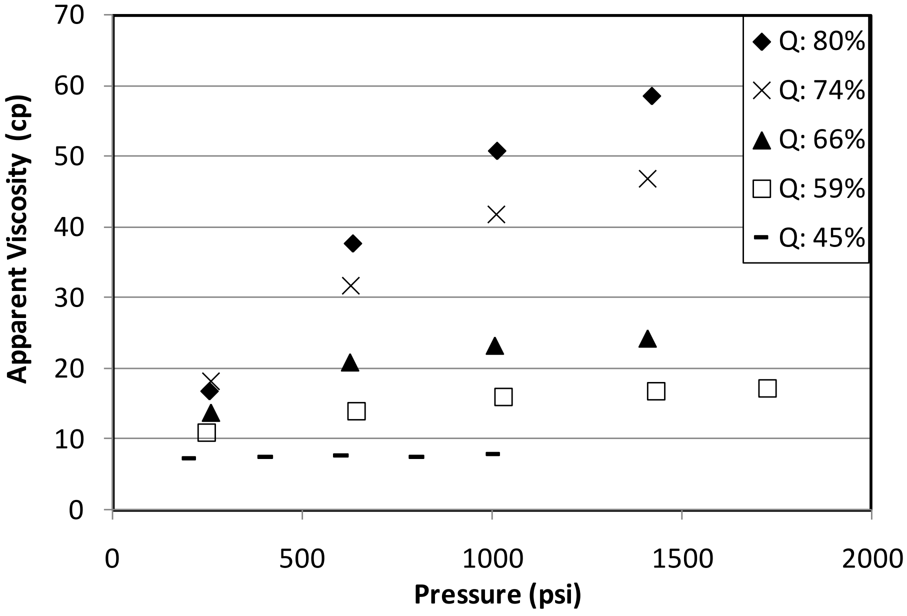

Figure 5.20: Pressure dependence of the apparent viscosity for foam A at 500 s^{-1}.

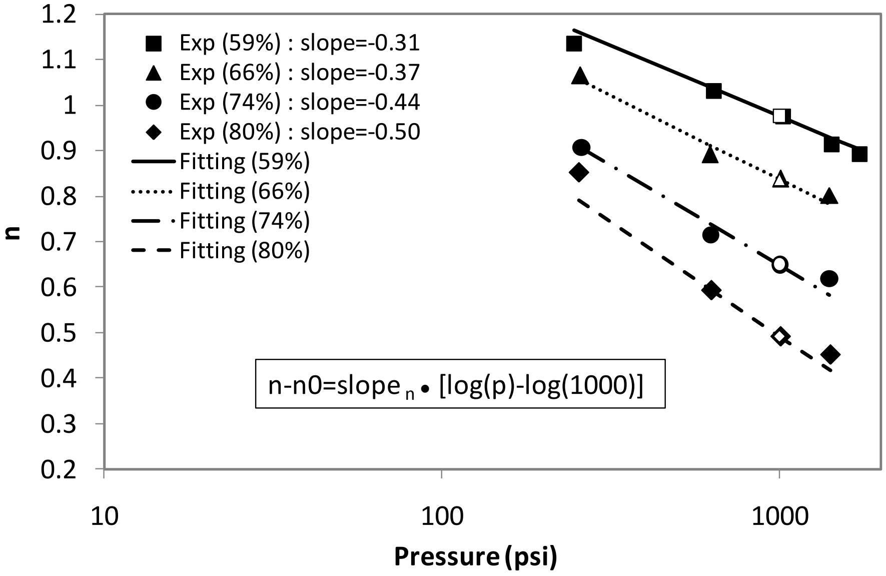

Figure 5.21: Pressure effect on the power law index *n* (solid dots: experimental results, lines: regression results, blank dots: predictions from Eqs. 5.22 &33).

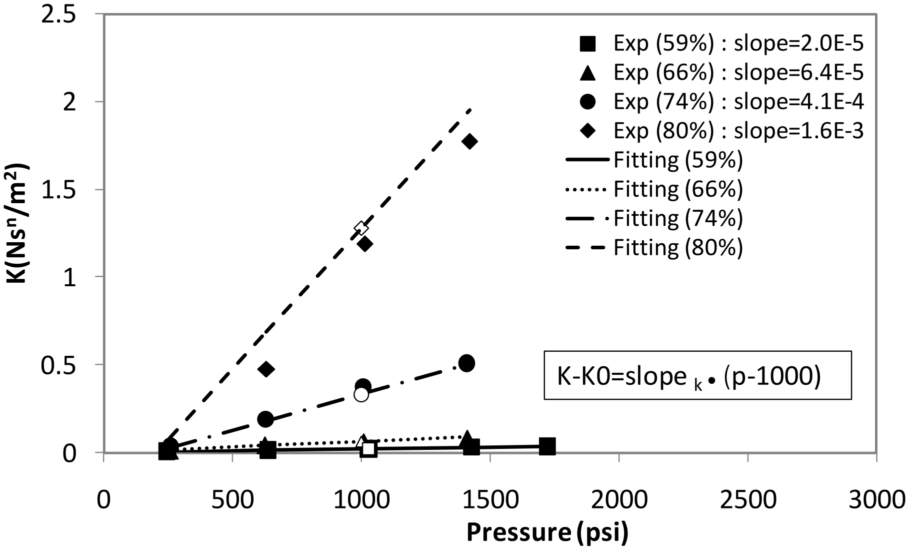

Figure 5.22: Pressure effect on the consistency index *K* (solid dots: experimental results, lines: regression results, blank dots: predictions from Eqs. 5.22 &33).

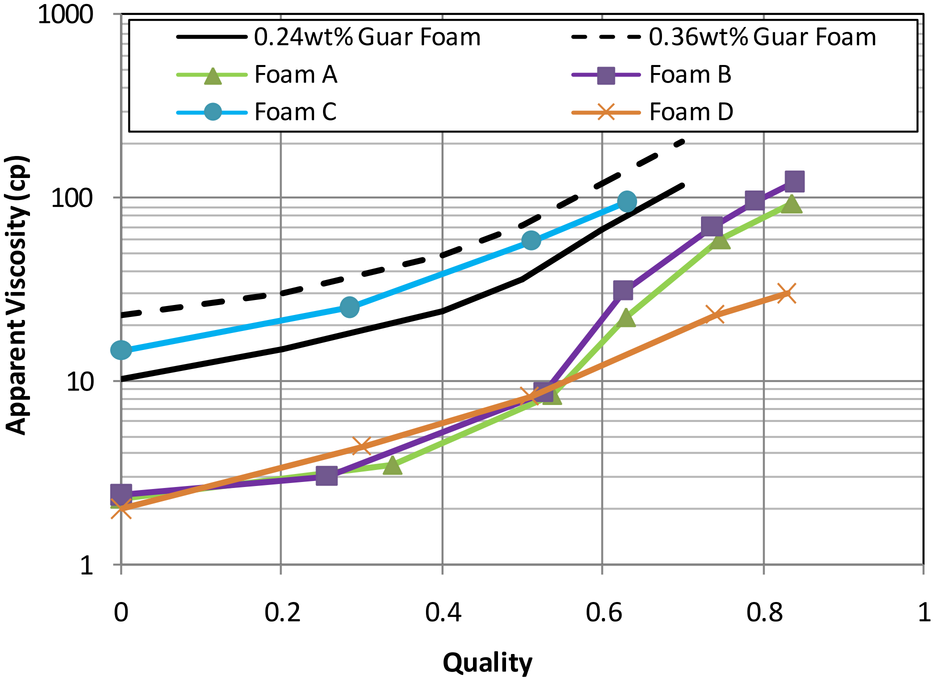

Figure 5.23: Effect of foaming agents on apparent foam viscosity at 95 °F, 1000 psi and 200^{-1}.

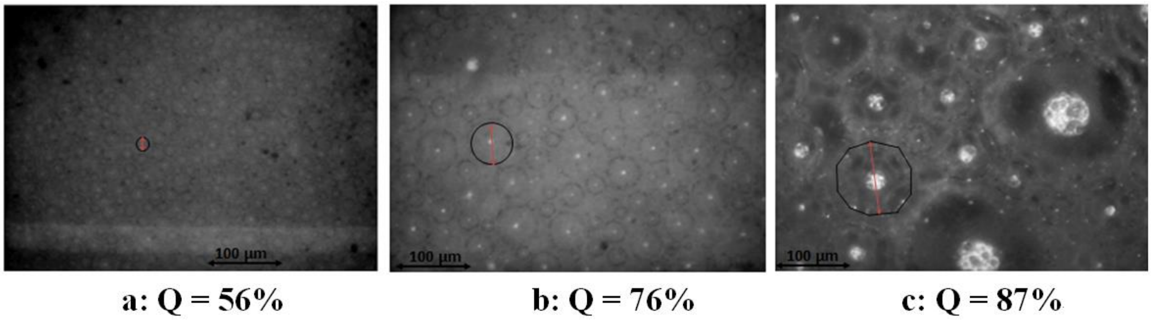

a: Q = 56%
b: Q = 76%
c: Q = 87%

Figure 5.24: Foam bubble texture images for foam A, 95 °F and 1000 psi.

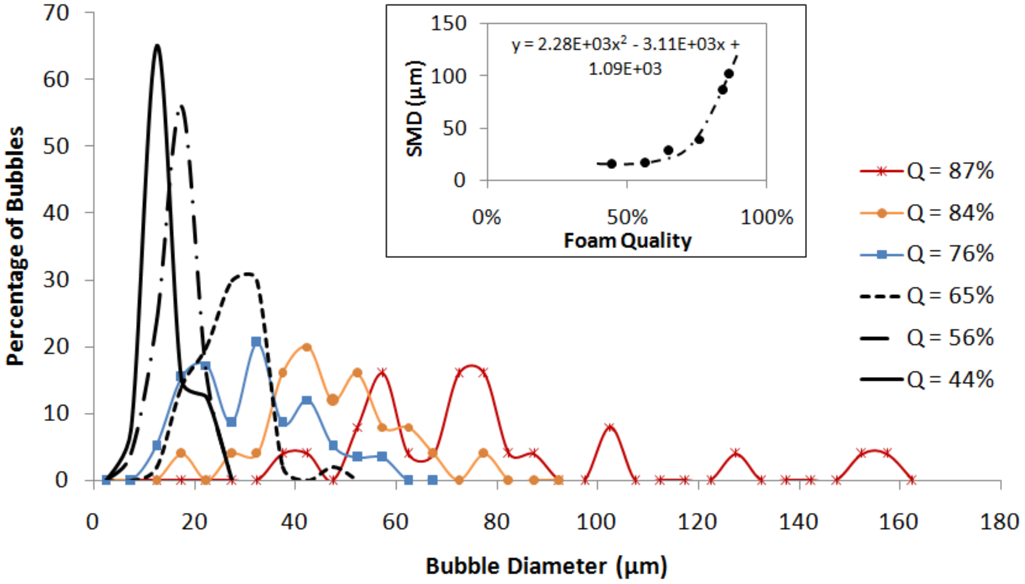

Figure 5.25: Bubble size distribution for foam A, 95 °F and 1000 psi.

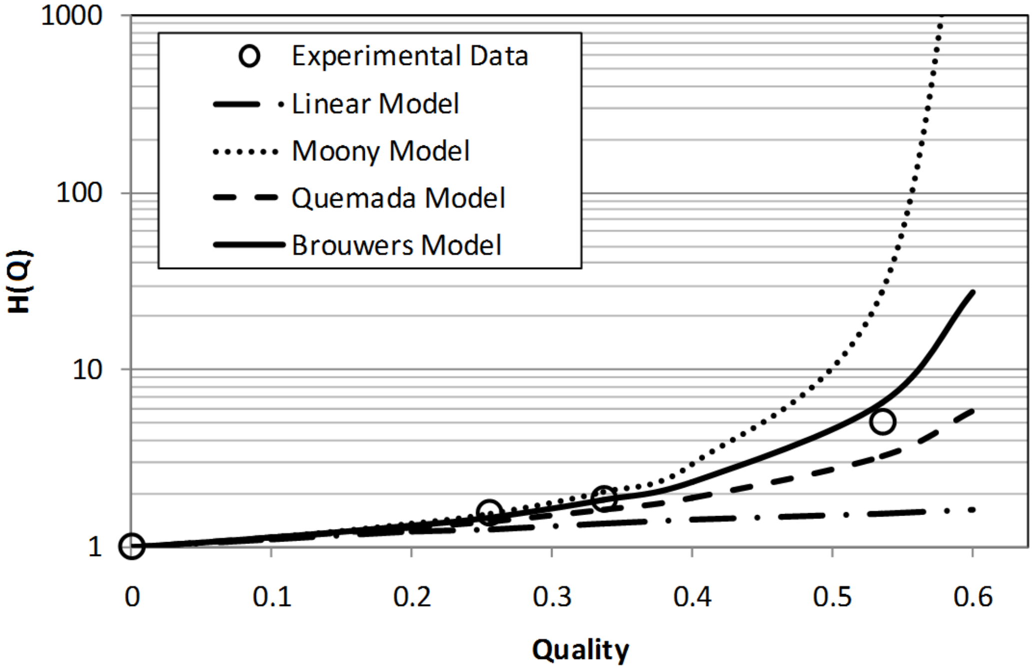

Figure 5.26: Viscosity ratio, *H* as a function of foam quality *Q* as predicted by different theoretical models and as measured (Foam A, 95 °F and 1000 psi).

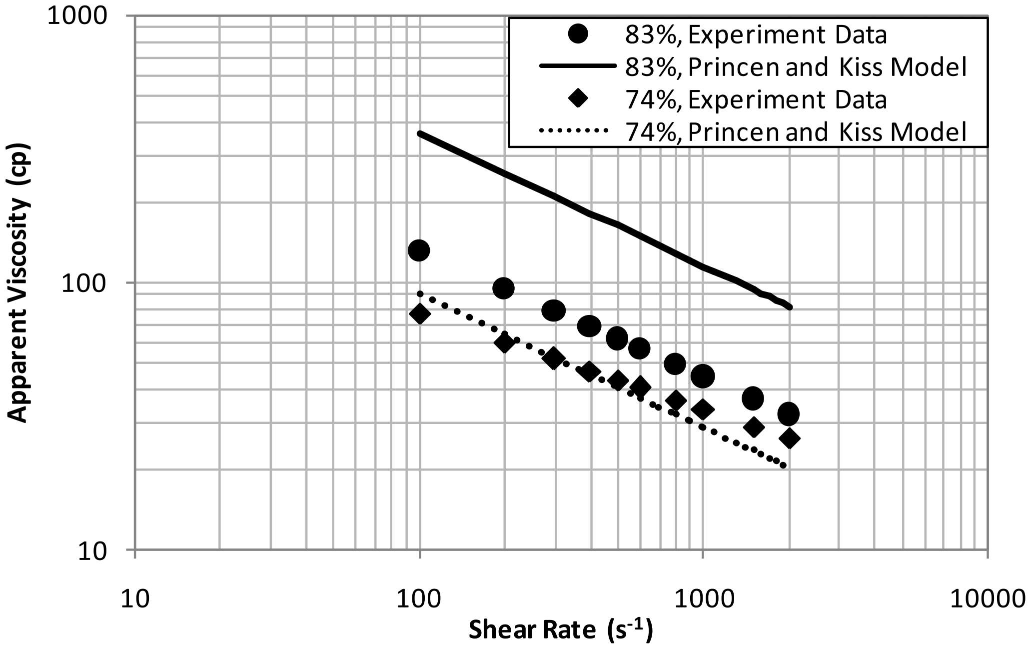

Figure 5.27: Comparison of the experimental results and predictions by Princen and Kiss model (Foam A, 95 °F and 1000 psi).

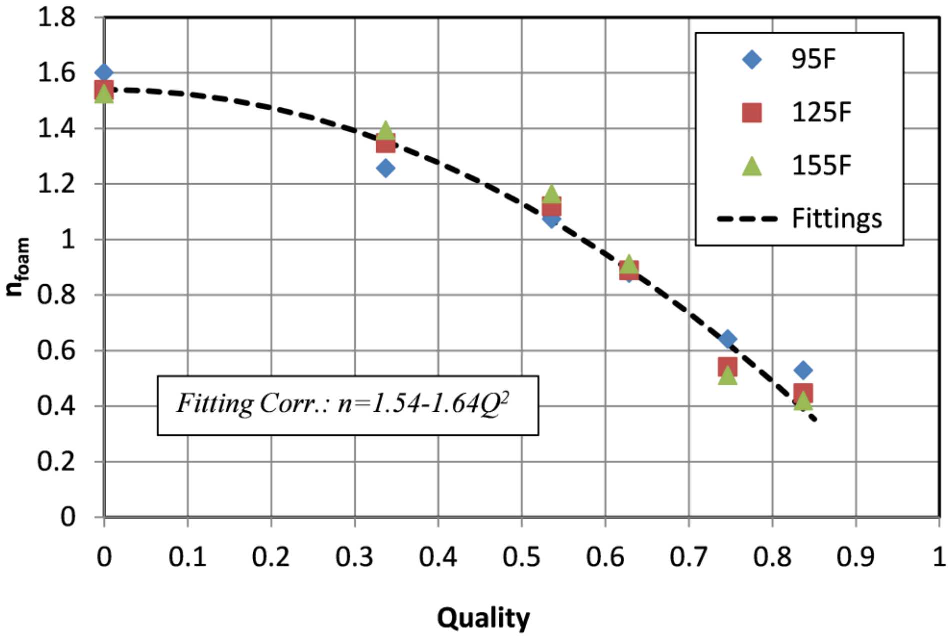

Figure 5.28: Power law index *n* for foam A at 1000 psi *(n_0)*.

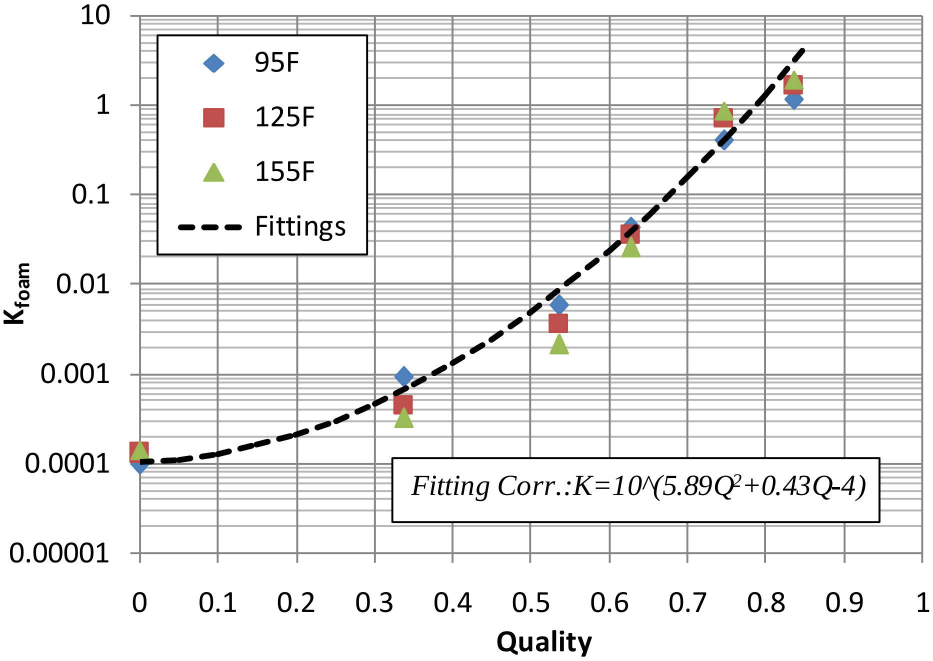

Figure 5.29: Consistency index *K* for foam A at 1000 psi *(K_0)*.

Chapter 6: Fracture Modeling and Simulation Study of Polymer-free Foam in Shale Fracturing

Slickwater can create long and skinny fractures, but cannot transport proppants efficiently. The previous studies have developed polymer-free foams with better proppant transport capacity, but those foams may shorten the length of the fractures due to their higher viscosity. As foam quality increases, the foam apparent viscosity increases, leading to an increase in uniformity of sand distribution and a decrease in fracture length. The goal of this chapter is to study the effect of foam quality on gas productivity of fractured wells in shale reservoirs. A comprehensive parametric study is conducted on foam fracturing treatment by combining the reservoir simulation model in Chapter 2, the fracturing model in Chapter 3, and the foam rheological model in Chapter 5 together.

6.1 OBJECTIVE

According to previous studies, foams can be formulated with different qualities (i.e., gas volume fraction). The foam quality highly affects its rheology and hence the fracture propagation, proppant transport, and foam leakage. As a result, the fracture geometry and conductivity distribution would be affected which would influence the effectiveness of the fracture in gas production. The goal of this work is to study the effect of foam quality on the effectiveness of hydraulic fractures by numerical simulations. The rheology model developed in Chapter 5 is included in the fracture modeling simulator developed in Chapter 3 to predict the fracture geometry and sand distribution for different foam qualities. The sand distribution is converted to the conductivity distribution and input into the reservoir model developed in Chapter 2 to evaluate the productivity of the resultant fractures. Based on the treatment costs, water volumes, and production values, Return-On-Fracturing-Investment ((ROFI) and Return-On-Water-Investment ((ROWI) are calculated for different foam qualities. The two indices are used to measure the effectiveness of the treatments.

Reservoir properties, fracturing fluid, proppant, and pumping schedule are all combined to determine the geometry, propped area and conductivity of the hydraulic fracture. The fracture geometry and conductivity distribution, in turn, control the gas productivity of the well. In this study, foam quality, proppant size, proppant concentration, pumping time and rock permeability are varied to generate different simulation cases. Through comparing the results of different cases, we can understand how polymer-free foams impact the efficiency of fracturing treatment at different treatment designs and reservoir conditions.

6.2 METHODOLOGY

6.2.1 Foam Rheological Model

In the previous experimental work in Chapter 5, the rheology of the polymer-free foam with 0.5wt% anionic surfactant (Bioterge AS40; 39% activity as supplied) was evaluated in a flow loop at different pressures and temperatures. The foams exhibited power-law rheological behavior,

$$\tau = K\gamma^{n} \tag{6.1}$$

where n is the power law index and K is the consistency index. The apparent foam viscosity is calculated by

$$\mu_{ap} = K\gamma^{n-1} \tag{6.2}$$

Foams showed shear thinning behavior at qualities above 60%, non-shear dependent behavior from 50% to 60%, and apparent shear thickening behavior below 50% (due to turbulence). Temperature has negligible impact on the foam viscosity from 95 ^{o}F to 155 ^{o}F, while pressure has negligible impact on the foam viscosity for a foam quality below 60%. Above 60% quality, increasing pressure leads to an increase of the foam viscosity. However, this pressure effect becomes smaller as pressure increases. These aqueous foams are half as viscous as 20 lbm/Mgal guar foams but more than 20 times as viscous as water, under a typical fracturing shear rate of 511 sec^{-1}.

The power law index (*n*) and the consistency index (*K*) were observed to depend on quality (Q) and pressure (P) in psi as follows:

$$n = \begin{cases} \left(1.54 - 1.64Q^2\right) & 0\% \leq Q < 60\% \\ \left(1.54 - 1.64Q^2\right) - \left(0.89Q - 0.21\right)\left[\log(P/1000)\right] & 60\% \leq Q < 85\% \end{cases} \tag{6.3}$$

and

$$K = \begin{cases} 10^{\left(5.89Q^2 + 0.43Q - 4\right)} & 0\% \leq Q < 60\% \\ 10^{\left(5.89Q^2 + 0.43Q - 4\right)} + 8.6\times10^{-11} e^{21Q}\left(P - 1000\right) & 60\% \leq Q < 85\% \end{cases} \tag{6.4}$$

According to the empirical rheological correlations, the rheology of the foam depends solely on the foam quality for qualities below 60%, and depends on both quality and pressure for qualities above 60%.

6.2.2 Propped Fracture Conductivity Model

In this study, two common conventional sands are adopted as proppants. The coarse one has an average mesh size of 20 (10/30), while the fine one has an average mesh size of 40 (30/50). Fracture conductivity is a measure of the flow capacity of a fracture and is defined as the product of the fracture width and the permeability of the proppant pack. The conductivity is dependent upon the fracture closure stress, proppant concentration, size, and strength. In the case of a fracture with a multilayer pack of proppant, the Kozeny-Carman relation can be used to estimate the permeability. The relation can be expressed as,

$$k = \frac{\phi^3}{CS^2(1-\phi)^2} \tag{6.5}$$

The pack permeability *k* is less sensitive to the number of layers of proppant pack as proppant pack thickens. Thus, for thick proppant pack, it can be assumed that multilayer conductivity is linearly correlated with the pack thickness, and hence the proppant areal concentration. To calculate the partial monolayer conductivity, a modified Kozeny-Carman relation, proposed by Darin and Huitt (1960), are adopted,

$$kw_{hf} = 1.1\times10^{10}\frac{w_{hf}}{S_P{}^2}\frac{\phi_P{}^3}{(1-\phi_P)^2} \tag{6.6}$$

where S_P is the wetted surface area per unit volume of propping agent contained between the fracture faces, Φ_P is the porosity, and w_{hf} is the fracture width of partial monolayer, which is determined by an embedment experiment (Huitt and McGlothlin, 1958),

$$w_{hf} = d_p\left[1-B\left(\frac{P_0}{d_p{}^2}\right)^m\right]^{1/2} \tag{6.7}$$

where P_0 is the confining stress on a single particle, *B* and *m* are characteristic constants of the formation, which are assigned values of 1 and 0.00003 in this case. The conductivity predicted by Eqs. 6.6 and 6.7 is valid for rigid, mono-sized, spherical particles under conditions where the propping agents embed in the fracture surfaces rather than being crushed under the overburden load. This usually happens when proppants are much harder than formation rocks. Figure 6.1 plots the estimated baseline conductivity as a function of the proppant areal concentration for two sands. To convert the baseline conductivity to dynamic conductivity, a safety factor of 1/3 is applied, which takes into consideration of proppant diagenesis with time (Duenckel et al., 2012).

6.2.3 Gas Production Simulation

The fracture conductivity distribution is input into a commercial reservoir simulator (CMG-IMEX) to evaluate the fracture gas productivity. Figure 6.2 shows the reservoir-fracture domain simulated for gas production. Similar to the reservoir simulation model shown in Chapter 2, only half of a bi-wing planar fracture and half of the matrix between two adjacent fractures are simulated. The fracture is modeled explicitly as discrete grid blocks. NX * NY * NZ grid blocks describe the matrix and NX * 1 * NZ grid blocks describe the fracture. The permeability of the primary fracture grid blocks (NY=1) are varied according to the fracture conductivity distribution obtained from the fracturing model. The wellbore is connected to the system at the first column of grid blocks. Initially, the matrix as well as the fracture are assumed to be filled with gas (SG = 0.55) at the initial reservoir pressure of 3300 psi. The wellbore pressure is set at 500 psi at time t=0. CMG IMEX calculates the subsequent pressure field, velocity field and gas production for 20 years.

Assuming all the fractures are the symmetric bi-wing planar fracture with the equal length, the wellbore production can be calculated by multiplying the simulated fracture productivity with the number four and the number of the fractures along the horizontal well.

6.2.4 Parametric Study Strategy

By incorporating the foam rheology (Eqs. 6.1-6.4) in the fracture propagation model, the fracture geometries created by different quality foams under a typical shale reservoir environment are predicted. Further solving the proppant transport equation, the proppant concentration distribution within the fracture can be simulated. The simulated proppant concentration distribution is subsequently converted to the fracture conductivity distribution by using Figure 6.1, which is input into the reservoir simulation model (Figure 6.2) to calculate the fractured well productivity. Based on the productivity, ROFI and ROWI can be calculated and compared for different treatment designs. The effects of important treatment parameters, such as foam quality, sand size, sand injection concentration, and pumping schedule on well performance in different permeability shale reservoirs are investigated. All the steps introduced above are combined together to form a parametric study loop shown in Figure 6.3.

The reservoir properties and treatment parameters assumed in the simulation model are listed in Table 6.1. The parameters of interest including foam quality, sand size, injected sand concentration, and shale permeability are varied, as shown in Table 6.2. The foams of quality (60-80%) are investigated and compared with the reference slickwater case which has a quality of 0%. In current study, we do not consider foams with quality below 60% because wet foams (Q<60%) have similar or even poorer proppant transport capacity compared with slickwater due to their slightly increased viscosity and lower apparent fluid density. Another reason is that wet foams (Q<60%) are not stable with two-phase segregation occurring at low shear rate. The sand size is either 20 mesh or 40 mesh. The sand injection concentration is varying from 0.02 volume fraction (v/v) to 0.1 volume fraction (v/v). For all the cases, the initial pad injection time is 20 minutes followed by 40 minutes of slurry injection and 20 minutes of shut-in. Finally, a range of shale permeability also needs to be determined for the current study. Tinni et al. (2012) used the GRI technique to test matrix permeability of different shale rocks including Eagle Ford, Ordovician and Haynesville. The values vary from 0.4 nD to 200 nD based on particle size. Zhou et al. (2013) measured the shale permeability for

Barnett and Eagle Ford using the pressure transient technique. The Barnett shale permeability is 337 nD and the cracked Eagle Ford shale sample has a permeability of 60 μD. Heller and Zoback (2013) conducted intact plug permeability measurements and found that Barnett has a permeability in the range of 60-160 nD, Eagle Ford in the range of 5-40 nD, and Marcellus in the rage of 20-60 nD. The carbonate streak improves the permeability to 0.8-1.8 μD in the Barnett and to 6-12 μD in the Eagle Ford. To cover a typical range of shale permeability, the shale permeabilities adopted in this study are 0.1, 1 and 10 μD.

6.3 RESULTS AND DISCUSSIONS

This section first discusses the fracture geometries created by slickwater pad and foam pads with different foam qualities. After that, the propped area, conductivity distribution, productivity, ROFI, and ROWI of all the cases in table 6.2 are simulated and compared. Based on the simulation results, the impact of the treatment parameters, such as foam quality, sand size, sand injection amount, and pumping time on shale fracturing effectiveness is investigated.

6.3.1 Fracture Geometry Created by Water Pad vs. Foam Pad

In this study, different clean fluid pads without proppants are studied under low permeability (0.1 μD), medium permeability (1 μD) and high permeability (10 μD) shale formations. Figures 6.4 - 6.6 show the fracture widths created by different quality foams (0, 60, 70, 80%) in three permeability shale reservoirs, respectively. All figures show that slickwater creates the narrowest fracture, due to its lowest viscosity. Generally speaking, for foams with a quality above 60%, the fracture length decreases and the fracture width increases with foam quality due to an increase of foam apparent viscosity. For 0.1 and 1 μD, water creates the longest fracture than all foams. As shale permeability increases to

10 μD, the fracture length of slickwater is decreased to lower than that of the 60% foam because of much poorer efficiency (higher leakage) of water compared with high quality foams.

Figure 6.7 shows the leak-off percentage for water and foams in different permeability shale reservoirs. It is observed that, for the slickwater cases, around 60% of water is lost to 10 μD formation, around 27% of water is lost to 1 μD formation, and 10% of water is lost to 0.1 μD formation, after 60 minutes treatment. As the quality increases, the leak-off percentage decreases. The largest drop of leak-off occurs at a quality between 40% and 60%.

From the above results, it can be noted that the fluid viscosity, by affecting the net pressure inside the fracture and the leak-off rate, is the key determinant of the fracture geometry. High viscosity leads to fracture width growth rather than length growth. Thus, for shale permeability lower than 1 μD, lower quality foams or water are better than higher quality foams in creating longer fractures. As reservoir permeability increases, leakage becomes a dominant factor which limits fracture propagation. Thus, for shale permeability of 10 μD, the fracture length created by water is largely decreased, which becomes comparable to those of 60-70% quality foams and 30% longer than that of 80% foam.

6.3.2 Conductivity and Propped Area Created by Slickwater vs. Foams

The reservoir properties and the treatment parameters adopted in the simulation model are listed in Table 6.1. The parameters of interest including foam quality, sand size, injected sand concentration, and shale permeability are varied, as shown in Table 6.2. The foams of quality (60-80%) are compared with slickwater with a quality of 0% and a constant viscosity of 5.7 cp. Sand size is either 20 mesh or 40 mesh. The sand injection volume concentration is varied from 0.02 volume fraction (14 lbm/bbl) to 0.1 volume fraction (70 lbm/bbl). Shale permeability of 0.1, 1 and 10 μD are considered. For all the cases, the initial pad injection time is 20 minutes followed by 40 minutes of slurry injection and 20 minutes of shut-in.

In this section, the conductivity distributions created by slickwater and different quality foams are compared. Figures 6.8, 6.9, 6.10 and 6.11 illustrate the two dimensional conductivity distributions (after closure) across the fracture face created by the slickwater, 60%, 70%, and 80% foams, respectively, in a 1 μD shale. The blue colored areas are the un-propped regions with little or no proppants. Their conductivities are the same as that of the reservoir. All other colored (red/yellow/green) areas are propped zones with different conductivities.

First of all, comparing slickwater and different quality foams with the same injection amount of the same mesh size sand, sand can be placed more uniformly along the vertical direction by higher quality foams, because the higher fluid viscosity due to the higher foam quality results in the lower sand settling rate. For the current permeability shale formation (1 μD), the propped distance is negatively correlated with foam quality. For example, sand is placed deepest in the fracture by the slickwater (but only at the bottom of the fracture) and shallowest by the 80% quality foam. The reason is that lower quality, lower viscosity foam (or water) travels faster and deeper into the formation.

Second, comparing the same fracturing fluid with different sand mesh sizes, the opened fracture widths are almost independent of the sand size. By using mesh 40 instead of mesh 20, the propped areas and the propped lengths are largely increased for the water and 60% quality foams, while they are almost the same for the higher quality foams (70-80%). From the Stokes Law, the settling rate is proportional to the square of proppant diameter. So if the sand diameter is decreased by 2, the settling rate should decrease by 4 in the Stokes flow regime. According to our study, the decrease of settling in high quality foams, where settling rate is already close to zero, is much less significant than that in low quality foams and slickwater, where settling rate is relatively high. So, fine sand is preferred in water and low quality foams, while coarse sand is preferred in high quality foams. When the sand size is reduced by half, the conductivity of the propped fracture is decreased from 1000-5000 md-ft to 10-1000 md-ft for both slickwater and all three foams. According to the previous critical conductivity study, the conductivity generated by mesh 20 is much larger than the critical conductivity of most shale fracturing conditions, but the conductivity generated by mesh 40 may be above or below the critical conductivity depending on the reservoir permeability, fracture length and production time.

Third, for each fracturing fluid and mesh size sand, the conductivity distributions generated from different proppant injection amount are compared. For slickwater, most of the sand accumulates at the bottom of the fracture to form a thin, high conductivity sand bed with a large amount of the upper zone un-propped at low injection concentration. As sand injection amount increases, the sand bed becomes larger with more upper areas propped. For 60% quality foam with 20 mesh sand, the similar pattern is observed: a higher sand bed is formed due to higher sand injection amount. For 60% foam with 40 mesh sand, and higher quality foams (70-80%) with both sands, because of their good sand suspension capability, the fracture face is fully covered by sand within the propped length at all sand injection concentrations. It is observed that the conductivity generated at lower sand injection concentration is larger than that at higher sand injection concentration. The reason is that at low sand injection concentration, a partial monolayer forms, which has conductivity comparable or larger than the multilayer conductivity according to Figure 6.1.

Finally, this section only presents the conductivity distribution results in a 1 μD shale. From the pad study in the previous section (Figures 6.4-6.7), the fracture geometry (length and width) of water and 60% quality foams are more affected by shale permeability, due to their higher leakage, as compared with higher quality foams. It is also true for the conductivity distributions. For high quality foams (70-80%), the conductivity distribution is almost the same for shale permeability of 0.1, 1 and 10 μD. For low quality foam (60%) and slickwater, as shale permeability increases from 0.1 to 10 μD, the sand bed becomes higher and shorter because of the increased limitation of fracture propagation due to higher leakage.

6.3.3 Fracture Productivity Generated by Slickwater vs. Foams

This section compares the short-term (1 year), medium-term (5 year) and long-term (10 year) fracture productivity generated by slickwater and different quality foams at the same pumping schedule. The effects of the reservoir property (e.g. permeability) and treatment parameters (e.g. foam quality, sand size, and sand injection amount) on fracture productivity are investigated.

6.3.3.1 Water vs. Foams for Different Permeability Shales

Figures 6.12, 6.13 and 6.14 plot the 1 year cumulative productions as a function of sand injection amount for different fracturing fluids in 0.1 μD, 1 μD and 10 μD shale reservoirs, respectively. Blue lines are slickwater, red lines are 60% quality foam, green lines are 70% quality foam, and purple lines are 80% quality foam. Solid lines denote 20 mesh sand and dashed lines denote 40 mesh sand. Similarly, Figures 6.15-17 plot the 5 year cumulative productions and Figures 6.18-20 plot the 10 year productions.

Focusing on 1-year production, comparing production results generated in different permeability reservoirs (Figs. 6.12, 6.13 & 6.14), a similar trend is observed: slickwater shows the worst productivity among all the fracturing fluids, while 70% foam shows the best productivity among all fracturing fluids carrying 20 mesh sand and 60% foam shows the best productivity among all fracturing fluids carrying 40 mesh sand. The reason is that in the short-term production, all three permeability reservoirs stay in the transient flow regime or transition regime. The productivity is proportional to the propped area and the conductivity within it. The larger the propped area is, the higher the short-term productivity could be. In this case, since slickwater has much poorer sand distribution efficiency, with most sand accumulating at the bottom of the fracture, than foams, it has the worst short-term productivity.

Focusing on 5-year production, for 0.1 and 1 μD permeability reservoir (Figs. 6.15 & 16), slickwater still yields the worst productivity while foam 60% and 70% yield the best productivity. As reservoir permeability increases to 10 μD, slickwater has better productivity than 80% foam at all sand injection concentrations and better productivity than 70% foam at a sand injection concentration higher than 0.08 v/v. The reason is that 0.1 and 1 μD reservoirs are still in the transient flow region where propped area dominates the production. So the production trends for different fracturing fluids are similar to the 1 year case. For 10 μD reservoir, because it is depleted much faster, the flow regime already changes from transient flow to the pseudo steady state flow after 1 year production. In this regime, the productivity is mainly dependent on the propped length. The longer propped length yields slower decrease of the production rate and hence the higher medium-term cumulative production. According to Figure 6.6, foam 60% has the longest propped length, slickwater has the second longest, and foam 80%

has the shortest propped length, which agrees well with the 5-year productivity trends in Figure 6.17.

Focusing on 10-year production, the comparison of 10 -year production generated by slickwater and different quality foams in a 0.1 μD shale (Fig. 6.18) shows a similar trend to that observed in medium and short-term production. For a 1 μD shale (Fig. 6.19), slickwater with mesh 40 yields a better productivity than 80% quality foam and a similar productivity as 70% foam at high injection concentration (> 0.08v/v). For a 10 μD shale (Fig. 6.20), slickwater and 60% foam have the best 10-year productivity while 80% foam has the worst 10-year productivity. The reason is similar to the one proposed in the 5-year production.

Overall, 60% and 70% foams carrying mesh 40 sand exhibits the best short, medium and long-term productivity in a 0.1 μD shale, short and medium-term productivity in a 1 μD shale, and short-term productivity in a 10 μD shale, due to their capacity of creating largest propped area with a uniform proppant distribution. Under most conditions, slickwater performs worse than the foams in production. Slickwater overtakes 80% quality foams only for the 10 year long-term production in a 1 μD shale and medium to long term-production in a 10 μD shale. Based on the productivity comparison, foams are preferred in low permeability shales (0.1, 1 μD) or high permeability shales (10 μD) for short & medium-term production. Among all the foam cases, 60-70% quality foams perform better than 80% quality foams in creating larger propped area, longer propped length and hence generating better short, medium and long-term productivity.

6.3.3.2 Water vs. Foams for Different Sand Sizes

For each simulation, sand of two mesh grades are simulated and plotted as solid lines (mesh 20) and dashed lines (mesh 40) in Figures 6.12 - 6.20. Comparing the dashed lines and solid lines at the same color in each figure, the impact of sand size on fracture productivity can be evaluated. For the 1 year short-term production in low permeability reservoirs (0.1 and 1 μD) (Figs. 6.12 & 6.13), decreasing sand size by half has the largest productivity improvement for 60% foam, the second largest productivity improvement for slickwater, the third largest productivity improvement for 70% foam, and negligible impact on the productivity of 80% foam. The productivity changes, due to the change of sand mesh size, match well with the observations for the propped area changes in Figures 6.8 – 6.11, where the 60% quality foam and slickwater has the largest propped area increase, while the 70 and 80% quality foams have little propped area increase, after the use of the 40 mesh sand instead of the 20 mesh. The reason is that for low permeability shales in short-term production, it is the propped area rather than the conductivity and propped length that determines the stimulated fracture productivity. Decreasing sand mesh size can help the proppant transport into a larger area and a longer distance in a low viscous fluid. For 1 year short-term production in the high permeability shale (10 μD) (Fig. 6.14), the production improvement due to the decrease of the sand size is smaller than those observed in the lower permeability cases. The productivity improvement is only observed in a partial monolayer concentration (low sand injection amount) for all four fracturing fluids. As injection amount increases, fracture productivities of using mesh 40 drop to similar levels of using mesh 20 (for 60% foam and slickwater) and to a lower level (for 70 & 80% foam). The reason is that, for high permeability shale (10 μD) in short-term production, propped area and conductivity both determine the fracture productivity. The productivity improvement due to an increase of propped area is offset by a decrease of conductivity by using smaller size sand. According to Figs. 6.8 - 6.11, the decrease of conductivity by using a finer sand is more significant in multi-layer proppant concentration created by a larger sand injection amount (> 0.04 v/v) than in partial monolayer concentration created by injecting sand at a small volume concentration of 0.02 v/v.

As production time increases to medium and long term (5-10 years), the relative improvement of fracture productivity by using finer sand are almost the same as that observed in 1 year production for two low permeability shales (0.1, 1 μD). The possible reason is that the low permeability shales are still in transient flow regime or transition flow regime after 5 or 10 years, and propped area is still the dominant factor for productivity in these flow regimes. For a 10 μD shale, using mesh 40 has a positive productivity impact on 60% foam and slickwater, but almost no impact on higher quality foams. The possible reason is that, after 5 years, the high permeability (10 μD) shale is in pseudo steady state flow regime, where propped length has a larger impact on productivity than propped area and conductivity. Figures 6.8 - 6.11 show that decreasing sand mesh size enlarges the propped distance only for two low viscous fluids. Thus, 60% foam and slickwater have medium and long-term productivity improvements in a 10 μD shale.

Overall, mesh 20 sand has a significant settling issue in slickwater and 60% quality foam. Using mesh 40 instead of mesh 20 can improve the settling issue and enlarge the propped areas and lengths for those low viscous fluids. Thus, decreasing sand size from 20 mesh to 40 mesh improves productivity more for 60% foam and slickwater than higher quality foams for both low permeability shales (0.1, 1 μD), which stay in transient flow regime in most of their production lives, and the high permeability shale (10 μD), which quickly step into pseudo steady state flow regime after 1 year production.

Based on previous critical conductivity analysis, mesh 40 can fulfill the conductivity requirements in most conditions for our three permeability shales, except the 10 μD shale in a short-term production within 1 year. Considering its better transport capacity with lower viscous fluids like water and 60% foam, it is a more ideal proppant candidate than mesh 20 in shale fracturing. In later ROFI and ROWI study, the simulation cases with mesh 40 are only considered and evaluated.

6.3.3.3 Water vs. Foams for Different Sand Concentrations

Given the same fracturing fluid and sand, the sand injection volume concentration is varied from 0.02 v/v (14 lbm/bbl) to 0.1 v/v (70 lbm/bbl). The fracture productivity is plotted against to injection concentration for all simulation cases as shown in Figures 6.12 - 6.20. For most conditions with different production time and different reservoir permeability, the impact of sand injection concentration on productivity decreases with increasing foam quality. For example, in a 0.1 μD shale, 1 year cumulative production is increased by 62% for slickwater, 47% for 60% foam, 21% for 70% foam, and 14% for 80% foam, when mesh 20 sand injection concentration is increased from 0.02 v/v to 0.1 v/v (solid lines shown in Fig. 6.12).

Besides, for some cases, the impact of sand concentration on productivity decreases with decreasing sand size. For example, in a 0.1 μD shale, 1 year cumulative production is increased by 11% for 60% foam, 7.8% for 70% foam, and 7.3% for 80% foam, when mesh 40 sand injection concentration is increased from 0.02 v/v to 0.1 v/v (dashed lines shown in Fig. 6.12). Comparing the results for mesh 40 with the results for mesh 20 shown in the previous paragraph, the productivity of foam fracturing with mesh 40 is less sensitive to the change of sand injection concentration.

Overall, as the proppant transport efficiency increases, the impact of the sand injection concentration decreases, because, with decreasing sand settling rate, increasing sand injection amount can only alter the conductivity, not the propped area and propped length. The conclusion is only valid for cases of low shale permeability or long production time, where propped area and propped length are the key determinants of productivity. For cases of high permeability shales (10 μD) or short production time, where fracture conductivity has a large impact on productivity, changing sand injection amount (volume concentration) can bring some changes to productivity (eg. red and green dashed lines shown in Fig. 6.14).

Generally speaking, when the low concentration of sand is used, high quality foams, benefiting from their good sand suspension capacity, can place the low concentration sand in a partial monolayer and get a similar productivity to that of the high sand concentration cases, while low quality foams and slickwater only place the sand as a multi-layer bed at the bottom and leave a large amount of upper area un-propped or insufficiently propped, leading to much poorer production performances than those of the high sand concentration cases.

6.3.4 ROFI Generated by Slickwater vs. Foams

The ROFI, return on fracturing investment, is a measure of the economic success of the stimulation work, which is defined as the fracture performance (value of the gas produced after certain time) relative to the cost of the hydraulic fracturing treatment (Brannon and Starks II, 2008, 2009). It can be estimated by simply subtracting the fracturing treatment cost from the value of the stimulated production. The fracturing treatment costs are highly variable, depending on equipment, materials, pumping costs and other service fees. In this section, for simplification, all the treatment fees, except the raw material fees, are ‘bundled’ to be a cost of \$2.5/gal of total pumping volume employed for slickwater, and \$2.9/gal of total pumping volume employed for foams (Burke et al., 2011). The price of the fresh water is assumed to be \$1/bbl. The foam treatment cost is the sum of the water cost and the nitrogen gas cost, which is assumed to be \$0.23/gal for the liquid nitrogen. The sand cost is \$40/ft^3. The estimated fluid/proppant volumes as well as their costs, the ‘bundled’ treatment costs, and the final total costs for each of the preceding examples are shown in Table 6.3. The gas production value has been estimated by multiplying cumulative production by a unit natural gas price of \$4/Mscf.

ROFI is calculated for slickwater and different quality foams with mesh 40 sand based on 1 year and 5 year production. The reason is that 1 to 5-year production periods are commonly used to evaluate NPV of a stimulated well in shale reservoirs. ROFI of each case is divided by the ROFI of reference case (slickwater + 0.1 v/v sand) to get the normalized ROFI. Figures 6.21 - 6.23 plot the normalized ROFIs for all fracturing cases in 0.1,1 and 10 μD permeability shales, respectively.

In a 0.1 μD permeability shale (Figure 6.21), 60% quality foam has the best ROFI, followed by 70% foam, 80% foam, and slickwater. For slickwater, ROFI is positively correlated with sand injection concentration. So the reference case has the largest ROFI among all slickwater cases. Other slickwater cases have a normalized ROFI lower than 1. For 60% and 70% foams, the ROFIs are not very sensitive to the sand injection concentration when the sand injection concentration is above 0.04 v/v. Within that injection concentration range, 60% foam has a ROFI around 1.7 to 1.8 times as large as that of the reference slickwater case after 1 year and 1.5 to 1.6 times as large as that of the reference case after 5 years. The 70% quality foam has a ROFI around 1.4 to 1.5 times as large as that of the reference slickwater case after 1 year and 1.3 times after 5 years. The 80% quality foam has a ROFI slightly above that of reference case at all sand injection concentrations. According to the results above, it is noted that, although the treatment cost of the foam fracturing is 10-20% higher than the reference slickwater case, the ROFI generated by our foams are still better than that generated by slickwater in a 0.1 µD shale. The ROFI benefits of using foams decreases with the time. The reason is the same as the one explaining why the productivity benefits of using foams decrease with time.

As shale permeability increases to 1 µD (Figure 6.22), the normalized ROFIs for all foams are decreased by different extents. The 60% quality foam has a ROFI around 1.4 to 1.5 times as large as that of the reference slickwater case after 1 year and 1.2 to 1.3 times as large as that of the reference case after 5 years. The 70% quality foam has a ROFI around 1.2 to 1.3 times as large as that of the reference slickwater case after 1 year and 1.05 to 1.08 times after 5 years. The 80% quality foam has a ROFI equivalent to that of the reference slickwater case after 1 year and a ROFI 10% poorer after 5 years.

Further increasing shale permeability to 10 µD (Figure 6.23), the ROFI benefit of using our foams instead of slickwater is further decreased. For this circumstance, the 60% quality foam has its best ROFI at partial monolayer sand concentration (0.02 v/v), with a value of 1.36 times as large as the ROFI of the reference slickwater case after 1 year and 1.07 times as large as that of the reference case after 5 years. The 70% quality foam also has its best ROFI at partial monolayer sand concentration (0.02 v/v), with a value of 1.19 times as large as the ROFI of the reference slickwater case after 1 year and 0.94 times as large as that of the reference case after 5 years. The 80% quality foam always yields a worse ROFI than slickwater no matter in the short-term (1 year) or medium-term (5 year).

Overall, the polymer-free foams can generate a better ROFI than conventional slickwater in all three permeability shales. Among all the cases, the 60% quality foam is the best and 70% quality foam is the second best. In low permeability shales (0.1, 1 μD), ROFI of foam treatments is not sensitive to sand injection amount once the sand injection volume concentration is above 0.04 v/v. In the high permeability shale (10 μD), the foams with 0.02 v/v sand injection concentration can create a high conductivity partial monolayer sand pattern and yield a better ROFI than other higher sand injection concentrations. The ROFI benefits of using foams decrease with production time.

6.3.5 ROWI Generated by Slickwater vs. Foams

There is another important index, the return on water investment (ROWI), which represents the fracture performance relative to the total consumption of the water. It is the economic profit generated at per unit of water consumed ($\$/m^3$), known as water economy for short. This index is applied under the circumstance where environmental issues, such as fresh water usage and waste water disposal, are emphasized. It is estimated by simply dividing the ROFI by the total water volume applied in the fracturing treatment.

Similar to the previous ROFI study, ROWI is calculated for slickwater and different quality foams with mesh 40 sand based on 1-year and 5-year production. Then, ROWI of each case is divided by the ROWI of the reference slickwater case (0.1 v/v sand) to get the normalized ROWI. Figures 6.24 - 6.26 plot the normalized ROWIs for all example fracturing cases in 0.1, 1 and 10 μD permeability shales, respectively. Comparing all calculated ROWIs, it is noted that the ROWI increases with the foam quality, decreases with the production time and shale permeability. The average ROWIs of using 80%, 70%, and 60% quality foams are around 4.7, 4, and 3.4 times as large as the ROWI of the reference slickwater case in all shales. The gap between the better foam case and the worse water case is larger in the Normalized ROWI charts compared to the Normalized ROFI charts. Thus, foams can be a much better alternative to the slickwater when the water economy and environment concerns are emphasized. Overall, considering both NPV and water economic efficiency, the 60% and 70% quality foams carrying 40 mesh sands with a partial monolayer concentration might be the best treatment design in shale reservoirs. For 0.1-1 μD permeability shales, the optimum sand injection volume concentration is 0.04 v/v, while for a 10 μD permeability shale, the optimum sand injection volume concentration is 0.02 v/v.

6.3.6 Slickwater vs. Foams at Different Pumping Schedules

The foam fracturing design is further optimized by varying the total pumping time from 30 minutes to 90 minutes. In all treatments, the initial pad injection time is half of the slurry injection time. Table 6.4 lists all the cases for the parametric study for the impact of pumping time on fracturing performance. In this study, fracturing fluids are slickwater (reference cases) and the 60% quality foam. In the stage of slurry injection, mesh 40 sand is injected at a volume concentration of 0.1 v/v. Each treatment is applied in three different permeability shales: 0.1, 1 and 10 μD.

Figure 6.27 compares the conductivity distributions for slickwater treatments and 60% foam treatments at different pumping time and different permeability shales. Generally speaking, propped area and propped length increase as the pumping time increases. For slickwater, the conductivity distribution becomes more non-uniform, leaving more upper area unpropped within the propped length, as pumping time increases, while, for 60% foam, the conductivity distribution is always uniform, making all areas propped within the propped length, at all pumping times. Furthermore, as shale permeability increases, there is an apparent decrease of the propped length for slickwater, and no obvious change for the foam. For all the cases studied, conductivity is slightly decreased when shale permeability increases from 0.1 to 1 μD, and is almost constant when shale permeability further increases from 1 to 10 μD.

Based on 5 year medium-term production, the ROFI and ROWI of all cases are calculated. The calculated ROFIs and ROWIs for all cases are divided by the ROFI and ROWI of the reference case (slickwater at 60 min pumping time) to obtain the normalized ROFI and normalized ROWI. Figures 6.28 - 6.30 compare the normalized ROFIs (solid lines) and normalized ROWIs (dashed line) of different pumping time for the 60% quality foam treatment and the slickwater treatment in 0.1, 1, and 10 μD permeability shales, respectively. Red color denotes the foam, and blue color denotes the slickwater. The stars are the reference points with a value of 1 for both normalized ROFI and normalized ROWI.

In a 0.1 μD shale (Fig. 6.28), the ROFI of the foam increases with pumping time, while the ROFI of the slickwater is almost constant across different pumping time. The ROFI of the foam treatment is always better than that of the slickwater treatment, which is 3% larger than the reference slickwater case at 30 minutes pumping time and 95% larger than the reference slickwater case at 90 minutes pumping time. Comparing the normalized ROWI of the foam case and the water case, both of them decrease with pumping time at a decreasing rate. For the same pumping time, the ROWI of the 60% foam case is always several times larger than the water case.

In a 1 μD shale (Fig. 6.29), the patterns of the normalized ROFIs and ROWIs are similar to those observed in a 0.1 μD shale. There are only two differences between two permeability shales. First, the ROFI of slickwater slightly increases with the pumping time for a 1 μD shale, but does not change with pumping time for a 0.1 μD shale. Second, the ROFI and ROWI benefits of using the 60% quality foam decreases with increasing shale permeability. For example, the ROFI of the foam treatment is worse than the reference slickwater case at 30 minutes and only 59% times larger than the reference slickwater case at 90 minutes, which are less than the values observed in the 0.1 μD shale.

As shale permeability further increases to 10 μD, the ROFIs of both the 60% quality foam and the slickwater increase with the pumping time at the similar trend. At the same pumping time, the foam and the slickwater generate the similar ROFI. The reason is that, for high permeability shales after 5 years production, fracture productivity is affected more by the propped length rather than propped area. Although the foam creates larger propped area, the propped length is similar to that created by the slickwater. So the two fracturing fluids exhibit the similar economic efficiency. However, the 60% quality foam still has a much better water economy (ROWI) than slickwater. The lowest ROWI of the foam cases is still twice as large as the ROWI of the reference slickwater case.

Overall, the ROFI improvement of using the 60% foam becomes larger as the pumping time increases or shale permeability decreases. Similar to ROFI, the ROWI benefit of using the foam is larger for longer pumping time and lower permeability shale. The water economic efficiency (ROWI) for both the foam and slickwater decreases with pumping time at a decreasing rate. However, the 60% quality foam with 90-min pumping time still yields a ROWI 68% larger than that of the slickwater treatment with 30-min pumping time in a 0.1 μD shale, 51% larger in a 1 μD shale, and 24% larger in a 10 μD shale.

6.4 CONCLUSIONS

In this chapter, the empirical rheological correlations of the polymer-free foam, developed in the experimental study in Chapter 5, are employed in the fracturing model (developed in Chapter 3) and reservoir simulation model (developed in Chapter 2) to evaluate the foam treatment efficiency in shale reservoirs. By comparing the results of the predicted fracture geometry, fracture conductivity distribution, and corresponding fracture productivity/ROFI/ROWI, the fracturing performance of our foam versus conventionally used slickwater is investigated for different shale permeability, foam quality, sand size, sand injection concentration, and pumping schedule. Listed below are some important conclusions.

- When the foam quality increases, the apparent fluid viscosity increases and the fluid leak-off decreases. The increase of the viscosity leads to fracture aperture growth at the expense of length growth, while the decrease of the leak-off increases the fracture length. For a low permeability shale (0.1, 1 μD), where the leak-off effect is relatively small, water creates the longest and narrowest fracture due to its smallest viscosity. As the shale permeability increases to 10 μD, the leak-off of the water becomes significant, making the foams outperform water in creating long fractures.
- For the whole production life of 0.1-1 μD shales and the short-term production of a 10 μD shale, the 60-70% quality foams yield the best production performance since they create the largest propped areas and relatively large propped length. For the long-term production of the 10 μD shale, the 60% foam and the slickwater yield the best production performance because they generate the longest propped fracture.

- Decreasing sand size from 20 mesh to 40 mesh leads to a significant increase of propped area and productivity for the lower quality foams (Q: 0-60%), but slight changes for the higher quality foams (Q: 70-80%).
- High quality foams (70-80%) can place the low concentration sand in a partial monolayer, which can get similar or even higher productivity compared with their multi-layer sand concentration treatments.
- Polymer-free foams with a quality of 60-70% can generate a better ROFI than slickwater in all three permeability shales. As the production time and shale permeability increase, the ROFI benefits of using foams decrease.
- In low permeability shales (0.1, 1 μD), ROFI of the foam treatments is not sensitive to the sand injection amount once the injection concentration is above 0.04 v/v. In a high permeability shale (10 μD), our foams with 0.02 v/v sand injection concentration can create a high conductivity partial monolayer sand pattern and yield a better ROFI than other higher sand injection concentrations.
- The ROWI benefit of using PFF increases with increasing foam quality, but decreases with increasing production time and shale permeability.
- Considering the economic profit (ROFI), the water economic efficiency (ROWI) and the sand consumption, the 60% and 70% quality foams carrying 40 mesh sands with a partial monolayer concentration of 0.4 v/v (0.88 lb/gal) can be the ideal treatment design for 0.1 - 10 μD shales.
- Both the ROFI and ROWI benefits of using the 60% quality foam instead of slickwater are larger for longer pumping time.
- The ROWI of both the 60% quality foam and slickwater decreases with increasing pumping time at a decreasing rate.

- Similar to the ULWP study, the foam performance evaluation is still limited to the planar bi-wing fracture scenario. Future work is recommended to evaluate the foam performance in complex primary-natural fracture networks.

Nomenclature

τ, shear stress, KPa

γ, shear rate, s^{-1}

K, power-law consistency index, Pa·s^{n}

n, power-law flow behavior index, no unit

μ_{ap}, apparent viscosity, Pa·s

Q, foam quality, no unit

P, fluid pressure, psi

ROFI, Return-On-Frac-Investment, $

ROWI, Return-On-Water-Investment, $\$/m^{3}$

k, proppant pack permeability, md

ϕ, porosity, no unit

C, Kozeny-Carman constant, no unit

S, surface area per unit volume, 1/inch

w_{hf}, fracture width, inch

P_0, confining stress, psi

d_p, proppant diameter, inch

B, constant related to formation, psi^{-m}

m, constant related to formation, no unit

Subscripts

ap, apparent value

hf, hydraulic fracture

p, propping agent

References

Brannon, H.D. and Starks II, T.R. 2008. The Impact of Effective Fracture Area and Conductivity on Fracture Deliverability and Stimulation Value. Paper SPE 116057, presented at the 2008 SPE Annual Technical Conference and Exhibition, Denver, Colorado, Sep. 21-24.

Brannon, H.D. and Starks II, T.R. 2009. Maximizing Return-On-Fracturing-Investment by Using Ultral-lightweight Proppants to Optimize Effective Fracture Area: Can Less Be More? Paper SPE 119385, presented at the SPE hydraulic fracturing technology conference, Woodlands, Texas, Jan. 19-21.

Burke, L.H., Nevison, G.W., and Peters, W.E. 2011. Improved Unconventional Gas Recovery With Energized Fracturing Fluids: Montney Example. Paper SPE 149344. In: Proceedings of the 2011 SPE SPE Eastern Regional Meeting, Columbus, Ohio, USA, August 17-19.

Darin, S.R. and Huitt, J.L. 1960. Effect of a Partial Monolayer of Propping Agent on Fracture Flow Capacity. Petroleum Transactions, AIME, 219: 31-37.

Duenckel, R., Conway, M.W., Eldred, B., and Vincent, M.C. 2012. Proppant Diagenesis - Integrated Analyses Provide New Insights into Origin, Occurrence, and Implications for Proppant Performance. SPE Prod. & Operations, 27 (2): 131-144.

Heller, R. and Zoback, M. 2013. Laboratory Measurements of Matrix Permeability and Slippage Enhanced Permeability in Gas Shales. Paper SPE 168856 presented at the Unconventional Resources Technology Conference held in Denver, Colorado, USA, Aug. 12-14.

Huitt, J.L. and McGlothlin, B.B. 1958. The Propping of Fractures in Formations Susceptible to Propping Sand Embedment. Dill. and Prod. Pra., API.

Tinni, A., Fathi, E., Agarwal, R., Sondergeld, C., Akkutlu, Y., and Rai, C. 2012. Shale Permeability Measurements on Plugs and Crushed Samples. Paper SPE 162235 presented at the SPE Canadian Unconventional Resources Conference held in Calgary, Alberta, Canada, Oct. 30-Nov. 1.

Zhou, J., Jung, C.M., Chenevert, M.E., and Sharma, M.M. 2013. A Systematic Approach to Petrophysical Characterization of Organic-Rich Shales in Barnett and Eagle Ford Formations. Paper SPE 168792 presented at the Unconventional Resources Technology Conference held in Denver, Colorado, USA, Aug. 12-14.

Table 6.1: Input of reservoir properties and completion parameters for parametric study of polymer-free foam fracturing.

Reservoir Properties				Completion Parameters	
Pr_{pore} (psi)	3300	E (psi)	2E6	L_{well} (ft)	5000
σ_{min} (psi)	4500	ν	0.25	Well Spc (ft)	3250
Temp (^oF)	130	P_L (psi)	468	Frac Spc (ft)	100, 200
φ	8%	V_L (scf/lb)	0.0425	H_{prop} (ft)	150
H_{pay}(ft)	150	ρ_{rock} (g/cc)	2.6	μ_{slw}(cp)	5.7
k_m (μD)	0.1-10	S_{wi}	20%	q_{inj} (m^3/s)	0.02
K_v/k_h	0.1	S_{gi}	80%		
C_{por} (1/psi)	6E-6	Methane	100%	BHP (psi)	500

Table 6.2: Cases of parametric study for polymer-free foam fracturing.

20 min pad + 40 min slurry + 20 min shutin, 200ft Frac Spacing						
20 mesh Sand						
Frac Fluid	k_m	Proppant Injection Volume Concentration				
Slickwater	0.1, 1, 10 μD	0.02 v/v	0.04 v/v	0.06 v/v	0.08 v/v	0.1 v/v
Foam 60%		0.02 v/v	0.04 v/v	0.06 v/v	0.08 v/v	0.1 v/v
Foam 70%		0.02 v/v	0.04 v/v	0.06 v/v	0.08 v/v	0.1 v/v
Foam 80%		0.02 v/v	0.04 v/v	0.06 v/v	0.08 v/v	0.1 v/v
40 mesh Sand						
Frac Fluid	k_m	Proppant Injection Volume Concentration				
Slickwater	0.1, 1, 10 μD	0.02 v/v	0.04 v/v	0.06 v/v	0.08 v/v	0.1 v/v
Foam 60%		0.02 v/v	0.04 v/v	0.06 v/v	0.08 v/v	0.1 v/v
Foam 70%		0.02 v/v	0.04 v/v	0.06 v/v	0.08 v/v	0.1 v/v
Foam 80%		0.02 v/v	0.04 v/v	0.06 v/v	0.08 v/v	0.1 v/v

Table 6.3: Treatment volumes and costs for single wing of a planar fracture.

	Water Vol. m^3	Water Cost, $	N_2 Vol.$_{res}$, m^3	N_2 Cost, $	Sand Vol., m^3	Sand Cost, $	Bundled Cost, $	Total Cost, $
SLW	72	604	0	0	0.96	1357	47551	49512
					1.92	2714	47551	50869
					2.88	4072	47551	52226
					3.84	5429	47551	53584
					4.8	6786	47551	54941
F60	28.8	242	43.2	1141	0.96	1357	55635	58375
					1.92	2714	55635	59732
					2.88	4072	55635	61089
					3.84	5429	55635	62446
					4.8	6786	55635	63803
F70	21.6	181	50.4	1332	0.96	1357	55635	58505
					1.92	2714	55635	59862
					2.88	4072	55635	61219
					3.84	5429	55635	62576
					4.8	6786	55635	63933
F80	14.4	121	57.6	1522	0.96	1357	55635	58634
					1.92	2714	55635	59992
					2.88	4072	55635	61349
					3.84	5429	55635	62706
					4.8	6786	55635	64063

Table 6.4: Cases for parametric study of impact of pumping time on foam fracturing.

Frac Fluid	k_m	Pumping Schedule					
Slickwater (Ref.)	0.1, 1, 10 μD	40 mesh Sand at 0.1 v/v					
		Ini. Pad	10 min	15 min	20 min	25 min	30 min
		Slurry	20 min	30 min	40 min	5 min	60 min
Foam 60%	0.1, 1, 10 μD	40 mesh Sand at 0.1 v/v					
		Ini. Pad	10 min	15 min	20 min	25 min	30 min
		Slurry	20 min	30 min	40 min	5 min	60 min

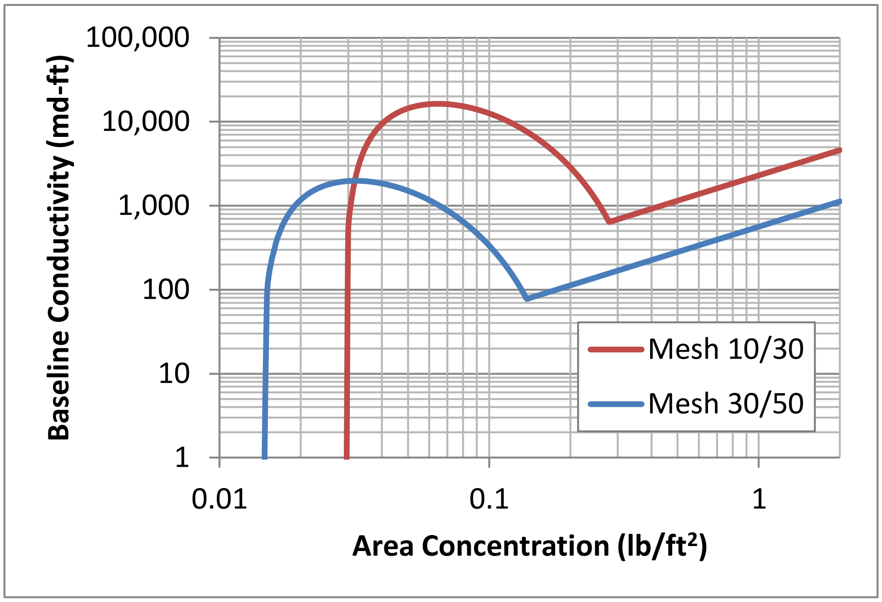

Figure 6.1: Conductivity of 20 and 40 mesh sands at 4000 psi confining pressure.

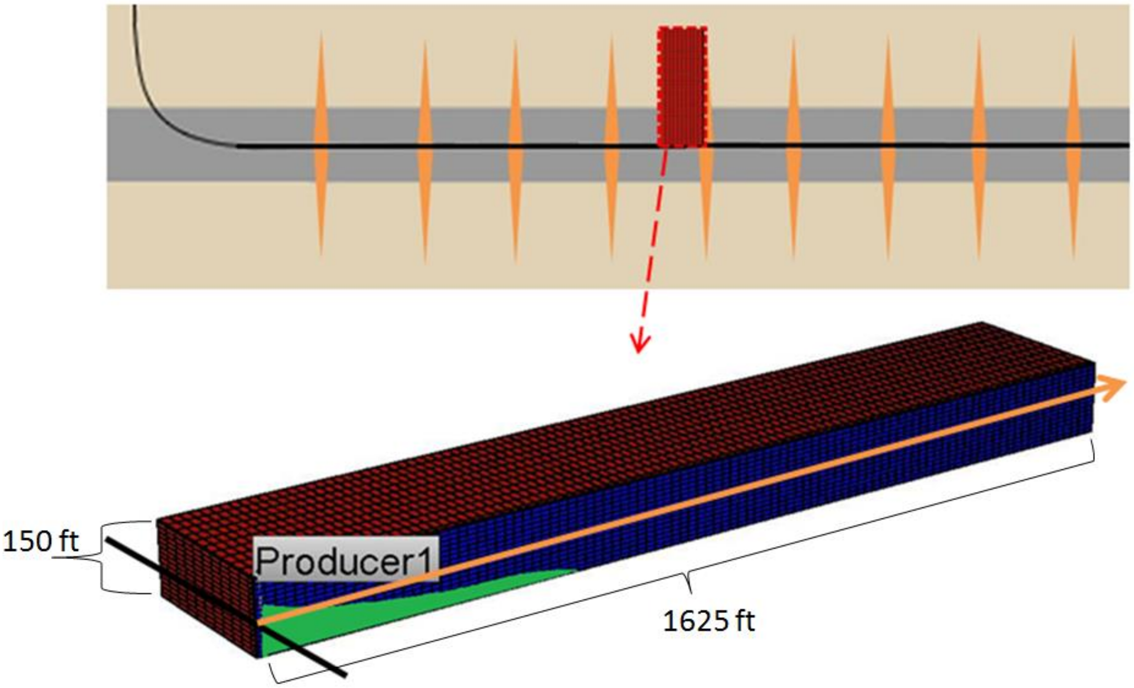

Figure 6.2: Schematic of the reservoir simulation model.

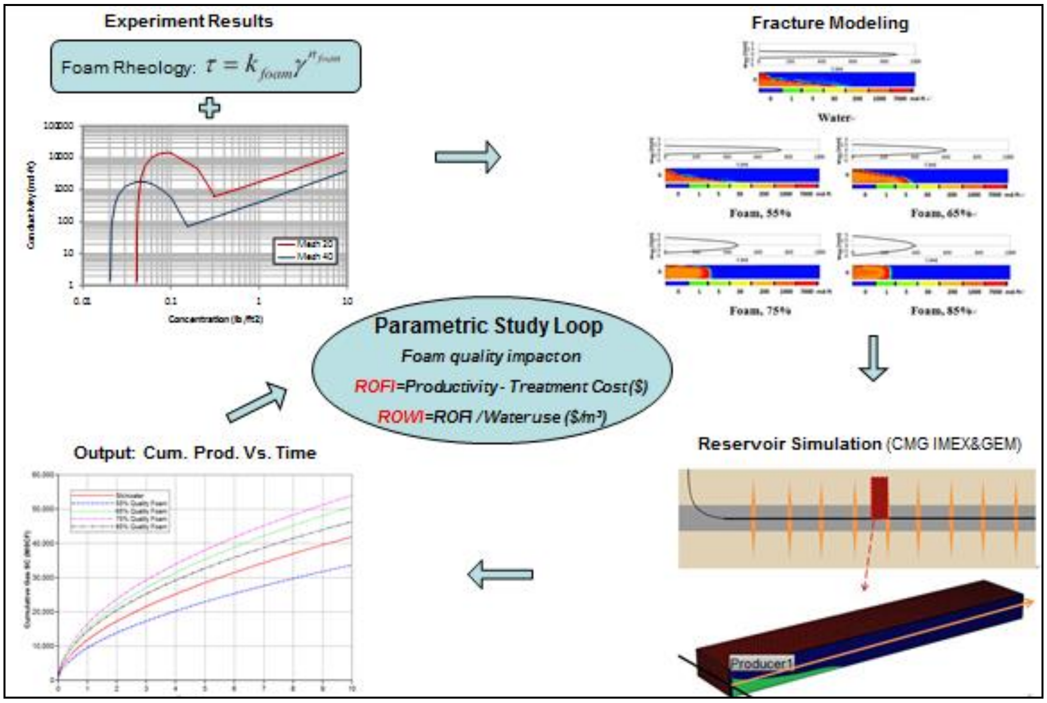

Figure 6.3: Schematic of the parametric study loop.

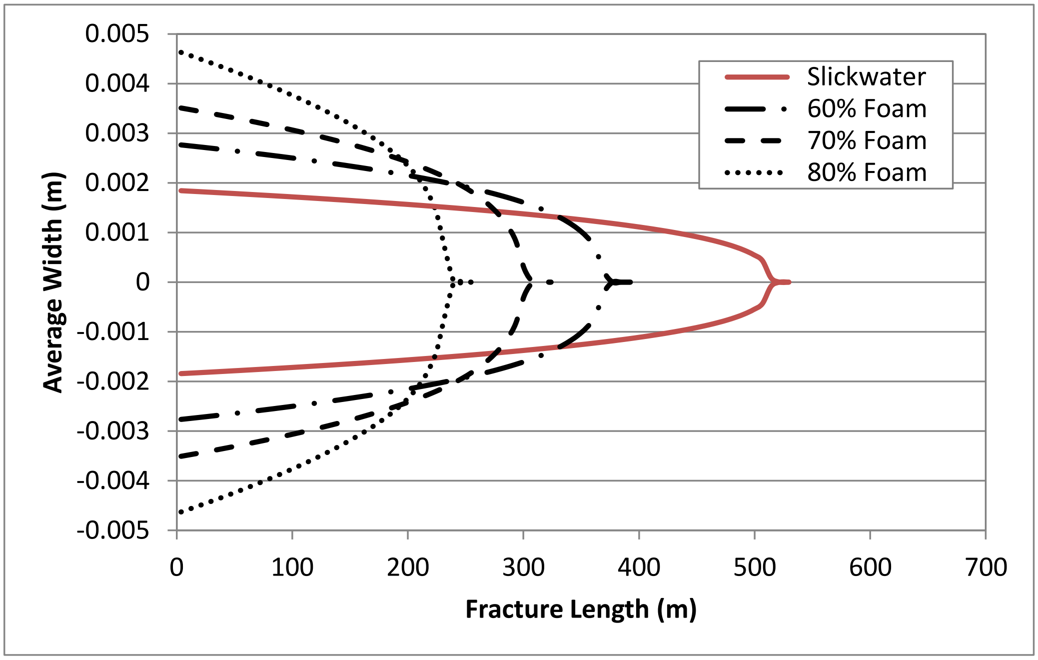

Figure 6.4: Average fracture widths along fracture length created by different pads for a 0.1 μD shale.

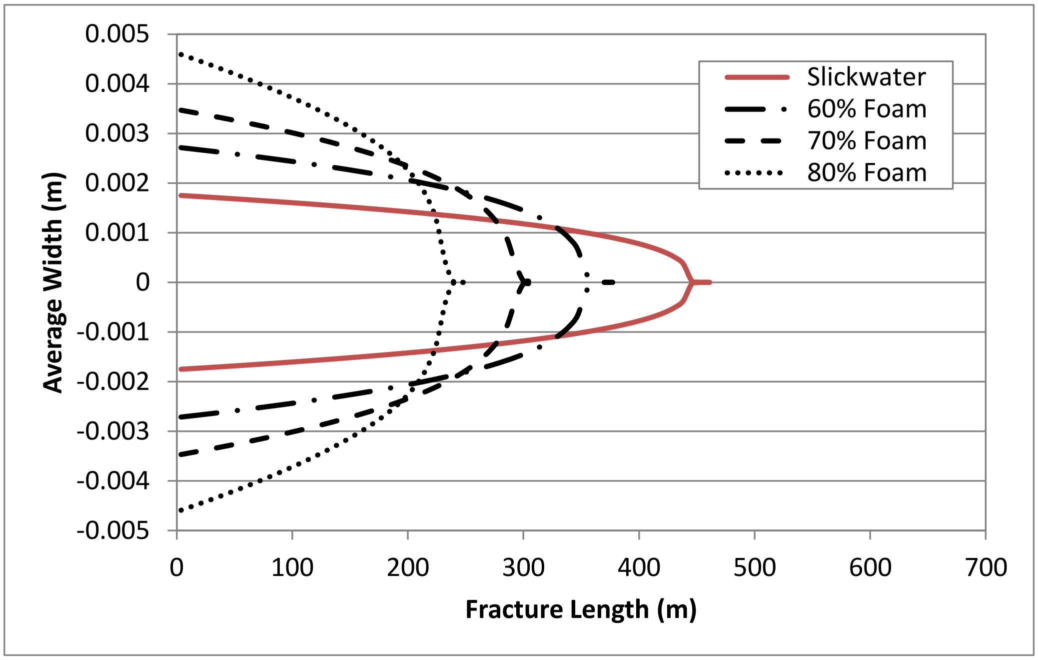

Figure 6.5: Average fracture widths along fracture length created by different pads for a 1 μD shale.

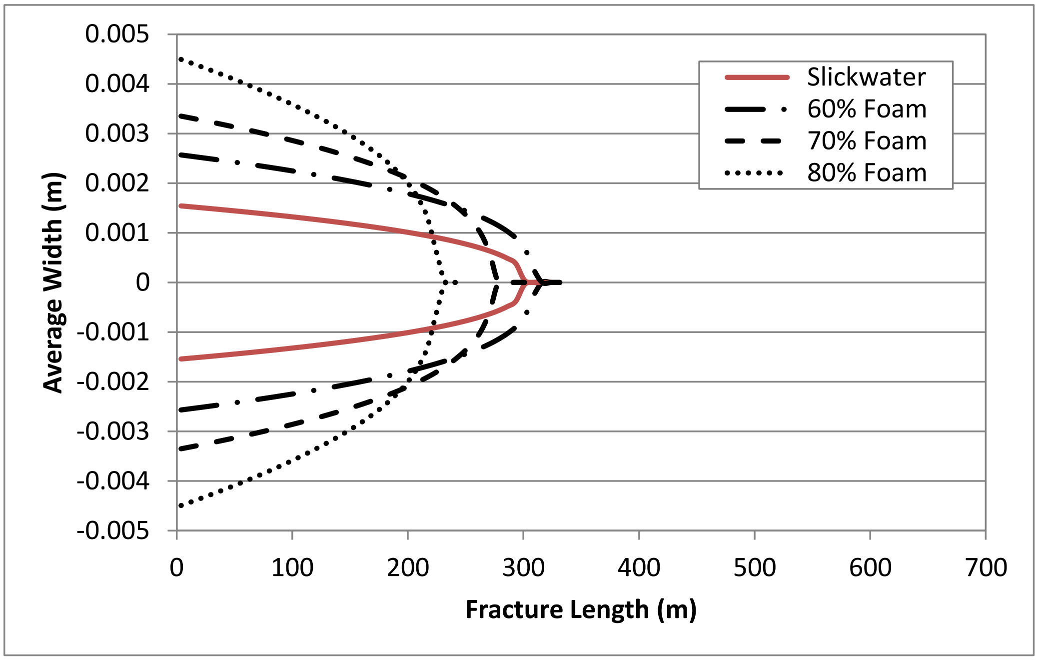

Figure 6.6: Average fracture widths along fracture length created by different pads for a 10 μD shale.

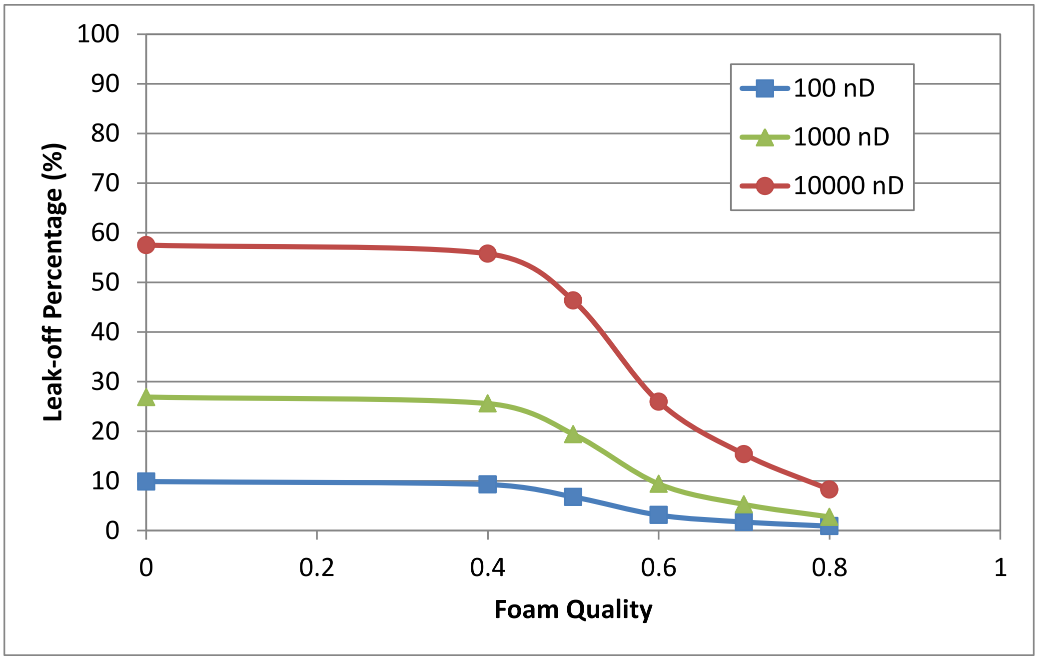

Figure 6.7: Leak-off volume percentages as a function of foam quality for different permeability shales.

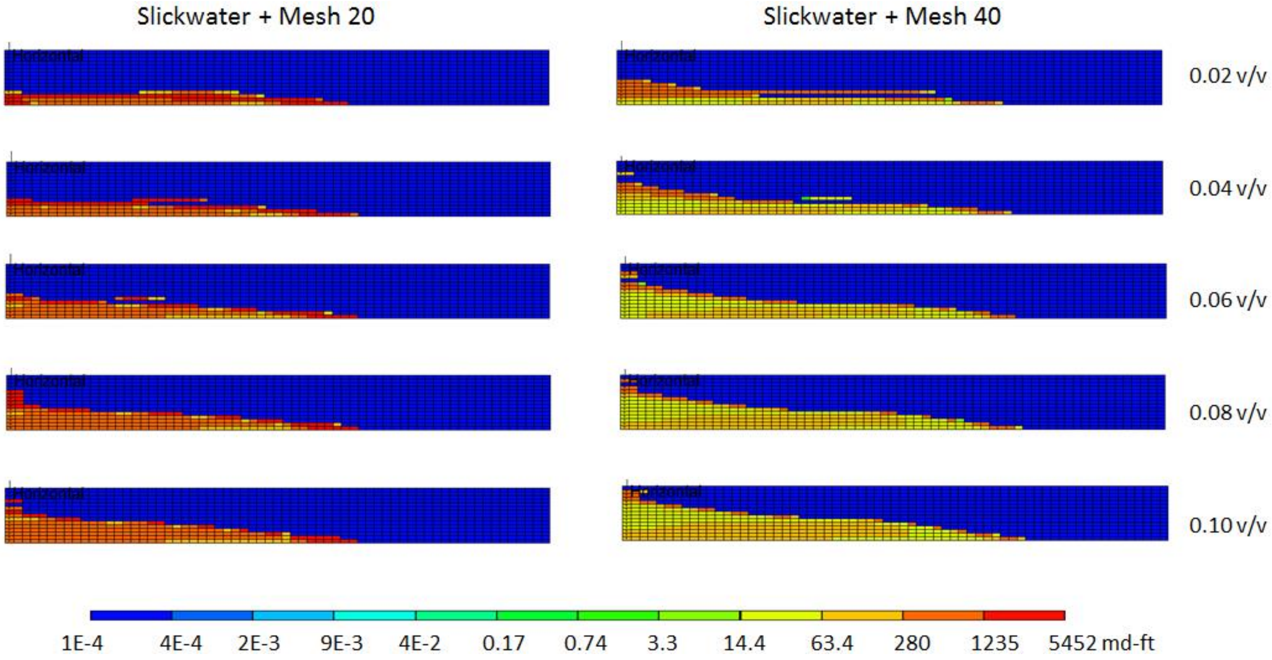

Figure 6.8: Conductivity distributions created by slickwater with mesh 20 and 40 sand in a 1 μD shale.

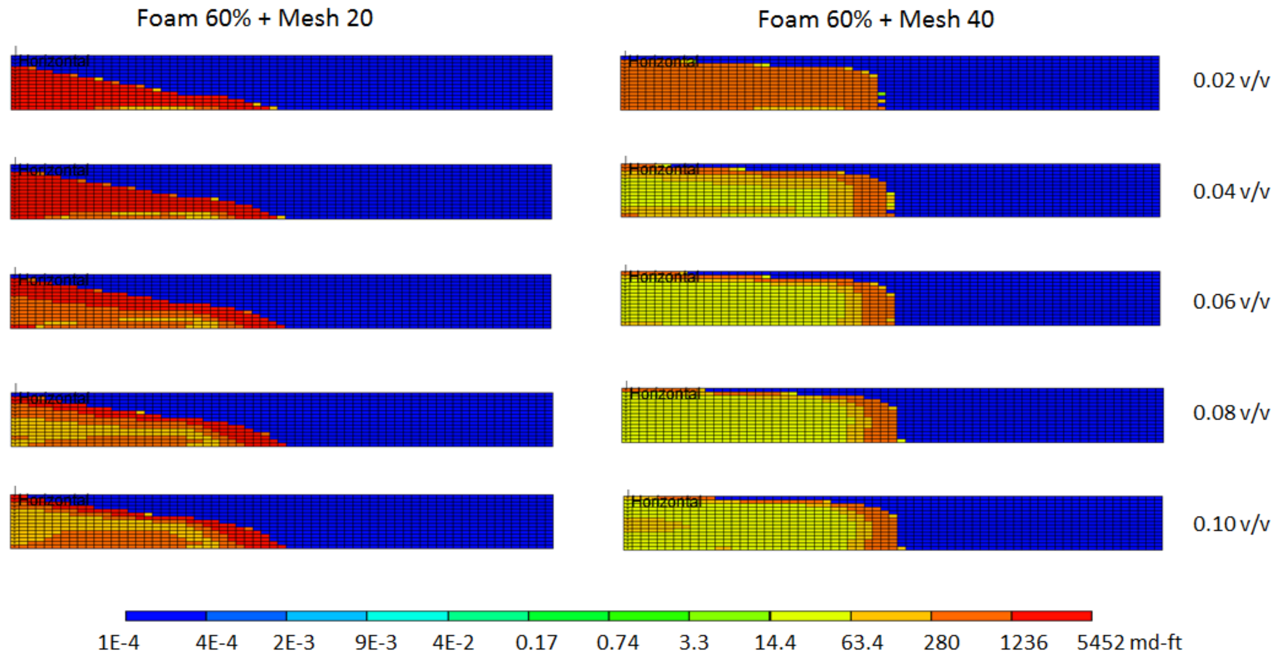

Figure 6.9: Conductivity distributions created by 60% foam with mesh 20 and 40 sand in a 1 μD shale.

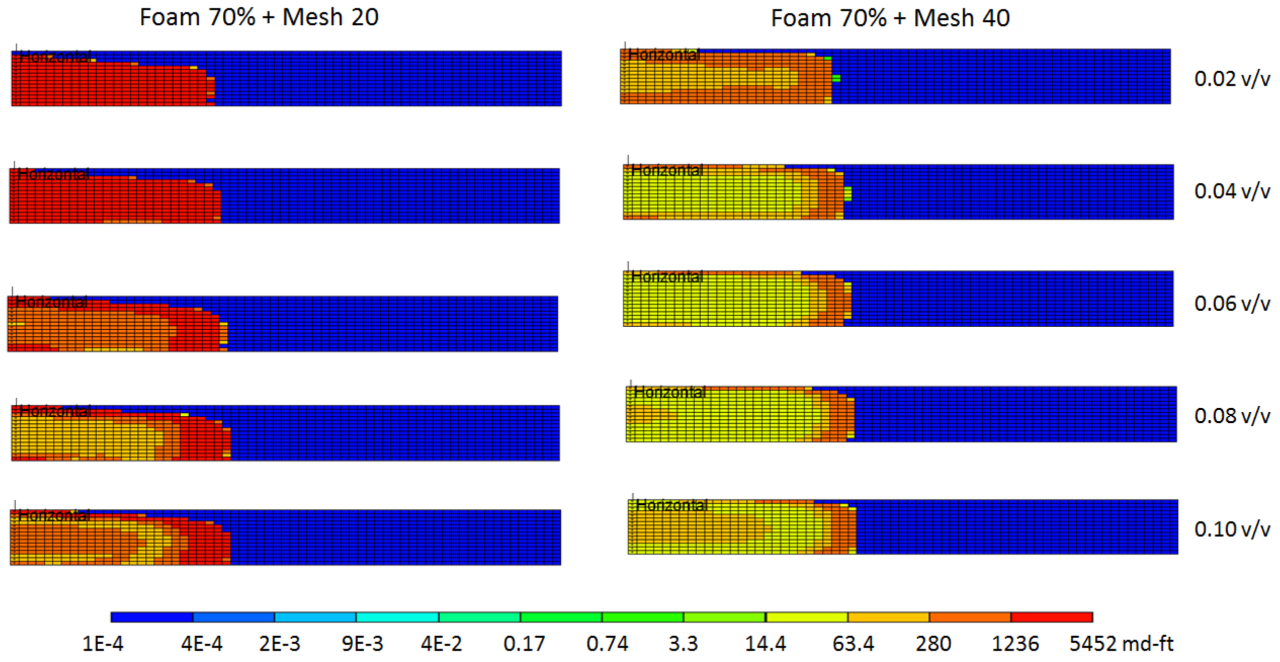

Figure 6.10: Conductivity distributions created by 70% foam with mesh 20 and 40 sand in a 1 μD shale.

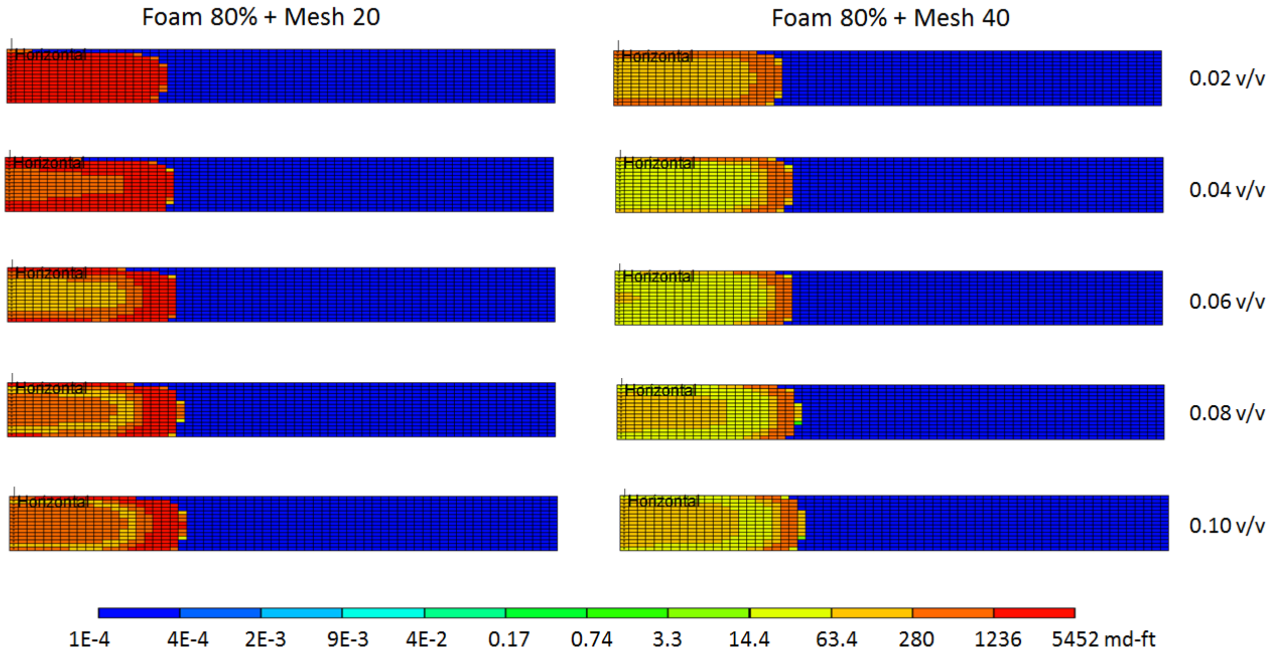

Figure 6.11: Conductivity distributions created by 80% foam with mesh 20 and 40 sand in a 1 µD shale.

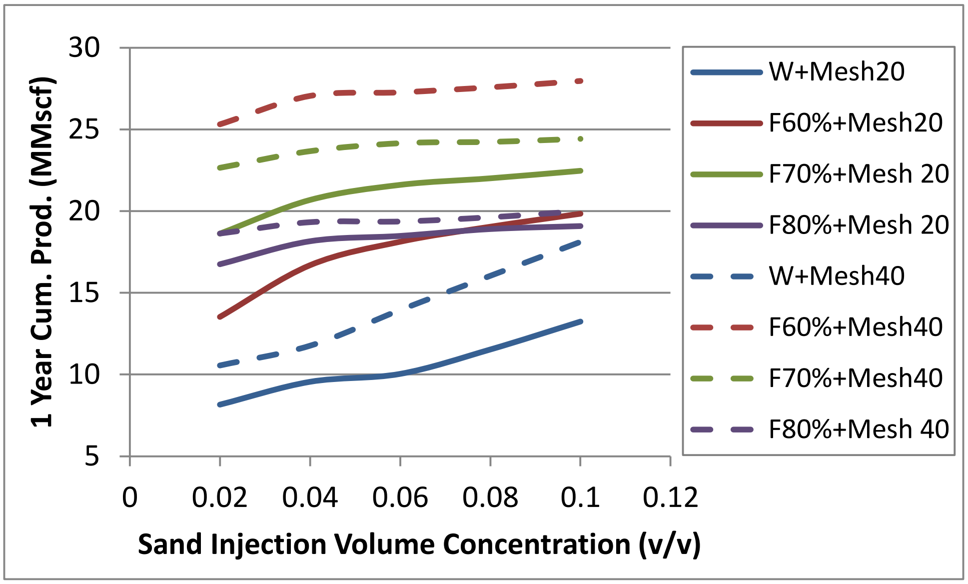

Figure 6.12: 1 Year Cumulative Productivity vs. Sand Injection Amount for slickwater and different quality foams in 0.1 µD.

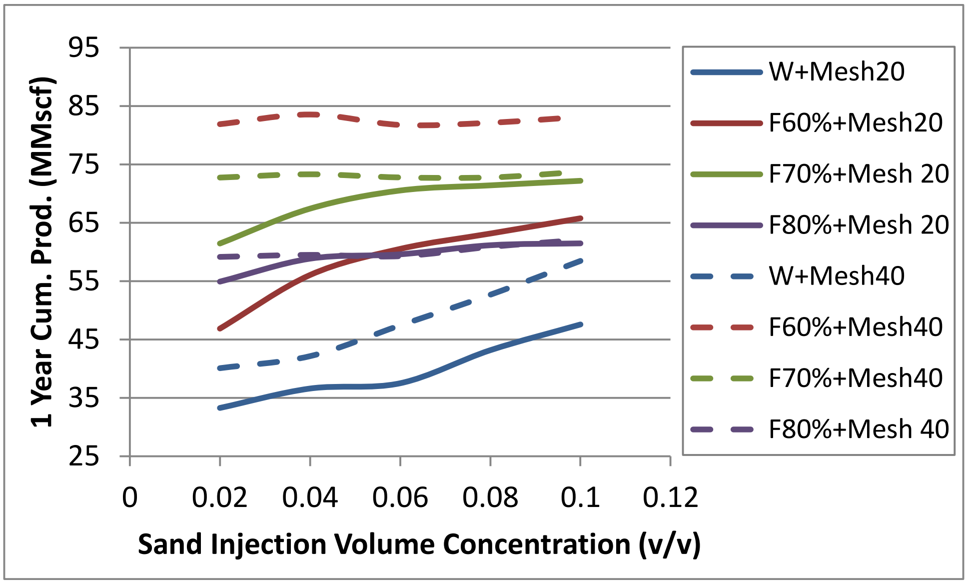

Figure 6.13: 1 Year Cumulative Productivity vs. Sand Injection Amount for slickwater and different quality foams in 1 μD.

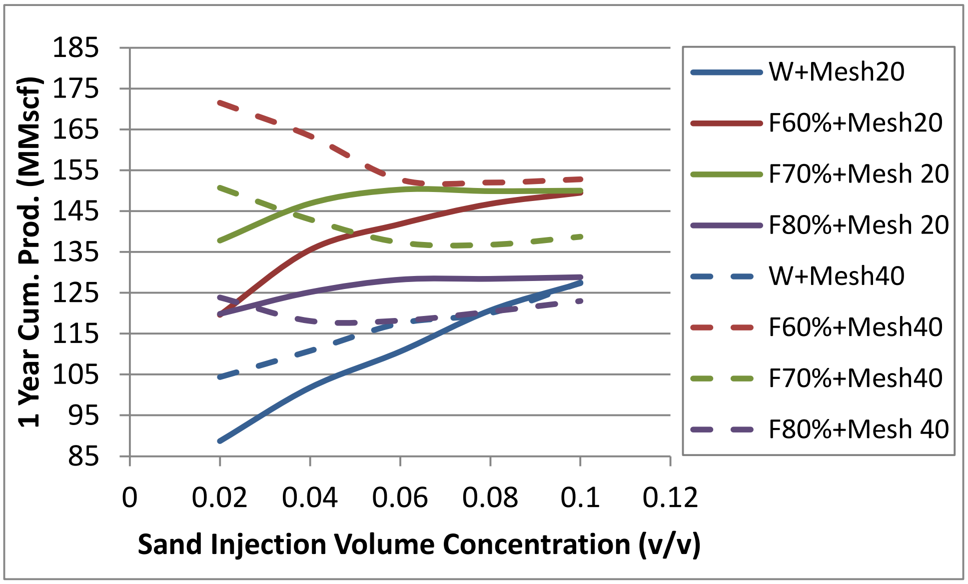

Figure 6.14: 1 Year Cumulative Productivity vs. Sand Injection Amount for slickwater and different quality foams in 10 μD.

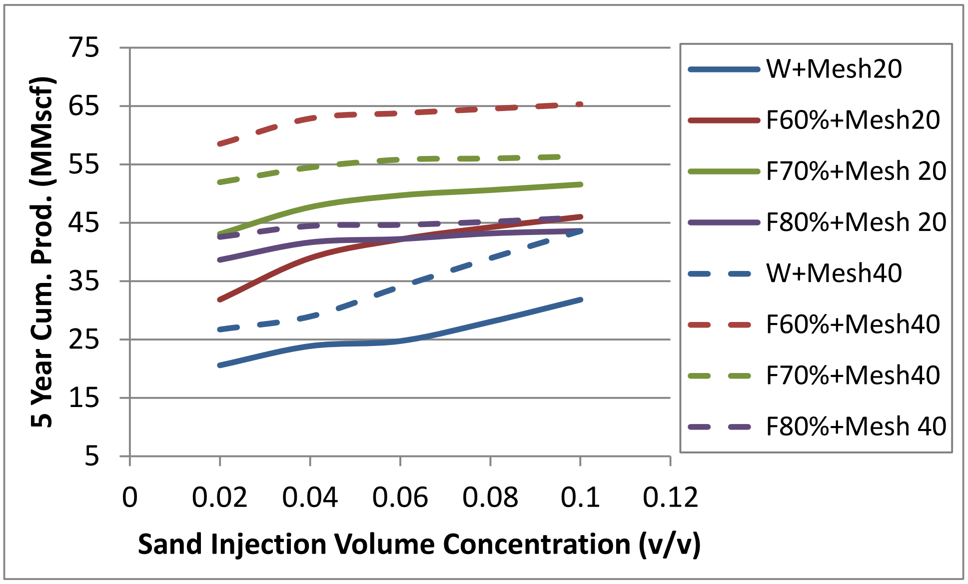

Figure 6.15: 5 Year Cumulative Productivity vs. Sand Injection Amount for slickwater and different quality foams in 0.1 µD.

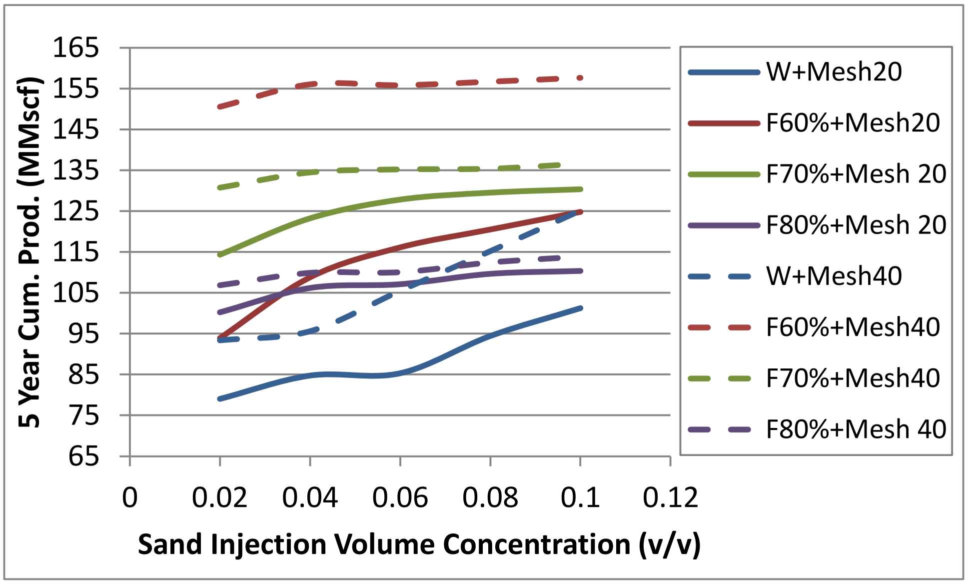

Figure 6.16: 5 Year Cumulative Productivity vs. Sand Injection Amount for slickwater and different quality foams in 1 µD.

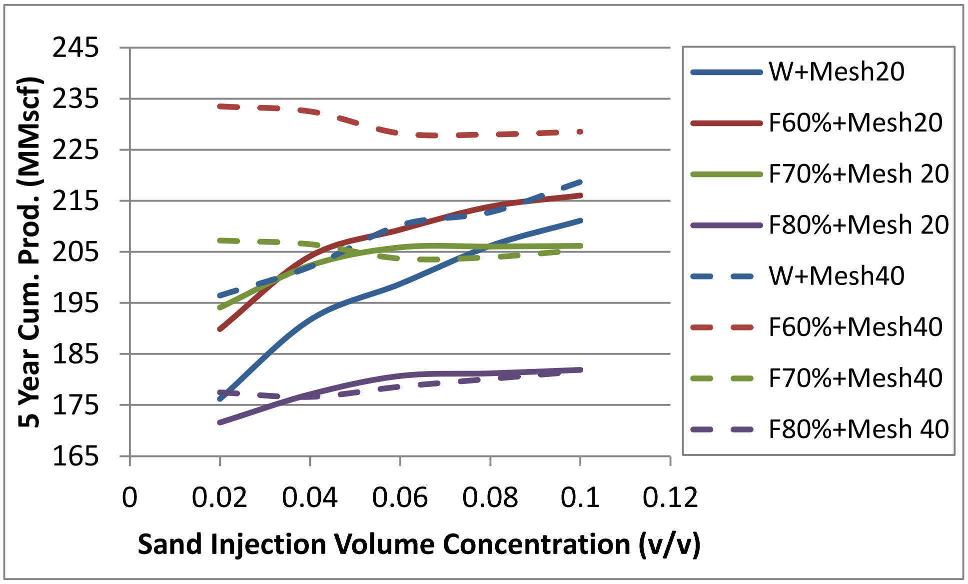

Figure 6.17: 5 Year Cumulative Productivity vs. Sand Injection Amount for slickwater and different quality foams in 10 µD.

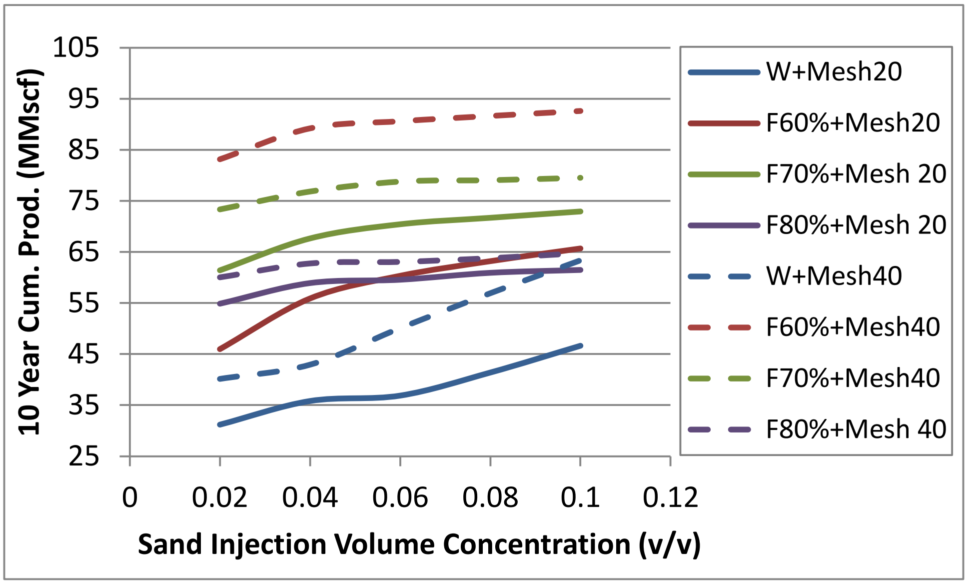

Figure 6.18: 10 Year Cumulative Productivity vs. Sand Injection Amount for slickwater and different quality foams in 0.1 µD.

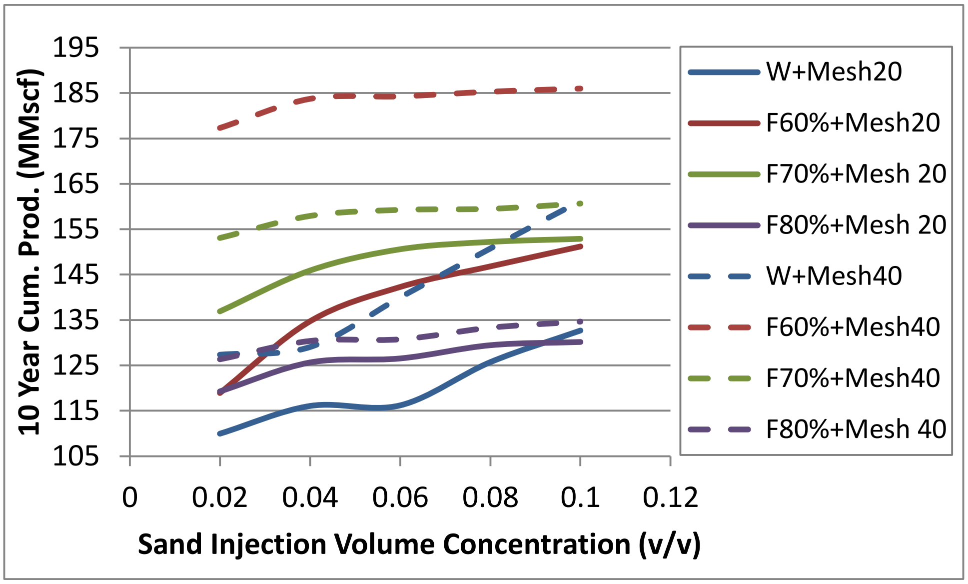

Figure 6.19: 10 Year Cumulative Productivity vs. Sand Injection Amount for slickwater and different quality foams in 1 μD.

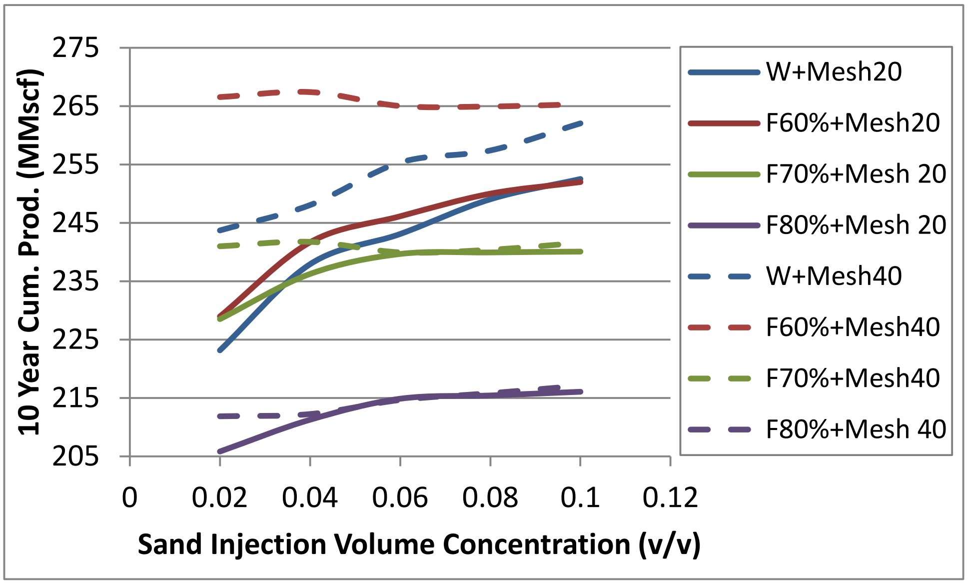

Figure 6.20: 10 Year Cumulative Productivity vs. Sand Injection Amount for slickwater and different quality foams in 10 μD.

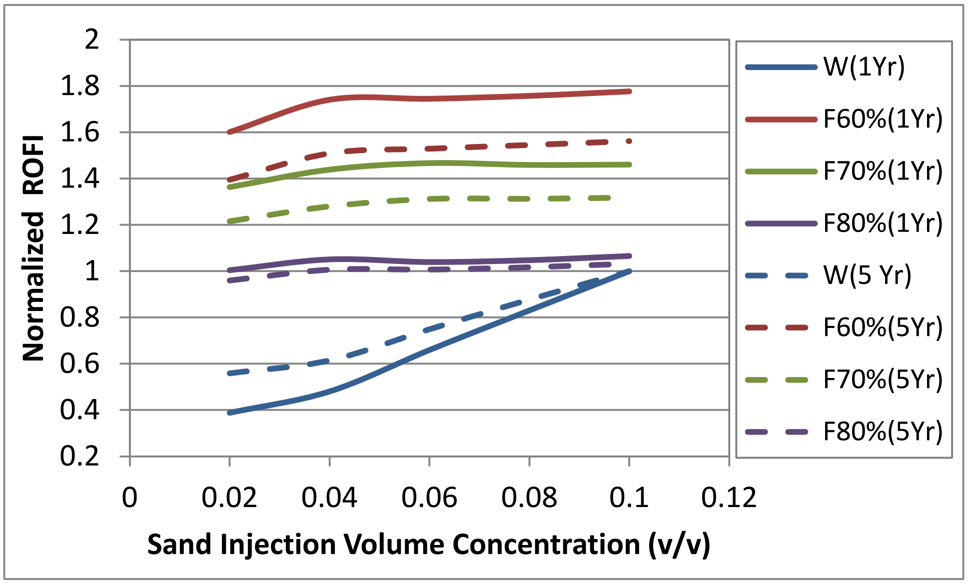

Figure 6.21: Normalized ROFI vs. Sand Injection Amount for slickwater and different quality foams in 0.1 μD.

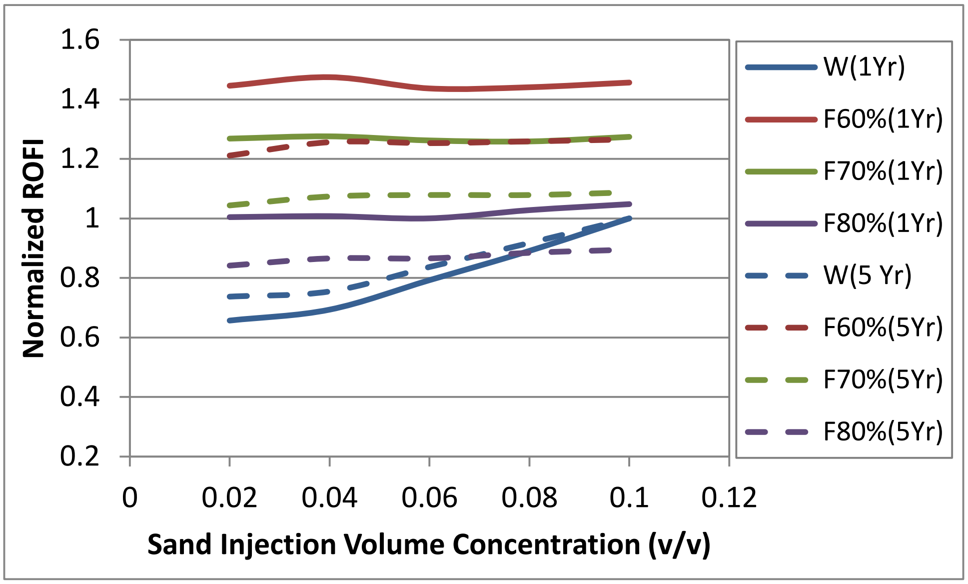

Figure 6.22: Normalized ROFI vs. Sand Injection Amount for slickwater and different quality foams in 1 μD.

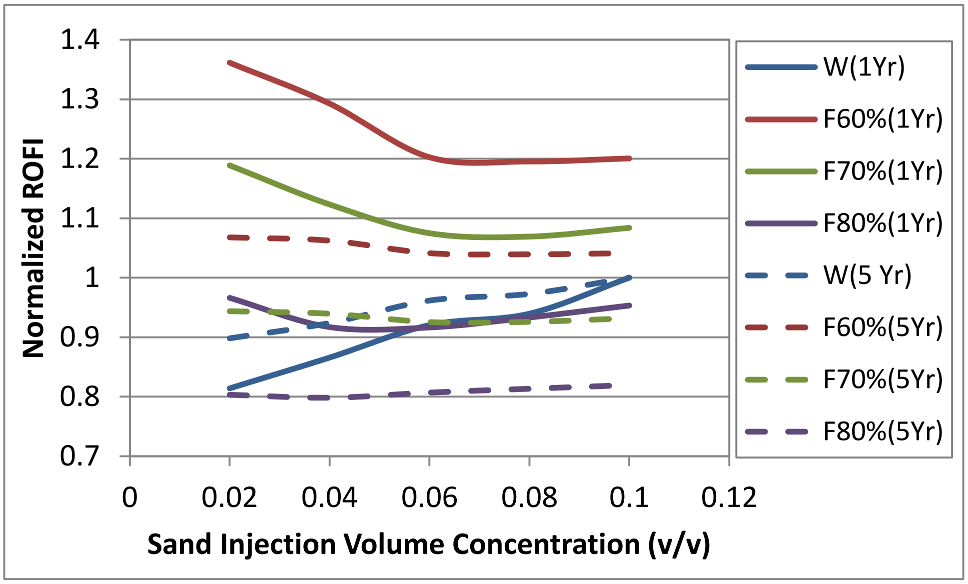

Figure 6.23: Normalized ROFI vs. Sand Injection Amount for slickwater and different quality foams in 10 μD.

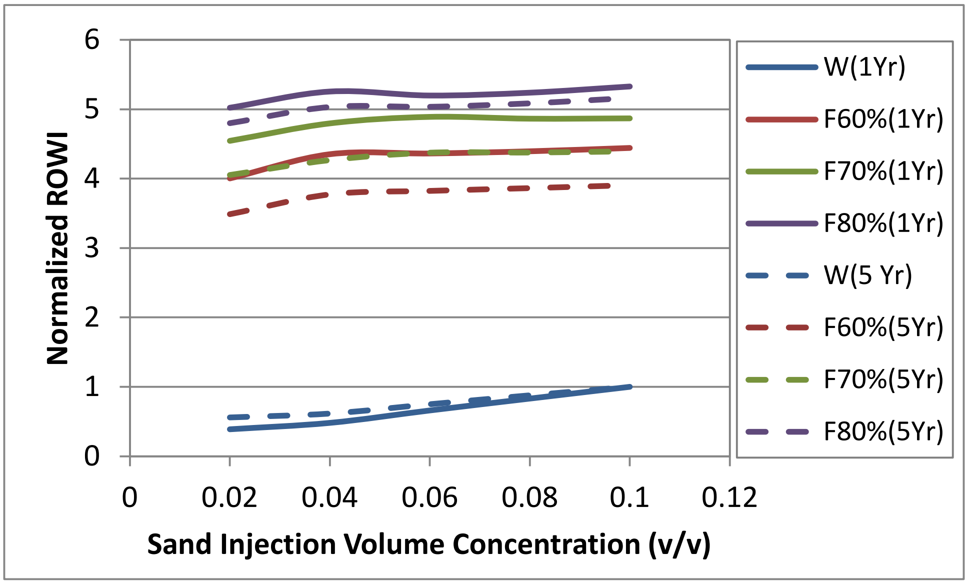

Figure 6.24: Normalized ROWI vs. Sand Injection Amount for slickwater and different quality foams in 0.1 μD.

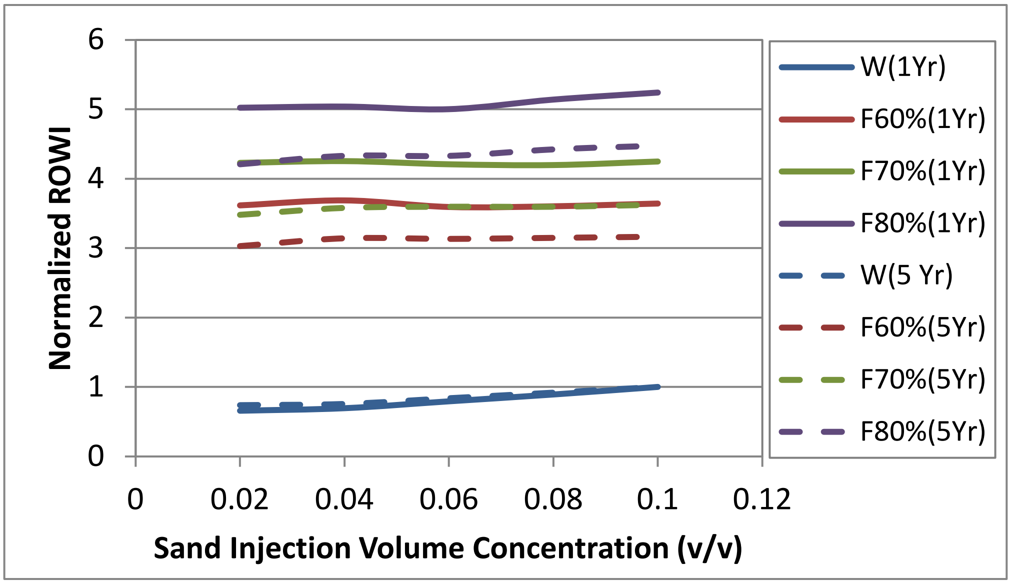

Figure 6.25: Normalized ROWI vs. Sand Injection Amount for slickwater and different quality foams in 1 μD.

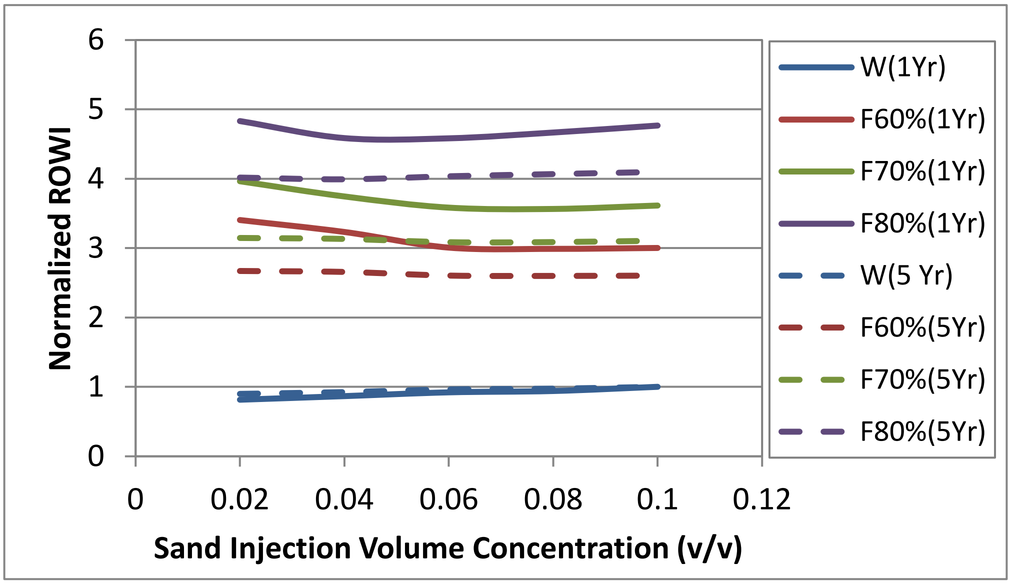

Figure 6.26: Normalized ROWI vs. Sand Injection Amount for slickwater and different quality foams in 10 μD.

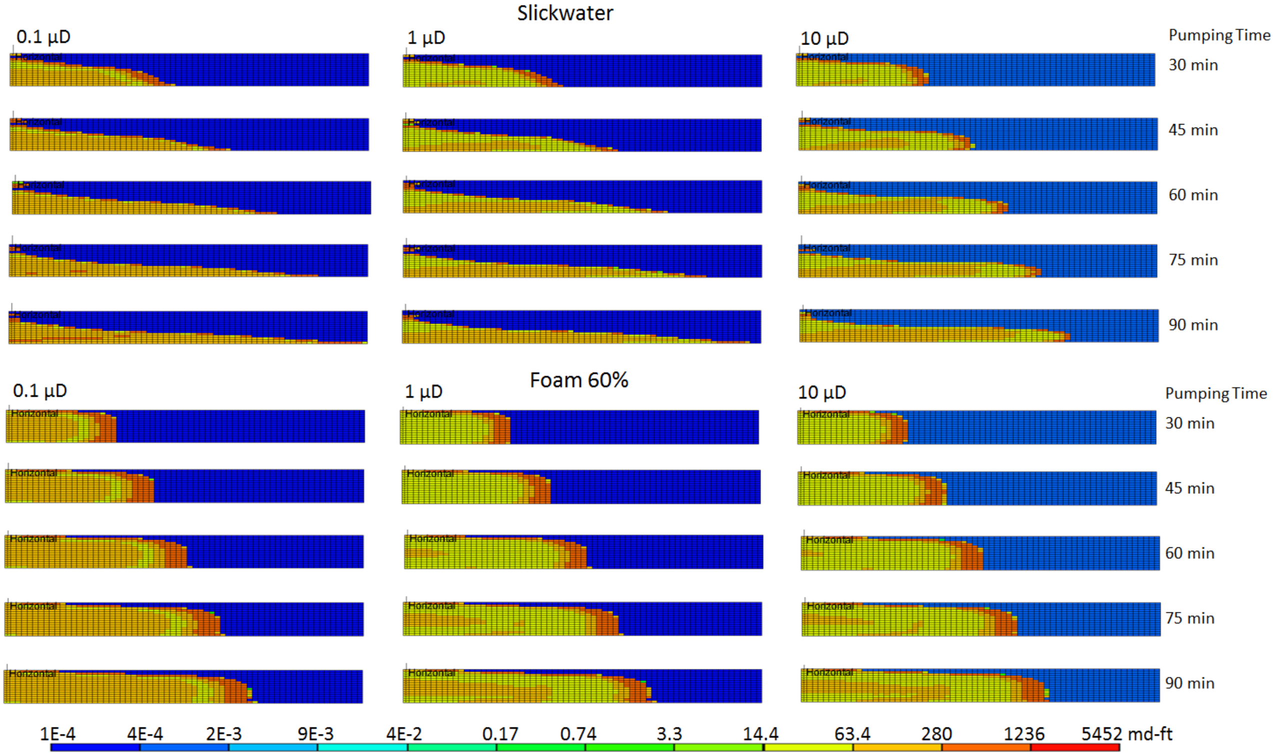

Figure 6.27: Conductivity distributions created by slickwater and 60% foam at different pumping time and different permeability shales.

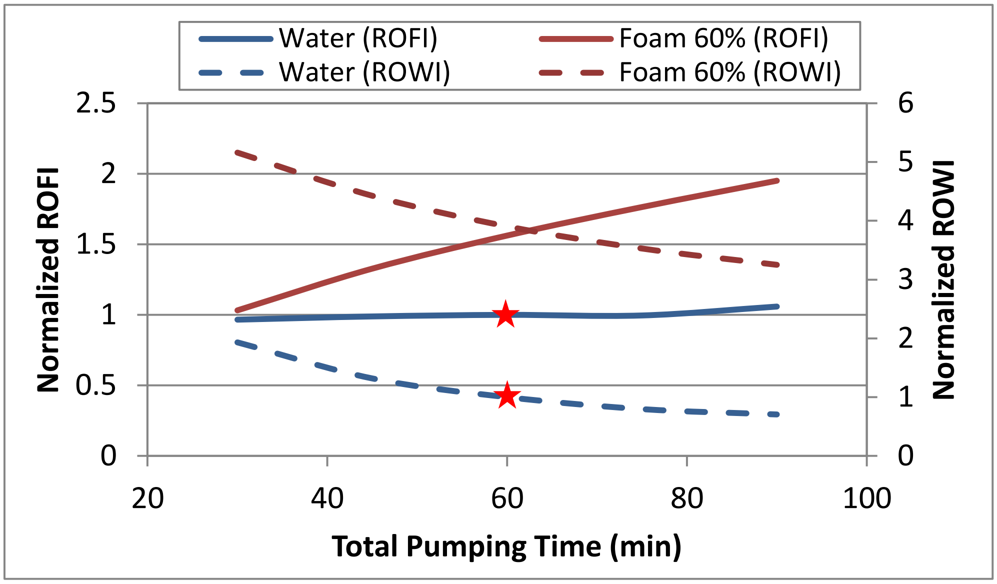

Figure 6.28: Normalized ROFI and Normalized ROWI vs. Total Pumping Time for slickwater and 60% foam in a 0.1 μD shale.

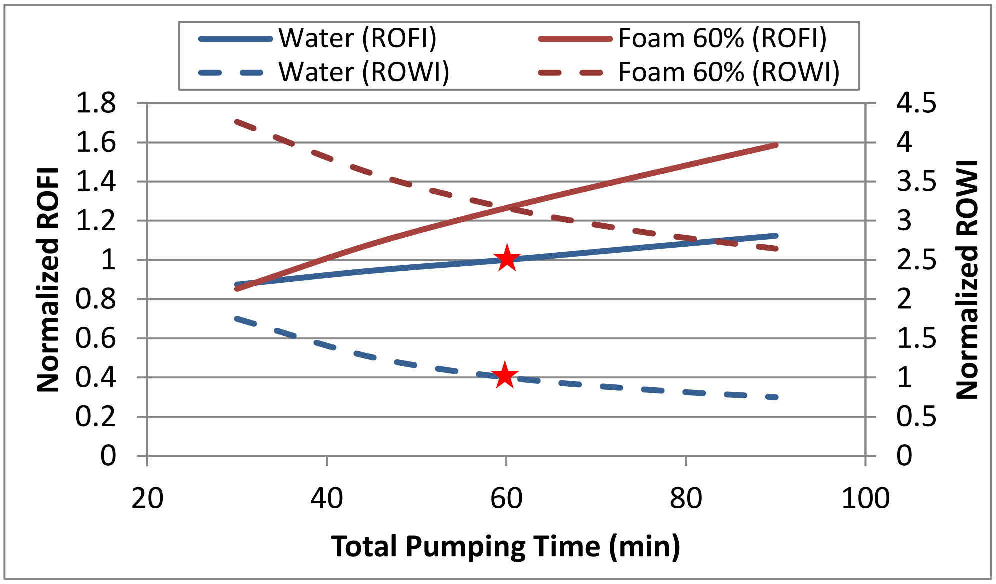

Figure 6.29 Normalized ROFI and Normalized ROWI vs. Total Pumping Time for Slickwater and 60% foam in a 1 μD shale.

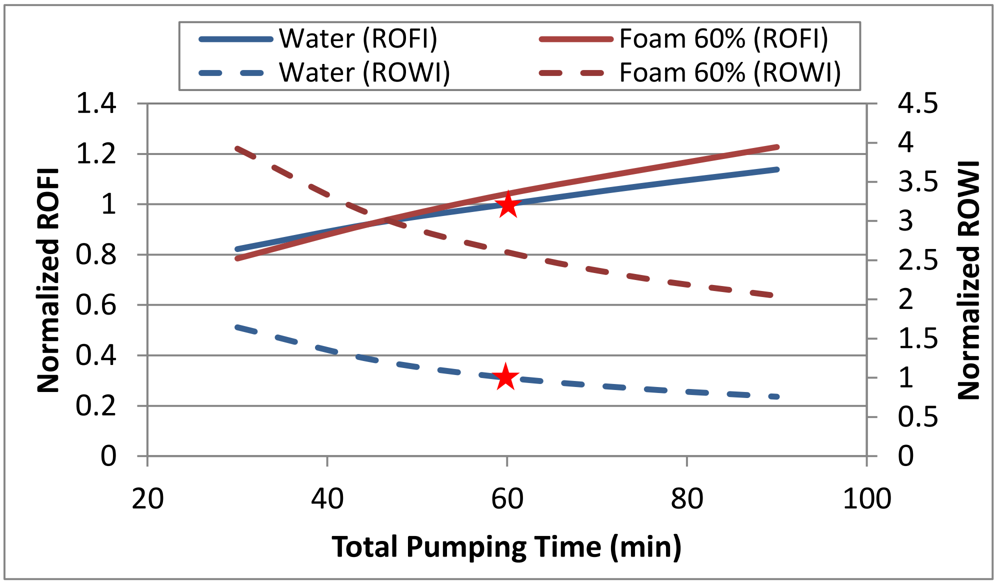

Figure 6.30: Normalized ROFI and Normalized ROWI vs. Total Pumping Time for Slickwater and 60% foam in a 10 μD shale.

Chapter 7: Summary, Conclusions, and Recommendations

7.1 SUMMARY

As the global demand for energy rises and discovery of new hydrocarbon resources drops, the recovery from unconventional resources such as shale gas becomes increasingly important. Shale reservoirs need to be hydraulically fractured to produce at an economic rate. Long propped fractures are preferred to maximize productivity for ultra-low permeability shale. Slickwater fracturing with sand produces long fractures, but only the near wellbore region is propped due to fast settling of sand. Gel fluid can create long propped fractures, but they damage the fracture surface and proppant pack. Both slickwater and gel fluid treatments require a large amount of water to be injected underground. A high percentage of the water will leak into the formation through matrix and natural fractures, and will not be recovered due to the high capillary pressure, low drawdown pressure and adverse mobility ratio (gas reservoirs). The trapped water leaves a water-saturated zone in the vicinity of the fracture and subsequently reduces gas flow. Besides, large volumes of water consumption and post-treatment water disposal raise environmental concerns from the public and the government.

In this dissertation, a non-damaging hydraulic fracturing treatment is developed for shale gas reservoirs, which can place proppants more efficiently and consumes less water compared with conventional slickwater-sand treatment. The new treatment either utilizes polymer-free foams instead of water to place sand or uses three ultra-light weight proppants instead of sand to be transported by water. A new technique combining experiment, modeling and simulation is developed to evaluate the application of new fracturing fluid and proppants in shale fracturing. With this technique, the optimal proppant injection amount and foam quality can be determined to prop the primary fracture more effectively, and thus significantly improve well economic performance

(Return-On-Fracture-Investment, ROFI) and water economic efficiency (Return-On-Water-Investment, ROWI).

7.2 CONCLUSIONS

In Chapter 2, a reservoir simulation model is built in CMG to study the impact of fracture conductivity and propped length on fracture productivity in naturally fractured shale reservoirs. Based on a parametric study of over 1000 cases, the minimum conductivity required to fully stimulate the reservoir for different propped lengths and different production times is obtained. The effect of natural fractures along with other parameters including fracture spacing, gas desorption, water recovery, reservoir fluid type, and flowing BHP are investigated. Through the study, the following key conclusions are obtained.

- For each propped length and production time, there is a critical conductivity beyond which production is insensitive to the conductivity.
- The critical conductivity increases with propped length and decreases with production time. The decreasing rate is positively correlated with reservoir flow capacity.
- Natural fractures increase the 1-year critical conductivity but decrease the 5-20 year critical conductivity for 200 nD, while it increases the 1-20 year critical conductivity for 20 nD.
- In addition to natural fractures, the critical conductivity is positively correlated with cluster spacing, water saturation and gas desorption, while it is negatively correlated with flowing BHP.

In Chapter 3, a fracturing model has been developed to simulate the fracture propagation and proppant transport. In this model, pressure effect and different leak-off models are considered for foam fracturing simulation.

In Chapter 4, strength test and API conductivity test are conducted for three ultra-light weight proppants, which are ULW-1 (polymeric), ULW-2 (resin coated and impregnated ground walnut hull) and ULW-3 (resin coated porous ceramic).

- Comparing the three ULWPs, ULW-1 is spherical with the lowest density (sg: 1.08), ULW-2 is highly angular with the intermediate density (sg: 1.25), and ULW-3 is slightly angular with the highest density (sg: 1.75).
- Strength test results show that ULW-1 is the most deformable with the lowest Young's modulus and no failure point, ULW-3 is the most brittle with the highest Young's modulus and a failure point of 4.5 lbf per particle, and ULW-2 has an intermediate elasticity with a failure point of 25 lbf per particle.
- Under 4000 psi closure stress, the conductivity of ULW-1 and 2 is on the order of 1-10 md-ft in both partial monolayer and multilayer, while the conductivity of ULW-3 has its conductivity increase monotonically with concentration, from 25 md-ft at partial monolayer to 1000 md-ft at multilayer.
- Empirical correlations of the conductivity as a function of proppant areal concentration and confining stress are developed for the three ULWPs.

The conductivity correlations of ULWPs are applied in our fracture modeling simulator to predict the conductivity distribution for the ULWPs in a slickwater treatment. The predictions are then input into the reservoir simulation model developed in Chapter 2 to calculate the fracture productivity and ROFI. Below are selected key points obtained from the simulation study.

- At the same volume injection concentration, ULW-1 covers the most area with the least average conductivity; ULW-2 covers the second most area with the second least average conductivity; ULW-3 covers the second least area with the second largest average conductivity; sand covers the least area with the largest average conductivity.
- ULW-1, 2 and 3 have strong productivity advantages over sand in a 0.1 μD reservoir. The optimum pumping volume concentration is 4% for ULW-1, 4-6% for ULW-2, and 10% for ULW-3. The productivity advantage of using ULWPs decreases with increasing shale permeability.
- ULW-1 and ULW-2 have higher productivity benefits for longer production time, while ULW-3 has relatively constant productivity benefits over time.
- Economic study shows that, for a 0.1 μD shale and a possible ULWP price range of \$67-670/ft^3, both ULW-1 and 2 generate the best Return-On-Fracturing-Investment (ROFI) at partial monolayer concentration, while ULW-3 generates better ROFI at higher multilayer concentrations.
- For 1 year production and 0.1 μD shale reservoirs, the acceptable maximum price is \$10/lb for ULW-1, \$6/lb for ULW-2, and \$2.5/lb for ULW-3. The maximum price increases as production time increases.
- By adding ULWPs into sand, both the high conductivity zone at the bottom and low conductivity zone at the upper and deeper zones can be preserved, which benefits both short and long-term production.

In Chapter 5, new types of polymer-free foams are developed based on foam stability test applied on over fourteen surfactants. The rheology of three different surfactant solutions (A, B: regular surfactant foams; C: VES foam, chosen from the stability test) as well as their foams was evaluated in a recirculating loop under high pressure and temperature. The effects of shear rate, foam quality, temperature, pressure, and chemical composition of the base fluid are investigated.

- Based on the stability test, three foam formulations are chosen as our polymer-free foam candidates. Formulation A is 0.5 wt% Bio-terge AS 40, formulation B is 0.5 wt% Bio-terge AS 40 and 2wt% glycerol, and formulation C is 0.5 wt% viscoelastic surfactant.
- All three PFFs exhibit power-law rheological behavior. The regular surfactant foams (A and B) show shear thinning behavior at qualities above 60%, non-shear dependent behavior from 50% to 60% and shear thickening behavior below 50% (due to turbulence). The VES foams show shear thinning behavior at both low and high qualities.
- Temperature has a negligible effect on the rheology of regular surfactant foams A and B, while pressure increases foam viscosity for high quality foams (Q>50%). The pressure impact increases with increasing foam quality and decreases with increasing pressure.
- The aqueous foam A and B are both less viscous than 0.24 wt% polymer (guar) foams, while the VES foam C has an apparent viscosity similar to that of 0.24-0.36 wt% guar foams.
- New Rheological correlations have been developed to describe the aqueous foam rheology as a function of shear rate, quality, and pressure at typical parameter range for hydraulic fracturing.

In Chapter 6, the foam rheological correlations are incorporated in the fracturing model and reservoir simulation model to evaluate the polymer-free foam fracturing efficiency. The fracture geometry, propped area, conductivity, productivity, ROFI and

ROWI of the polymer-free foam A are compared with the slickwater for fracturing three typical permeability shale reservoirs. Through the study, we found that,

- For a low permeability shale (0.1, 1 μD), where the leak-off effect is relatively small, water creates the longest and narrowest fracture due to its low viscosity. As the shale permeability increases to 10 μD, the leak-off of the water becomes significant, making the foams outperform water in creating long fractures.
- For the whole production life of 0.1-1 μD shales and short production term of 10 μD shale, the 60-70% quality foams yield the best productivity since they create the largest stimulation areas and relatively large propped length. For the long term production of the 10 μD shale, the 60% foam and the slickwater yield the best production performance because they generate the longest propped length.
- The PFFs with a quality of 60-70% can generate a better ROFI than slickwater in 0.1-10 μD shales. As the production time and shale permeability increase, the ROFI benefits of using foams decrease.
- The ROWI benefits of using PFF increases with increasing foam quality, but decreases with increasing production time and shale permeability.
- Considering the economic profit (ROFI), water economy (ROWI) and sand consumption, the 60-70% quality foams carrying 40 mesh sand with a partial monolayer concentration of 0.04 v/v (0.88 lb/gal) can be the ideal treatment design for 0.1-10 μD shales.
- Both the ROFI and ROWI benefits of using the 60% quality foam instead of slickwater are larger for longer pumping time.

7.3 RECOMMENDATIONS FOR FUTURE WORK

Based on the present study, further research in the following areas is recommended:

I. In the fracture model, it is simply assumed that fracture width decreases at a certain rate during the shut-in process and proppants are fixed at the position once the shut-in process is done. A major improvement for simulating the post-treatment process is adding the flowing back model for slurry in a closing fracture to better understand how light proppant distributes after water flows back.

II. Our fracturing model assumes that there is no stress interference between neighboring fractures. For Plug & Perf completions, where several clusters closely arranged in each stage are stimulated simultaneously, the growth of each fracture generates a local stress change perturbing the growth of the surrounding fractures, which is known as stress shadow. To simulate this scenario, a reservoir geomechanics model should be added to evaluate the surrounding stress alteration due to fracture growing (Manchanda and Sharma 2013, Wu and Olson 2013). At the inlet boundary of each fracture, a pressure constraint calculated from wellbore flow is applied to calculate the fraction of the total flow rate entering each fracture.

III. The simulator is using the linear elasticity model proposed by PKN model to relate the fracture geometry with the net pressure. For ductile shales, where the deformation is plastic, the model would underestimate fracture width and overestimate fracture height and length. To improve that, an empirical plastic model (Zaki et al. 2004) is needed to replace the current model.

IV. This dissertation assumed a single bi-wing fracture and a few reactivated natural fractures intersecting it. In reality, the fractures are never that simple. Complex fractures develop and intersect natural fractures as elucidated in previous publications (Warpinski et al. 1993, Laubach et al. 2004, Fisher et al. 2005, Laubach and Gale 2006, Gale et al. 2007, Gale and Holder 2008, Weng et al. 2011, Olson et al. 2012, Wang et al. 2013) because of the local heterogeneity. Future research should simulate these complex fractures, transport of proppants in these fractures and calculate the final conductivity distributions. These complex fracture conductivity distributions should be simulated in a reservoir simulator to calculate its effect on production.

V. Due to the limit of the tubing we used, our foam loop has an upper pressure limit of 2000 psi and an upper temperature limit of 160 ^{o}F. To increase the pressure and temperature ranges, it is suggested to use finer stainless-steel tubing and pipes to rebuild a smaller experimental system in an oven.

VI. In current fracture modeling, foams are assumed to be homogeneous Newtonian fluids with a local apparent viscosity determined by shear rate, pressure and foam quality, when predicting proppant settling in foams. To better modeling proppant settling in foam, a dynamic settling test should be designed for foams under different shear rates and high pressure.

VII. To better model the injection of sand-light proppant mixture, a comprehensive settling test on proppant mixtures is recommended. The study will lead to a better understanding of the interaction between light proppant and sand in a dynamic settling process. The empirical interaction factor can be included in our fracture modeling simulator to better predict the distribution of proppant mixtures.

VIII. After pumping proppant mixtures inside fracture, some areas of the fracture face will be covered by sand and light proppant at different mixing ratios. The conductivity of those areas with mixed proppants is still not well understood. API conductivity can be conducted to evaluate the conductivity of proppant mixtures by mixing different kinds of proppants at different ratios.

IX. This study has had limited field verification. Collaboration with field operators is needed to confirm the fracturing performance of the polymer-free foams and ultra-light weight proppants seen in simulations of this study.

References

Fisher, M.K., Wright, C.A., Davidson, B.M., Goodwin, A.K., Fielder, E.O., Buckler, W.S., and Steinsberger, N.P. 2005. Integrating Fracture-Mapping Technologies To Improve Stimulations in the Barnett Shale. SPE Production & Facilities 20(2): 85-93.

Gale, J.F.W., and Holder, J. 2008. Natural Fractures in the Barnett Shale: Constraints on Spatial Organization and Tensile Strength with Implications for Hydraulic Fracture Treatment in Shale-Gas Reservoirs. ARMA, US Rock Mechanics Symposium, July.

Gale, J.F.W., Reed, R.M., and Holder, J. 2007. Natural Fractures in the Barnett Shale and Their Importance for Hydraulic Fracturing Treatments. AAPG Bulletin 91 (4): 603-22.

Laubach, S.E., and Gale, J.F.W. 2006. Obtaining Fracture Information for Low-Permeability (Tight) Gas Sandstones from Side Well Cores. Journal of Petroleum Geology, 147-158.

Laubach, S.E., Olson, J.E., and Gale J.F.W. 2004. Are Open Fractures Necessarily Aligned With Maximum Horizontal Stress? Earth and Planetary Science Letters 222: 191-5.

Manchanda, R. and Sharma, M.M. 2013. Time-Delayed Fracturing: A New Strategy in Multi-Stage, Multi-Well Pad Fracturing. Paper SPE 166489, presented in Annual Technical Conference and Exhibition, New Orleans, Louisiana, Sep. 30-Oct. 2.

Olson, J.E., Bahorich, B., and Holder, J. 2012. Examining Hydraulic Fracture-Natural Fracture Interaction in Hydrostone Block Experiments. Paper SPE 152618 presented at the SPE Hydraulic Fracturing Technology Conference held in The Woodlands, Texas, USA, Feb. 6-8.

Wang, W., Olson, J.E., and Prodanović, M. 2013. Natural and Hydraulic Fracture Interaction Study Based on Semi-Circular Bending Experiments. Paper SPE 168714 presented for presentation at the Unconventional Resources Technology Conference held in Denver, Colorado, USA, Aug. 12-14.

Warpinski, N.R., Lorenz, J.C., Branagan, P.T., Myal, F.R., and Gall, B.L. 1993. Examination of a Cored Hydraulic Fracture in a Deep Gas Well. SPE Production & Facilities 8(3): 150-8.

Weng, X., Kresse, O., Cohen, C., Wu, R., and Gu, H. 2011. Modeling of Hydraulic Fracture Network Propagation in a Naturally Fractured Formation. Paper SPE 140253 presented at the SPE Hydraulic Fracturing Technology Conference and Exhibition held in The Woodlands, Texas, USA, Jan. 24-26.

Wu, K. and Olson, J.E. 2013. Investigation of Critical In Situ and Injection Factors in Multi-Frac Treatments: Guidelines for Controlling Fracture Complexity. Paper

SPE 163821, presented in SPE Hydraulic Fracturing Technology Conference, The Woodlands, TX, Feb. 04-06.

Zaki, K.S., Wang, G., Meng, F., and Abou-Sayed, A.S. 2004. A 3-D Plastic Fracture Simulation To Assess Fracture Volumes in Compacting Reservoir. Presented to the 6th North America Rock Mechanics Symposium (NARMS), Houston, Texas, June 5-9.

Bibliography

Abé, H., Mura, T., and Keer, L. 1976. Growth-rate of a Penny-shaped Crack in Hydraulic Fracturing of Rocks. J. Geophys. Res., 81 (35): 6292-98.

Agarwal, R.G., Carter, R.D., and Pollock, C.B. 1979. Evaluation and Performance Prediction of Low-permeability Gas Wells Stimulated by Massive Hydraulic Fracturing. JPT: 362-72.

Baihly, J., Altman, R., Malpani, R., and Luo, F. 2010. Shale Gas Production Decline Trend Comparison Over Time and Basins. Paper SPE 135555, presented at the SPE Annual Technical Conference and Exhibition, Florence, Italy, Sep. 19-22.

Biot, M.A. and Medlin, W.L. 1985. Theory of Sand Transport in Thin Fluids. Paper SPE 14468, presented at the SPE Annual Technical Conference and Exhibition, Las Vegas, Nevada, Sep. 22-25.

Bird, R.B. 1965. Polymer Fluid Dynamics. Selected Topics in Transport Phenomena, Chemical Engineering Progress Symposium Series 58. 61, Chap. 6.

Bonilla, L.F. and Shah, S.N. 2000. Experimental Investigation on the Rheology of Foams. Paper SPE 59752. Presented at the SPE/CERI Gas Technology Symposium, Alberta, Canada, Apr. 3-5.

Brannon, H.D. and Starks II, T.R. 2008. The Impact of Effective Fracture Area and Conductivity on Fracture Deliverability and Stimulation Value. Paper SPE 116057, presented at the 2008 SPE Annual Technical Conference and Exhibition, Denver, Colorado, Sep. 21-24.

Brannon, H.D. and Starks II, T.R. 2009. Maximizing Return-On-Fracturing-Investment by Using Ultral-lightweight Proppants to Optimize Effective Fracture Area: Can Less Be More? Paper SPE 119385, presented at the SPE hydraulic fracturing technology conference, Woodlands, Texas, Jan. 19-21.

Brannon, H.D., Malone, M.R., Rickards, A.R., Wood, W.D., Randall Edgeman, J., and Bryant, J.L. 2004. Maximizing Fracture Conductivity with Proppant Partial Monolayers: Theoretical Curiosity or Highly Productive Reality? Paper SPE 90698, presented at the SPE Annual Technical Conference and Exhibition, Houston, Texas, USA, Sep. 26-29.

Brouwers, H.J.H. 2010. Viscosity of a Concentrated Suspension of Rigid Monosized Particles. Phys. Rev. E, 81 (05): 1402-12.

Bulova, M., Nosoca, K., Willberg, D., and Lassek, J. 2006. Benefits of the Novel Fiber-laden Low-viscosity Fluid Systems in Fracturing Low-permeability Tight Gas Formations. Paper SPE 102956, presented at the SPE Annual Technical Conference and Exhibition, San Antonio, Texas, Sep. 24-27.

Burke, L.H., Nevison, G.W., and Peters, W.E. 2011. Improved Unconventional Gas Recovery With Energized Fracturing Fluids: Montney Example. Paper SPE 149344. In: Proceedings of the 2011 SPE SPE Eastern Regional Meeting, Columbus, Ohio, USA, August 17-19.

Carman, P.C. 1937. Fluid Flow Through a Granular Bed. Trans. Inst. Chem. Eng. 15: 150-6.

Cinco, L.H., Samaniego V.F., and Dominguez A.N. 1978. Transient Pressure Behavior for a Well with Finite-Conductivity Vertical Fracture. Soc. Pet. Eng. J.: 253-64.

Cipolla, C.L., Lolon, E.P., Erdle, J.C., and Rubin, B. 2009a. Reservoir Modeling in Shale-Gas Reservoirs. Paper SPE 125530, presented at the SPE Eastern Regional Meeting, Charleston, West Virginia, USA, Sep. 23-25.

Cipolla, C.L., Lolon, E.P., Mayerhofer, M.J., and Warpinski, N.R. 2009b. The Effect of Proppant Distribution and Un-Propped Fracture Conductivity on Well Performance in Unconventional Gas Reservoirs. Paper SPE 119368 presented at the SPE Hydraulic Fracturing Technology Conference held in The Woodlands, Texas, USA, Jan. 19-21.

Cipolla, C.L., Warpinski, N.R., Mayerhofer, M.J., Lolon, E.P., and Vincent, M.C. 2008. The Relationship Between Fracture Complexity, Reservoir Properties, and Fracture-Treatment Design. Paper SPE 115769 presented at the SPE Annual Technical Conference and Exhibition held in Denver, Colorado, USA, Sep. 21-24.

Clark, N.O. and Blackman, M. 1948. The Degree of Dispersion of the Gas Phase in Foam. Faraday Soc. Than. 44: 1-7.

Cohen, C.E., Abad, C., Weng, X., England, K., Phatak, A., Kresse, O., Nevvonen, O., Lafitte., V., and Abivin, P. 2013. Optimum Fluid and Proppant Selection for Hydraulic Fracturing in Shale Gas Reservoirs: a Parametric Study Based on Fracturing –to-Production Simulations. Paper SPE 163876 presented at the SPE Hydraulic Fracturing Technology Conference, The woodlands, TX, USA, Feb. 4-6.

Cohen, C.E., Xu, W., Weng, X., and Tardy, P.M.J. 2012. Production Forecast After Hydraulic Fracturing in Naturally Fractured Reservoir: Coupling a complex Fracturing Simulator and a Semi-Analytical Production Model. Paper SPE 152541 presented at the SPE Hydraulic Fracturing Technology Conference and Exhibition held in The Woodlands, Texas, USA, Feb. 6-8.

Coulter, G.R., Benton, E.G., and Thomson, C.L. 2004. Water Fracs and Sand Quantity: A Barnett Shale Example. Paper SPE 90891, presented at the SPE Annual Technical Conference and Exhibition, Houston, Texas, Sep. 26-29.

Darin, S.R. and Huitt, J.L. 1960. Effect of a Partial Monolayer of Propping Agent on Fracture Flow Capacity. Petroleum Transactions, AIME, 219: 31-37.

Duenckel, R., Conway, M.W., Eldred, B., and Vincent, M.C. 2012. Proppant Diagenesis - Integrated Analyses Provide New Insights into Origin, Occurrence, and Implications for Proppant Performance. SPE Production & Operations, 27 (2): 131-144.

Economides, M.J. and Martin, T. 2007. Modern Fracturing, 1st Edition.

Einstein, A. 1906. Effect of Suspended Rigid Spheres on Viscosity. Ann. Phys. 19: 289-306.

Evans, R.D. and Civan, F. 1994. Characterization of Non-Darcy Multiphase Flow In Petroleum Bearing Formations. Report, U.S. DOE Contract No. DE-AC22-90BC14659.

Fisher, M.K., Wright, C.A., Davidson, B.M., Goodwin, A.K., Fielder, E.O., Buckler, W.S., and Steinsberger, N.P. 2005. Integrating Fracture-Mapping Technologies To Improve Stimulations in the Barnett Shale. SPE Production & Facilities 20(2): 85-93.

Fredd, C.N., McConnell, S.B., Boney, C.L., and England, K.W. 2000. Experimental Study of Hydraulic Fracture Conductivity Demonstrates the Benefits of Using Proppants. Paper SPE 60326, presented at the SPE Rocky Mountain Regional/Low-Permeability Reservoirs Symposium and Exhibition, Denver, Colorado, March 12-15.

Fredd, C.N., McConnell S.B., Boney C.L., and England K.W. 2001. Experimental Study of Fracture Conductivity for Water-Fracturing and Conventional Fracturing Applications. SPE Journal 6(3): 288-98.

Friehauf, K. and Sharma, M.M. 2009. A New Compositional Model for Hydraulic Fracturing with Energized Fluids. SPE Production & Operations, 24 (4): 562-72.

Gadde P.B., Liu Y., Norman J., Bonnecaze R., and Sharma M.M. 2004. Modeling Proppant Settling in Water-Fracs. Paper SPE 89875. In: Proceedings of the 2004 SPE Annual Technical Conference and Exhibition, Houston, September 26-29.

Gadde, P.B. and Sharma, M.M. 2005. The Impact of Proppant Retardation on Propped Fracture Lengths. Paper SPE 97106, presented at the SPE Annual Technical Conference and Exhibition, Dallas, Texas, Otc. 9-12.

Gale, J.F.W. and Holder, J. 2008. Natural Fractures in the Barnett Shale: Constraints on Spatial Organization and Tensile Strength with Implications for Hydraulic Fracture Treatment in Shale-Gas Reservoirs. ARMA, US Rock Mechanics Symposium, July.

Gale, J.F.W., Reed, R.M., and Holder, J. 2007. Natural Fractures in the Barnett Shale and Their Importance for Hydraulic Fracturing Treatments. AAPG Bulletin 91 (4): 603-22.

Gaurav, A. 2010. Ultra-Light Weight Proppants in Shale Gas Fracturing. Thesis of Master of Science in Engineering. University of Texas at Austin.

Gaurav, A., Dao, E.K., and Mohanty, K.K. 2010. Ultra-lightweight Proppants for Shale Gas Fracturing. Paper SPE 138319, tight gas completions conference, San Antonio, Texas, Nov. 2-3.

Gaurav, A., Gu, M., and Mohanty, K.K. 2012. Improvement of Fracturing for Gas Shales. RPSEA Final Report 07122-38, August.

Geertsma, J. and de Klerk, F.A. 1969. A Rapid Method of Predicting Width and Extent of Hydraulically Induced Fractures. J. Pet. Tech., 21: 1571-81.

Gidley, J.L., Holditch, S.A., Nierode, D.E., and Veatch Jr., R.W. 1989. Recent Advances in Hydraulic Fracturing. SPE Monograph 12, Society of Petroleum Engineers, Richardson, TX.

Gu, H. and Leung, K.H. 1993. 3D Numerical Simulation of Hydraulic Fracture Closure with Application to Minifracture Analysis. JPT, p: 206-11.

Harris, P.C. 1989. Effects of Texture on Rheology of Foam Fracturing Fluids. SPE Production Eng. 4 (3): 249-57.

Harris, P.C. 1995. A Comparison of Mixed Gas Foams with N_2 and CO_2 Foam Fracturing Fluids on a Flow Loop Viscometer. SPE Prod. & Faci. 10 (3): 197-203.

Harris, P.C. 1996. Rheology of Crosslinked Foams. SPE Prod. & Faci. 11 (2): 113-16.

Harris, P.C., and Reidenbach, V.G. 1987. High-Temperature Rheological Study of Foam Fracturing Fluids. J. of Petroleum Tech. 39 (5): 613-19.

Heller, R. and Zoback, M. 2013. Laboratory Measurements of Matrix Permeability and Slippage Enhanced Permeability in Gas Shales. Paper SPE 168856 presented at the Unconventional Resources Technology Conference held in Denver, Colorado, USA, Aug. 12-14.

Herzhaft, B., Kakadjian, S., and Moan, M. 2005. Measurement and Modeling of the Flow Behavior of Aqueous Foams Using a Recirculating Pipe Rheometer. Colloids and Surfaces A: Physicochem. Eng. Aspects. 263: 153-64.

Howard, G.C. and Fast, C.R. 1970. Hydraulic Fracturing, Monograph Series, SPE, Richardson, 2, 55.

Huitt, J.L. and McGlothlin, B.B. 1958. The Propping of Fractures in Formations Susceptible to Propping Sand Embedment. Dill. and Prod. Pra., API.

Hutchins, R.D. and Miller, M.J. 2005. A Circulating-foam Loop for Evaluating Foam at Conditions of Use. SPE Production & Facilities. 20 (4): 286-94.

Jacot, R.H., Bazan, L.W., and Meyer, B.R. 2010. Technology Integration - A Methodology to Enhance Production and Maximize Economics in Horizontal

Marcellus Shale Wells. Paper SPE 135262 presented at the SPE Annual Technical Conference and Exhibition, Florence, Italy, Sep. 19-22.

Kendrick, D.E., Puskar, M.P., and Schlotterbeck, S.T. 2005. Ultralightweight Proppants: A Field Study in the Big Sandy Field of Eastern Kentucky. Paper SPE 98006, presented at the 2005 SPE Eastern Regional Meeting held in Morgantown, W.V., Sep. 14-16.

Khade, S.D. and Shah, S.N. 2002. New Empirical Friction Loss Correlation For Foam Fluids in Coiled Tubing. Paper SPE 74810. In: Proceedings of the 2002 SPE/ICoTA Coiled Tubing Conference and Exhibition, Houston, April 9-10.

Khan, A.M. 2013. Multi-Frac Treatments in Tight Oil and Shale Gas Reservoirs: Effect of Hydraulic Fracture Geometry on Production and Rate Transient. Thesis of Master of Science in Engineering. University of Texas at Austin.

Khristianovitch, S.A. and Zheltov, Y.P. 1955. Formation of Vertical Fractures by Means of Highly Viscous Fluids. In: Proceeding of the 4th World Petroleum Congress, Rome, Italy. 2:579-86.

King, G.E. 2010. Thirty Years of Gas Shale Fracturing: What Have We Learned? Paper SPE 133456, SPE Annual Technical Conference and Exhibition, Florence, Italy, Sept. 19-22.

Kovscek, A.R. and Radke, C.J. 1994. Fundamentals of Foam Transport in Porous Media. Advances in Chemistry Series, Washington, DC. 242: 115-63

Laubach, S.E. and Gale, J.F.W. 2006. Obtaining Fracture Information for Low-Permeability (Tight) Gas Sandstones from Side Well Cores. Journal of Petroleum Geology, 147-158.

Laubach, S.E., Olson, J.E., and Gale J.F.W. 2004. Are Open Fractures Necessarily Aligned With Maximum Horizontal Stress? Earth and Planetary Science Letters 222: 191-5.

Lee, D.I. 1970. Packing of Spheres and Its Effect on the Viscosity of Suspensions. J. Paint Technology. 42: 579-87.

Lemlich, R. 1978. Predition of Changes in Bubble Size Distribution Due to Interbubble Gas diffusion in a Foam. Ind. Eng. Chem. Fundam. 17(2): 89-93.

Liu, Y. 2006. Settling and Hydrodynamic Retardation of Proppants in Hydraulic Fractures. Dissertation of Doctor of Phylosophy. University of Texas of Austin.

Mahoney, R.P., Soane, D., Kincaid, K.P., Herring, M., and Snider, P.M. 2013. Self-suspending Proppant. Paper SPE 163818, presented at the SPE hydraulic fracturing technology conference, Woodlands, Texas, Feb. 4-6.

Manchanda, R. and Sharma, M.M. 2013. Time-Delayed Fracturing: A New Strategy in Multi-Stage, Multi-Well Pad Fracturing. Paper SPE 166489, presented in Annual Technical Conference and Exhibition, New Orleans, Louisiana, Sep. 30-Oct. 2.

Mayerhofer, M.J., Lolon, E.P., Youngblood, J.E., and Heinze, J.R. 2006. Integration of Microseismic Fracture Mapping Results With Numerical Fracture Network Production Modeling in the Barnett Shale. Paper SPE 102103 presented at the SPE Annual Technical Conference and Exhibition held in San Antonio, Texas, USA, Sep. 24-27.

McDaniel, B.W. 2010. Horizontal Wells with Multi-Stage Fracs Provide Better Economics for Many Lower Permeability Reservoirs. Paper SPE 133427. SPE Asia Pacific Oil and Gas Conference and Exhibition, Brisbane, Queensland, Australia, Oct. 18-20.

Mcguire, W.J. and Sikora, V.J. 1960. The Effect of Vertical Fractures on Well Productivity. Trans., AIME 219: 401-03.

Meyer, B.R. and Lucas, W.B. 2011. A Discrete Fracture Network Model for Hydraulically Induced Fractures: Theory, Parametric and Case Studies. Paper SPE 140514 presented at the SPE Hydraulic Fracturing Technology Conference held in The Woodlands, Texas, USA, Jan. 24-26.

Mooney, M. 1951. The Viscosity of a Concentrated Suspension of Spherical Particles. J. Colloid Sci. 6: 162-70.

Myers, R., Potratz, J., and Moody, M. 2004. Field Application of New Lightweight Proppant in Appalachian Tight Gas Sandstones. Paper SPE 91469, presented at the 2004 SPE Eastern Regional Meeting held in Charleston, West Virginia, USA, Sep. 15-17.

Nakhwa A.D., Huggins K., and Sweatman R. 2013. New Technologies in Fracturing for Shale Gas Wells Are Addressing Environmental Issues. Paper SPE 164270. In: Proceedings of the 2013 SPE Middle East Oil and Gas Show and Conference, Manama, Bahrain, March 10-13.

Newell, R. 2011. Shale Gas and the Outlook for U.S. Natural Gas Markets and Global Gas Resources. Presented to the Organization for Economic Cooperation and Development (OECD), Paris, France.

Nordgren, R.P. 1972. Propagation of a Vertical Hydraulic Fracture. Society of Petroleum Engineering Journal, 253: 306-14.

Olson, J.E. and Wu, K. 2012. Sequential versus Simultaneous Multi-zone Fracturing in Horizontal Wells: Insights from a Non-planar, Multi-frac Numerical Model. Paper SPE 152602 presented at the SPE Hydraulic Fracturing Technology Conference held in The Woodlands, Texas, USA, Feb. 6-8.

Olson, J.E., Bahorich, B., and Holder, J. 2012. Examining Hydraulic Fracture-Natural Fracture Interaction in Hydrostone Block Experiments. Paper SPE 152618 presented at the SPE Hydraulic Fracturing Technology Conference held in The Woodlands, Texas, USA, Feb. 6-8.

Ouyang, L., Yango, T., Zhu, D., and Hill, A.D. 2012. Theoretical and Experimental Modeling of Residual Gel Filter-Cake Displacement in Propped Fractures. SPE Production & Operations. 27(4): 363-70.

Palisch, T.T., Vincent, M.C., and Handren, P.J. 2010. Slickwater Fracturing: Food for Thought. SPE Production & Operations. 25(3): 327-44.

Peles, J., Wardlow, R.W., Cox, G., Haley, W., Dusterhoft, R., Walters, H.G., and Weaver, J. 2002. Maximizing Well Production With Unique Low Molecular Weight Frac Fluid. Paper SPE 77746. Presented at the SPE Annual Technical Conference and Exhibition, San Antonio, Texas, Sep. 29 - Oct 2.

Perkins, T.K. and Kern, L.R. 1961. Widths of Hydraulic Fractures. J. Pet. Tech., 13: 937-49.

Posey, D. and Strickland, B. 2005. The Effect of Using a Lightweight Proppant in Treatment of a Low-Permeability, Dry Gas Reservoir: A Case Study. Paper SPE 97998, presented at the 2005 SPE Eastern Regional Meeting, Morgantown, West Virginia, Sep. 14-16.

Princen, H.M. and Kiss, A.D. 1989. Rheology of Foams and Concentrated Emulsions IV. An Experiment Study of the Shear Viscosity and Yield Stress of Concentrated Emulsions. J. Colloid Interface Sci. 128: 176-86.

Quemada, D. 1977. Rheology of Concentrated Disperse Systems and Minimum Energy Dissipation Principle. Rheol. Acta. 16: 82-94.

Reidenbach, V.G. Harris, P.C., Lee, Y.N., and Lord, D.L. 1986. Rheological Study of Foam Fracturing Fluids Using Nitrogen and Carbon Dioxide. SPE Production Engineering. 1 (1): 31-41.

Ribeiro, L.H. and Sharma, M.M. 2013. A New 3D Compositional Model for Hydraulic Fracturing with Energized Fluids. SPE Prod. & Operations, 28(3): 259-67.

Rickards, A.R., Brannon, H.D., Wood, W.D., and Stephenson, C.J. 2003. High Strength, Ultra-Lightweight Proppant Lends New Dimensions to Hydraulic Fracturing Applications. Paper SPE 84308, presented at the SPE Annual Technical Conference and Exhibition, Denver, Colorado, USA, Oct. 5-8.

Rosen, M.J. 1989. Surfactants and Interfacial Phenomena. Second Edition. John Wiley & Sons, New York City 276-303.

Rubin, B. 2010. Accurate Simulation of Non-Darcy Flow in Stimulated Fractured Shale Reservoirs. Paper SPE 132093 presented at the SPE Western Regional Meeting, Anaheim, California, USA, May 27-29.

Sani, A.M., Shah, S.N., and Baldwin, L. 2001. Experimental Investigation of Xanthan Foam Rheology. Paper SPE 67263. Presented at the SPE Production and Operations Symposium, Oklahoma City, Oklahoma, March 24-27.

Schein, G.W., Carr, P.D., Canan, P.A., and Richey, R. 2004. Ultra Lightweight Proppants: Their Use and Application in the Barnett Shale. Paper SPE 90838, presented at the SPE Annual Technical Conference and Exhibition, Houston, Texas, USA, Sep. 26-29.

Schramm, L.L. 1994. Foam Sensitivity to Crude Oil in Porous Media. Advances in Chemistry Series, Washington, DC. 242: 165-197.

Settari, A. and Cleary, M.P. 1986. Development and Testing of a Pseudo-three dimensional Model of Hydraulic Fracture Geometry. SPE Prod. Eng., 1 (6): 449-66.

Sita Ram Sarma, D.S.H., Pandit, J., and Khilar, K.C. 1988. Enhancement of Stability of Aqueous Foams by Addition of Water-Soluble Polymers- Measurements and Analysis, J. of Colloid and Interface Science. 124(1): 339-48.

Sousa, J.L.S., Carter, B.J., and Ingraffea, A.R. 1993. Numerical Simulation of 3D Hydraulic Fracture Using Newtonian and Power-law Fluids. Int. J. Rock Mech. Min. Sci. & Geomech. Abstr., 30: 1265-71.

Sudhakar, D.K. and Shah, S.N. 2002. New Empirical Friction Loss Correlation for Foam Fluids in Coiled Tubing. Paper SPE 74810. Presented at the SPE/ICoTA Coiled Tubing Conference and Exhibition, Houston, Texas, April 9-10.

Sudhakar, D.K. and Shah, S.N. 2003. New Rheological Correlations for Guar Foam Fluids. Paper SPE 88032. Presented at the SPE Production and Operations Symposium, Oklahoma City, Oklahoma, March 22-25.

Tannich, J.D. and Nierode, D.E. 1985. The Effect of Vertical Fractures on Gas Well Productivity. Paper SPE 15902, presented at the SPE Annual Technical Conference and Exhibition, New Orleans, Louisiana, October 5-8.

Taylor, G.I. 1932. The Viscosity of a Fluid Containing Small Drops of Another Fluid. Proc. R. Soc. Ser. A. 138: 41-45.

Thompson, J.M., M'Angha, V.O., and Anderson, D.M. 2011. Advancements in Shale Gas Production Forecasting – A Marcellus Case Study. Paper SPE 144436 presented at the SPE Americas Unconventional Gas Conference and Exhibition, The Woodlands, Tx, USA, June 14-16.

Tinni, A., Fathi, E., Agarwal, R., Sondergeld, C., Akkutlu, Y., and Rai, C. 2012. Shale Permeability Measurements on Plugs and Crushed Samples. Paper SPE 162235 presented at the SPE Canadian Unconventional Resources Conference held in Calgary, Alberta, Canada, Oct. 30-Nov. 1.

Tinsley, J.M., Williams Jr., J.R., Tiner, R.K., and Malone, W.T. 1969. Vertical Fracture Height – Its Effect on Steady-State Production Increase. JPT, AIME 246: 633-38.

Wang, W., Olson, J.E., and Prodanović, M. 2013. Natural and Hydraulic Fracture Interaction Study Based on Semi-Circular Bending Experiments. Paper SPE 168714 presented for presentation at the Unconventional Resources Technology Conference held in Denver, Colorado, USA, Aug. 12-14.

Warpinski, N.R., Kramm, R.C. Heinze, J.R., and Waltman, C.K. 2005. Comparison of Single- and Dual- array Microseismic Mapping Techniques in the Barnett Shale. Paper SPE 95568, presented at the 2005 SPE Annual Technical Conference and Exhibition, Dallas, Texas, Oct. 9-12.

Warpinski, N.R., Lorenz, J.C., Branagan, P.T., Myal, F.R., and Gall, B.L. 1993. Examination of a Cored Hydraulic Fracture in a Deep Gas Well. SPE Production & Facilities 8(3): 150-8.

Warpinski, N.R., Mayerhofer, M.J., Vincent, M.C., Cipolla, C.L, and Lolon, E.P. 2008. Stimulating Unconventional Reservoirs: Maximizing Network Growth While Optimizing Fracture Conductivity. Paper SPE 114173 presented at the SPE Unconventional Reservoirs Conference held in Keystone, Colorado, USA, Feb. 10-12.

Warpinski, N.R., Mayerhofer, M.J., Vincent, M.C., Cipolla, C.L., and Lolon, E.P. 2009. Stimulating Unconventional Reservoir: Maximizing Network Growth While Optimizing Fracture Conductivity. J. of Canadian Petro. Tech. 48 (10): 39-51.

Weng, X., Kresse, O., Cohen, C., Wu, R., and Gu, H. 2011. Modeling of Hydraulic Fracture Network Propagation in a Naturally Fractured Formation. Paper SPE 140253 presented at the SPE Hydraulic Fracturing Technology Conference and Exhibition held in The Woodlands, Texas, USA, Jan. 24-26.

Williams, B.B. 1970. Fluid Loss from Hydraulically Induced Fractures. JPT, AIME 249: 882-88.

Williams, B.B., Gidley, J.L., and Schechter, R.S. 1979. Acidizing Fundamentals. Monograph Series, SPE, Richardson, TX (1979) 6.

Wood, W.D., Brannon, H.D., Rickards, A.R., and Stephenson, C. 2003. Ultra-Lightweight Proppant Development Yields Exciting New Opportunities in Hydraulic Fracturing Design. Paper SPE 84309, presented at the SPE Annual Technical Conference and Exhibition, Denver, Colorado, USA, Oct. 5-8.

Wu, K. and Olson, J.E. 2013. Investigation of Critical In Situ and Injection Factors in Multi-Frac Treatments: Guidelines for Controlling Fracture Complexity. Paper SPE 163821, presented in SPE Hydraulic Fracturing Technology Conference, The Woodlands, TX, Feb. 04-06.

Xu, B., Hill, A.D. and Zhu, D. 2011. Experimental Evaluation of Guar-Fracture-Fluid Filter-Cake Behavior. SPE Production & Operations. 26(4): 381-7.

Yu, W. and Sepehrnoori, K. 2013. Optimization of Multiple Hydraulically Fractured Horizontal Wells in Unconventional Gas Reservoirs. Paper SPE 164509 presented at the SPE Production and Operations Symposium held in Oklahoma City, Oklahoma, USA, Mar. 23-26.

Zaki, K.S., Wang, G., Meng, F., and Abou-Sayed, A.S. 2004. A 3-D Plastic Fracture Simulation To Assess Fracture Volumes in Compacting Reservoir. Presented to the 6th North America Rock Mechanics Symposium (NARMS), Houston, Texas, June 5-9.

Zhang, J., Kamenov, A., Zhu, D., and Hill, A.D. 2013. Laboratory Measurement of Hydraulic Fracture Conductivities in the Barnett Shale. Paper SPE 163839 presented at the SPE Hydraulic Fracturing Technology Conference held in The Woodlands, Texas, USA, Feb. 4-6.

Zhou, J., Jung, C.M., Chenevert, M.E., and Sharma, M.M. 2013. A Systematic Approach to Petrophysical Characterization of Organic-Rich Shales in Barnett and Eagle Ford Formations. Paper SPE 168792 presented at the Unconventional Resources Technology Conference held in Denver, Colorado, USA, Aug. 12-14.

Vita

Ming Gu graduated from Bashu High school in his hometown of Chongqing, China in 2003. He entered Tsinghua University in fall of 2003. He received a Bachelor of Engineering degree in 2007 and a Master of Engineering degree in 2009 from Tsinghua University. In fall of 2009, he enrolled in the department of Petroleum Engineering at the University of Texas at Austin, where he has worked under the supervision of Dr. Kishore K. Mohanty for the completion of his Ph.D. degree.

Permanent e-mail address: gumingcqcn@gmail.com

This dissertation was typed by the author.